

Synthesis of Aluminum-Aluminum Nitride Nanocomposites by Gas-Liquid Reactions

by

Cecilia Borgonovo

A Thesis

Submitted to the Faculty

of

WORCESTER POLYTECHNIC INSTITUTE

in partial fulfillment of the requirements for the

Degree of Doctor of Philosophy

in

Material Science & Engineering

May 2013

APPROVED:

Makhlouf M. Makhlouf, Advisor

Director of Advanced Casting Research Center

Richard D. Sisson Jr.

George F. Fuller Professor

Director of Manufacturing and Materials Engineering

Abstract

An innovative method has been developed for synthesizing aluminum-aluminum nitride nanocomposite materials wherein the reinforcing nano-sized aluminum nitride particles are formed in-situ in a molten aluminum alloy. This method, which circumvents most issues associated with the traditional ways of making nanocomposites, involves reacting a nitrogen-bearing gas with a specially designed molten aluminum alloy. The method ensures excellent dispersion of the nanoparticles in the matrix alloy, which is reflected in enhanced mechanical properties. In this thesis, the author reviews the limitations of the conventional methods of manufacturing nanocomposites and develops thermodynamic and kinetic models that allow optimizing the in-situ gas-liquid process to produce quality nanocomposite material. Also, in this thesis, the author reports the measured room temperature and elevated temperature tensile properties of materials that were made by the optimized process and compares the measured values to their counterparts obtained for the base alloy. A 75 pct. increase in room temperature yield strength is obtained when the base alloy is reinforced with one pct. nano-size aluminum nitride particles and this significant increase in yield strength is accompanied by only negligible loss of ductility.

Acknowledgments

I would like to express all my gratitude to my advisor, Professor Makhlouf M. Makhlouf. He has always been available for me and patient in trying to follow my scheme of thoughts. He has believed I could develop excellent experimental skills and always valued my mathematical and analytical capabilities. Nevertheless he has surprised me every day with the incredible amount of knowledge in various engineering fields that he showed me at every meeting. He has inspired my research and helped me to understand what I am really good at.

I sincerely thank Professor Diran Apelian for being of such guidance for me not only as advisor for my MS thesis, but also as a constant presence in my life since I arrived to this country. He gave me the chance to pursue my education at WPI and supported me in many ways.

I thank Professor Richard Sisson for highlighting the importance of taking the engineering education out of the university and into society. He has taught me to master my ability to communicate my ideas and my work in a professional yet effective manner.

My gratitude also goes to Dr. James Bredt for being always available to discuss my operational issues and for providing me the 3D printed ceramic rotors.

I also thank Carol Garofoli, Renee Brodeur and Maureen Plunkett for the continuous assistance in my work.

I thank my colleagues, Lance, Libo, Yangyang, Hao. I also want to thank Shaymus, Aaron and Luke for supporting me in the final stage of my work. Thanks to Roger Steele for the assistance with the equipment.

Ultimately I thank my family, that has accepted to give up to some time together for my future and has always supported me and encouraged me during the most difficult times.

Table of Contents

Abstract	i
Acknowledgments.....	ii
Table of Contents.....	iii
Executive Summary.....	iv
Paper I: <i>Processing Methods for Aluminum Nanocomposite Materials</i>	1
Paper II: <i>Synthesis of Aluminum-Aluminum Nitride Nanocomposites</i>	45
<i>by Gas-Liquid Reactions – Thermodynamic and Kinetic</i>	
<i>Considerations</i>	
Paper III: <i>Synthesis of Aluminum-Aluminum Nitride Nanocomposites</i>	71
<i>by Gas-Liquid Reactions – Microstructural Evaluation and</i>	
<i>Mechanical Properties</i>	
Appendix 1: Matlab-Based Calculation Code for the Dispersion Factor (DI)...	95
Appendix 2: Compilation of Articles by the Authors on In-Situ Gas-Liquid	
Process.....	103

Executive Summary

Motivation

Current aluminum casting alloys are not useful at temperatures exceeding 200°C and pressures around 200 MPa, which are conditions that prevail in many applications such as the crown area of automotive pistons. Nano-structured composite materials provide high strength, wear resistance, hardness, and exceptional microstructure stability when used in these severe conditions², and therefore they are suitable for such applications. Nanocomposite materials ensure performances far superior than alloys strengthened by micro-size particles. For example, the tensile strength of a 1 volume pct. Si₃N₄ reinforced nanocomposite in which the average size of the SiC particles is 10 nm is comparable to that of a 15 volume pct. SiC reinforced microcomposite in which the average size of the SiC particles is 3.5 μm. Also, Ren and Chen [3] fabricated 7075 aluminum matrix reinforced with SiC nanoparticles -50 nm- via powder metallurgy, and noticed a significant increase in wear resistance and resistance to high temperature creep compared to the composite reinforced by 13 μm SiC particles. However, and despite their attractive properties, the use of nanocomposite materials in structural applications has been limited; mainly because robust economical methods for making these materials have not been developed. The majority of the currently available methods for fabricating nanocomposite materials fail to produce a homogeneous distribution of the reinforcing particles in the matrix alloy and the ones that do are either not cost effective or are not easily scalable to industrial application.

A class of novel nanocomposite materials, wherein the nanoparticles are formed in-situ within the matrix by means of a chemical reaction has been developed. Among these methods is the gas injection process, which involves introducing a reactive gas into a molten alloy at temperatures that promote chemical reactions that lead to formation of the reinforcing nano size particles. Among the many advantages of this method are that (1) it can produce uniform distribution of nanoparticles in the metal matrix, (2) it ensures absence of contaminants from the interfaces between the particles and the matrix, and (3) it is easily scalable and inexpensive.

This work focuses on the synthesis of aluminum-aluminum nitride nanocomposite materials. Aluminum nitride has low density (3.026 g/cm³), low coefficient of thermal expansion ($4.5 \times 10^{-6} \text{ K}^{-1}$, in the temperature range 293-673 K), and good thermal conductivity (110-170 W m⁻¹K⁻¹), which makes it attractive as reinforcing particles in aluminum alloys. Moreover, aluminum nitride may be easily wetted by aluminum, and it is chemically stable and interfacial reactions between it and the aluminum matrix do not occur. However, the use of nanosize aluminum nitride particles as a reinforcing phase in metal matrix composites has not been widely spread because of its very high cost.

Objectives

The objectives of this work are:

- (1) Establish the feasibility of the gas-liquid in-situ method for the economical production of aluminum-aluminum nitride nanocomposites; this entails:
 - (i) Establishing the thermodynamic and kinetic principles that govern the process and,
 - (ii) Develop mathematical models based on thermodynamic and kinetic principles, which allow determining the optimum process parameters for the process
- (2) Design and build a robust, scalable apparatus for making aluminum-aluminum nitride nanocomposite materials and produce sample materials for characterizing the microstructure and measuring the room temperature and elevated temperature tensile properties of the material.

Methodology

1. An extensive review of the literature pertaining to methods of manufacturing aluminum matrix nanocomposite materials has been performed (Chapter 1: Paper I). Each process is described and its advantages and drawbacks are highlighted. Both ex-situ methods, wherein external reinforcing particles are added to the matrix, and in-situ methods, wherein the reinforcing particles are synthesized directly in the matrix by exothermic reactions, are discussed.
2. Thermodynamic and kinetic considerations associated with the in-situ gas-liquid reaction have been addressed (Chapter 2: Paper II) including the effect of oxygen on and the catalytic effect of magnesium and lithium. The rate of formation of AlN has been mathematically modeled and a sensitivity analysis of the process variables has been performed.
3. The effect of the following process parameters: (i) gas composition (nitrogen, ammonia or a combination of the two), (ii) matrix composition (2.5 weight pct. Li, vs. 5 weight pct. Li), (iii) processing time, and (iv) impeller rotational speed on the amount, size and distribution of AlN has been studied (Chapter 3: In Paper III). Particle distribution in the matrix is quantified by a distribution index (DI) calculated by a Matlab-based program (Appendix 1). Concentrated nanocomposite materials have been diluted with aluminum alloy A356 to produce 0.5 volume pct. AlN, 1 volume pct. AlN, and 2 volume pct. AlN materials. Samples of these materials were used to measure the tensile properties of the material at room and high temperature (300°C).

Outcomes

The various pathways to manufacturing aluminum matrix nanocomposites have been presented and discussed in this critical review. It is clear that the challenges we face in manufacturing nanocomposite materials for structural applications are daunting. Our ability to achieve a homogeneous distribution of the reinforcing particles in the metal matrix and in the same time assure ease of scalability of the manufacturing process is a critical issue. Ex-situ methods wherein externally manufactured nanoparticles are introduced into the

metallic alloy are sub-optimal in this sense. They tend to yield materials that are plagued by particle clustering, interface de-bonding, contamination, and porosity; and the processes are not cost effective. Homogeneous distribution of the nanoparticles is more readily attained by in-situ processing methods wherein the reinforcing particles are created directly in the aluminum alloy. One of these methods involves the reaction between a gas and a liquid. Synthesizing Al/AlN nanocomposite materials by injecting a nitrogen bearing gas into molten aluminum is thermodynamically and kinetically feasible, provided that the oxygen content of the system is maintained at a low level. Thermodynamic and kinetic analysis of the process has been carried out and showed that attaining this low oxygen content may be helped by alloying aluminum with magnesium and/or lithium; with lithium being the more efficient of the two elements in this regard. As little as 1 wt. pct. lithium is sufficient to suppress oxidation of aluminum and promote its nitridation. The analysis also shows that an increase in process temperature significantly increases the density of reactive gas bubbles. In addition, the analysis shows that a relatively high flow rate of the reactive gas increases the gas-liquid interfacial area. This 'additional' gas-liquid interfacial area affects diffusion at the gas-liquid interface and positively affects the size and distribution of the AlN particles in the matrix alloy. Finally, the analysis shows that an increase in the pressure above the melt increases the density number of reactive gas bubbles and reduces the bubble volume; as a result, the bubbles rise more slowly, their residence time in the melt increases, and their coalescence is minimized. Experiments have been carried out to assess the effect of process variables on vol.% of AlN, size of AlN, clusters of AlN. The experimental results of the in-situ gas liquid process have been presented. Particle size has been brought down to around 60 nm for high impeller rotational speed and particle clusters are almost absent. It has been noticed that ammonia enhances the nitridation reaction as well as high amounts of Li. This is most likely due to their oxygen-getter actions. Impeller speed mainly affect particle size by affecting the size of the gas bubbles. A distribution index (DI) between 0 and 1 has been defined and used to quantitatively evaluate particle dispersion. Ultrasonic energy has shown to be efficient in degassing the material. Mechanical properties both at room and high temperature (300 °C) show a dramatic increase. The increase in YS and Young's modulus is almost 100% at room temperature while the UTS is about 46% for 2%vol. of AlN. The strengthening effect of the particle is likely to Orowan bowing, but further TEM investigation will be carried out to confirm this. UTS and YS have been both improved by around 50% at high temperature but the most enhancement is attained for the Young's modulus which increases of around 200%.

References

1. F.S.Silva, *Engineering Failure Analysis*, 2006, **13**, 480-492.
2. D.B.Miracle, *Composites Science and Technology*, 2005, **65**, 2526-2540.
3. Z.Ren and S. L. I. Chen: 'Mechanical properties of nanometric particulates reinforced aluminum composites', *The University of New South Wales, Poster*,
URL:http://www.arclightmetals.org.au/archive/content/documents/workshop_posters/2007/Poster%20PS2-17%20Zheng%20Ren.pdf

Processing Methods for Aluminum Nanocomposite Materials

Cecilia Borgonovo and Makhoulouf M. Makhoulouf

Department of Mechanical Engineering

Worcester Polytechnic Institute

Worcester, MA 01609

Keywords: aluminum, composite materials, nanocomposites, manufacturing methods, ex-situ processing, in-situ processing, gas-liquid reactions

Abstract

The use of aluminum alloys in automotive and aerospace applications has increased significantly in the last few decades mainly because of their high strength-to-weight ratio, which allows improvements in vehicle fuel efficiency while answering the strict environmental regulations imposed on car manufacturers by the United States and many European governments. Unfortunately, the strength of aluminum alloys begins to deteriorate at around 250°C, which makes them unsuitable for use in many high temperature applications. Aluminum alloys reinforced with nanoparticles are able to withstand temperatures in excess of 250°C without losing their strength, and for this reason they are continually finding new applications, and methods for manufacturing them are earnestly being developed. In this review, the processing methods for making aluminum nanocomposite materials are presented and discussed. After brief discourses on the market trends and applications of aluminum composite materials, the general characteristics of particle reinforced aluminum alloys, and a description of the strengthening mechanisms that are operative in particle reinforced alloys, the remainder of the review is a detailed presentation of the various methods that have been devised for manufacturing aluminum nanocomposite materials, including advantages and shortcomings of each method and the challenges and opportunities that it provides.

1. Introduction

1.1. Markets and Applications of Aluminum Composite Materials

Aluminum alloys have garnered considerable interest in recent years as suitable materials for structural applications, and they are now used extensively by the automotive, aerospace, and defense industries. This appeal for aluminum alloys is mainly due to their high specific strength and their high thermal conductivity, which translate into reduction in overall vehicle weight, lower fuel consumption, and ultimately an undeniable economic advantage¹⁻⁸. It is estimated that a 10 pct. reduction in vehicle weight results in 8 to 10 pct. improvement in

fuel economy. Moreover, the quality of recycled aluminum alloys has gradually improved over the years to the extent that recycled (also called secondary) aluminum alloys are now comparable in their quality to primary alloys. The direct use of secondary aluminum alloys, and the partial substitution for primary alloys by their secondary counterparts significantly adds to the economic advantage of aluminum-based alloys as materials for structural applications. On the downside, aluminum based alloys in general exhibit low hardness and are unable to retain their strength when used for long periods of time at temperatures exceeding 250°C. This shortcoming compromises the reliability of structural components made from aluminum alloys when subjected to thermal cycling or to tribological stresses, which are typical forms of loading in many automotive and aerospace applications. Major efforts to alleviate these shortcomings focused on adding micro-sized ceramic particles to carefully-tailored aluminum alloys in order to make hard, strong aluminum matrix particle reinforced composite materials without sacrificing the light-weight advantage of aluminum alloys⁷. The emergence of metal matrix composite materials was mainly in response to demands for improved performance from advanced military systems. However, by the late 1970s, the reduction in new military acquisitions, which was brought about by a decline of active military campaigns as the Cold War era approached its end, made research and development of innovative, often expensive, materials such as metal matrix composites, a low priority⁸. Nevertheless, driven mainly by the aerospace and the defense sectors, research in metal matrix composites was reinvigorated in the 1980s; and technology programs such as the National Aero Space Plane (NASP) provided a focal point for the development of new materials needed for making the high-performance high-integrity components required for service in extreme environments such as those encountered in space missions⁸. By the mid 1980's, programs for developing metal matrix composites were in full swing in several major aluminum producing companies⁹⁻¹⁰. These programs focused on developing materials for application in ground transportation vehicles; and the first major application of metal matrix composites in an automobile was a selectively reinforced piston produced by liquid metal infiltration of ceramic preforms. It was made for Toyota Diesel engines in 1983. By 1999, aerospace applications accounted for only 14 pct. of the worldwide metal matrix composite market while applications in ground transportation accounted for nearly 62 pct. In March 2012, Global Industry Analysts, Inc. released a comprehensive global report on the metal matrix composites market in which it projected the market to exceed \$322 million by the year 2017¹¹. The report claims that the growth will be driven primarily by expansion in end-use applications in high-end products including parts for the automotive, aerospace, defense, and semiconductor industries. Today, Corporate Average Fuel Economy (CAFE) standards are at their highest level, and they are projected to continue to rise for OEM fleets including light trucks¹². In response to these tight regulations, the use of aluminum in a typical vehicle is expected to double in 2025 compared to its 2008 level as shown in Fig. 1¹³. Ford Motor Co. has placed the monetary value of vehicle weight reduction at between \$0.35 and \$3.50 per kg depending on vehicle platform⁸. In freight transport by heavy-duty trucks, where vehicle weight savings translate to additional freight

that can be hauled, these savings are estimated to be between \$2–\$16 per kg depending on the equipment's operational cycle.

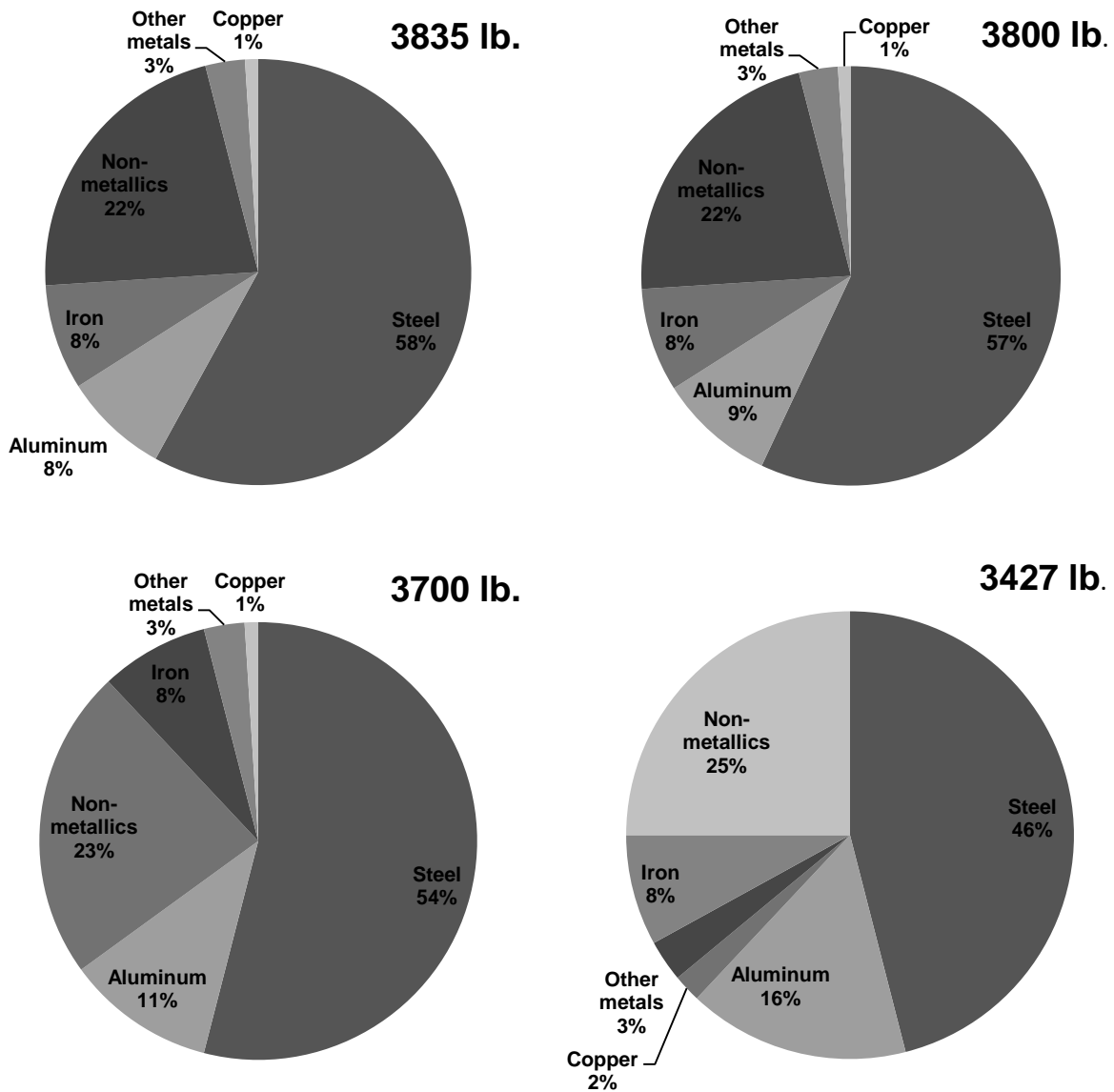


Figure 1. Light vehicle material mix from 2008 to 2025. EPA baseline vehicle¹¹.

Compared to traditional aluminum-based composite materials, the fraction of the total composites market occupied by aluminum nanocomposites is small. In 2010, the aluminum nanocomposites market segment totaled \$250 million, 80 pct. of which was in automotive applications. Silicon, titanium, tungsten, and tantalum carbides, as well as titanium diboride, aluminum nitride, aluminum oxide, and silicon nitride are the most commonly used nanoparticles in aluminum alloy matrices¹⁴⁻¹⁵.

1.2. Characteristics of Aluminum Alloys Reinforced with Nanoparticles

Although metal matrix composites offer many advantages, they do have shortcomings; paramount among them are low fracture toughness, low ductility, and poor machinability. Dispersing the second phase particles in the metal matrix and achieving a strong interfacial bond between the matrix and the particles are the two main processing challenges¹⁶⁻¹⁷. Most fabrication processes fall short of answering these challenges resulting in materials in which the particles cluster together, have weak interfaces with the matrix alloy and hence compromised ductility⁸. As far as machining composite materials is concerned, the problem demonstrates itself in excessive tool wear caused by the abrasive nature of the ceramic reinforcing particles. Consequently, selection of machining tools is limited to a small group made of extremely hard and expensive materials such as polycrystalline diamond. Non-traditional machining processes such as water jet cutting, abrasive water jet cutting, electrical discharge machining, ultrasonic machining, and laser cutting, provide precision finish, but they are beset by high costs and slow production rates¹⁶⁻¹⁷.

Research work on metal matrix composites reinforced with micrometric particles have shown that although with careful processing the particles can be uniformly dispersed in metallic alloys, they are less effective in strengthening the matrix alloy than nanometric particles (i.e., particles that are in the range of 10-200nm). In general, particles larger than 1.5 μ m are susceptible to cleavage, and particles between 200nm-1,500nm tend to form cavities at their interface with the matrix, but particles smaller than 200nm tend to bond well with the matrix resulting in excellent mechanical properties and attractive thermal and electrical characteristics¹⁸. Moreover, the same strength can be achieved in a metal matrix by incorporating a smaller amount of nano-size particles than micro-size particles¹⁹⁻²⁴. Metal matrices reinforced with nanoparticles are characterized by a change in their fracture mode from an inter-granular mode to a transgranular mode, and also by significant improvement in strength accompanied by moderate improvement in fracture toughness, significant improvement in creep resistance, thermal shock resistance, and wear resistance, as well as enhanced dimensional stability at elevated temperature. Aigbodion¹⁹ compared the properties of 356 aluminum alloy with their counterparts for the same alloy reinforced with 15 pct. micro-size (65 μ m) SiC and 15 pct. nano-size (20, 30, and 40nm) SiC particles. His findings, which are summarized in Figs. 2 and 3, clearly demonstrate the superiority of nano-size particles over micro-size particles in enhancing the yield and ultimate tensile strengths of the alloy. Both strength magnitudes are 20-25 pct. higher for the alloy reinforced with nano-size particles than for the alloy reinforced with micro-size particles. Moreover, as Fig. 4 shows, impact strength, which is reduced to almost half of its value for the un-reinforced alloy by the presence of the micro-size particles, is not affected by the presence of the 30nm particles. As a matter of fact, it is improved by more than 30 pct. when 20nm particles are used. El-Kady²⁰ et al. investigated the effect of particle size and volume pct. on the strength of aluminum alloys reinforced with nano-size Al₂O₃ particles. Their results are summarized in Fig. 5 and show a 20 pct. increase in yield strength when 1 volume pct. 60nm Al₂O₃ is added

to the matrix alloy compared to the case when 1 volume pct. 200nm Al_2O_3 particles are added. Their results also show that the improvement in strength with volume pct. particles begins to level off at 3-5 volume pct. particles, irrespective of particle size. This is most likely due to the tendency of the particles to cluster together at the high particle content. Similarly, Mazaheri²¹ et al. reported a decrease in strength when the amount of nano-size (50nm) SiC particles added to 356 alloy exceeds 3.5 volume pct. as shown in Fig.6. The addition of nano-size particles to aluminum also significantly improves the high temperature properties of the metal. Zebarjad²² et al. compared the effect of adding 25 μm , 5 μm , and 70nm SiC particles to aluminum on the metal's dimensional stability at elevated temperature. Their results, which are summarized in Fig. 7, show that both the micro- and nano-size silicon carbide particles improve the high temperature dimensional stability of aluminum. Ren and Chan²³ showed that adding 50nm SiC particles to 7075 aluminum alloy enhanced the alloy's wear and high temperature creep resistance compared to the alloy reinforced with 13 μm SiC particles. Furthermore, they showed that the same improvement in wear and high temperature creep resistance could be attained with much less 50nm SiC particles than with 13 μm SiC particles. Finally, while the critical size below which reinforcing particles may improve the metal's properties have been reported¹⁵ (see Table 1), the mechanism responsible for the improvement in each property still remains a matter of debate.

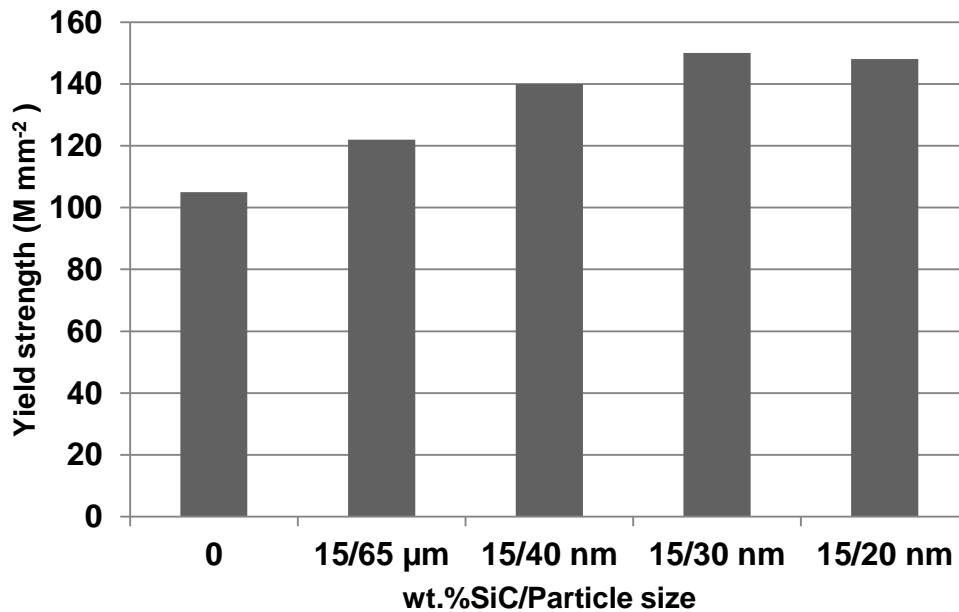


Figure 2. Yield strength versus wt.% SiC¹⁹.

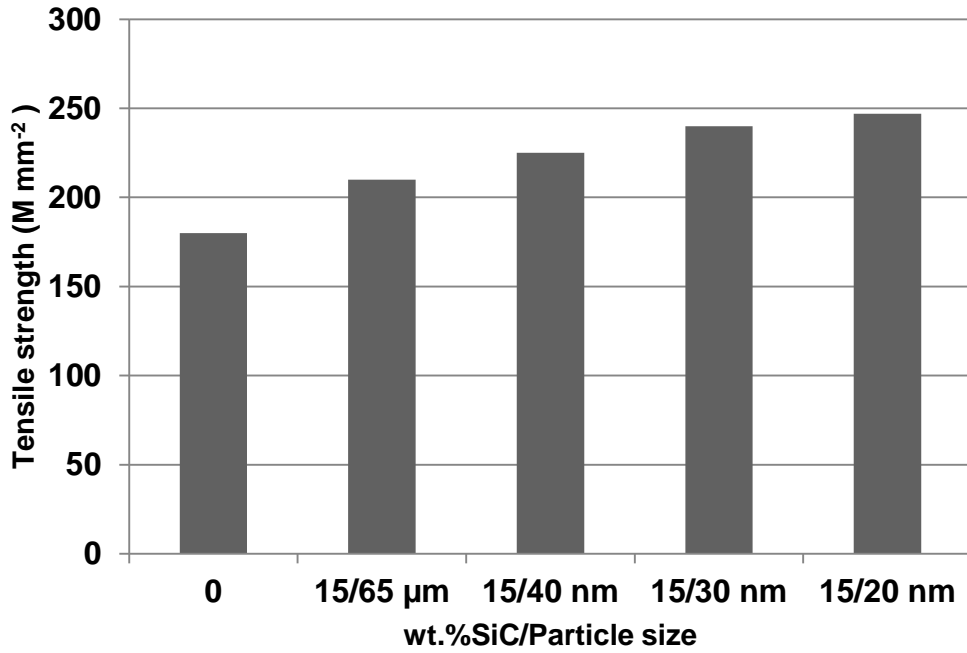


Figure 3. Tensile strength versus wt.% SiC¹⁹.

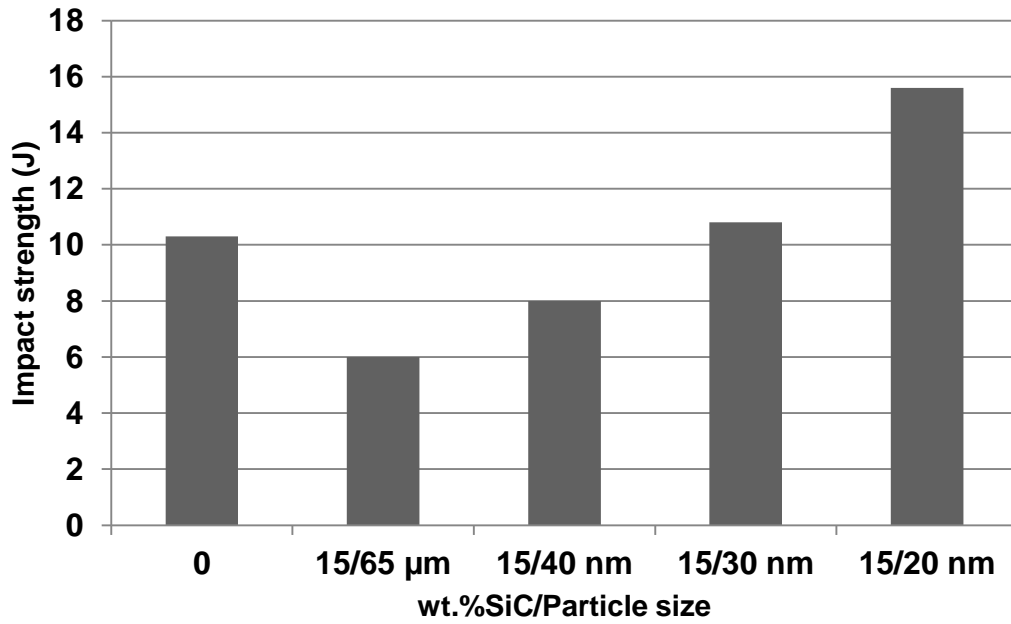


Figure 4. Impact strength versus wt.% SiC¹⁹.

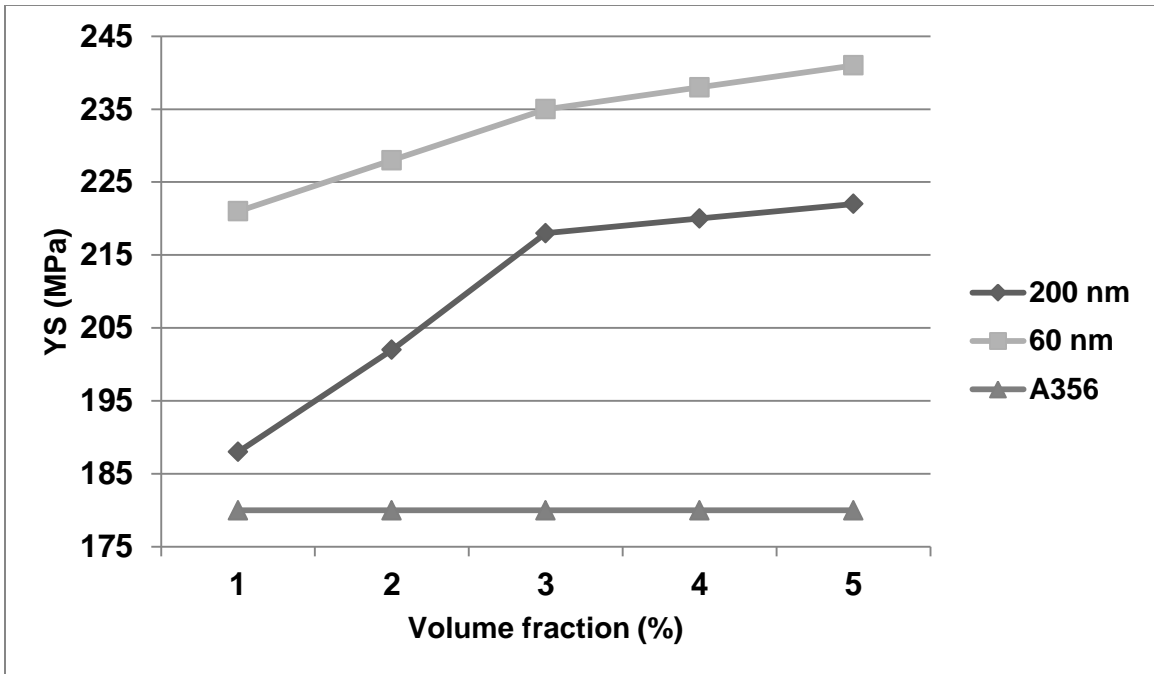


Figure 5. Yield strength versus vol.% SiC. Comparison for 60 and 200 nm²⁰.

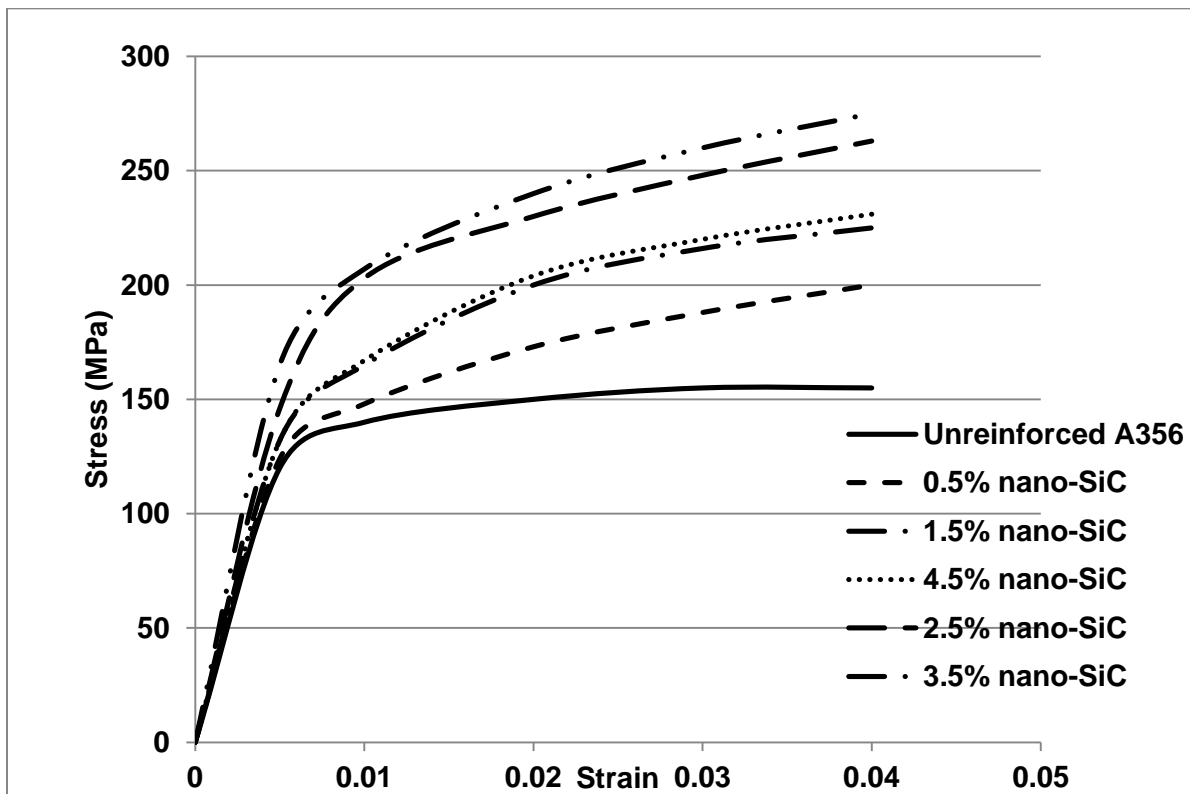


Figure 6. Stress vs. strain curve for different vol.% SiC²¹.

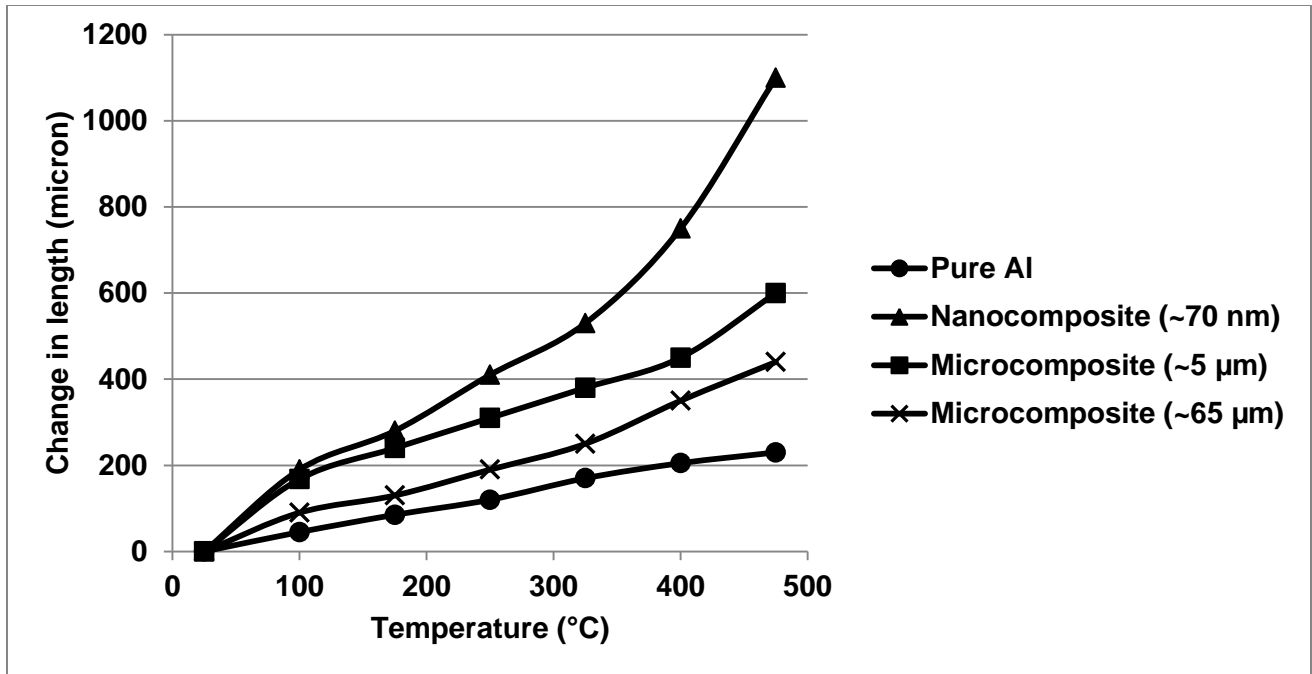


Figure 7. Change in length versus temperature for aluminum and its composites at constant SiC content (7.5 Vol% SiC)²².

Table I. Critical particle size for improving nanocomposite properties¹⁵.

Property	Critical size of reinforcing particles (nm)
Catalytic activity	<5
Softening of hard magnetic materials	<20
Changing of refractive index	<50
Producing electromagnetic phenomena, such as super paramagnetism	<100
Strengthening and toughening	<100
Modifying hardness and plasticity	<100

1.3. Operative Strengthening Mechanisms in Particle Reinforced Aluminum Alloys

Theories that use a continuum approach to describe the strengthening effect observed in metals to which ceramic particles have been added are not useful because they invariably ignore the influence of the particles on the micromechanics of deformation. Five main mechanisms have been reported to be responsible for the strengthening effect of nanoparticle addition. These are Orowan looping, particle shearing, load transfer, thermal mismatch and grain refinement. Several approaches have been formulated to estimate the

enhanced matrix strength incorporating the effect of these mechanisms and assessing which one is predominant²⁵. The most popular ones are (i) the Modified Shear Lag theory of Nardone and Prewo²⁶, which considers load transfer the main strengthening mechanism; (ii) the Eshelby-Based Particle-Compounded Model²⁷, where the reinforcement constraints to matrix plastic flow and matrix dislocation motion are accounted for the strengthening action of the particles – dislocation arise for thermal mismatch or elastic misfit and loop around the particle- (iii) and the Effective Medium Approximation (EMA) model by Stroud²⁸, which has been applied to nanocomposite materials by considering the increase in ‘interface density’, that can be related to grain refinement. In what follows the five strength contributions will be elucidated²⁹⁻³⁸:

Orowan Looping – The interaction of the glissile dislocations with dispersed particles increases the critical resolved shear stress of the alloy (and therefore its yield strength) by an amount $\Delta\tau$ that is a function of the parameters that characterize the dislocation-particle interaction. Since in this case the particles are far apart, the dislocations moving under an applied stress will bow out between them. The strengthening increment $\Delta\sigma_{OR}$ may be calculated from Eq. (1)

$$\Delta\sigma_{OR} = M \frac{0.1Gb\sqrt{f}}{r} \ln\left(\frac{\lambda}{2r_0}\right) \quad (1)$$

where

$$\lambda = \left(\sqrt{\frac{2\pi}{3f}} - \frac{\pi}{2}\right)r$$

Particle shearing – A strengthening mechanism that is often observed in age-hardened alloys but is seldom used to explain strengthening in nanocomposite materials is particle shearing (i.e., particle cutting) by dislocations. Particle shearing is described by the Anti-Phase Boundary (APB) mechanism^{30,31} where the strengthening increment $\Delta\sigma_{APB}$ may be calculated by Eq. (2).

$$\Delta\sigma_{APB} = M \frac{(\gamma_{APB})^{\frac{3}{2}}}{b^2} \sqrt{\frac{rf}{G}} \quad (2)$$

The Orowan Looping and Anti Phase Boundary mechanisms described by Eq. (1) and Eq. (2), respectively, correspond to two extremes: the case where the second phase particles are very small and lie very close to one another, and the case of relatively coarse particles that are far apart. If the particles are far apart, the dislocations moving under an applied stress will bow out between them (Orowan Looping). If this model is to apply, then the particles must be so hard that the dislocations cannot pass through them. On the other hand, if the average particle diameter is very small, the shear stress on each particle is very large and the particles may be sheared (Anti Phase Boundary). The critical particle radius beyond which the particles are looped rather than sheared is given by Eq. (3)³¹⁻³³.

$$R_c = \sqrt{\frac{3}{2}} \left(\frac{Gb^2}{2\gamma_{APB}} \right) \left(1 + 1.53 \sqrt{\frac{f}{\pi}} \right) \quad (3)$$

In Eqs. (1-3), G is the shear modulus, b is burgers vector, f is the volume fraction of particles, r is the average radius of the particles, r_o is the dislocation core radius (often taken to be equal to one burgers vector), γ_{APB} is the anti-phase boundary energy, and M is the Taylor factor. The Taylor factor relates the macroscopic yield strength to the critical resolved shear stress so that $\sigma_y = M\Delta\tau_{CRSS}$. For texture-free fcc metals, Hutchinson³¹ gives $M = 2.6$. Fig. 8 shows the correlation between shear stress and particle size. Zhang and Chen^{25,34} showed that Orowan strengthening reaches its maximum at a critical particle size below which strengthening does not occur. They also showed that for the Mg/Al₂O₃ and the Ti/Y₂O₃ systems, the critical size is 5.44 times the Burgers vector, and the critical particle size is independent of the volume fraction of particles.

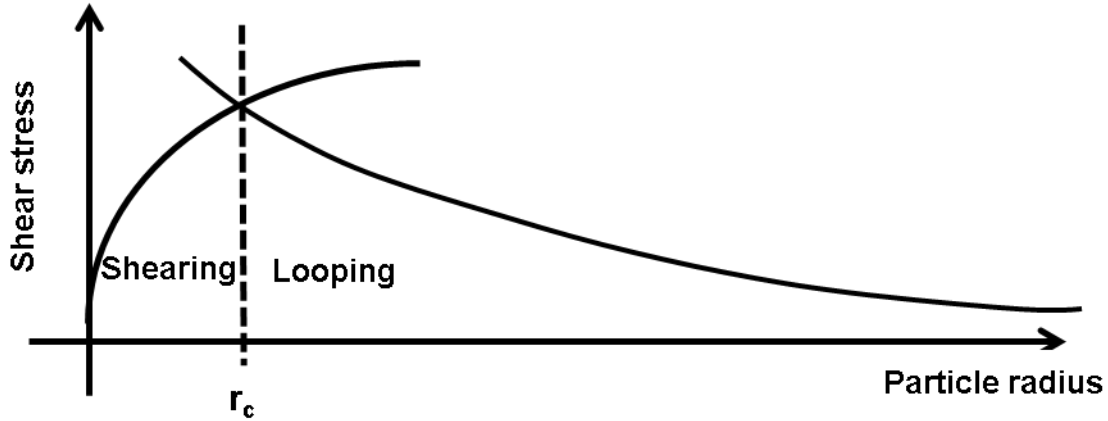


Figure 8. Trend of shear stress versus particle size. Shearing and looping regions underlined.

Load Transfer – In this model, the strength contribution is due to the strong cohesion at the atomic level between the matrix and the reinforcing particles, i.e. the particles are directly bonded to the matrix³⁴⁻⁴⁰.

Thermal mismatch– Thermal mismatch due to the difference in the coefficient of thermal expansion between the matrix and the reinforcing particles causes plastic strain and increase the dislocation density (ρ)³⁴⁻³⁰. The strengthening increment $\Delta\sigma_{TH}$ may be calculated from Eq. (4)

$$\sigma_{TH} = M\beta G_m b \sqrt{\rho} \quad (4)$$

where

$$\rho = \frac{A\Delta\alpha\Delta TV_P}{bd(1-V_P)}$$

In Eq. (4), M is the Taylor factor, β is a constant (≈ 1.25), $\Delta\alpha$ is the difference in the coefficients of thermal expansion between the matrix and the reinforcing particles, ΔT is the difference between the processing and service temperatures, and A is a geometric constant, which varies between 10 and 12 depending on the geometry of the reinforcing particles.

Grain refining (The Hall-Petch effect) – The flow stress of a metal is almost always observed to increase as the size of its grains decreases, and experimental data almost always displays a linear relationship between flow stress and the reciprocal of the square root of the grain diameter as shown in Eq. (5)

$$\sigma = \sigma_o + \frac{k}{\sqrt{d}} \quad (5)$$

where σ_o and k are constants obtained from linear fitting of measured data and d is the average grain diameter^{36,39}. Eq. (5) is known as the Hall-Petch equation and the strengthening increment caused by refining the grain size is

$$\Delta\sigma_{GB} = \frac{k}{\sqrt{d}} \quad (6)$$

The rationale behind Eq. (5) is that in order for deformation to occur, dislocations have to move from a deformed grain to an un-deformed grain with grain boundaries acting as obstacles to this motion. Therefore the smaller the average size of the grains, the more obstacles there are to dislocation motion, and the higher the strength of the alloy. Nanoparticles may act as grain refiners and by doing so they contribute to the alloy's strength.

Zhang and Chen^{25,34} demonstrated that the strengthening increments due to Orowan looping and thermal-mismatch increase significantly with decreasing particle size and increasing volume fraction of the reinforcing nanoparticles. They also demonstrated that the relative contribution of Orowan looping to the material's strength increases as the size of the reinforcing nanoparticles decreases. Magnesium-based composites have also been studied and similar conclusions have been reached. Poirier et al.⁴⁰ modeled strengthening in Al-Al₂O₃ composites and observed (Fig.9) that the yield strength increment calculated from the thermal mismatch model and from the Orowan looping model are similar and higher than the value calculated by the Load Transfer model. Load transfer between the matrix and the reinforcing particles is at the origin of the mechanical behavior of composites with high volume fraction of reinforcing particles due to the tendency of the nanoparticles to cluster together when present in high concentrations. Poirier et al.⁴⁰ also concluded that the Orowan looping mechanism is insignificant for particles larger than 1 μm because for these large particles, the inter-particle distances are too high to effectively impede dislocation motion. Sanaty-Zadeh³⁶ confirmed the importance of the strengthening contributions from Orowan looping and thermal mismatch (Fig.10), and underlined the importance of the contribution from the Hall-Petch effect in Mg-based nanocomposite materials.

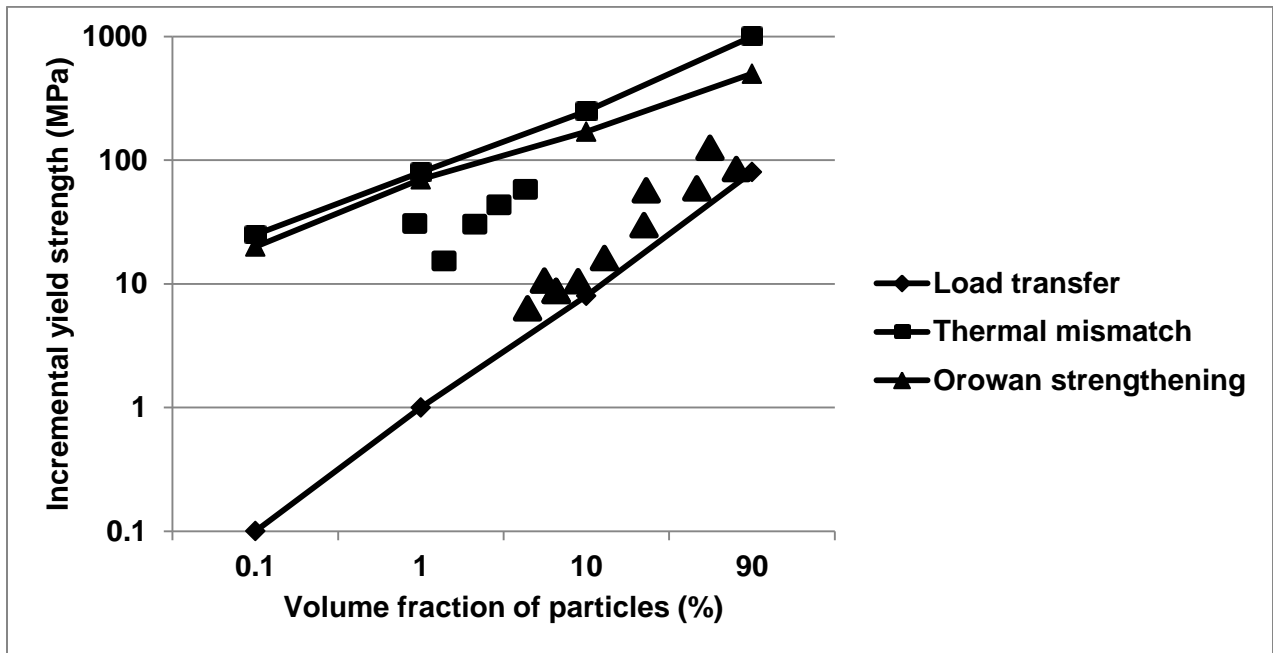


Figure 9. Incremental yield strength with Al_2O_3 addition. The triangles and squares represent experimental results for Al_2O_3 particle size above and below 500nm respectively⁴⁰.

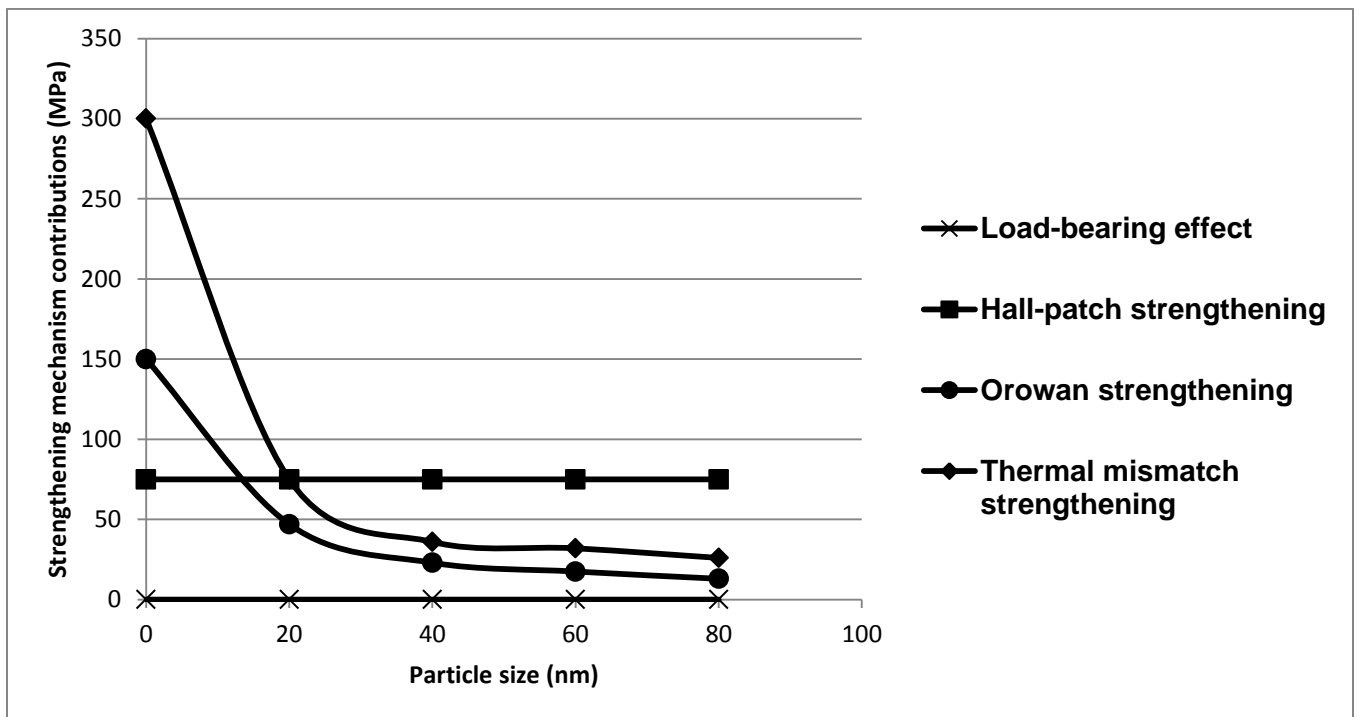


Figure 10. Contribution of strengthening mechanisms versus particle size. $\text{Mg}/\text{Y}_2\text{O}_3$ system³⁶.

2. Manufacturing Methods for Aluminum Nanocomposite Materials

Manufacturing methods for aluminum nanocomposite materials may be divided into two broad categories: (1) ex-situ methods, and (2) in-situ methods. Ex-situ methods involve adding reinforcing particles to the matrix alloy from a source external to the matrix. In-situ methods, on the other hand, involve synthesizing the reinforcing particles within the matrix during processing^{42,45}.

Ex-situ manufacturing methods may be further divided into two subcategories^{42,47}: (a) solid-state processing methods, and (b) liquid-state processing methods. Among the solid-state processing methods, powder metallurgy methods and methods based on mechanical attrition are the most popular. With these methods, particles can be easily reduced to the nanoscale, but the cost is significantly high and the processing times are usually long (sometimes more than 100 hours). In addition, oxide contamination of the precursor powders can cause cracking and de-bonding at the particle/matrix interface; and high processing temperatures are usually necessary, which often result in coarse-grained, relatively weak materials. Moreover, the final product often contains significant amounts of pores that reduce the fatigue resistance of the composite material and necessitates further metalworking, such as high pressure consolidation⁴¹⁻⁴⁴. Similarly, liquid-state processing methods may be divided into three subcategories: (a) methods based on infiltration of performs made from nanoparticles, (b) methods based on agitation of melts containing nanoparticles (e.g., stir casting), and (c) ultrasonic cavitation-based solidification of melts⁴⁶. Liquid metal is generally less expensive to make and easier to handle than powders, and the flexibility offered by casting over powder metallurgy methods in making complex shapes constitutes a significant advantage for liquid state processing methods over solid state processing methods. Liquid state processing methods are generally fast and easy to scale-up; however, poor wetting of the reinforcing particles by the molten metal and unwanted reactions at the particle/matrix interface may degrade the quality of the resulting composite material. Moreover, liquid state processing methods are usually limited to low melting point metals^{41,42}.

In-situ manufacturing methods are not plagued by the shortcomings that are typical of ex-situ manufacturing methods, although control of the process variables may sometimes be difficult. In-situ manufacturing methods may be divided into two major categories: (a) reactive methods, where the reinforcing particles are synthesized within the metal by means of a gas-liquid, liquid-liquid, solid-solid or solid-liquid reaction, or (b) morphological methods, where a favorable composite architecture evolves as a consequence of processing.

Other manufacturing methods that are not typically used for mass producing near net shape components have also been reported in the literature and include methods based on laser deposition, spray deposition, sol-gel synthesis, and electroplating. These are all costly manufacturing methods and their application is unlikely to be extended to producing components on an industrial scale^{43,47}. They are generally used for depositing coatings and

thin films on substrates. Only those manufacturing methods that are suitable for large production volumes and that can be easily adapted to existing industrial infrastructures will be considered in this review. Table 2 lists these manufacturing methods and summarizes their main features.

Table II. Manufacturing methods suitable for mass production of metal matrix nanocomposites.

Manufacturing Method	System	Reinforcing Particle size (nm)	Main Features
Ex-situ Solid State			
Powder Metallurgy	Al/Al ₂ O ₃ Al/Si ₃ N ₂	~15-100	+ Near net shape + Scalable - Contamination
Mechanical Alloying	Al/Al ₄ C ₃ Al-Fe/Al ₃ Fe ₂ Al/SiC	~10-100	- Particle clustering - Cracking - Expensive - Long time
Ex-situ Liquid State			
Stir Casting	Al/SiC Al/Al ₂ O ₃	40-50	+ Easily scalable + Inexpensive - Particle clustering - Particle/matrix de-bonding
Infiltration	Al-Cu- Mg/Al ₂ O ₃	50	+ Good mechanical properties - Expensive equipment - Uneasy to scale
Ultrasonic-assisted Cavitation	Al-Si/SiC Al/Al ₂ O ₃	20-100	+ Good particle dispersion + Inexpensive - Not easily scalable
In-situ Reactive Methods (Solid-Solid)			
Mechanochemical Synthesis	Cu/MnO Cu/ZnO Al/Al ₂ O ₃ Al/Al ₄ C ₃ Al-Zn/Al ₂ O ₃ Al-Ti/Al ₃ Ti	10-50 10-50	+ Very small particle size + Versatile - Long time - Contamination - Difficult to scale up - Challenging reaction control
Friction Stir Processing	6061/SiC 7050/WC Al-Ti/Al ₃ Ti Al-Fe/ Al ₁₃ Fe ₄	50 50 100	+ Inexpensive + Versatile - Difficult to scale up - Sensitive to process parameters

In-situ Reactive Methods (Solid-Liquid)			
Combustion Synthesis (SHS)	Al/TiB ₂ Al/TiC Al-Fe/Al ₂ O ₃ Ni-Ti/TiC	30-100	+ Good particle dispersion + Inexpensive + Fast + Versatile - Difficult process control
Exothermic Dispersion (XD)	Al/TiB ₂ Al/TiC Al/TiO ₂	700	
Substitutional Chemical Reaction	Al/Al ₃ Zr+Al ₂ O ₃	80	
	Cu-Ti/TiB ₂	50	
In-situ Reactive Methods (Liquid-Liquid)			
Mixalloy	Cu/TiB ₂	50	
In-situ Reactive Methods (Gas-Liquid)			
Gas-Liquid Process	Al-Mg-Li/AlN Al-Mg/AlN Al-Li/AlN Al/AlN Al-Si/SiC Al-Ti/TiC	50-1000	+ Good particle dispersion and good bonding + Inexpensive + Fast + Adaptable to many systems - Difficult to control
In-situ Morphological Methods			
Rapid Solidification	Al/TiC	40-80	+ Very small particle size
	Al-Fe/Al _{100-x} Fe _x	20-150	+ Ultra-fine grains
Severe Plastic Deformation	Al/Al ₂ O ₃	50	+ Small particle size
	Al-Fe/Al ₁₃ Fe ₄ Al2009/SiC	10	- Very difficult to scale up

2.1 Liquid State Ex-situ Methods

Among all the liquid state ex-situ manufacturing methods, stir casting and solidification methods are the least expensive for making microcomposite materials and hence numerous attempts have been made to extend their application to particles whose size is in the nanometer range. Unfortunately, these attempts are met with many challenges brought about by: (i) the potential for inhomogeneous dispersion and poor wetting of the nanoparticles by the molten metal, (ii) the potential for rejection of the nanoparticles by the solidifying metal front, (iii) the potential for unwanted reactions at the interface between the nanoparticles and the melt, (iv) increased melt viscosity due to the increased surface-to-volume ratio, and (v) the need for large capillary pressures to initiate infiltration of a preform made from nanoparticles by molten metal^{8,43-45}.

2.1.1 Stir Casting

Stir casting methods, which are widely used to mix micron size particles in metallic melts, have recently been adapted to dispersing small quantities of nanoparticles in molten alloys. The problems encountered with using nanoparticles stem from the large surface area of the particles, their small size, and their low wettability by the melt, which combine to make inserting the particles into the melt and homogeneously dispersing them difficult. Inserting the particles into the melt by means of a gas stream and creating a vortex to enhance particle dispersion has been used, but only with limited success⁴⁸. El-Kady et al.²⁰ observed severe clustering in stir cast 356 aluminum alloy reinforced with nanosize Al₂O₃ particles when the reinforcing particles are added in amounts higher than 3.5 volume pct. Similar results were obtained by Mazaheri et al.²¹ Experiments and computer simulations made it clear that mechanical stirring by means of a rod to disperse nanoparticles in molten metal cannot overcome particle clustering, and hence alternative stirring tools have been designed to improve the dispersion of the particles.

When a moving solid/liquid interface approaches mobile solid particles that are suspended in the liquid, the particles can be either captured or pushed away by the interface. If the particles are captured by the growing solid, minor redistribution of the particles will occur during solidification, and hence the distribution of the particles in the solidified material will be almost as uniform as it was in the liquid. On the other hand, if the particles are pushed by the solidifying metal front, then their distribution will be significantly changed to become ultimately segregated in the last pools of liquid to solidify^{8,49,50}. Three particle/solidifying metal front interactions are possible: (1) the particle may be pushed ahead of the solidifying front causing a buildup of particles in areas of the matrix that solidify last (Particle Pushing – PP), (2) The particle may be engulfed by the solidifying front (Particle Engulfment – PEG), and (3) the particles may be mechanically entrapped by the solidifying front (Particle Entrapment – PET)^{49,50}. These possible particle/solidifying metal front interactions are shown schematically in Figure 11, and which one of them occurs depends on the velocity of the solidifying metal front and on the solidification process. When a planar interface is maintained and the heat transfer is unidirectional, the particles can only be pushed or engulfed by the solidifying metal front; but in multidirectional, i.e., dendritic solidification, which is typical of metal casting, the particles can also be entrapped in the interdendritic regions. This mechanism does not depend very much on the velocity of the solid/liquid interface and is usually detrimental to the material's properties because the particles tend to accumulate in grain boundaries. In addition to the shape of the solidifying metal front, other factors may affect the interaction between the particles and the solidifying metal front. These include the interfacial energy between the particle, the liquid, and the solid; particle aggregation; convection in the melt; viscosity of the melt; density of both melt and particles; particle shape and size; and the temperature gradient ahead of the solidification front⁴⁹⁻⁷¹.

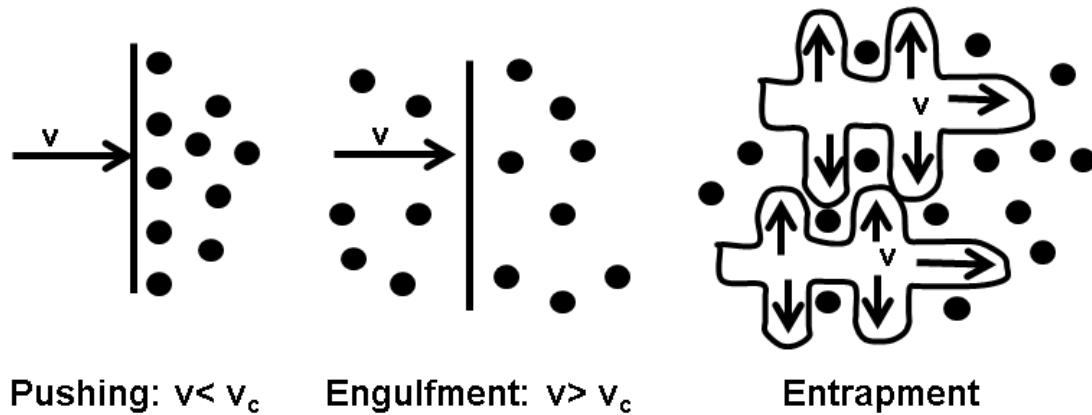


Figure 11. Interaction modes of particles with a solidifying interface in metals. In the case of a planar solidification front particles are pushed at velocities lower than the critical velocity (left) or are engulfed at higher velocities (middle). During dendritic solidification particles can be entrapped in the interdendritic region (right) without dependence from interface velocity⁵⁰.

In addition to the characteristics of the solidification process discussed in the preceding paragraph, the velocity of the solidifying metal front plays an important role in dictating whether or not the reinforcing particles will be captured by the advancing metal front. The critical velocity is the velocity below which the particles are pushed and above which they are engulfed by the metal. Theoretical approaches⁴⁹⁻⁹⁰ have resulted in relations between the critical velocity, V_C , and the particle diameter, D , such as Eq. (7) in which C is a constant that depends on the material and solidification conditions and the exponent m depends on the particles and metal system.

$$V_C D^m = C \quad (7)$$

Many models⁵²⁻⁹⁰ have been put forth to express the forces that act on the particle, and hence the critical velocity of the particle. The most important of these models are given in Table III. Note that none of these models accounts for the possible presence of foreign species on the surface of the particle (such as oxide layers, etc.)⁴⁹ and none of them accounts for the crystallographic orientation of the particle relative to the solidifying metal although these factors have been observed to influence the critical velocity^{53,65,71}. In addition, some models [] indicate that V_c is proportional to the surface energy of the particles which, as shown in Table IV, increases significantly when the size of the particles is in the nano range⁹³. This means that very high velocities are necessary in order to engulf nanoparticles by typical metals. This is often difficult to achieve with conventional casting techniques, particularly when making large sections. In such cases, the particles tend to cluster at grain boundaries and in the regions that freeze last. Attempts to accurately

determine critical velocity values by means of numerical simulations have also been carried out^{89,90}.

Table III. Critical velocity values according to different models.

model	features & assumptions	m	critical velocity V_c^b
Omenyi et al. ⁷⁶⁻⁷⁸	Based only on thermodynamic criterion. Valid for negligible body forces and slow solidification rates.	-	No V_c expression $\Delta\gamma_0 = \gamma_{PS} - \gamma_{PL}$ $\Delta\gamma_0 < 0$ engulfment $\Delta\gamma_0 > 0$ pushing
Uhlmann et al. ⁷⁵	Repulsive interfacial forces and attractive drag forces considered. V_c derived by solving the diffusion equation on the particle/interface gap. Particle irregularities are considered.	2	$V_c = \frac{n+1}{2} \left(\frac{La_0 \Omega D_l}{k_b T R^2} \right)$ $n = 4 - 5$
Chernov et al. ^{79,80}	Considers Van der Waals repulsive forces as disjoining pressure between particle and front and drag forces responsible for particle engulfment. Introduced the effect of mismatch in thermal conductivities of liquid and particle.	4/3	For $R < 50 \mu m$ $V_c = \frac{0.14 B^{2/3} \gamma_{SL}^{1/3}}{\eta R^{4/3}}$
Zubko et al. ⁸¹	Experimental derivation of engulfment solely based on the ratio $\left(\frac{k_p}{k_l}\right)$	-	$\frac{k_p}{k_l} > 1$ engulfment $\frac{k_p}{k_l} < 1$ pushing
Kim and Rohatgi ^{82,83}	Introduced the effect of the thermal gradient G across the interface on the shape of the solidification front and on	1	$V_c = \frac{a_0 \Delta\gamma_0}{18\eta} \left[\frac{G a_0}{\Gamma} \left(\frac{\frac{k_p}{k_l} - 1}{3} + \frac{1}{R} \right) \right]$

^b Refer to Appendix A for Nomenclature.

	the critical velocity. Considered the disjoining pressure.		$\Gamma = \frac{\gamma_{SL} T_m}{\rho_s L}$ curvature of the solid/liquid interface: $k = \frac{G a_0}{\Gamma} \left(\frac{\alpha-1}{3} \right)$
Bolling and Cisse ^{84,85}	More rigorous determination of the effect of the shape of the solidification front Treats smooth and rough particles	3/2	$V_c = \left(\frac{1.36 k_b T a_0 \gamma_{SL}}{\pi} \right)^{1/2} \frac{1}{3 \eta R^{3/2}}$
Surappa and Rohatgi ⁸⁶	Replaced the thermal conductivity criterion with an experimental criterion based on thermal diffusivities.	-	$\left(\frac{k_P c_P \rho_P}{k_l c_l \rho_l} \right)^{1/2} > 1$ engulfment $\left(\frac{k_P c_P \rho_P}{k_l c_l \rho_l} \right)^{1/2} < 1$ pushing
Stefanescu et al. ⁷²⁻⁷⁴	Considered the effect of thermal conductivity mismatch and solute redistribution ahead of the solidification front caused by the change in curvature	1/2	$V_c = \left(\frac{\Delta \gamma_0 a_0^2 k_l}{3 \eta k_p R} \right)^{1/2}$
Potsche and Rogge ⁸⁷	Repulsive Van der Waals forces and thermal conductivity mismatch considered	1	$V_c = \frac{0.084 a_0 k_l \Delta \gamma_0}{\eta k_p R}$
Sen et al. ⁸⁸	Extend Stefanescu et al. ⁷²⁻⁷⁴ approach to account for the effect of particle clustering. Used X-rays to monitor the change of the interface shape as it approached the particle.	1/2	$V_c = \left(\frac{\Delta \gamma_0 a_0^2 k_l n_1 R}{3 \eta k_p R_c} \right)^{1/2}$ where n_1 is the number of particles interacting with the interface and R_c is the radius of a circle with the same area as that of the cluster

Table IV. Variation of surface energy of 1 g sodium chloride with particle size⁹³.

Particle size (cm)	Surface area (cm ²)	Surface energy [J/g]
0.1	28	5.6×10 ⁻⁴
0.01	280	5.6×10 ⁻³

0.001	2.8×10^3	5.6×10^{-2}
10^{-4}	2.8×10^4	0.56
10^{-7}	2.8×10^7	560

Brownian motion also contributes to particle agglomeration. It causes continuous collisions between the nano-sized particles in a random fashion, which makes it very unlikely for a large number of particles to come into contact with the solidifying front⁹¹⁻⁹⁴. It has been demonstrated that a suspended particle is randomly bombarded from all sides by thermally-excited molecules coming from the liquid. Einstein showed that if one solid particle is small enough to behave like a gas molecule, it is continuously run into and displaced by liquid molecules. The magnitude of the displacement d_B follows a Gaussian statistic distribution according to Eq. (8)

$$d_B = \sqrt{\frac{2kTt}{6\eta\pi r}} \quad (8)$$

where η is the viscosity of the medium, t is the time, r is the particle radius, T is the temperature, and k is the Boltzmann constant. The displacement increases with decreasing particle radius, thus enhancing the probability of a collision to occur. It has been confirmed that the aggregation rate for 20nm particles is four orders of magnitude higher when compared to that of 1 μ m particles⁹³. This behavior can be explained by the fact that as the particle size increases, the potential energy of repulsion between particles increases, thus making aggregation less likely. It may be concluded that agglomeration of nanoparticles during stir casting remains an unresolved issue.

2.1.2 Infiltration of Porous Nanoparticle Preforms

This process consists of infiltrating porous preforms made from the reinforcing nanoparticles with the matrix alloy. Obviously, capillary forces and viscous drag through the preform's interstices act to hinder wetting of the nanoparticles by the melt. Evans et al.⁴² noted that metals generally do not bond to non-metals, and concluded that the chemistry of the system must be modified, or external pressure must be applied in order to enhance wetting. Chemical modification includes coating the reinforcing particles with an appropriate material, adding special elements to the melt, or using special atmospheres^{42,95}. Pressures of around ten atmospheres are often needed to force molten metal into 1 μ m wide pores; however the high pressure may cause fragmentation and deformation of the fragile preform, which in turn may result in uneven distribution of the reinforcing material⁹⁵. There exists a threshold pressure (P_{th}) and temperature that must be exceeded in order for the liquid metal to successfully infiltrate the closely packed particle structure of the preform. Assuming that most ceramic particles are non-wetted by molten metals, the onset of flow is achieved when the infiltrating pressure exceeds this threshold value. The dependency of the infiltrating

pressure on the average radius of the particles can be obtained from the Young-Laplace equation as shown in Eq. (9)^{96,98}

Using the “closely-packed, equal spheres” model, Kaptay^{96,98} assumed that penetration of the liquid metal into the perform occurs perpendicular to the (111) plane of this fcc-like structure. This allowed him to calculate a critical wetting angle $\theta_{cr} = 50.7^\circ$; so that for a given melt-particle system if the wetting angle is larger than θ_{cr} , infiltration would occur spontaneously. He modified the Young-Laplace equation for particles with $\theta < 100^\circ$ as shown in Eq. (10),

$$P_{th} \cong \frac{4\sigma}{R} (\cos 50.7 - \cos \theta) \quad (10)$$

Experiments show that P_{th} decreases with increasing temperature, and it may also be lowered by a wettable coating deposited on the surface of the particle. Particle shape and surface texture also affect the threshold pressure. When infiltration is performed against gravity, the equilibrium height to which the melt rises is given by Eq. (11),

$$h_e = \frac{\varepsilon^*}{\rho_l g} (P_o - P_{th}) \quad (11)$$

In Eq. (11), ε^* is a parameter that ranges from 1.73 for $\theta < 76.5^\circ$ to 0.357 for $\theta > 110^\circ$, and P_o is atmospheric pressure. Gierlotka et al.⁹⁷ used a toroid cell at pressures up to 7.7 GPa and temperatures up to 2,000 °C to infiltrate an Al₂O₃ preform (average grain size = 10nm). Similarly, Schultz et al. succeeded in infiltrating an Al₂O₃ preform (average particle size = 50nm) with A206 aluminum alloy and produced composites with a 19 pct. increase in hardness compared to the base alloy. An important downside to this method for making nanocomposites is the high cost of the nano-size ceramic performs, and the extreme pressures and temperatures necessary for successful infiltration.

2.1.3 Ultrasonic Cavitation-Assisted Solidification

High-intensity ultrasonic waves (>25 W/cm²) can generate strong non-linear effects in liquids such as transient cavitation and acoustic streaming. These waves produce a dispersive effect and tend to homogenize melts. In the ultrasonic cavitation-assisted solidification method for making nanocomposite materials, an ultrasonic probe is immersed into the melt to create such an acoustic field (Fig. 12) and nano-size particles are added to the melt during the process¹⁰⁰⁻¹⁰⁴. The acoustic bubbles burst creating hot micro-spots that locally raise the temperature of the melt. This enhances wetting of the nanoparticles by the melt and enhances their dispersion.

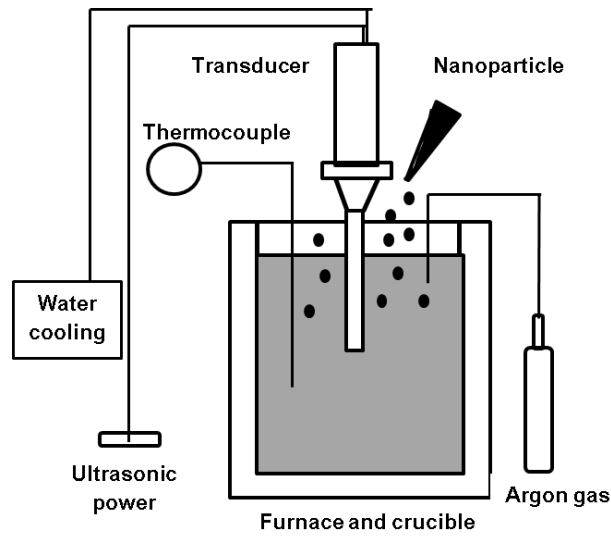


Figure 12. Schematics of ultrasonic apparatus¹⁰⁴.

Fig. 13 shows that the nanocomposite material produced by the ultrasonic cavitation-assisted solidification method employing 3.5 kW ultrasonic power has tensile ultimate and yield strengths that are significantly higher than the base metal¹⁰⁴. One limitation of this method is the high tendency of the ultrasonic probe to dissolve in the molten metal at the process temperature. In order to overcome this problem, a non-contact method wherein the probe does not come in direct contact with the liquid metal has been devised¹⁰³.

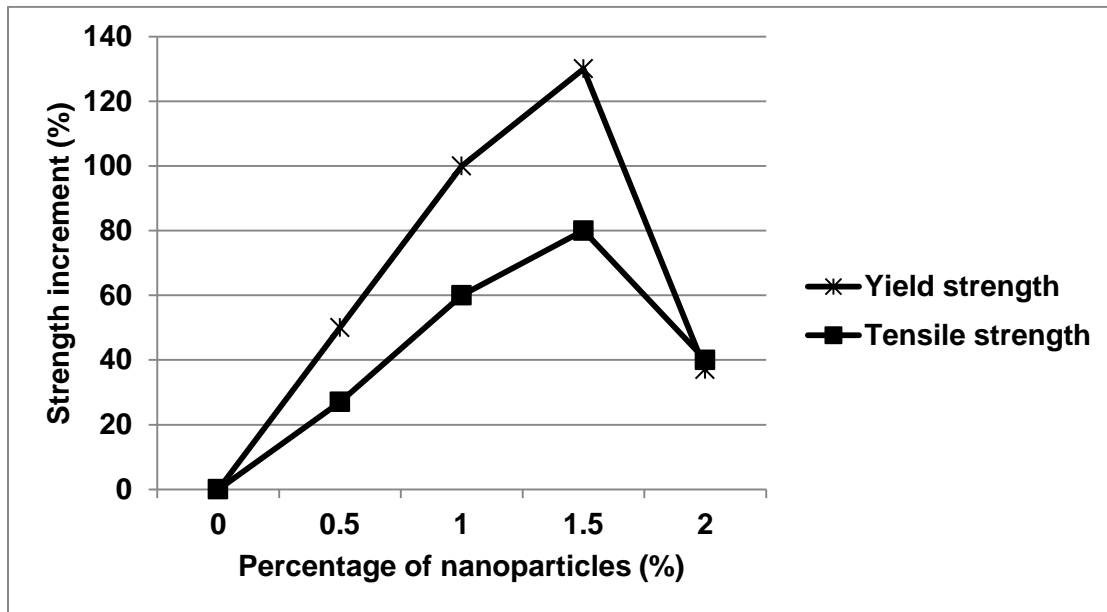


Figure 13. Strength increment versus vol.% SiC¹⁰⁴.

In this case, the mold used to cast the nanocomposite material (rather than the melt) was subjected to ultrasonic vibrations. Another limitation of the method is its small yield. The amount of material processed with ultrasonic cavitation-assisted solidification generally does not exceed 200g at a time and the ultrasonic power necessary to achieve good particle dispersion is proportional to the amount of material processed^{101,102}. Therefore, quantities suitable for industrial production require prohibitively large power supplies.

2.2. Solid State Ex-situ Methods

2.2.1 Powder Metallurgy

Early attempts to manufacture nanocomposite materials involved the use of powder metallurgy techniques; i.e., mixing matrix alloy and reinforcing powders together, followed by hot or cold pressing the resulting mix, and then sintering it at an elevated temperature^{24,45}. The major advantage of the process is its flexibility and its ability to produce near-net shape components; however, it is not cost-effective. The powder metallurgy method was used to manufacture aluminum-alumina nano-composite materials²⁴ wherein 50nm alumina particles were wet mixed with aluminum powder in pure ethanol; the slurry was then dried at 150°C and cold isostatically pressed. The compacts were then vacuum-sintered at 620°C. The resulting material showed excessive particle clustering that increased when smaller nanoparticles were used. Ma et al.¹⁰⁵ used powder metallurgy methods to fabricate nanometer Si₃N₂-reinforced aluminum composites, and they too reported the presence of several agglomerates in the aluminum matrix. A cost effective method was devised by Peng et al.¹⁰⁶ in which they used powder metallurgy to make aluminum matrix nanocomposites reinforced with oxide particles by using the Al₂O₃ surface layer that invariably exists on aluminum particles as reinforcing material. They achieved good particle distribution, but the process cannot be controlled and the scalability of the method remains to be proven.

2.2.2 Mechanical Alloying

Mechanical alloying as a means of making nanocomposite materials was first introduced by J. Benjamin¹⁰⁷. In this method, high-energy ball milling produces repeated cold welding, fracturing, and re-welding of powder particles without changing their state of aggregation^{44,108,109}. The process was initially employed to produce oxide dispersion-strengthened nickel-base and iron-base superalloys for use in the aerospace industry, and then its use was extended to making composite materials. A good example of a material made with this method is DISPAL (an aluminum alloy reinforced with Al₄C₃ particles)²⁴. Mechanical alloying progressively increases the total surface area of the solid particles, but the mechanical energy supplied to the particles is used not only to create new surfaces, but also to produce physical changes in the particles, such as inelastic deformation and increase in temperature¹¹³. However, size reduction of solids by mechanical means is an energy intensive and highly inefficient process. Rittiger suggested that the energy required

for particle size reduction is directly proportional to the area of the new surface created as shown in Eq. (12) ¹⁰⁹

$$E = C_R \left(\frac{1}{X_1} - \frac{1}{X_2} \right) \quad (12)$$

where C_R is a constant and X_1 is the starting particle size, and X_2 is the final particle size. Eq. (12) does not account for the energy absorbed during elastic deformation of the particles, which is several times higher than the energy required for creating the new surfaces. Kirpičev and Kick used stress analysis and produced¹⁰⁹ Eq. (13), which is not applicable to fine and ultrafine milling.

$$E = C_K \ln \frac{X_2}{X_1} \quad (13)$$

Bond suggested the more useful equation shown as Eq. (14)

$$E = 10W \left(\frac{1}{\sqrt{X_1}} - \frac{1}{\sqrt{X_2}} \right) \quad (14)$$

In Eq. (14), W is known as the Bond Work index, which is the energy required to reduce the size of a unit mass of material from infinity to 100 μm .

It has been reported that the input power necessary to grind nanoparticles increases by about ten times when the desired final size decreases from 80nm to 30nm¹⁰⁹⁻¹¹⁰. In addition to the high energy required for the milling process, Zhang et al.¹¹¹ also showed that there exists a particle size below which further size reduction cannot be achieved. Below this threshold size, the stress necessary to fracture the particle is above the process capabilities. The stress required for processing is given by Eq. (15)

$$\sigma_f = \frac{K_c}{\sqrt{\pi a_c}} \quad (15)$$

Where σ_f is the fracture stress, K_c is the fracture toughness, and a_c is the average size of material defects. When the particles are reduced to the nano-range, internal defects and notches on the surface of the particles are considerably reduced. In this case, σ_f approaches the theoretical strength of the material. The impact stress of silicon carbide is over 15GPa, which would be the value needed to fracture a defect-free silicon carbide nanoparticle. Such high stress magnitudes are not achievable with conventional high-energy mechanical mills. Nano-size powders are commonly prepared with agitated ball mills, which provide shear stress in addition to compression stress. Despite this, a lower threshold for particle size still exists. It appears that the threshold size is in the range of 25nm to 40nm for a variety of ceramic particles (both oxides and carbides). Rao et al.¹¹⁴ investigated ball milling of SiC particles and found that only after milling for 50 hours it is possible to reduce the powder size to 35nm. Also, Indris et al.¹¹⁵ comminuted lithium oxide particles to 25nm, but they needed over 100 hours for the powder to reach this size. Rostamzadeh and

Shahverdi¹¹² synthesized Al-5%SiC nanocomposites via ball milling and experimented that progressive milling from 0 to 25 h change the morphology of the powder particles from flaky to near-spherical. Castro et al.¹⁰⁸ found the threshold limit for the size to be around 25nm for several oxides (Fig. 14). In addition to the existence of a threshold particle size below which further size reduction is not feasible, mechanical milled material is prone to contamination from the milling tools and the atmosphere. Milling of refractory metals (e.g., tungsten) in a high-frequency shaker for extended times can result in iron contamination of more than 10at. pct. In order to prevent contamination, the process is typically performed in an inert atmosphere and the mills are coated¹⁰⁶.

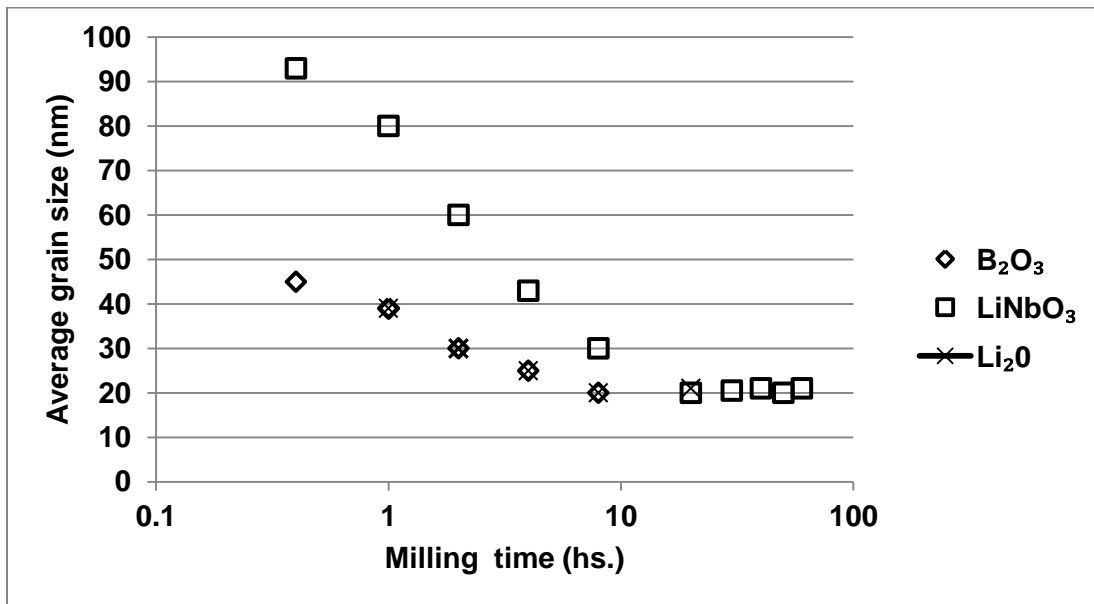


Figure 14. Grain size versus milling time for oxides¹¹⁵.

When nano-composite materials are synthesized by any one of the in-situ processes, many of the fabrication issues that are associated with ex-situ methods are mitigated, or they are completely alleviated. The benefits that in-situ manufacturing methods provide include⁸:

- They produce composite materials that are thermodynamically stable at high temperatures.
- They produce a clean interface between the particles and the metal matrix, which results in strong particle/matrix interfacial bonding.
- Detrimental phases are eliminated, and the creation of the nascent interface can be guided by careful control of the manufacturing process.
- The range of particle sizes in the nanocomposite material is typically narrower than what is available with ex-situ particles.
- Improved particle distribution gives rise to superior mechanical properties.

- Nanocomposite materials with a broad variety of matrix materials (e.g., aluminum, titanium, copper, nickel and iron) and reinforcing particles (borides, carbides, nitrides, oxides and their mixtures) can be produced by in-situ methods.
- In-situ methods are usually easy to scale up for industrial practice and they are usually cost effective.

Nevertheless and despite their great potential, commercial use of in-situ methods is limited, mainly because of the complexity of the reactions involved.

2.2.3 Severe Plastic Deformation

Severe plastic deformation (SPD) is a method used to manufacture nanocrystalline materials by applying high pressures at relatively low temperatures (usually less than $0.4 T_M$) to a metallic material. The process is formally defined as “Any method of metal forming under an extensive hydrostatic pressure that may be used to impose a very high strain on a bulk solid without the introduction of any significant change in the overall dimensions of the sample and having the ability to produce exceptional grain refinement.”¹¹⁶ Conventional deformation methods, such as drawing and rolling produce refined microstructures with low-angle interfaces; but SPD processing creates ultrafine-grained structures with high-angle grain boundaries. SPD methods can overcome issues such as residual porosity in compacted samples and impurities from ball milling. The process is also scalable and can produce large billets. Common SPD methods are equal-channel angular (ECA) pressing and severe plastic torsional straining (SPTS). Both methods are shown schematically in Fig. 15¹¹⁶⁻¹¹⁷.

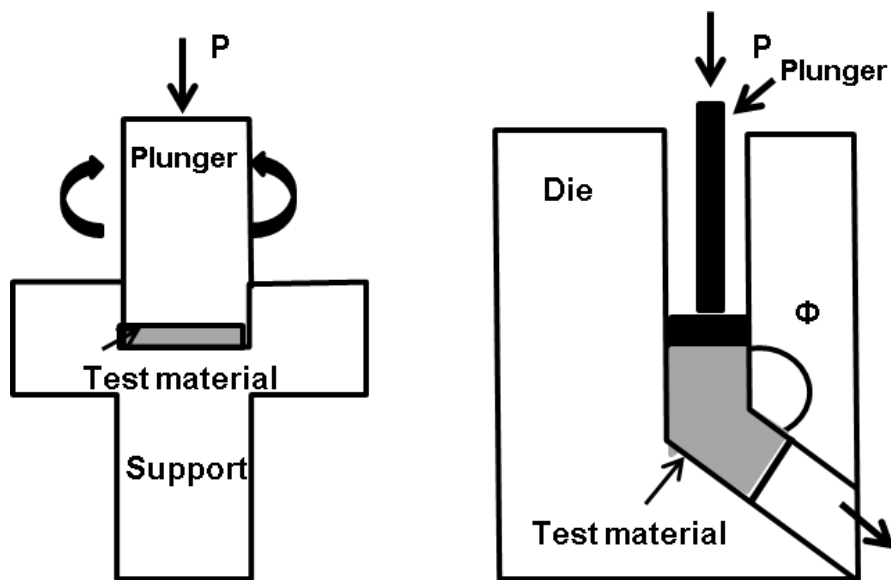


Figure 15. Schematics of a) SPTS process; b) ECA process¹¹⁶.

Equal channel angular pressing (ECA), which is considered¹¹⁸ to be the most promising of the SPD methods, is a relatively new technique for producing ultra-fine grain structures by

introducing a large amount of shear strain into the material without changing its overall shape or dimensions. The process is well suited for aluminum alloys and has been shown to be capable of producing ultra-fine grain structures with grain sizes ranging between 200 and 500 nm¹¹⁶⁻¹²¹. Quang et al.¹¹⁹ made carbon nanotube-copper composites from powders that were consolidated by ECAP at room temperature and showed that the measured high strength is a result of matrix strengthening and also improved nanotube-matrix bonding. They concluded that ECAP of powders is a viable method to achieve full density carbon nanotube-copper nanocomposites. Similarly, starting with powders, Goussous et al.¹¹⁶ produced fully dense Al-C and Al-Al₂O₃ nanocomposites by combining two severe plastic deformation processes, namely mechanical milling to mix the particles, and back pressure equal channel angular pressing (BP-ECAP) to consolidate them. The BP-ECAP consolidation was performed at 400 °C by up to 24 passes. The clusters (about 500nm in size) present in the as-received carbon black powder were broken and dispersed homogeneously in the Al matrix releasing individual carbon particles that were 100nm in size. The Al-Al₂O₃ nanocomposite material contained Al₂O₃ particles that were around 50nm in size and they were well dispersed in the Al matrix. Also, Zhang et al.¹¹⁸ used a modified ECAP extrusion method to manufacture Ni-Ti based composites reinforced with 5 wt.% nano-size (50nm in diameter) Al₂O₃ particles. Nanostructures obtained by SPTS consolidation of Cu and Al micro-size powders and SiO₂ nano-size powders were recently investigated¹²⁰. Due to the applied severe torsion straining, a homogeneous structure with a mean grain size of about 100nm was formed in Al6061/10pct.Al₂O₃ and Al2009/15pct.SiC composites. Alexandrov et al.¹²¹ succeeded in incorporating 5 vol. pct. nano-size Al₂O₃ particles into an Al matrix and 5 vol. pct. SiO₂ into a Cu matrix by means of SPTS. The materials had good strength and moderate ductility. Moreover, the ultrafine-grained Al-Al₂O₃ material exhibited superplastic-like behavior during tensile testing at 400 °C.

2.3 In-situ Solid-Solid Reactive Processing Methods

In-situ solid-solid reactive processing of nanocomposite materials involves reacting together two or more solid species to form a composite. These methods are typically limited to small size components and they are difficult to scale up to industrial production. Effective control of the reactions that lead to particle formation is also an issue. However, the starting materials are inexpensive and it is possible to obtain very small reinforcing particles with these methods. Mechanochemical synthesis is the most commonly used method in this category, and more recently, friction stir processing has emerged as a viable manufacturing method.

2.3.1 Mechanochemical Synthesis

When a chemical reaction occurs entirely in the solid state, the reaction volume is continuously reduced as the reactants convert into products and become physically separated from one another. As a result, the kinetics of these reactions is controlled by the rate at which the reacting species are able to diffuse across phase boundaries and through

product layers¹²². Therefore, high processing temperatures are necessary to ensure diffusion. Consequently, coarse-grained materials, undesirable because of their reduced strength and wear resistance, are produced¹²². Mechanochemical milling has been recognized as an effective way to activate solid-state chemical reactions at low temperatures, and it involves a precursor powder mixture that reacts during milling and changes its chemical composition. When the reaction enthalpy is sufficiently high, sudden release of heat starts a self-propagating combustion reaction that is responsible for this change in chemical composition of the reactant powder mix. Most mechanochemical reactions investigated to date are of the type given by Eq. (16) in which a metal oxide (MO) is reduced by a reducing agent, R to form the pure metal M.



Hot pressing of the reaction products normally follows. The advantages of this process are that it allows the direct formation of powder products, and it is possible to produce an alloy without passing through the conversion from oxides to pure metals. Moreover, given the severe plastic deformation that occurs during milling, nanocrystalline structures can be easily synthesized. The main drawback is the milling time that can range from 60 to more than 140 hours. Mechanochemical reduction of copper oxide with different reducing agents, such as Fe, Al, Ti, Ca, Ni and C, has been widely investigated¹²³⁻¹²⁸. The outcome is a dispersion of metal oxides in a Cu matrix, such as Cu-Al₂O₃, Cu-MnO, and Cu-ZnO. The Fe-Al₂O₃ system has also been extensively studied¹²⁹⁻¹³³. Hwang et al.^{134,135} were able to synthesize 10nm to 20nm Al₂O₃ particles in aluminum and reported an increase in the Rockwell hardness of the nanocomposite material of more than 30 pct. over the matrix material. Wu and Li¹³⁶ employed mechanochemical synthesis to manufacture nanostructured aluminum matrix composites reinforced with CuAl₂ (100–500nm), Al₂O₃, and Al₄C₃ (10–50nm). Similarly, Tavooosi et al.^{137,138} made an Al–13.8 wt. pct. Zn alloy reinforced with 5 vol. pct. Al₂O₃ nano-particles by mechanochemically reacting an Al-ZnO powder mixture in an inert atmosphere and hot pressing the resultant material. Nikfar et al.¹³⁹ used a planetary mill to react Al powder and Ti powder to create a very fine Al-Al₃Ti dispersion. They investigated the effect of pressure and temperature employed in hot pressing the resulting material on abnormal grain growth and porosity, which are common issues in composite materials manufactured by the mechanochemical synthesis process.

2.3.2 Friction Stir Processing

Friction stir processing is a solid state welding technique introduced by Mishra¹⁴⁰, and it employs a rotating tool equipped with a small pin that is pushed against the material. The tool is guided along a straight line in order to modify the microstructure of the region of interest. Friction between the tool and the material results in localized heating that plastically deforms the material. The severe plastic deformation helps to promote mixing and refining of the constituent phases. Nano-sized (50nm) SiC particles have been added to 6061 Al alloy by packing them in a 1 mm deep groove specially created in the metallic alloy¹⁴¹. Using specific values of rotational speed and transverse speed, the nano-particles

were successfully mixed into the matrix alloy as shown in Fig.16a, whereas particles are heavily clustered if such values are not adopted (Fig.16b).

Berbon et al.¹⁴² applied friction stir processing to billets of cryomilled powders that have been hot isostatically pressed. Two ternary aluminum alloys powders (Al-10%Ti-2%Cu and Al-10%Ti-2%Ni) have investigated. After cryomilling, the Al based powder was a severely clustered dispersion of crystals of 200nm in size, which friction stir processing was able to break. Moreover, submicron Al₃Ti intermetallic particles have also been formed by the repeated heating and cooling of the processed areas¹⁴³. Lee et al.¹⁴⁴ have also exploited the localized heat of friction stir processing to trigger a reaction in Al-10%Fe billets and precipitate Al₁₃Fe₄ with an average size of 100nm. Newkirk et al.¹⁴⁵ achieved good ductility (~8%) when adding nano-sized WC particles to 7050 Al alloy also by carving a slot right below the surface of the component. In every application reported so far, the incorporation of nano-sized particle via friction stir processing has taken place close to the surface of the piece. Bulk production of nano-composite materials using this route appears to be challenging.

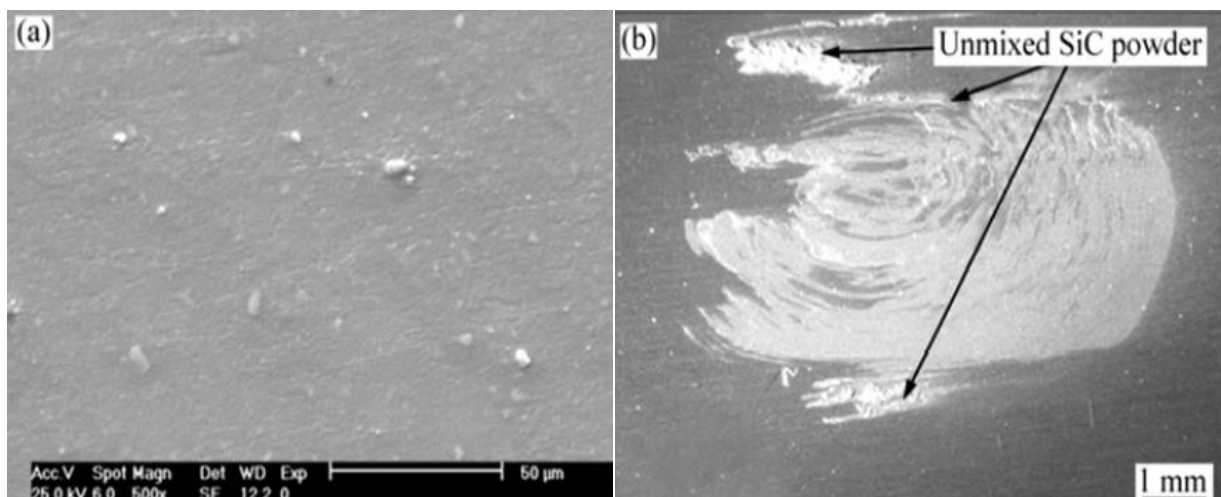


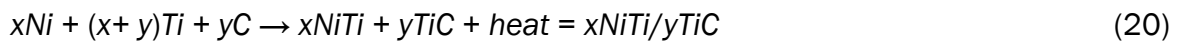
Figure 16. a) Well dispersed SiC nanoparticles. b) Heavily clustered SiC powders. Low rotational speed and penetration depth¹⁴¹.

2.4 In-situ Solid-Liquid Reactive Processing Methods

In-situ solid-liquid reactive processes involve elements (or compounds) that react in the presence of a metallic liquid phase that acts as a solvent. The reinforcing particles are formed by diffusion of these elements in the metal matrix⁸. Among In-situ solid-liquid reactive processes, combustion synthesis, exothermic dispersion, and methods that depend on substitutional chemical reactions have been successfully used to synthesize nano-composite materials.

2.4.1 Combustion Synthesis

Combustion synthesis, also known as self-propagating high-temperature synthesis (SHS) was invented by Merzhanov et al.¹⁴⁶. SHS is a promising method for the synthesis of several classes of advanced materials such as ceramics, intermetallics, and more recently nano-composites. The process starts with milling and pressing powder mixtures to form loosely-compacted pellets. The pellets are added to a solvent that may be molten Al, Mg, or Ti in which other non-metallic elements, such as C and/or B, are present¹⁴⁶⁻¹⁵². The powder mixture is then locally ignited to initiate a highly exothermic and self-sustaining reaction. Ignition can be made by means of a laser beam, induction, resistance, microwaves, chemical waves, or a spark source⁸. The exothermic reaction rapidly increases the temperature of the pellet so that it quickly surpasses the combustion temperature. The heat released during the chemical reaction keeps the propagation front stable by heating up the unreacted portion of the pellet¹⁴⁷. The equipment is simple, processing times are short due to the very high combustion rates (typically 0.15 m/s), and it is possible to form unique metastable phases with improved properties as a result of the non-equilibrium conditions that prevail (i.e. the steep thermal gradients and the high heating and cooling rates). In addition, volatile impurities evaporate because of the high temperatures involved. Typical SHS reactions include the following



Lee et al.¹⁴⁸ produced sub-micron TiC particles in Al from Al-Ti-C powder. Aluminum was found to affect ignition by providing an easier route for reactant mass transfer. Also, ignition has been reported to derive from the reaction between titanium and carbon at the interface between the titanium-containing aluminum melt and the graphite by diffusion of titanium through the aluminum melt to the interface. Talako et al.¹⁴⁹ produced FeAl-Al₂O₃ nano-composite material by the SHS process after mechanical activation of the precursor powders. Burkes et al.¹⁵⁰ synthesized NiTi-TiC sub-micron composites with more than 50 vol. pct. particles. The resulting material showed excellent strength but poor ductility. In general, material produced by the self-propagating synthesis method is pure, but they it is porous (around 50 pct. of theoretical density). Post processing operations, such as high-pressure consolidation (HIP) is often necessary to eliminate the pores. In addition, the scale of the heterogeneities of the reactants (10 μm to 100 μm) can alter or hinder the combustion reaction. Aruna et al.¹⁵¹ investigated post processing options to optimize materials made by the SHS method; these included intensive milling, mechanical activation, chemical treatment, and chemical dispersion. They also discussed SHS with additives, such as salts, to enhance nano-particle nucleation and dispersion and carbon combustion synthesis (CCS), where carbon is used as the reaction fuel instead of the pure metals that are typically used

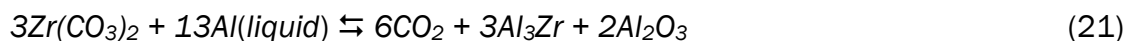
in conventional SHS. Process control is major issue in the SHS process. The fast rate of SHS reactions and the many physical and chemical phenomena that are involved in the process make monitoring and optimizing the process rather challenging and controlling the composition, size and morphology of the resultant reinforcing material very difficult. Moreover, it has been reported that the strong exothermicity of the reaction may generate a combustion wave that passes through the pellets and ignite reactions that can result in unwanted products or prevent the desired reaction from happening. Zuccaro et al.¹⁵² have carried out numerical simulations to predict and thus control the dynamics of the SHS process.

2.4.2 Exothermic Dispersion

The Exothermic Dispersion (XD) process was developed by Martin Marietta Corporation and has been extensively applied to the manufacturing of light-weight materials. Weight savings of 30 to 50 pct. have been achieved in the manufacture of jet engine turbine blades with the XD process. In this method, ceramic phase(s) and a metallic phase are brought together and heated above the melting point of the metallic phase in order to produce a sustained high-temperature synthesis process^{153,154}. Sub-micron composite materials have been produced by this method wherein a mixture of elemental boron, titanium, and aluminum powders is compacted and then sintering at around 800°C. Sintering is accompanied with strong heat release that ignites the XD reaction and result is in the spontaneous formation of titanium diboride and titanium aluminide. The resulting material can contain up to 75 pct. TiB₂, although a Ti-Al alloy reinforced with only 7 pct. TiB₂ made by the XD process has yield strength at 980°C that is significantly higher than that of Inconel 713¹⁵⁵. Chunhu et al.¹⁵⁶ investigated the potential of producing Ti-Al/TiC composite materials by means of the exothermic dispersion method. Their resulting material, which contained about 20 pct. sub-micron size TiC particles, showed a 20 pct. improvement in Vickers hardness over the matrix alloy. The exothermic reaction minimizes the potential for oxidation, and creates clean particle/matrix interfaces. However, controlling the reaction remains an issue due to its fast rate and the sudden heat release, and hot isostatic pressing of the final material is almost always necessary in order to reduce porosity in the final product.

2.4.3 Substitutional Chemical Reaction

An in situ copper matrix composite with 3.5 wt. pct. TiB₂ particles was prepared by a thermic reaction between B₂O₃, carbon (as reducing agent), and titanium in a copper-titanium melt¹⁵⁷. The TiB₂ particles that resulted from the reaction were about 50nm in size and exhibited a homogenous dispersion in the copper matrix. Due to the reinforcing action of these nanoparticles, the tensile strength and hardness of the matrix significantly improved. The composite material also had high electrical conductivity. Similarly, Zhao et al.¹⁵⁸ synthesized nano-size Al₂O₃ and Al₃Zr particles in an aluminum matrix in the system Al-Zr(CO₃)₂ according to the reaction



They applied a magnetic field to the reaction chamber in order to enhance the chemical reaction and reported that the mean particle size was about 80nm and the particles were well distributed in the aluminum matrix. Also, the ultimate tensile strength and yield strength of the nanocomposite material were higher than the ultimate tensile strength and yield strength of similar material synthesized without the magnetic field.

2.5 In-situ Liquid-Liquid Reactive Processing Methods

The MixAlloy Process patented by Sutek Corporation^{159,160} has been applied to the production of nano-composite materials. In this process, two streams of molten metal containing ceramic particles interact with each other in a reaction chamber to form refractory particles. The mixture is then rapidly cast or atomized. 50nm titanium boride particles were produced in a copper matrix with this method. In the first patent disclosure¹⁵⁹, the impingement of the two metal streams onto each other is direct while in the subsequent patent disclosure¹⁶⁰ the impingement is indirect so that instabilities in the metal streams are mitigated. However, it is believed that the impingement of the two metal streams onto each other may not provide adequate energy for mixing; in addition, some un-reacted elements have been detected in the resulting material, even though the stoichiometry is locally maintained.

2.6 In-Situ Gas-Liquid Reactive Processing Methods

In these methods a gas is injected into a specially designed molten metal alloy. The gas reacts with the molten metal alloy and forms reinforcing particles. The chemical composition of the reinforcing particles that form is dictated by the composition of the reacting gas and the molten metal alloy¹⁶¹⁻¹⁶⁴. Fig. 17 is a schematic representation of the apparatus used in the initial phase of feasibility assessment. AlN can be observed in Fig.18a and confirmed by EDS analysis (Fig.18b). The concept on which the process is based on has been first introduced and patented by Koczak and Kumar¹⁶⁵ and has the following advantages/disadvantages

- The gases used are relatively inexpensive and the nano-particles are synthesized in-situ eliminating the cost of expensive ceramic nano-particles.
- Particle surface contaminants are absent since there is no contact with air; accordingly, interfacial bonding is enhanced.
- The process has a wide process window and can be easily controlled by controlling reaction temperature, gas composition, and melt composition.
- Homogeneous microstructures are obtained.
- The temperatures necessary for the reaction to occur are somewhat high (1000-1200 °C) depending on the gas and the matrix alloy).

- Process times may be long.
- The process is not applicable to materials with high melting temperatures.
-

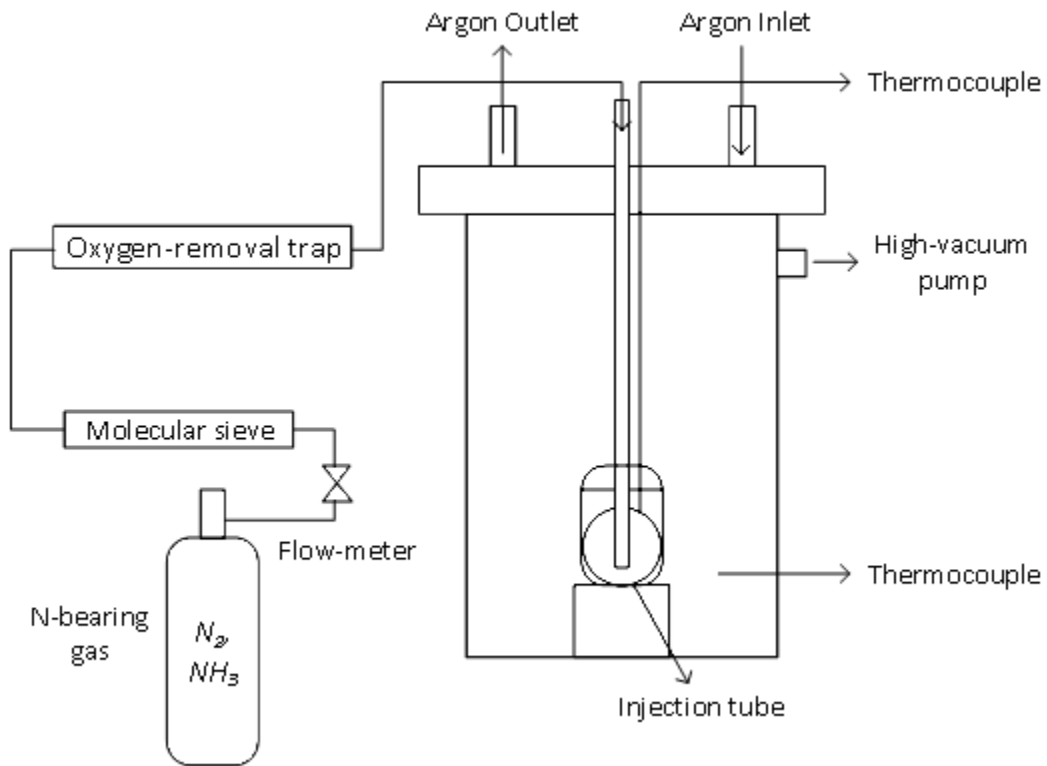


Figure 17. Schematic of in-situ gas-liquid process¹⁶⁷.

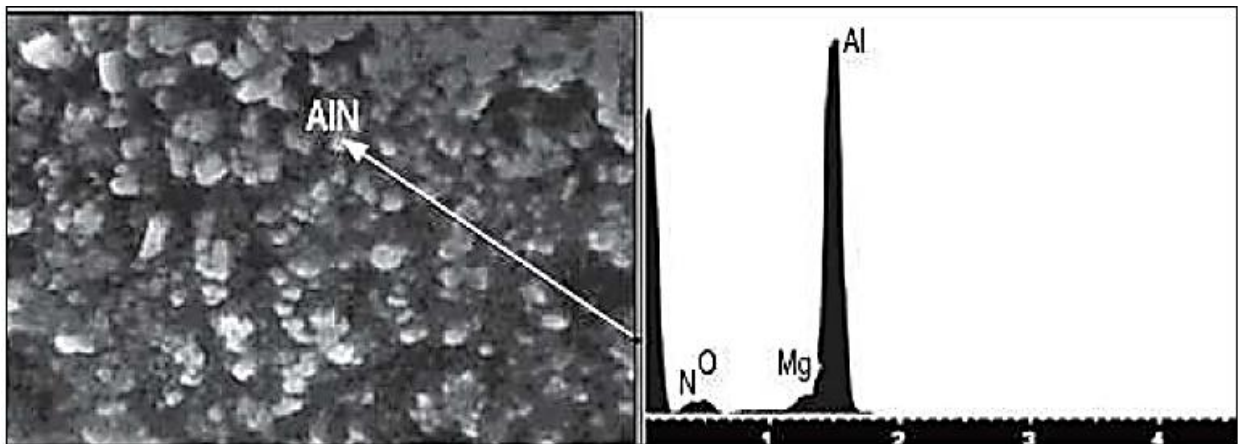


Figure 18. AlN and MgO in Al-15 wt% Mg¹⁷⁰.

Borgonovo and Makhlouf¹⁶⁶⁻¹⁷⁰ and Borgonovo and Apelian^{171,172} investigated two alloy systems in-situ gas-liquid reactive processing of Al-AlN nanocomposites; namely, Al-Mg and Al-Li alloys; and they investigated three nitrogen-bearing gases: pure nitrogen, pure anhydrous ammonia, and a mixture of the two. They assessed the feasibility of the process, and studied the role of the alloy composition, the oxygen content of the reaction atmosphere, and the processing time on the characteristics of the resulting Al-AlN composite material, including particle size, particle size distribution, and the distribution of the AlN particles in the alloy matrix. They performed several experiments and were able to synthesize submicron AlN with processing times ranging between 4 to 6 hours. They report that, with optimum processing conditions, excellent dispersion of 60nm AlN particles in the matrix alloy is possible and their conclusions can be summarized as follows

- Ammonia has an eight times higher nitridation rate than nitrogen when used to nitride an Al-20 wt. pct. Mg alloy. The AlN particle size and particle distribution in the metal matrix are also influenced by the type of reactive gas and nitridation with ammonia gas produces a more uniform particle distribution and smaller AlN particles than nitridation with nitrogen gas.
- Lithium is more efficient than magnesium in catalyzing the nitridation reaction. Only 1.15 wt. pct. Li produces around 11 vol. pct. AlN particles whereas 20 wt. pct. Mg is needed to form 17 vol. pct. AlN particles.
- Particle distribution in the Li-containing alloy is improved when ammonia gas is used instead of nitrogen gas. In this case, the particle size is more uniform and the particle shape is almost spherical. The grain size is considerably decreased and the hardness is improved by around 50 pct. relative to the base alloy.

2.7 In-situ Morphological Processing Methods

Nayak et al.^{173,174} melted Al-Fe alloys under an argon atmosphere and then they rapidly solidified them by means of a single roller melt spinner that is equipped with a copper wheel. The cooling rate was estimated to be around 104K/s. Ultra-fine Al_{100-x}Fe_x particles embedded in the α -Al matrix were found in the melt spun Al-2.5Fe alloy as shown in Fig. 19. Most of the particles were less than 20nm in size. Similarly, TiC particles in an aluminum alloy were synthesized by melting a mixture of aluminum, titanium, and graphite powder in an argon atmosphere. Chill block melt spinning was used to prepare rapidly solidified samples from these melts⁴⁷. The TiC particles that formed in this material were found to be between 40-80nm in size. However, some particle clusters were detected at the grain boundaries.

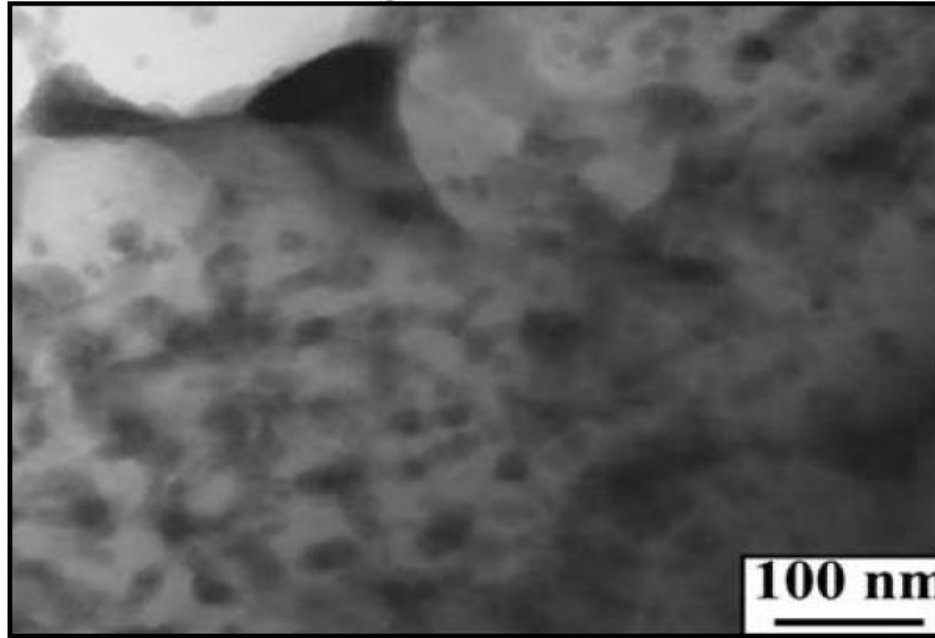


Figure 19. Ultra-fine Al_{100-x}Fe_x precipitates embedded in the α-Al matrix¹⁷³.

3. Summary and Concluding Remarks

The various pathways to manufacturing aluminum matrix nanocomposites have been presented and discussed in this critical review. It is clear that the challenges we face in manufacturing nanocomposite materials for structural applications are daunting. Our ability to achieve a homogeneous distribution of the reinforcing particles in the metal matrix and in the same time assure ease of scalability of the manufacturing process is a critical issue. Ex-situ methods wherein externally manufactured nanoparticles are introduced into the metallic alloy are sub-optimal in this sense. They tend to yield materials that are plagued by particle clustering, interface de-bonding, contamination, and porosity; and the processes are not cost effective. Homogeneous distribution of the nanoparticles is more readily attained by in-situ processing methods wherein the reinforcing particles are created directly in the aluminum alloy. Some of these methods, e.g., methods that rely on reactions between a gas and liquid aluminum to create the reinforcing particles, are cost-effective and have the potential to be scaled up for industrial practice with minimum investment in materials and equipment. Moreover, the method produces particle/matrix interfaces that are clean and it allows easy tailoring of the matrix alloy and reinforcing particles to meet the requirements of specific applications.

Appendix A: Nomenclature

α = interface shape factor

$\Delta\gamma_0$ = interfacial energy change

γ_{PL} = particle-liquid interfacial energy

γ_{SL} = solid-liquid interfacial energy

γ_{PS} = particle-solid interfacial energy

η = dynamic viscosity of the liquid

ρ_l = density of the liquid

ρ_p = density of the particle

ρ_s = density of the solid

Ω = atomic volume

a_0 = interatomic distance

A = Hamaker constant

B = disjoining pressure (also called effective Hamaker constant)

D_l = diffusion coefficient in the liquid

G = thermal gradient in the liquid gap

k = curvature of solid/liquid interface

k_b = Boltzmann's constant

k_l = thermal conductivity of liquid

k_p = thermal conductivity of particle

L = latent heat of fusion

R = particle radius

R_b = radius of particle irregularities

T = temperature

T_m = melting temperature

V_c = critical velocity

4. References

1. S.Rawal, *Journal of Materials*, 2001, **53** (4), 14-17.
2. W. H. Hunt, and D. R. Herling: "Applications of Aluminum Metal Matrix Composites: Past, Present, and Future," International Symposium of Aluminum Applications: Thrusts and Challenges, Present and Future, ASM International, Pittsburgh, Pennsylvania, October 2003.
3. W. H. Hunt, and D. R. Herling, *Advanced Materials & Processes*, 2004, **162**(2), 39–42.
4. S. Choi, and H. Awaji, *Science and Technology of Advanced Materials*, 2005, **6**, 2-19.
5. W.H. Hunt, C.R Cook, and R.R. Sawtell: 'Cost-Effective High Performance P/M Aluminum Matrix Composites for Automotive Applications', SAE Paper 910834, Warrendale, PA, 1991.
6. W. Hoover: 'Metal Matrix Composite—Processing, Microstructures and Properties', 12th Riso International Symposium, ed. N. Hansenetal, 1991, Roskilde, Denmark, 1991, 387–392.
7. C.Borgonovo, and D. Apelian, *Materials Science Forum*, 2011, **678**, 1-22.
8. National Aeronautics and Space Administration USA: 'Aeronautics and Space Report of the President', 1992, *Fiscal Year 1991 Activities*, Washington DC, USA, 1-193.
9. V.M. Kevorkijan, *Journal of Materials* , 1999, **51** (11), 54-58.
- 10.J. E. Allison, and G. S. Cole, *Journal of Materials*, 1993, **45**(1), 19-24.
- 11.Global Industry Analysts, Inc.: 'Metal matrix composites: a global strategic business report', March 2013, 1-257.
- 12.European Aluminium Association: 'Aluminium in cars', 2007, Brussels, Belgium, 1-15.
- 13.Randall Scheps: 'Industry survey finds aluminum use in autos at all-time high; average per vehicle use expected to more than double from 2012 by 2025', *Green Car Congress*, 16 April 2013.
URL:<http://www.greencarcongress.com/2011/09/aluminum-20110912.html>
- 14.D. Miracle, *Composites Science and Technology*, 2005, **65**(15-16), 2526-2540.
- 15.P.E.C. Camargo, K. G. Satyanarayama, and F. Wypych, *Material Research*, 2009, **12** (1), 1-39.
- 16.M. El-Gallaba, and M. Skladb, *Journal of Materials Processing Technologies*,1998, **83**, 277–285.
- 17.S. Jahanmir, M. Ramulu, and P. Koshy: 'Machining of Ceramics and Composites', 1999, edited by CRC Press, Boca Raton, Florida, USA.
- 18.S. Chatterjee, and A. B. Mallick, *Materials Science Forum*, 2012, **736**, 72-80.
- 19.V.S. Aigbodion, *Recent Patents on Nanotechnology*, 2011, **5**, 234-238.
- 20.E.-S. Y. El-Kady, *Materials Sciences and Applications*, 2011, **02**(05), 390-398.
- 21.A. Mazahery, and M. O. Shabani, *Iraqi Journal of Applied Physics*, 2012, **8**(3), 25-30.
- 22.S. M. Zebarjad, S. A. Sajjadi, and E. Z. Vahid Karimi, *Research Letters in Material Science*, 2008, ID. 835746, 1-4.

23. Z. Ren, and S. L. I. Chen: 'Mechanical properties of nanometric particulates reinforced aluminum composites', *The University of New South Wales, Poster*,
URL:
http://www.arclightmetals.org.au/archive/content/documents/workshop_posters/2007/Poster%20PS2-17%20Zheng%20Ren.pdf
24. L. Fischer: 'Literature Survey Report: Nano-Dispersion Strengthening of Aluminum', MCEN 5218, Introduction to research, 2004, University of Colorado, 1-10.
25. Q. Zhang, and D. L. Chen, *Scripta Materialia*, 2006, **54**, 1321-1326.
26. N. Ramakrishnan, *Acta Materialia*, 1996, **44**(1), 69-77.
27. B. Y. Zong, Y. Wang, J. Li, and N. Xu, *International Journal of Modern Physics*, 2009, **23B**, 1627-1633.
28. A. Minnich, and G. Chen, *Applied Physics Letters*, 2007, **91**(7), 073105, 1-3.
29. S. Banerjee, and P. Mukhopadhyay: 'Phase Transformations: Examples from Titanium and Zirconium Alloys', 1st edn; 2007, London, UK, Elsevier.
30. P. Haansen: 'Physical Metallurgy', 3rd edn; 1996, Cambridge, UK, Press Syndacate of the University of Cambridge.
31. G. E. Totten, and D. S. MacKenzie (eds.): 'Handbook of Aluminum. Physical Metallurgy and the Effect of Alloying Additions', 2003, 2003, New York, Marcel Dekker.
32. B. H. Kear, and J. M. Oblak, *Le Journal de Physique Colloques*, 1974, **35**(C7), C7-35-C37-45.
33. D. N. Seidman, E. A. Marquis, and D. C. Dunand, *Acta Materialia*, 2002, **50**, 4021-4035.
34. Z. Zhang, and D. L. Chen, *Materials Science and Engineering*, 2008, **483-484A**, 148-152.
35. Z. W. Wang, Y. B. Wang, X. Z. Liao, Y. H. Zhao, E. J. Lavernia, Y. T. Zhu, Z. Horita, and T. G. Langdon, *Scripta Materialia*, 2009, **60**(1), 52-55.
36. A. Sanaty-Zadeh, *Materials Science and Engineering*, 2012, **531A**, 112-118.
37. J. Moon, S. Kim, J.-i. Jang, J. Lee, and C. Lee, *Materials Science and Engineering*, 2008, **487A**(1-2), 552-557.
38. N. Chawla, and Y. L. Shen, *Advanced Engineering Materials*, 2001, **3**(6), 357-370.
39. K. U. Kainer: 'Metal Matrix Composites: Custom-made Materials for Automotive and Aerospace Engineering', Chap. 1, 'Basics of Metal Matrix Composites', 1-54; 2006, Weinheim, FRG, Wiley-VCH Verlag GmbH & Co. KGaA.
40. D. Poirier, R. A. L. Drew, M. L. Trudeau, and R. Gauvin, *Materials Science and Engineering*, 2010, **527A**(29-30), 7605-7614.
41. S. Suresh, A. Mortensen and A. Needleman: 'Fundamentals of Metal Matrix Composites', 1993, 1993, London, UK, Butterworth-Heinemann.
42. A. Evans, C. San Marchi, and A. Mortensen: 'Metal Matrix Composites in Industry: An Introduction and a Survey', 2003, New York, US, Springer.
43. P. M. Ajayan, L. S. Schadler, and P. V. Braun, 'Nanocomposite Science and Technology', 2003, Berlin, Germany, Wiley-VCH.

44. C. C. Koch: 'Nanostructured Materials: Processing, Properties, and Applications', 2006, Norwich, NY, US, William Andrew.
45. N. Chawla, and K. Chawla: 'Metal Matrix Composites', 2006, New York, US, Springer.
46. N.K. Tolochko, A.A. Andrushevic, and Y. A. Shienok, *Advanced Materials Research*, 2009, **79-82**, 425-428.
47. G. Cao: 'Nanostructures & Nanomaterials: Synthesis, Properties & Applications', 2004, London, UK, Imperial College Press.
48. L. Xiaodan, 139th Annual Meeting and Exhibition, Supplemental Proceedings, Vol. 2, Materials Characterization, Computation, Modelling and Energy, TMS, Seattle, WA, October 2010.
49. Y.M. Youssef, R.J. Dashwood, and P.D. Lee, *Composites*, 2005, **36A**, 747-763.
50. T. Lierfeld, M. Kolbe, G. Eggeler, and D. M. Herlach, *Advanced Engineering Materials*, 2008, **10(6)**, 547-553.
51. A. Mortensen, and I. Jin, *International Materials Reviews*, 1992, **37(3)**, 101-128.
52. A.W. Rempel, and M.G. Worster, *Journal of Crystal Growth*, 1999, **205**, 427-440.
53. B. K. Dhindaw, *Bullettin of Material Science*, 1999, **22(3)**, 665-669.
54. G. Kaptay, *Metallurija-Journal of Metallurgy*, 2004, **10(3)**, 243-250.
55. G. Kaptay, *Metallurgical and Materials Transactions*, 1999, **30A**, 1887-1890.
56. Á. Borsik, K. K. Kelemen, G. Kaptay, *Materials Science Forum*, 2003, **414-415**, 371-376.
57. G. Kaptay, *Metallurgical and Materials Transactions*, 2001, **32A**, 993-1005.
58. J. Hashim, L. Looney, M.S.J. Hashmi, *Journal of Materials Processing Technology*, 2002, **123**, 251-257.
59. L. Hadji, *Physical Review E*, 1999, **60(5)**, 6181-6184.
60. A. I. Raitchenko, and K. Mukai, *Journal of Applied Physics*, 1999, **86(4)**, 2291.
61. J. W. Garvin, and H. S. Udaykumar, *Journal of Crystal Growth*, 2004, **267(3-4)**, 724-737.
62. M. Kolbe, X. R. Liu, T. Volkman, R. Röstel, P. K. Galenko, G. Eggeler, B. Wei, and D. M. Herlach, *Materials Science and Engineering: A*, 2004, **375-377**, 524-527.
63. S. Mukherjee, and D. M. Stefanescu, *Metallurgical and Materials Transactions*, 2004, **35A**, 613-621.
64. G. Wilde, M. Byrnes, and J.H. Perepezko, *Journal of Non-Crystalline Solids*, 1999, **250-252**, 626-631.
65. M. K. Chaudhury, *Materials Science and Engineering R*, 1996, **16**, 97-159.
66. M.A. Azouni, and U. P. Casses, *Advances in Colloid and Interface Science*, 1998, **75**, 83-106.
67. J.W. Garvin, Y. Yang, and H.S. Udaykumar, *International Journal of Heat and Mass Transfer*, 2007, **50**, 2969-2980.
68. F. R. Juretzko, B. K. Dhindaw, D. M. stefanescu, S. Sen, and P. A. Curreri, *Metallurgical and Materials Transactions*, 1998, **29A**, 1691-1696.

- 69.A. V. Catalina, S. Mukherjee, and D. M. Stefanescu, *Metallurgical and Materials Transactions*, 2000, **31A**, 2559-2568.
- 70.J. W. Garvin, and H. S. Udaykumar, *Journal of Crystal Growth*, 2003, **252**(1-3), 451-466.
- 71.P. L. Schaffer, D. N. Miller, and A. K. Dahle, *Scripta Materialia*, 2007, **57**(12), 1129-1132.
- 72.D.M. Stefanescu, B. K. Dhindaw, S.A. Kacar, and A. Moitra, *Metallurgical Transactions*, 1988, **19A**, 2847-2855.
- 73.D.M. Stefanescu, A. Moitra, A.S. Kacar, and D.K. Dhindaw BK, *Metallurgical and Materials Transactions*, 1990, **21A**, 231-239.
- 74.D.M. Stefanescu, F.R. Juretzko, B.K. Dhindaw, A. Catalina, S. Sen, and P.A. Curreri, *Metallurgical and Materials Transactions*, 1998, **29A**, 1697-1706.
- 75.D. R. Uhlmann, B. Chalmers, and K. A. Jackson, *Journal of Applied Physics*, 1964, **35** (10), 2986-2993.
- 76.S. N. Omenyi, and A. W. Neumann, *Journal of Applied Physics*, 1976, **47** (9), 3956-3962.
- 77.S. N. Omenyi, *Journal of Applied Physics*, 1981, **52**(2), 789.
- 78.S. N. Omenyi, *Journal of Applied Physics*, 1981, **52**(2), 796.
- 79.A.A. Chernov, D.E. Temkin, and A.M. Melnikova, *Soviet Physics-Crystallography* , 1976, **21**(4), 369-374.
- 80.A.A. Chernov, D.E. Temkin, and A.M. Melnikova, *Soviet Physics-Crystallography*, 1977, **22**(6), 656-658.
- 81.A.M. Zubko, V.G. Lobanov, and V.V. Nikonova, *Soviet Physics-Crystallography* ,1973, **18**(2), 239-241.
- 82.J.K. Kim, and P.K. Rohatgi, *Metallurgical and Materials Transactions*, 1998, **29A**, 351-358.
- 83.J. K. Kim and P. K. Rohatgi, *Acta Materialia*, 1998, **46**(4), 115-1123.
- 84.G.F. Bolling, and J.A. Cisse', *Journal of Crystal Growth*, 1971, **10**, 56-66.
- 85.G.F. Bolling, and J.A. Cisse', *Journal of Crystal Growth*,1971, **10**, 67-76.
- 86.M. K. Surappa, and P.K. Rohatgi, *Journal of Material Science*, 1981, **16**(2), 562-564.
- 87.J. Pötschke, and V. Rogge, *Journal of Crystal Growth*, 1989, **94**(3), 726-738.
- 88.S. Sen, W.F. Kaukler, P. Curreri, and D.M. Stefanescu, *Metallurgical and Materials Transactions*,1997, **28A**, 2129-2135.
- 89.R. Sasikumar, T.R. Ramamohan, and B.C. Pai, *Acta Metallurgica*, 1989, **37**(7), 2085-2091.
- 90.R. Sasikumar, and T.R. Ramamohan, *Acta Metallurgica*, 1991,**39**(4), 517-522.
- 91.R. E. McDuff: 'Particle Collisions and Aggregation', *Oceanography* 540, Marine Geological Processes , Autumn Quarter 2012,
URL: <http://www2.ocean.washington.edu/oc540/lec02-26/>
- 92.G Cao, J. Kobliska, H. Konishi, and X. li, *Metallurgical and Material Transactions*, 2008, **39A**, 880-886.

- 93.S. Melis, and A. Sorti, *Americal Institute of Chemical Engineers Journal*, 2009, **45** (7).
- 94.R. Lee-Desautels, *Educational Resources for Particle Technology*, 051Q-Lee, 1-8.
- 95.R. Ashtana: 'Solidification Processing of Reinforced Metals', 1995, Switzerland, Trans. Tech Publications.
- 96.G.Kaptay, Proc. of the 2nd Int. Conf. High Temperature Capillarity, edited by N.Eustathopoulos and N.Sobczak, published by Foundry Research Institute, Cracow, Poland, 1998, 388-393 .
- 97.S. Gierlotka, *Solid State Phenomena*, 2006, **101-102**, 157-164.
- 98.B. F. Schultz: 'Stir mixing and pressureless infiltration synthesis of aluminum alloy metal matrix nanocomposites', Ph.D thesis, The University of Wisconsin - Milwaukee, Milwaukee, WI, 2009, 1- 208.
- 99.G. Kaptay, *Materials Science Forum*, 2003, **414-415**, 419-424.
- 100.Y. Yang, and X. Li, *Journal of Manufacturing Science and Engineering*, 2004, **129**, 497-501.
- 101.Y. Yang, J. Lan, and X. Li, *Materials Science and Engineering*, 2004, **380A**, 378-383.
- 102.Y. Yang, X. Li, and X. Cheng, *Journal of Material Science and Engineering*, 2004, **39**, 3211-3212.
- 103.S. Mula, P. Padhi, S. C. Panigrahi, S. K. Pabi, and S. Ghosh, *Materials Research Bulletin*, 2009, **44**(5), 1154-1160.
- 104.X. Li, Y. Yang, and D. Weiss: 'Ultrasonic cavitation based dispersion of nanoparticles in aluminum melts for solidification processing of bulk aluminum nanocomposites: theoretical study, fabrication and characterization', *AFS Transactions*, 2007, Paper 07-133(02), 1-12.
- 105.Z.Y. Ma, Y.L. Lia, Y. Liang, L F. Zheng , J. BP, and S.C. Tjong, *Material Science and Engineering*, 1996, **219A**, 229-231.
- 106.J. Peng, U.S. Patent 7,297,310, 2007.
- 107.T. P. Yadav, R. M. Yadav, and D. P. Singh, *Nanoscience and Nanotechnology*, 2012, **2**(3), 22-48.
- 108.C. L. De Castro, and B. S. Mitchell: 'Synthesis, Functionalization and Surface Treatment of Nanoparticles', 2002, American Scientific Publishers.
- 109.P. Balaz: 'Mechanochemistry in Nanoscience and Minerals Engineering', Chap.2, 'High-Energy Milling', 103-132, 2008, Berlin-Heidelberg, Germany, Springer-Verlag.
- 110.S. Zhu, J. Ma, M. Zhang and C. Wu: 'Advances in nanocomposites - synthesis, characterization and industrial applications', Chap. 38, 'Mechanical alloying: for formation of nanocomposite WC/MgO materials', 883-904, 2011, Dr. Boreddy Reddy (Ed.), ISBN: 978-953-307-165-7.
- 111.D.L. Zhang, J. Liang and J. Wu: *Mat. Sci. Eng. Vols. A375-377* (2004), pp. 911-916.
- 112.T. Rostamzadeh, and H. R. Shahverdi, *Iranian Journal of Materials Science & Engineering*, 2011, **8**(1), 32-39.
- 113.P. Katiyar: ' Processing, microstructural and mechanical characterization of mechanically alloyed Al-Al₂O₃ nanocomposites', Ph.D thesis, College of Engineering

- and Computer Science at the University of Central Florida, Orlando, Florida, 2004, 1-116.
- 114.J. B. Rao, G. J. Catherin, I. N. Murthy, D.V. Rao, and B. N. Raju, *International Journal of Engineering, Science and Technology*, 2011, **3**(4), 82-88.
- 115.S. Indris, D. Bork, and P. Heitjans, *Journal of Materials Synthesis and Processing*, 2000,**8**(3-4), 245-250.
- 116.A. Bachmaier: 'Generation of bulk nanocomposites by severe plastic deformation', PhD thesis, University of Leoben, Leoben, Austria, 2011, 1-95.
- 117.S. Goussous, W. Xu, and K. Xia, *Journal of Physics: Conference Series*, 2010, **240**, 012106.
- 118.S. Zhang and J. Bai, and K. Shue: 'Bulk nanocomposites produced by thermally activated severe plastic deformation', M3TechCenter LLC, Canton, MI, USA, 2008.
- 119.P.Quang, Y.G.Jeong, S.C.Yoon, S.H.Hong, and H.S.Kim, *Journal of Materials Processing Technology*, 2007, **187-188**, 318-320.
- 120.R.Z. Valiev, R.K. Islamgaliev, I.V. Alexandrov, *Progress in Materials Science*, 2000, **45**, 103-189.
- 121.I.V. Alexandrov, Y.T. Zhu, T.C. Lowe, R.K. Islamgaliev, and R.Z. Valiev, *Metallurgical and Materials Transactions*, 1998, **29A**, 2253-2260.
- 122.M. Khodaei, M.H. Enayati, and F. Karimzadeh: 'Advances in nanocomposites - synthesis, characterization and industrial applications', Chap. 8, 'Mechanochemically synthesized metallic-ceramic nanocomposite; mechanisms and properties', 157-180, 2011, Dr. Boreddy Reddy (Ed.), ISBN: 978-953-307-165-7.
- 123.D.Y. Ying, and D.L. Zhang, *Materials Science and Engineering*, 2000, **286A**,152-156.
- 124.X. Shengqi, Q. Xiaoyan, M. Mingliang, Z. Jingen, Z. Xiulin, and W. Xiaotian, *Journal of Alloys and Compounds*, 1998, **268**, 211-214.
- 125.H. Arami, A. Simchi, and S.M. Seyed Reihani, *Journal of Alloys and Compounds*, 2008, **465**, 151-156.
- 126.H. Arami and A. Simchi, *Material Science and Engineering*, 2007, **464A**, 225-232.
- 127.S. Sheibani, M. Khakbiz, and M. Omid, *Journal of Alloys and Compounds*, 2009, **477**, 683-687.
- 128.H.L. Castricum, H. Bakker, and E.K. Poels, *Materials Science and Engineering* , 2001, **304A-306A**, 418-423.
- 129.M. Khodaei, M.H. Enayati, and F. Karimzadeh, *Journal of Materials Science*, 2008, **43A**, 132-138.
- 130.D. Oleszak, and M. Krasnowski, *Materials Science Forum*, 2001, **360-362**, 235-240.
- 131.V. Rajkovic, D. Bozic, and M.T. Jovanovic, *Journal of Alloys and Compounds*, 2008, **459**,177-184.
- 132.R.H. Fan, H.L. Lu, K.N. Sun, W.M. Wang, and X.B. Yi, *Thermochemica Acta*, 2006, **440**, 129-131.

- 133.F. Karimzadeh, M.H. Enayati, and M. Tavoosi, *Materials Science and Engineering*, 2008, **486A**, 45–48.
- 134.S.J. Hwang, D. Wexler, and A. Calika, *Journal of Materials Science*, 2004, **39**, 4659–4662.
- 135.S.J. Hwang, and J. Lee, *Materials Science and Engineering*, 2005, **405A**, 140–146.
- 136.J.M. Wu, and Z.Z. Li, *Journal of Alloys and Compounds*, 2000, **299**, 9–16.
- 137.Tavoosi, M., Karimzadeh, F. & Enayati, and M.H., *Materials Letters*, 2008, **62**, 282–285.
- 138.Tavoosi, M., Karimzadeh, F., Enayati, and M.H. & Heidarpour, *Journal of Alloys and Compounds*, 2008, **475**, 198–201.
- 139.B. Nikfar, H. Ghiabakloo, H. R. M. Hosseini, and A. V. Mohammadi, *IOP Conference Series: Materials Science and Engineering*, 2012, **40**, 012005.
- 140.R.S. Mishraa, and Z.Y. Mab, *Materials Science and Engineering*, 2005, **50R**, 1–78.
- 141.M. Salehi, M. Saadatmand, and J. Aghazadeh Mohandesi, *Transactions of Nonferrous Metals Society of China*, 2012, **22**(5), 1055-1063.
- 142.P. B. Berbon, W. H. Bingel, R. S. Mishra, C. C. Bampton, and M. W. Mahoney, *Scripta Materialia*, 2001, **44**, 61–66.
- 143.C. J. Hsu, C. Y. Chang, P. W. Kao, N. J. Ho, and C. P. Chang, *Acta Materialia*, 2006, **54**(19), 5241-5249.
- 144.S. Lee, P. W. Kao, and N. J. Ho, *Intermetallics*, 2008, **16**(9), 1104-1108
- 145.J.W. Newkirk, R. Mishra, J. Thomas, and J.A. Hawk, *Advances in Powder Metallurgy and Particulate Materials*, 2003, MPIF, 6.60-6.70.
- 146.A.G.Merzhanov, A.S.Rogachev, and A.E.Sychev, *Doklady Physical Chemistry*, 1998, **362**(1-3), 217-221.
- 147.N.Z.Lyakhov, P.A.Vityaz, T.F. Grygoryeva, T.L. Talako, A.P. Barinova, I.A. Vorsina, A.I. Letzko, and S.V. Cherepanova, *Reviews on Advanced Materials Science*, 2008, **18**, 326-328.
- 148.W. Lee, and S. Chung, *Journal of the American Ceramic Society*, 1997, **80** (1), 53–61.
- 149.T. L. Talako, T. F. Grigoryeva, A. I. Letsko, A. P. Barinova, P. A. Vityaz, and N. Z. Lyakhov, *Combustion, Explosion, and Shock Waves*, 2009, **45** (5), 551–558.
- 150.D. E. Burkes, G. Gottoli, H. C. Yi, and J. J. Moore, *Metallurgical and Materials Transactions*, 2006, **37A**, 235-242.
- 151.S. T. Aruna, and A. S. Mukasyan, *Current Opinion in Solid State and Materials Science*, 2008, **12**(3-4), 44-50.
- 152.G. Zuccaro, G. Lapenta, and G. Maizza, *Computer Physics Communications*, 2004, **162** (15), 89-101.
- 153.C.M.Ward-Close, R. Minor, and P.J. Doorbar, *Intermetallics*, 1996, **4**, 217-229.
- 154.S.C. Tjong, and Z.Y. Ma, *Material Science and Engineering*, 2000, **29**, 49-113.
- 155.K. Shenghong, and D. Yuhan, *Journal of Wuhan University of Technology: Material Science Edition*, 2005, **20** (4),1-5.

- 156.T. Chunhu, and W. Shoukai: 'XD synthesis and reactive mechanism of TiAl intermetallics and TiC/TiAl composite', 19960104 024, National Air Intelligence Center, OH, USA, 1995.
- 157.J.Tu, N.Wang, Y.Yang and W.Qu, *Materials Letters*, 2002, **52** (6), 448-452.
- 158.Y.Zhao, S.Zhang, G.Chen, X.Cheng, and Q.Wang, *Composites Science and Technology*, 2008, **68**, 1453-1470.
- 159.Nam P. Suh Sutek Corporation, U.S. Patent 4278622 and 4279843, 1981.
- 160.Nam P. Suh Sutek Corporation, U.S. Patent 4,706,730 and 4,890,662, 1987.
- 161.R.F. Shyu, F.T. Weng, and C.T. Ho, *Journal of Materials Processing Technologies*, 2002, **122**, 301-304.
- 162.R.F. Shyu, and C.T. Ho, *Journal of Materials Processing Technologies*, 2006, **171**, 411-416.
- 163.M.Dyzia, and J.Sleziona, *Archives of Material Science and Engineering*, 2008, **31**, 17-20.
- 164.S.Tyagi, Q.Zheng, and R. Reddy, *Aluminum 2004*, edited by S. K. Das, TMS, Warrandale, 2004, 63-72.
- 165.R. G. Reddy, US Patent 6,343,640, 2002.
- 166.C. Borgonovo, and M.M. Makhlof: "A Novel Method for Manufacturing Aluminum-Aluminum Nitride Nanocomposites," Proceedings of MS&T, Columbus, Ohio, 2011.
- 167.C. Borgonovo and M.M. Makhlof: "The Synthesis of Die-Castable Nano-Particle Reinforced Aluminum Matrix Composite Materials by In-Situ Gas-Liquid Reaction," Proceedings of High Tech Die Casting, Vicenza, 2012.
- 168.C.Borgonovo and M.M. Makhlof: "In-Situ Manufacturing of Nano-Particle Reinforced Metal Matrix Composites," Proceedings of AFS, Columbus, Ohio, 2012.
- 169.C.Borgonovo and M.M. Makhlof: "In-Situ Manufacturing of Aluminum Based Metal Matrix Composites," Proceedings of the 15th European Conference on Composite Composite Materials, Venice, Italy, 2012.
- 170.C. Borgonovo, D. Apelian, and M.M. Makhlof, *Journal of Materials*, 2011, 51-58.
- 171.C. Borgonovo, and D. Apelian, *Materials Science Forum*, **690**, 2011, 187-191, 2011.
- 172.C. Borgonovo, and D. Apelian, *Materials Science Forum*, 2011, **678**, 115-123.
- 173.S. S. Nayak, B.S.Murty, and S.K.Pabi, *Bulletin of Material Science*, 2008, **31** (8),249-254.
- 174.S. S. Nayak, D. H. Kim, S. K. Pabi, and B. S. Murty, *Transactions of the Indian Institute of Metals*, 2012, **65**(6), 647-651.

Synthesis of Aluminum-Aluminum Nitride Nanocomposites by Gas-Liquid Reactions – Thermodynamic and Kinetic Considerations

Cecilia Borgonovo and Makhoulouf M. Makhoulouf

Department of Mechanical Engineering
Worcester Polytechnic Institute
Worcester, MA 01609

Keywords: nanocomposites, in-situ manufacturing, gas/liquid reaction, aluminum, magnesium, lithium, aluminum nitride, nitridation, gas bubbles

Abstract

In-situ fabrication of the reinforcing particles directly in the metal matrix is an answer to many of the challenges encountered in manufacturing metal matrix nanocomposite materials. In this method, the nano-sized particles are formed directly within the melt by means of a chemical reaction between a specially designed metallic alloy and a reactive gas. The thermodynamic and kinetic characteristics of this chemical reaction dictate the particle size and distribution in the matrix alloy, as well as the nature of the particle/matrix interface; and consequently they govern many of the material's mechanical and physical properties. This article focuses on aluminum-aluminum-nitride nanocomposite materials that are synthesized by injecting a nitrogen-bearing gas into a molten aluminum alloy. The thermodynamic and kinetic aspects of the process are modeled, and the detrimental role of oxygen is elucidated. Also explained are the effects on the AlN particle size and distribution of the matrix and gas composition, the process temperature and time, and the average size of the gas bubbles.

1. Introduction

Aluminum matrix nanoparticle composite materials have mechanical and physical properties that make them attractive for many applications in the aerospace, automotive and microprocessor industries. These properties derive from the lightweight of aluminum and the attractive properties of aluminum nitride, which include low density (3.026 g.cm^{-3}), low average coefficient of thermal expansion ($4.5 \times 10^{-6} \text{ K}^{-1}$), and good thermal conductivity ($110\text{-}170 \text{ W.m}^{-1}.\text{K}^{-1}$). However, producing these materials on a large scale remains difficult despite the many attempts that have been made to overcome the issues associated with their manufacture. Recently, Borgonovo and Makhoulouf¹ reviewed the various methods used to manufacture nanocomposite materials and concluded that manufacturing methods that are based on adding ex-situ particles to molten metal and employing mechanical stirring to disperse them, as well as methods that are based on liquid infiltration of ceramic

substrates, and methods that are based on powder metallurgy have serious limitations when dealing with nanometer size particles. Paramount among these limitations are the high tendency of the particles to cluster and particle/matrix interface de-bonding. Also the review asserts that more recent fabrication methods, such as spray deposition, ultrasonic-assisted cavitations, and plasma synthesis are not easily scalable and invariably costly. Synthesizing the reinforcing particles inside the metal matrix overcomes many of these issues because the nanoparticles are formed directly within the molten metal by means of a controlled chemical reaction between the liquid alloy and an appropriate gas. In-situ particle synthesis ensures good distribution of the reinforcing particles in the matrix alloy, a relatively small particle size, and a clean thermodynamically stable particle/matrix interface². Moreover, production costs of the final component are comparatively low because the expensive nanoparticles are formed in-situ. In-situ synthesis of nanocomposite materials is typically performed by introducing a reactive gas into a molten metal alloy to cause a chemical reaction that produces the reinforcing particles. The present article focuses on the synthesis of aluminum-aluminum nitride nanocomposites by injecting a nitrogen-bearing gas into molten aluminum that has been pre-alloyed with magnesium and/or lithium. The underlying thermodynamic and kinetic aspects of the process are investigated, and the mechanism of formation of the aluminum nitride particles is explained. Also, the effect on particle size and particle distribution of the matrix and gas composition, the process temperature and time, and the level of melt stirring during gas injection are elucidated. Finally, the process is mathematically modeled in order to provide means for process control and optimization.

2. Apparatus and Procedure for Synthesizing Al-AlN Nanocomposites

Borgonovo and Makhlouf³⁻⁷ designed and built the apparatus shown schematically in Fig. 1 and used it to synthesize Al-AlN nanocomposite material. This apparatus is used here to study the thermodynamic and kinetic aspects of the process. Prior to use, the furnace chamber is thoroughly cleaned in order to remove any contaminants such as dust. A conically-shaped alumina crucible that is 7 cm high and that has a 5 cm upper diameter is positioned in the furnace with the help of a fiberscope video camera. The camera is inserted from the top of the furnace through a re-sealable fitting and the cover of the furnace is then closed. Care is taken to locate the crucible in a uniform temperature region in the furnace (at least 35 cm from the top) in order to achieve and maintain the correct temperature for the synthesis reaction. A specially designed gas injection rotating impeller that has been previously coated with boron nitride is inserted from the top into the furnace chamber and its alignment inside the crucible is insured by means of the fiberscope camera. Once the alignment is completed, the camera is extracted and the fittings are placed. A high vacuum pump is then connected to the furnace and the chamber is evacuated to 10^{-2} torr. The furnace is then flushed with high purity Argon gas (Grade 5) for 15 minutes. Evacuation and back filling of the chamber with Argon gas is repeated four times in order to remove as much

oxygen from the reaction chamber as possible. Then the heating process is started. Once the melt reached 1273 K, the rotating impeller is dipped into the crucible and the reactive gas is injected into the melt. Either nitrogen gas or ammonia gas are used, and in both cases the flow rate of the reactive gas is maintained between 0.2 and 0.5 L/min. The temperature is monitored by two k-type thermocouples and during the heating process a flux of Argon gas flowing at 0.2 L/min is maintained in the furnace. Two high capacity oxygen getter traps are placed in series along the gas delivery line and the gas is bubbled through them before reaching the furnace. These oxygen removal traps have a removal efficiency that allows less than 1 ppb oxygen in the gas stream.

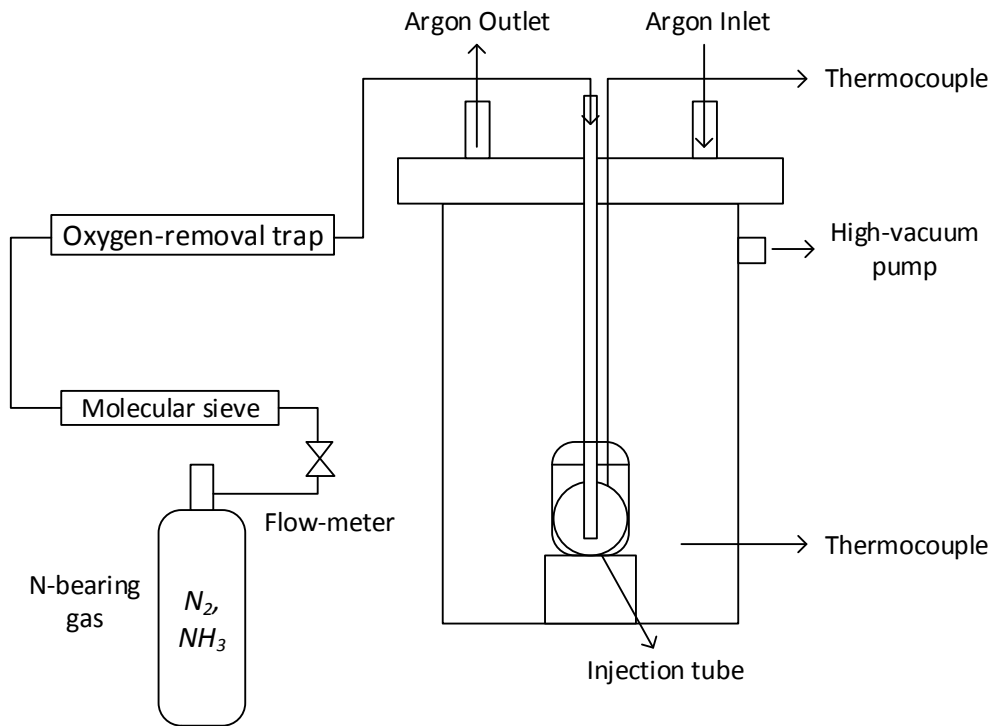


Figure 20. Experimental apparatus.

3. Thermodynamic Considerations

The detrimental effect of oxygen – The chemical affinity between oxygen and aluminum is higher than that between nitrogen and aluminum. Consequently, as the Ellingham diagram in Fig. (2) shows, aluminum oxidation is more likely to occur than aluminum nitridation. Therefore, it is necessary to determine the minimum amount of oxygen that can be tolerated as impurity in the nitrogen-bearing gas so that nitridation is not hindered.

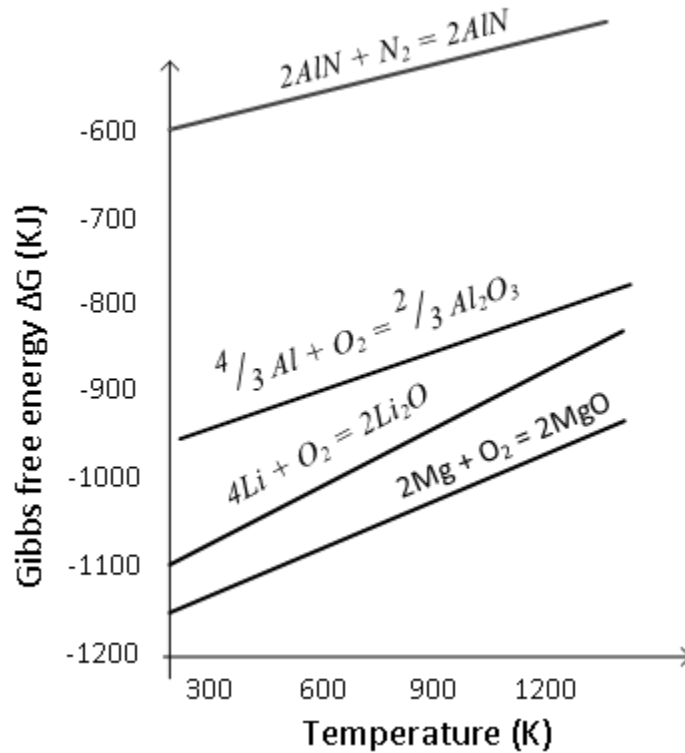


Figure 21. Ellingham diagram of oxidation and nitridation of O_2 and oxidation of Mg and Li.

When oxygen is present in the gas stream, Eqs. (1) and (2) will occur with Eq. (2) being preferred. Eq. (3) can be deduced from Eqs. (1) and (2)



The Gibbs free energy of formation of Eq. (3), ΔG_{36} , as a function of temperature is given by Eq. (4)

$$\Delta G_{36} = 4\Delta G_{AlN} + 3\Delta G_{O_2} - 2\Delta G_{Al_2O_3} - 2\Delta G_{N_2} = 2078000 - 185T \quad (4)$$

The permissible partial pressure of oxygen in the gas stream, P_{O_2} , and hence the maximum tolerable amount of oxygen for Eq. (3) to proceed towards the right is

$$\Delta G_{36} = -RT \ln P_{36} = -RT \ln \frac{\left(\frac{P_{O_2}}{P_{atm}}\right)^3}{\left(\frac{P_{N_2}}{P_{atm}}\right)^2} \approx -RT \ln \left(\frac{P_{O_2}}{P_{atm}}\right)^3 \quad (5)$$

Since the nitrogen flow rate is very low (~0.2 l/min), the calculation can be simplified by assuming that the partial pressure of nitrogen, P_{N_2} , is equal to the total pressure in the reaction system $P_{atm} = 1 \text{ atm} = 1.01325 \times 10^5 \text{ Pa}$. From Eq. (3) and Eq. (5), and using thermodynamics data from^{8,9}, Eq. (6) is derived to describe the change in P_{O_2} with temperature

$$\ln P_{O_2} = 19 - \frac{82487}{T} \quad (6)$$

By employing Eq. (6) it is found that the permissible partial pressure of oxygen for aluminum nitridation at 1273K is $5 \times 10^{-20} \text{ Pa}$, which is extremely low, and unlikely to be achieved even with ultra-high purity (Grade 5) nitrogen gas. When ammonia gas is employed instead of nitrogen, the partial pressure of oxygen may be determined from Eqs. (7) and (8)



The Gibbs energy of formations for Eqs. (7) and (8), i.e., ΔG_{40} and ΔG_{41} , are

$$\Delta G_{40} = 2\Delta G_{AlN} + 3\Delta G_{H_2O} - \Delta G_{Al_2O_3} - \Delta G_{N_2} - 3\Delta G_{H_2} = 313000 + 29T \quad (9)$$

$$\Delta G_{41} = \Delta G_{H_2O} - \frac{1}{2}\Delta G_{O_2} - \Delta G_{H_2} = -242000 + 134T \quad (10)$$

Expressing ΔG_{40} and ΔG_{41} in terms of partial pressures yields Eqs. (11) and (12)

$$\Delta G_{40} = -RT \ln P_{40} = -RT \ln \frac{\left(\frac{P_{H_2O}}{P_{atm}}\right)^3}{\left(\frac{P_{N_2}}{P_{atm}}\right)\left(\frac{P_{H_2}}{P_{atm}}\right)^3} \approx -RT \ln \left(\frac{P_{H_2O}}{P_{H_2}}\right)^3 \quad (11)$$

$$\Delta G_{41} = -RT \ln P_{41} = -RT \ln \frac{\left(\frac{P_{H_2O}}{P_{atm}}\right)}{\left(\frac{P_{H_2}}{P_{atm}}\right)\left(\frac{P_{O_2,amm}}{P_{atm}}\right)^{1/2}} \quad (12)$$

The permissible partial pressure of oxygen when ammonia is use for nitridation is determined from Eqs. (9- 12) to be around $5 \times 10^{-3} \text{ Pa}$, which is possible to achieve even with commercial grade anhydrous ammonia gas. Fig. 3 compares the permissible oxygen partial pressure for nitriding aluminum by nitrogen gas to the permissible oxygen partial pressure for nitriding aluminum by ammonia gas¹⁰. It is obvious from the Fig. that nitridation of aluminum is easier when ammonia, rather than nitrogen, is used.

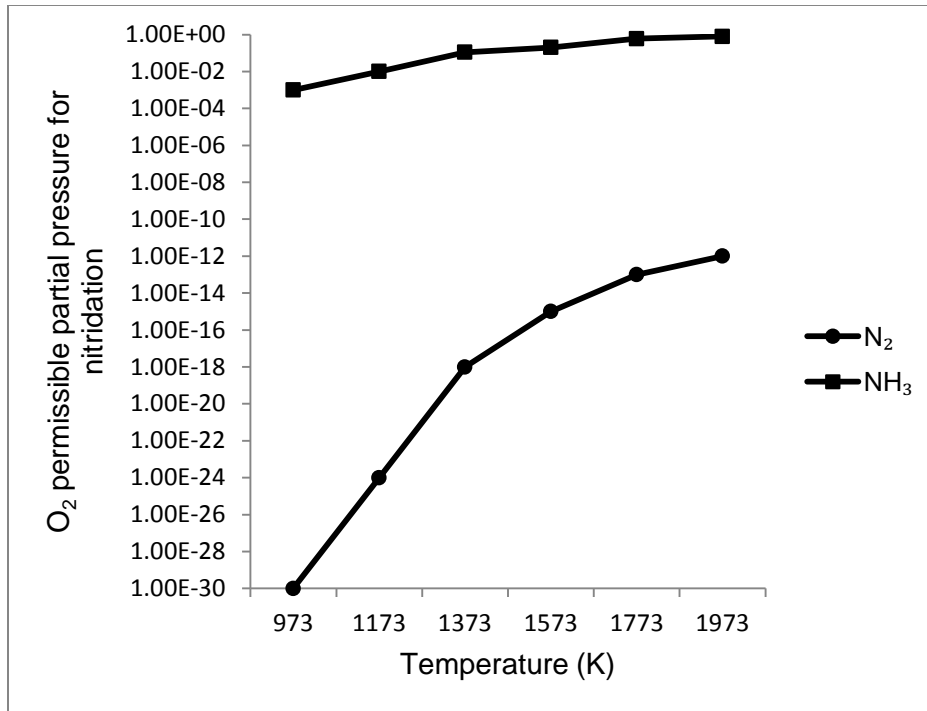


Figure 22. Permissible partial pressure of O₂ for Al nitridation versus temperature. N₂-NH₃ gases¹⁰.

The role of alloying elements, Mg and Li – Given the harmful effect of oxygen on the nitridation reaction, the oxygen partial pressure in the melt may be lowered by adding elements such as magnesium and/or lithium to aluminum^{3-7,11-13}. These elements act as catalysts to ‘get’ oxygen and mitigate the aluminum oxidation reaction. Magnesium and lithium are ideal for this purpose because, as shown in Fig. 3, the Gibbs free energy for their oxidation is lower than that for oxidation of aluminum, and so oxygen will preferentially combine with them rather than with aluminum. The continuous flow of the nitrogen-bearing gas in the furnace chamber removes the evaporating species (magnesium and MgO, and/or lithium and Li₂O) from the reaction chamber, thus it maintains a non-equilibrium condition in the melt, which is conducive to high mass flow of the volatilizing lithium (or magnesium). Both magnesium and lithium have been used from Borgonovo and Makhlouf³⁻⁷, and Borgonovo and Apelian^{11,12} to encourage nitridation of aluminum surfaces and also to synthesize AlN powder.

Knowing the partial pressure of oxygen after it reacts with magnesium or lithium allows establishing which of the two elements is a more effective ‘oxygen-getter’. Magnesium volatilizes when Al-Mg alloys are melted at elevated temperature, i.e., 1273K, which is typically used to synthesize AlN. The vapor pressure of pure magnesium, P_{Mg}^* , at 1273K is 136.45 kPa¹⁴, and the vapor pressure of magnesium in Al-Mg alloys, P_{Mg} , is given by Eq. (13) in which α_{Mg} is the activity of magnesium in Al-Mg alloys.

$$P_{Mg} = P_{Mg}^* \alpha_{Mg} \quad (13)$$

The chemical reaction that leads to formation of MgO is given by Eq. (14), and the Gibbs free energy of this reaction, ΔG_{47} , is given by Eqs. (15) and (16)



$$\Delta G_{47} = -748000 + 223T \quad (15)$$

$$\Delta G_{47} = -RT \ln \frac{1}{\left(\frac{P_{Mg}}{P_{atm}}\right) \left(\frac{P_{O_2}}{P_{atm}}\right)^{1/2}} \quad (16)$$

Combining Eqs. (13), (15), and (16) yields

$$\lg P_{Mg} = 42.8 - \frac{889061}{T} - \frac{1}{2} \ln P_{O_2} \quad (17)$$

By using these equations, the partial pressure of magnesium and the permissible partial pressure of oxygen in the gas stream when aluminum is alloyed with magnesium are calculated to be 5564 Pa and 3×10^{-28} Pa, respectively.

In the case of alloying aluminum with lithium, phase equilibrium calculations in the Al-Li-O-N system predict that lithium combines with oxygen to form Li_2O at low oxygen levels and $LiAlO_2$ at higher oxygen levels according to Eqs. (18) and (19)



The oxygen content in the high purity nitrogen bearing gases typically used in the synthesis of AlN is in the order of parts per billion (ppb), i.e., the partial pressure of oxygen in the nitrogen bearing gas is $\approx 10^{-9}$ Pa, and Eq. (18) is the relevant reaction. Similar to magnesium, lithium volatilizes at the temperatures used to make AlN. The vapor pressure of pure lithium, P_{Li}^* , at 1273K is 136.45 kPa¹⁵, and the vapor pressure of lithium in Al-Li alloys, P_{Li} , is given by Eq. (20) in which α_{Li} is the activity of lithium in Al-Li alloys^{16,17}

$$P_{Li} = P_{Li}^* \alpha_{Li} \quad (20)$$

The chemical reaction that leads to formation of Li_2O is given by Eq. (18) and the Gibbs free energy of this reaction, ΔG_{51} , is given by Eqs. (21) and (22)

$$\Delta G_{51} = -919700 + 343T \quad (21)$$

$$\Delta G_{51} = -RT \ln \frac{1}{\left(\frac{P_{Li}}{P_{atm}}\right)^2 \left(\frac{P_{O_2}}{P_{atm}}\right)^{1/2}} \quad (22)$$

Combining Eqs. (20), (21), and (22) yields

$$\lg P_{Li} = 41.4 - \frac{110807}{T} - \frac{1}{2} \ln P_{O_2} \quad (23)$$

By using these equations, the partial pressure of lithium and the permissible partial pressure of oxygen in the gas stream when aluminum is alloyed with lithium are calculated to be 2635 Pa and 4.7×10^{-49} Pa, respectively. Add to this the fact that the energy required to ionize lithium atoms (5.37 volts) is lower than that required to ionize magnesium atoms (7.61 Volts) – which suggests that lithium is more reactive than magnesium – and it becomes clear that lithium is much better at removing oxygen from the system than magnesium, and hence a significantly smaller amount of lithium compared to magnesium is necessary to facilitate aluminum nitridation.

4. Kinetic Considerations

In order to react with the aluminum melt, nitrogen gas has to diffuse from inside the gas bubble to the bulk liquid aluminum where AlN forms according to the reaction¹⁸



The diffusion-reaction process has been modeled with the two film approach, which is represented schematically in Fig. 4 and is typically used for gas-liquid interactions in bubble column reactors¹⁹⁻³³. Several assumptions were made in order to facilitate the analysis; they are as follows: (1) the bubble is spherical, (2) diffusion of gas in and out of the bubble, and the consequent bubble shrinkage (or growth) occurs isothermally, (3) the liquid domain is finite and steady, (4) the liquid is incompressible, (5) the gas within the bubble is pure and obeys the ideal gas law, (6) the bubble surface is free of contaminants, (7) liquid phase resistance controls mass transfer in the melt, (8) Henry's law applies at the gas-liquid interface to couple the gas pressure in the bubble with the dissolved gas concentration at the bubble surface, (9) mass transfer in the liquid phase is ruled by Higbie's penetration theory¹⁹⁻³³, (10) the initial concentration of nitrogen in the liquid bulk is zero, and finally (11) the confining walls of the crucible have negligible effect on the bubbles.

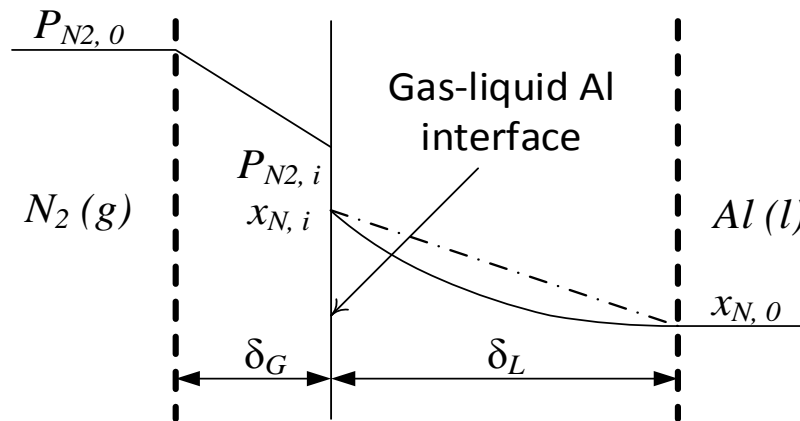


Figure 23. Two-film model for N_2 diffusion outside the gas bubble^{18,20-33}.

Close examination of the reaction that leads to the formation of the aluminum nitride particles reveals that the following five steps are involved

Step 1: dissociation of ammonia into hydrogen and nitrogen molecules (this step does not occur when nitrogen is employed as the nitriding gas)

Step 2: mass transfer of nitrogen molecules from the gas bulk to the gas-liquid interface

Step 3: chemisorption of nitrogen molecules at the gas-liquid interface according to Eq. (25)



Step 4: mass transfer of nitrogen atoms into the liquid boundary layer according to Eq. (26)



Step 5: growth of solid AlN particles in the liquid boundary layer and in the liquid bulk according to Eq. (27)



If nitrogen is used as the nitriding gas, then Step 3, i.e., chemisorption of nitrogen molecules and their conversion into nitrogen atoms at the gas-liquid interface, is rate limiting¹⁸. This can be concluded from Eq. (28), which gives the rate of chemisorption of nitrogen atoms

$$r_N = c(2\pi MRT)^{-\frac{1}{2}}(P_{N_2,i} - \frac{x_{N,i}}{K_{(12)}})\exp\left(\frac{-E_a}{RT}\right) \quad (28)$$

Eq. (28) shows that once the nitrogen molecules are physisorbed by the gas-liquid interface, they have to overcome an energy barrier (E_a) in order to be chemisorbed into the interface. If they do not possess this energy, they eventually become desorbed into the gas bulk. The activation energy E_a for nitrogen chemisorption is very high (308 kJ.mol⁻¹) compared to the reversible physisorption state (around 50 kJ.mol⁻¹)³⁴, which makes the rate of nitrogen chemisorption very slow. On the other hand, chemisorption of oxygen molecules into the gas-liquid interface is much more favorable since it consistently lowers the Gibbs free energy of the system compared to the physisorbed state as shown in Fig.5. Consequently, if present in the nitriding gas, oxygen will occupy the majority of the bonding sites at the gas-liquid interface thus further hindering the chemisorption of nitrogen into the gas-liquid interface. The extent of occupancy of the available adsorption sites in the gas-liquid interface is given by the 'coverage', θ ,^c which is expressed as the ratio of occupied adsorption sites q_{ads} and total (saturation) adsorption sites q_{sat} ; and the rate of chemisorption is proportional to the number of free adsorption sites; so that ^{34,35,36}

$$\theta = \frac{q_{ads}}{q_{sat}} \quad (29)$$

^c In Eq. (28), coverage (θ) is accounted for in the constant c

$$r_N \propto (1 - \theta) \quad (30)$$

Because the rate of chemisorption of nitrogen atoms into the gas-liquid interface is proportional to the number of free adsorption sites, it is important to minimize the amount of oxygen in the nitrogen gas before its injection into the melt.

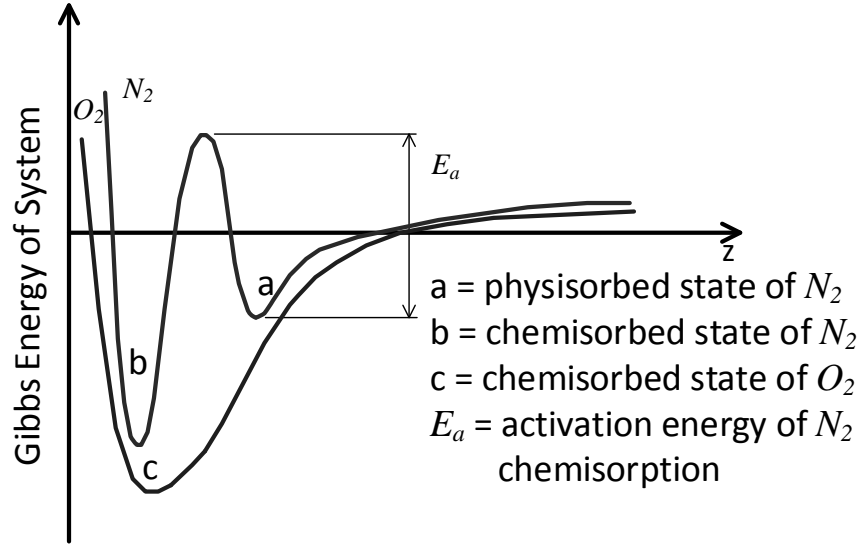
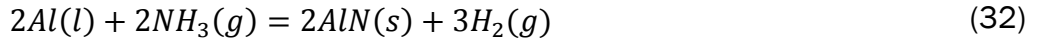


Figure 24. Diagram of energy change of the system caused by chemisorption of $N_2 - O_2$ ^{18,34}.

Another factor that can lower the rate of chemisorption of nitrogen molecules into the gas-liquid interface is the distribution of nitrogen molecules on the interface. If the nitrogen molecules in the gas bulk are unevenly distributed or clustered, then their chemisorption will not be homogenous on the gas-liquid interface. When ammonia is employed as reactive gas, molecular hydrogen dissociates at temperatures higher than 773 K according to Eq. (31) and the aluminum nitridation reaction proceeds according to Eq. (32)



It has been observed^{1,3-7} that free hydrogen is an oxygen getter that lowers the oxygen content in the reaction atmosphere, and by doing so it enhances the adsorption of N_2 molecules at the gas-liquid interface and accelerates the rate of AlN formation. When anhydrous ammonia, rather than pure nitrogen, is employed as the reactive gas, Step 3 becomes faster and the rate-limiting step of the reaction becomes Step 4 because of the very low diffusion coefficient of nitrogen atoms in liquid aluminum^b. Zheng et al.¹⁰ have analyzed the kinetics of AlN formation in aluminum alloys and found that the mean rate of

^b $D_N = 3.75 \times 10^{-7} \exp\left(\frac{-3184}{T}\right)$

forming AlN from ammonia is ten times that from nitrogen; also Experiments No. 1 and 2 of this work showed that, when nitrogen is used, it is possible to synthesize only 6 vol. pct. AlN in 5 hours, but when ammonia is used, it is possible to synthesize 17 vol. pct. AlN in only 2 hours. The quantity of AlN, W_{AlN} , that forms during a given gas injection time, t , depends on: (1) the rate of AlN formation, r_{AlN} , and (2) the total area of the gas bubbles that are dispersed in the melt, A_t , as given by Eq. (33)

$$W_{AlN} = \int_0^t r_{AlN} A_t dt \quad (33)$$

Rate of AlN formation (r_{AlN}) – Higbie's penetration theory considers the gas-liquid interface to be composed of a variety of elements continuously brought up to the interface from the bulk of the liquid. The diffusion domain of nitrogen atoms in the liquid is a liquid boundary layer of thickness δ_l given by Eq. (34)¹⁹⁻³³

$$\delta_l = \frac{\sqrt{D_N \pi t_d}}{2} \quad (34)$$

The local diffusion time, t_d , indicates how long the bubble stays in contact with a single element ahead of its interface and therefore, it indicates the time available for nitrogen atoms to diffuse into the liquid metal. It depends on the diameter of the bubble, d , and its rising velocity, U_b , according to Eq. (35)

$$t_d = \frac{d(P_{N_2,l}, x_{N,i})}{U_b(d)} \quad (35)$$

The rate of AlN formation r_{AlN} can be written as

$$r_{AlN} = EK_L(x_{N,i} - x_{N,0}) \quad (36)$$

In Eq. (36), the mass diffusion coefficient of nitrogen in the boundary layer, K_L , is given by Eq. (37) and the enhancement factor, E , which is a non-dimensional parameter that accounts for the decreasing level of nitrogen atoms in the melt due to the formation of AlN, is given by Eqs. (38-40)²⁰.

$$K_L = 2 \sqrt{\frac{D_N}{\pi t_d}} \quad (37)$$

$$E = \frac{\sqrt{M' \left(E_i - \frac{E}{E_i} - 1 \right)}}{\tanh \sqrt{M' \left(E_i - \frac{E}{E_i} - 1 \right)}} \quad (38)$$

$$M' = \frac{\pi}{4} K_{AlN} x_{Al} t_d \quad (39)$$

$$E_i = \sqrt{\frac{D_N}{D_{Al}} + \frac{x_{N,i}}{x_{Al,i}}} \sqrt{\frac{D_{Al}}{D_N}} \quad (40)$$

Total area of gas bubbles (A_t) – The total surface area of gas bubbles in the melt is determined by the properties of the gas and the liquid, the gas flow rate, and the size of the nozzle, as well as the number of bubbles in the melt, N_b , during the injection time and their residence time in the melt, t_r , as shown in Eq. (41)⁴¹

$$A_t = N_b A_b = N_b \frac{\pi}{4} d^2 \quad (41)$$

$$N_b = t_r f_b = \frac{L}{U_b(d)} f_b \quad (42)$$

The frequency of formation of gas bubbles, f_b , can be derived from Eqs. (43) to (47) and it is a function of the nozzle diameter of the injection tube, d_{no} , the hydrostatic pressure in the melt at the injection depth, P_{GO} , and of the state of the gas at the inlet of the tube (P_{in}, V_{in}, T_{in})

$$f_b = \frac{V_g}{V_{bo}} \quad (43)$$

$$V_{bo} = \frac{4}{3} \pi \left(\frac{d_o}{2} \right)^3 \quad (44)$$

$$d_o = \left(\frac{6 d_{no} \gamma}{g(\rho_l - \rho_g)} \right)^{1/3} \quad (45)$$

$$V_g = \frac{P_{in} T}{P_{GO} T_{in}} V_{in} \quad (46)$$

$$P_{GO} = P_{atm} + \rho_l g L + \frac{4\gamma}{d_{no}} \quad (47)$$

$$f_b = \frac{g V_{in} P_{in} (\rho_l - \rho_g) T}{\pi \gamma P_{GO} T_{in} d_{no}} \quad (48)$$

In terms of gas flow rate, Eq. (48) may be written as:

$$f_b = \frac{79.5 Q T}{0.001 (P_{atm} + \rho_l g L) + 4\gamma} \quad (49)$$

Previous work⁴² calculated A_t and r_{AIN} as constants across the entire liquid domain; as a consequence, these calculations show the amount of reinforcement, W_{AIN} , that form near the bottom regions of the crucible to be equal to that formed in the topmost regions. In

reality, this is not the case because the nitrogen bubbles tend to lose mass to the liquid and are subjected to decreasing hydrostatic pressure as they rise. The former effect causes the bubbles to shrink whereas the latter causes them to expand. Therefore, the bubble diameter varies continuously in the liquid and r_{AIN} and A_t vary with it according to their dependencies on bubble diameter given by Eqs. (35), (37), (41), and (42). The Navier-Stoke simplified expression for the problem of a rising bubble in a liquid wherein the bubble size varies with time is shown as Eq. (50)

$$\frac{dr}{dt} = \frac{(P_{N_2,i} - P_l)}{4\eta} - \frac{\gamma}{2\eta} \quad (50)$$

The pressure and concentration at the bubble surface are coupled through Henry's law, Eq. (51), and conservation of mass at the interface, Eq. (52)

$$x_{N,i} = \frac{P_{N_2,i}}{He} \quad (51)$$

$$\frac{d}{dt} \left(\frac{4\pi P_{N_2,i} r^3}{3RT} \right) = 4\pi r^2 D_N \left. \frac{\partial c}{\partial R} \right|_{R=r} \quad (52)$$

The concentration gradient at the bubble surface, $\left. \frac{\partial c}{\partial R} \right|_{R=r}$, is determined by means of Fick's second law of diffusion, Eq. (53), with the initial condition for pressure inside the gas bubble expressed by Eq. (47)

$$\frac{\partial c}{\partial t} = D_N \frac{\partial^2 c}{\partial r^2} \quad (53)$$

Figs. 6 and 7 show respectively the progressive decrease in the total surface area of gas bubbles, and the progressive decrease in the number of bubbles as the bubbles rise towards the surface of the melt. Figs. 6 and 7 were obtained from calculations based on the preceding analysis. It is believed that bubble coalescence is responsible for this decrease in the total surface area of the gas bubbles and the associated decrease in their number. This belief has been confirmed by others; e.g.³⁷. When two bubbles that are rising in a liquid coalesce, the process occurs in three steps³⁷⁻⁴⁰: (1) the two bubbles collide and trap liquid between them, (2) The surface of the bubbles flatten and the liquid film that was initially trapped between them thins as the liquid drains out, and (3) the two bubbles coalesce into one.

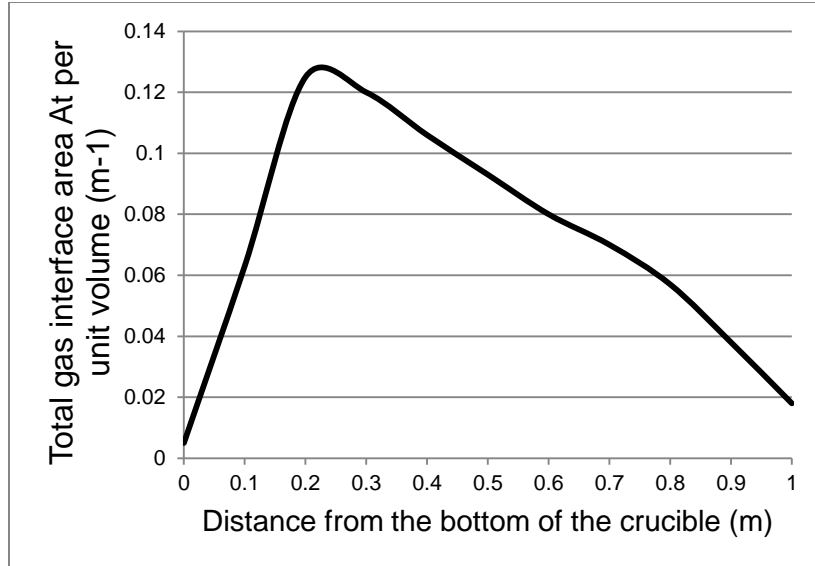


Figure 25. Total gas interface area A_t per unit volume vs. distance from the bottom of the crucible.

The second of the three steps is normally rate limiting. The rate of thinning of the liquid film between the two bubbles may be expressed by Eq. (54) in which l is the original liquid film thickness, R_d is the liquid disk between the coalescing bubbles, Φ is a measure of the surface drag or velocity gradient at the surface due to the absorbed layer of gas, and μ is the static viscosity of the liquid, in this case, aluminum³⁷⁻⁴⁰.

$$\frac{dl}{dt} = -\frac{32l^3\gamma}{3\Phi R_d^2\mu d} \quad (54)$$

Eq. (54) shows that liquids that have high surface energies, such as aluminum ($\gamma = 813$ dyn/cm at 1273K), are more prone to bubble coalescence. Bubble coalescence adversely affects the total concentration of the nitrogen gas that diffuses into the liquid boundary layer ahead of the gas-liquid interface^c; which in turn adversely affects the rate of formation of AlN particles. Fig. 8 shows the decrease in concentration of nitrogen gas with melt depth.

^cThis is a consequence of the drop of partial pressure of nitrogen in the bubble, $P_{N_2,i}$, as the bubbles coalesce (Henry's law).

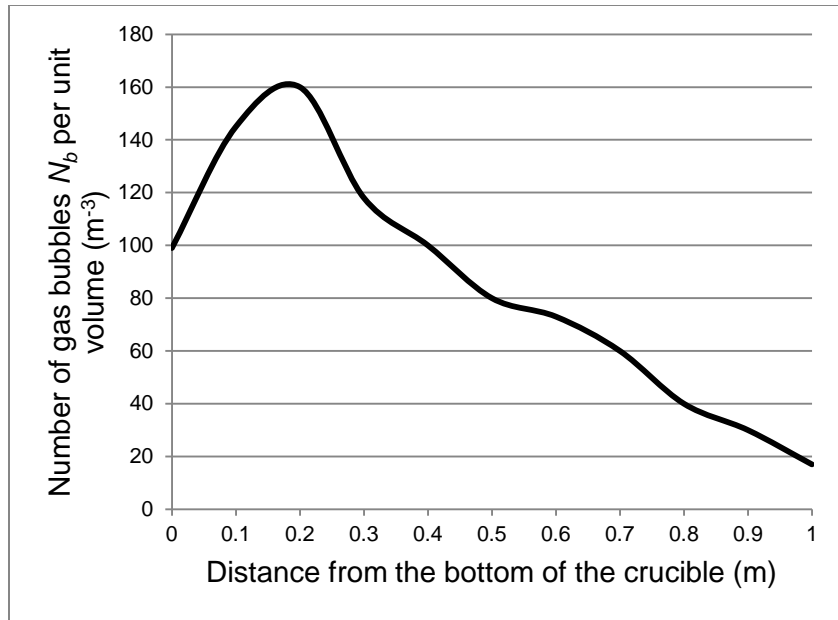


Figure 26. Number of gas bubbles N_b per unit volume vs. distance from the bottom of the crucible.

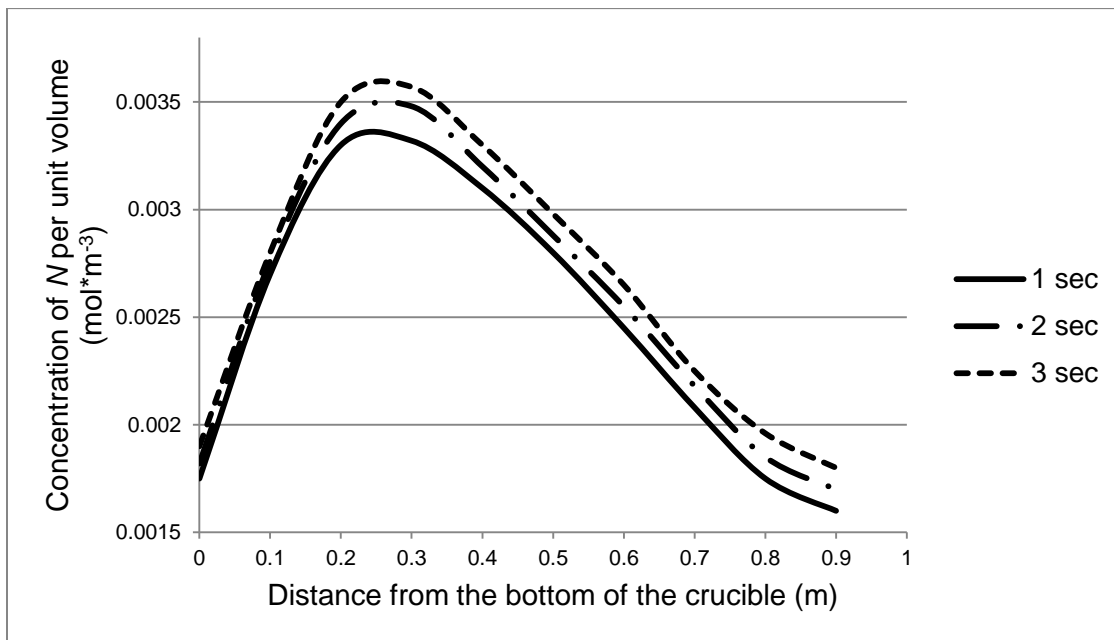


Figure 27. Concentration of N per unit volume vs. distance from the bottom of the crucible.

5. Sensitivity Analysis

Effect of melt temperature (T) – Figs.9 and 10 show respectively that when the temperature of the melt is increased from 1273K to 1573 K, the gas-liquid interfacial area doubles and the density of gas bubbles increases by about ten times.

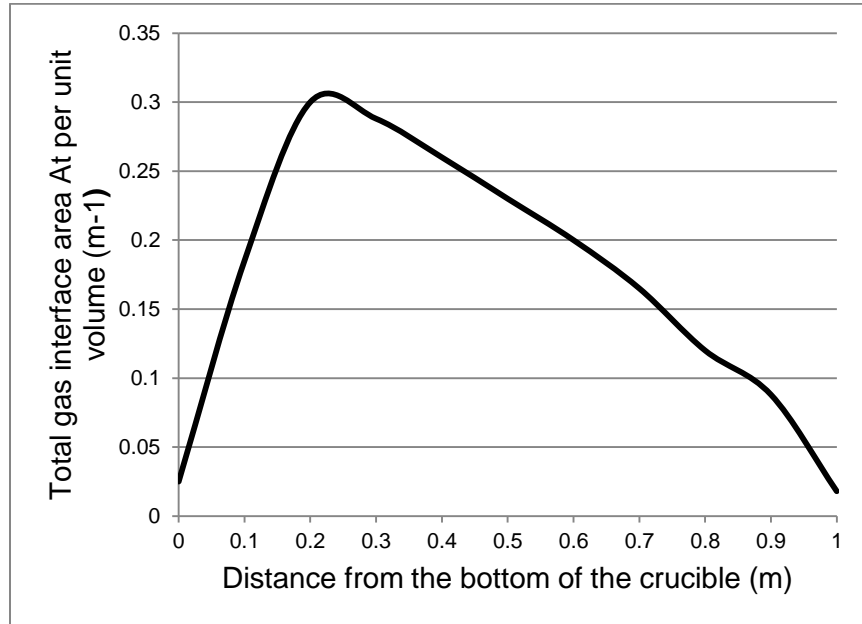


Figure 28. Total gas interface area A_t per unit volume vs. distance from the bottom of the crucible. $T= 1573$ K.

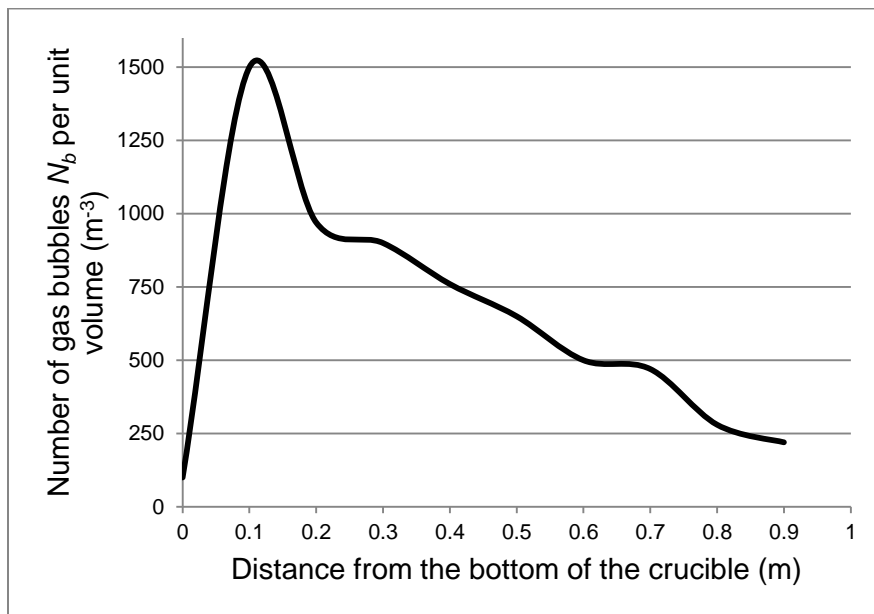


Figure 29. Number of gas bubbles N_b per unit volume vs. distance from the bottom of the crucible. $T= 1573$ K.

Effect of gas flow rate (Q) – The model presented herein is based on the assumption that the effect of gas flow rate on the bubble volume at the time of its detachment from the nozzle, V_{bo} , is negligible. However, when the gas flow rate exceeds a threshold value, the gas flow may transfer into the ‘constant-frequency’ regime in which V_{bo} , and hence d_{no} , correlates with gas flow rate according to Eq. (55)⁴¹

$$V_{bo} = 1.378 \left(\frac{Q^2}{g} \right)^{3/5} \quad (55)$$

Figs. (11, 12, and 13) confirm the occurrence of the constant-frequency regime as they show that the number of gas bubbles, N_b , does not increase with increasing flow rate whereas the gas-liquid interfacial area increases significantly. This is due to the effect on the detaching bubble diameter, d_{no} , which influences the size of the bubble during its rise. This ‘additional’ gas-liquid interfacial area affects diffusion at the gas-liquid interface and leads to a nitrogen concentration in the melt that is almost three times higher compared to its value with the lower gas flow rate. The increase in amount of AlN particles that form with the increase in gas flow rate has been observed by others¹⁰.

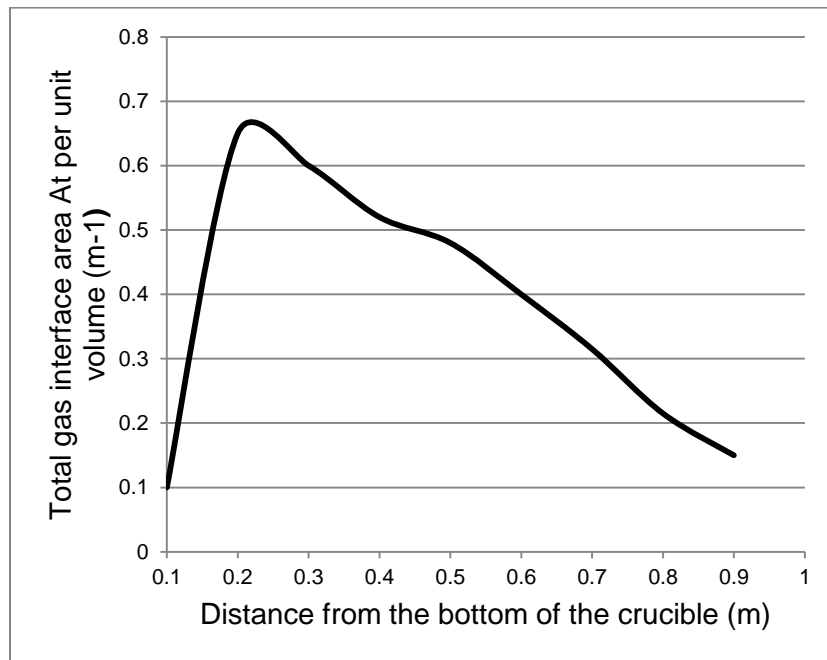


Figure 30. Total gas interface area A_t per unit volume vs. distance from the bottom of the crucible. $Q= 1$ l/min.

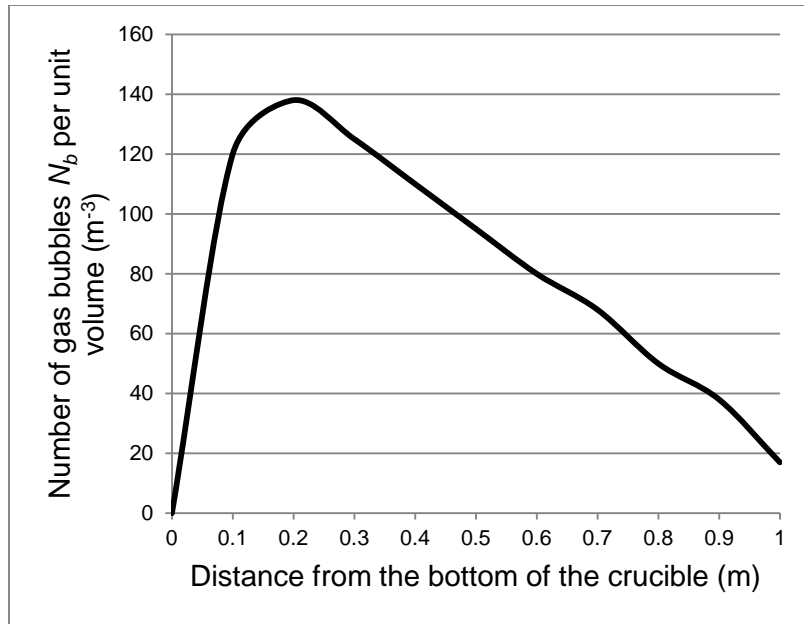


Figure 31. Number of gas bubbles N_b per unit volume vs. distance from the bottom of the crucible. $Q= 1$ l/min.

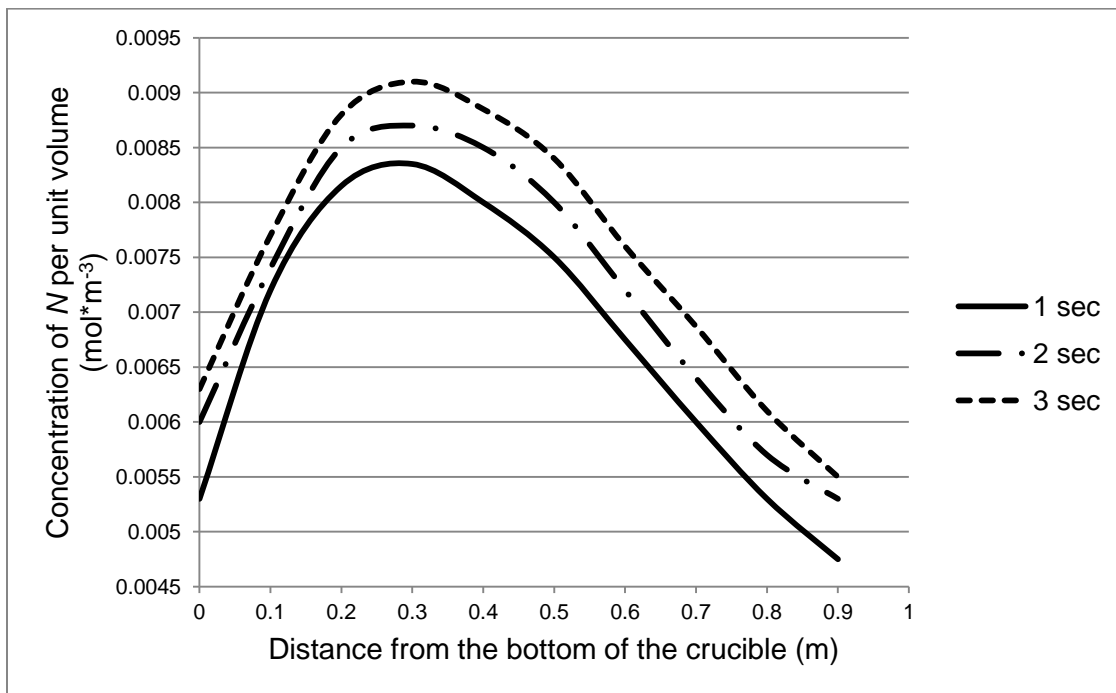


Figure 32. Concentration of N per unit volume vs. distance from the bottom of the crucible. $Q= 1$ l/min.

Effect of pressure in the chamber (P_{atm}) – Fig. 15 shows that when the pressure above the melt is increased from 1 atm to 5 atm, the density number of bubbles, N_b , increases since the frequency of bubble formation, f_b , increases, as suggested by Eq. (48). The increase in pressure affects the bubble volume, V_g , according to Eq. (46) in that its diameter at the high pressure is smaller than at the low pressure. As a result, the bubble rises more slowly and its residence time in the melt, t_r , is longer, which, according to Eq. (42), further contributes to a higher N_b . Fig. 14 shows that the total interface area, A_t , is not increased by the increase in pressure since the average bubble size is smaller for $P_{atm} = 5$ atm than for $P_{atm} = 1$ atm. However, the total interface area reaches a fairly stable value, which is very important to ensure homogeneous distribution of AlN particles in the melt. Figs. 16 and 17 show that at $P_{atm} = 5$ atm, the gas velocity is more or less constant throughout the melt and it is almost 10 times smaller than its value at $P_{atm} = 1$ atm, which results in longer bubble residence times in the melt. The most noteworthy consequence of employing high pressure is the nitrogen concentration profile which, as shown in Fig. 18 exhibits values that are three orders of magnitude higher than those for $P_{atm} = 1$ atm. Moreover, bubble coalescence is minimized by the increased pressure. It is known that surface tension decreases and liquid viscosity increases with increasing pressure³⁹⁻⁴⁰, also the parameter Φ increases with increased pressure³⁸⁻⁴⁰. These changes contribute to reducing the bubble coalescence rate with increased pressure as indicated by Eq. (54). Furthermore, the frequency of bubble collisions, which is the first step in bubble coalescence, decreases with increasing pressure.

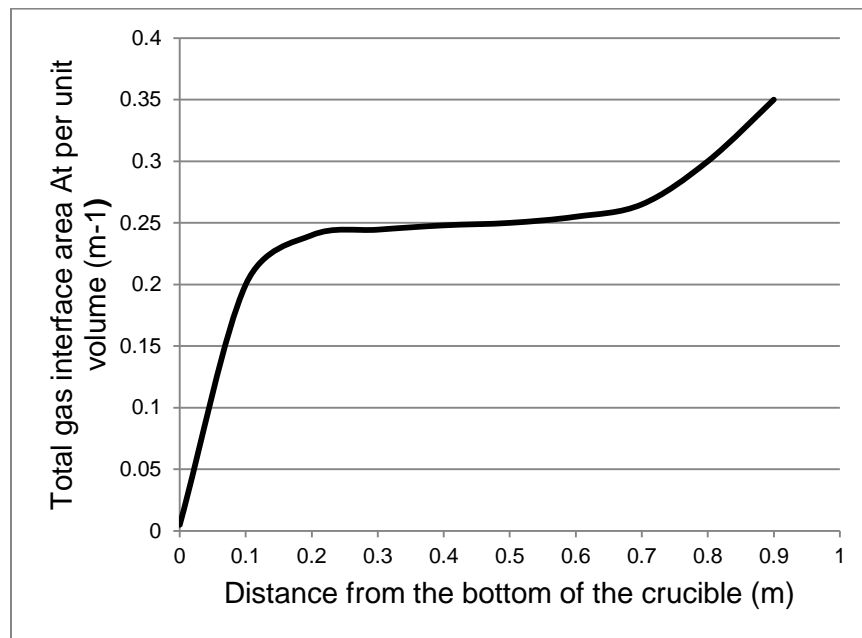


Figure 33. Total gas interface area A_t per unit volume vs. distance from the bottom of the crucible. $P_{atm} = 5$ atm.

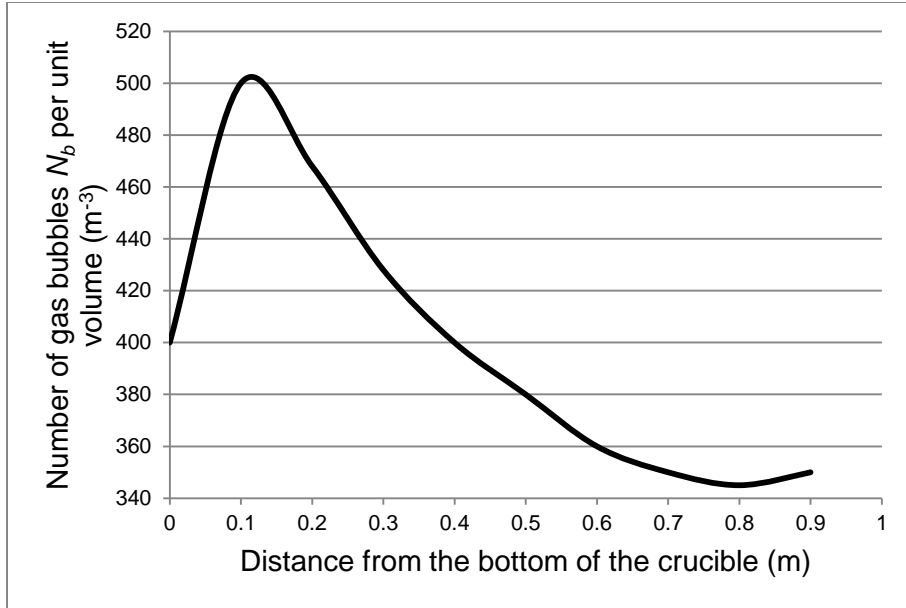


Figure 34. Number of gas bubbles N_b per unit volume vs. distance from the bottom of the crucible. $P_{atm} = 5$ atm.

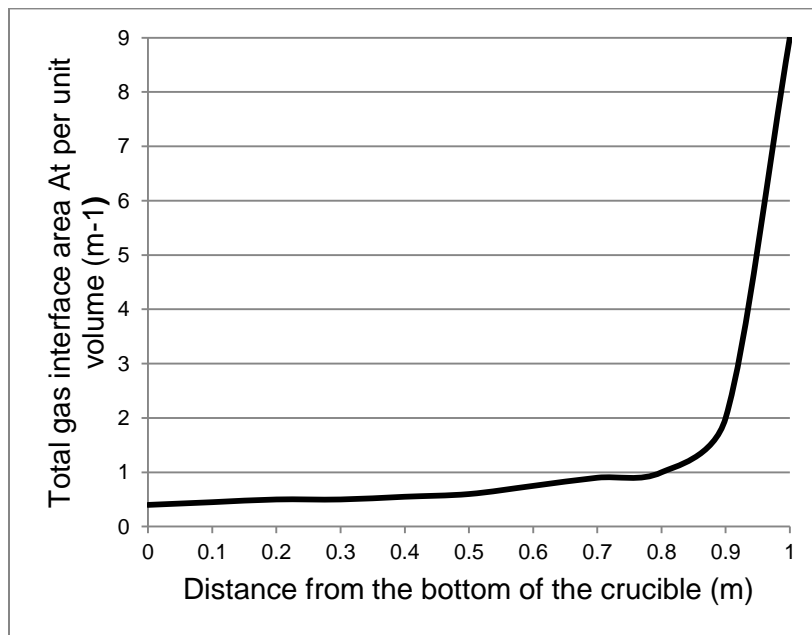


Figure 35. Gas velocity vs. distance from the bottom of the crucible. $P_{atm} = 1$ atm.

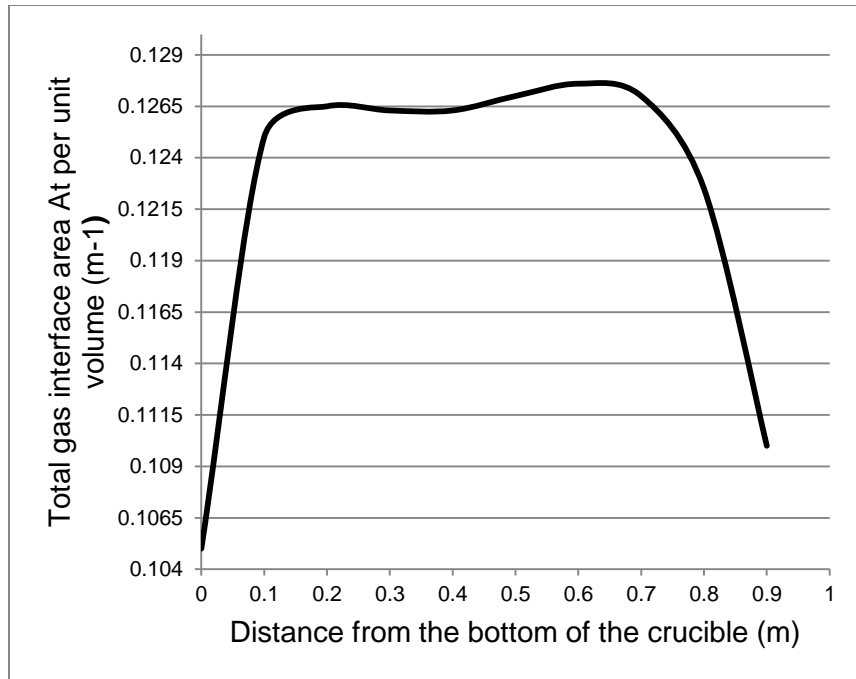


Figure 36. Gas velocity vs. distance from the bottom of the crucible. $P_{atm} = 5$ atm.

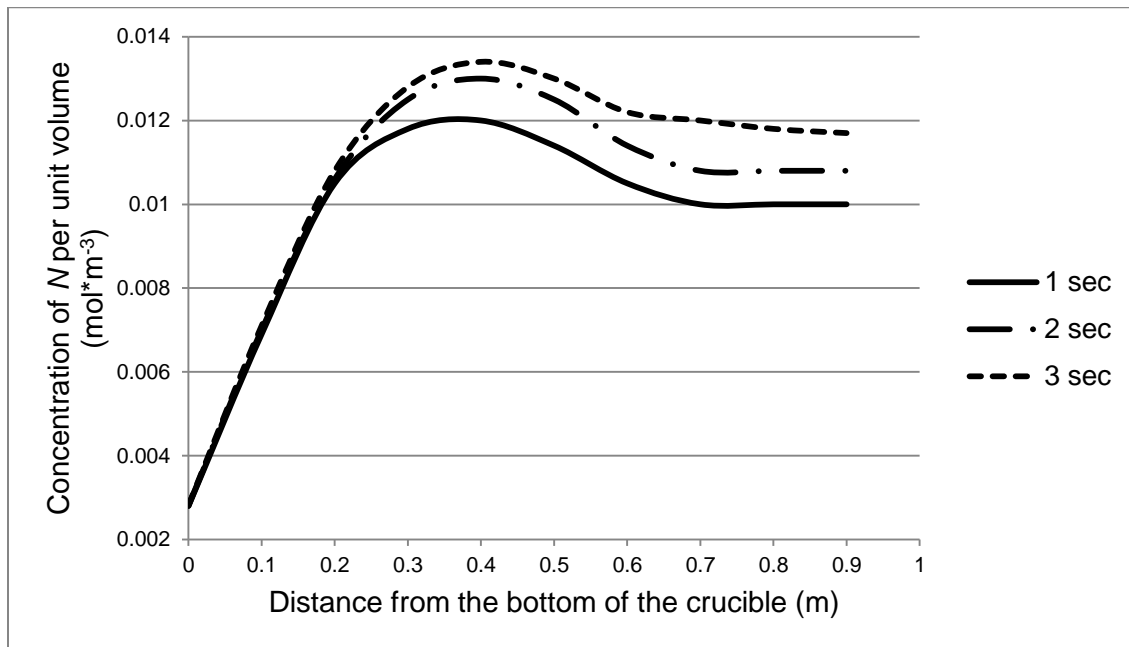


Figure 37. Concentration of N per unit volume vs. distance from the bottom of the crucible. $P_{atm} = 5$ atm.

6. Conclusions

Synthesizing aluminum-aluminum nitride nanocomposite materials by injecting a nitrogen bearing gas into molten aluminum is thermodynamically and kinetically feasible, provided that the oxygen content of the system is maintained at a low level. Thermodynamic and kinetic analysis of the process show that attaining this low oxygen content may be helped by alloying aluminum with magnesium and/or lithium; with lithium being the more efficient of the two elements in this regard. As little as 1 wt. pct. lithium is sufficient to suppress oxidation of aluminum and promote its nitridation. The analysis also shows that an increase in process temperature significantly increases the density of reactive gas bubbles. For example, when the process temperature is increased from 1273K to 1573K, the density of reactive gas bubbles increases by about ten times, and the gas-liquid interfacial area doubles. This has positive consequences on the size and distribution of the AlN particles in the matrix alloy. However, high temperature adversely affects the equipment's life expectancy, particularly the rotating impeller and furnace walls. The temperature should be maintained around 1273K for best results. In addition, the analysis shows that a relatively high flow rate of the reactive gas increases the gas-liquid interfacial area. This 'additional' gas-liquid interfacial area affects diffusion at the gas-liquid interface and positively affects the size and distribution of the AlN particles in the matrix alloy. Although high purity nitrogen and anhydrous ammonia are not prohibitively expensive, for economic reasons, the gas flow rate should be kept no higher than 0.5 l/min. Finally, the analysis shows that an increase in the pressure above the melt increases the density number of reactive gas bubbles and reduces the bubble volume; as a result, the bubbles rise more slowly, their residence time in the melt increases, and their coalescence is minimized.

Nomenclature

α_{Li}	activation extent of Li in Al-Li alloys at high Li content (>5%)
α_{Mg}	activation extent of Mg in Al-Mg alloys at high Mg content (>5%)
γ	surface tension of aluminum
δ_G	thickness of the diffusion layer in the gas bulk
δ_L	thickness of the diffusion layer in the liquid bulk
η	dynamic viscosity of liquid aluminum
θ	coverage, defined as $\theta = \frac{q_{ads}}{q_{sat}}$
Φ	measure of the surface drag or velocity gradient at the surface due to the absorbed layer of the gas
μ	static viscosity of aluminum
ρ_g	density of gas
ρ_l	density of liquid aluminum

A_t	total gas-liquid interface area
c	constant in Equation 28
d	bubble diameter
D_{Al}	diffusion coefficient of aluminum
D_N	diffusion coefficient of nitrogen in aluminum
d_o	bubble diameter at bubble detachment
d_{no}	diameter of the nozzle of the tube
E	Enhancement Factor
E_a	activation energy for chemisorption of nitrogen atoms
f_b	frequency of formation of gas bubbles
He	Henry's constant for N_2 in liquid Al at $T=1273$ K
$K_{(12)}$	partition coefficient of Reaction 25
K_{AlN}	equilibrium constant of Equation 27
K_L	mass transfer coefficient of nitrogen in the liquid boundary layer
l	thickness of liquid film in between coalescing bubbles
L	depth of the melt
M	molar mass of the gas molecule
N_b	number of gas bubbles in the melt
P_{GO}	pressure of the gas bubble at the moment of detachment from the injection tube
P_l	pressure in the liquid at the injection level
$P_{N_2,0}$	partial pressure of nitrogen in the gas bulk
$P_{N_2,i}$	partial pressure of nitrogen at the gas-liquid interface
P_{in}, T_{in}, V_{in}	initial state of reactive gas at the inlet of the injection tube
P_{Li}^*	vapor pressure of pure Li at 1273 k
P_{Mg}^*	vapor pressure of pure Mg at 1273 K
Q	gas flow rate
q_{ads}	occupied adsorption sites on the gas-liquid interface
q_{sat}	total adsorption sites on the gas-liquid interface
R	bubble radius that varies in the melt. $R=r$ at the interface
R_d	radius of the liquid disk between the coalescing bubbles
r_N	rate of chemisorption of nitrogen atoms

T	temperature
t	gas injection time
t_d	local diffusion time
t_r	residence time of the gas bubble in the melt
U_b	velocity of the gas bubble
V_{bo}	volume of gas bubble at bubble detachment
V_g	volume of the gas bubble
W_{AlN}	amount of AlN formed
x_{Al}	concentration of aluminum
$x_{Al,i}$	concentration of aluminum at the gas-liquid interface
$x_{N,i}$	concentration of nitrogen atom on the gas-liquid interface
$x_{N,0}$	concentration of nitrogen atoms in the liquid bulk

References

1. C. Borgonovo and M.M. Makhlof: *submitted to Int. Mater. Rev.*, 2013.
2. R. G. Reddy: US Patent 6,343,640, 2002.
3. C. Borgonovo and M.M. Makhlof: "A Novel Method for Manufacturing Aluminum-Aluminum Nitride Nanocomposites," Proceedings of MS&T, Columbus, Ohio, 2011.
4. C. Borgonovo and M.M. Makhlof: "The Synthesis of Die-Castable Nano-Particle Reinforced Aluminum Matrix Composite Materials by In-Situ Gas-Liquid Reaction," Proceedings of High Tech Die Casting, Vicenza, Italy, 2012.
5. C. Borgonovo and M.M. Makhlof: "In-Situ Manufacturing of Nano-Particle Reinforced Metal Matrix Composites," Proceedings of AFS, Columbus, Ohio, 2012.
6. C. Borgonovo and M.M. Makhlof: "In-Situ Manufacturing of Aluminum Based Metal Matrix Composites," Proceedings of the 15th European Conference on Composite Composite Materials, Venice, Italy, 2012.
7. C. Borgonovo, D. Apelian, and M.M. Makhlof: *JOM*, 2011, Vol. 63 (2), pp. 57-64.
8. D.D. Wagman, W.H. Evans, V.B. Parker, R.H. Schumm, I. Halow, S.M. Bailey, K.L. Churney, and R.L. Nuttall: *J. Phys. Chem. Ref. Data*, 1982, Vol. 11 (2).
9. L.V. Gurvich, I.V. Veyts, and C.B. Alcock: 'Thermodynamic Properties of Individual Substance's, Fourth Edition, Vol. 3, 1994, CRC Press, Boca Raton, FL.
10. Q. Zheng, B. Wu, and R. Reddy: *Adv. Eng. Mater.*, 2003, Vol. 5 (3), pp. 167-173.
11. C. Borgonovo and D. Apelian: *Mater. Sci. Forum*, 2011, Vol. 690, pp. 187-191, 2011.
12. C. Borgonovo and D. Apelian: *Mater. Sci. Forum*, 2011, Vol. 678, pp. 115-123.

13. C.M. Little, R.A. Murie, and M. Warren: US Patent, 3,607,046, 1971.
14. M. M. Avedesian and Hugh Baker (eds.): 'Magnesium and Magnesium Alloys', ASM International, 1999.
15. D. W. Jeppson, J. L. Ballif, W. W. Yuan, and B. E. Chou: 'Lithium literature review: lithium's properties and interactions', Hanford Engineering Development Laboratory, April 1978, HEDL-TME 78-15, UC-20.
16. P. C. Yao and D. J. Fray: *Met. Trans. B*, 1985, Vol. 16 (1), pp. 41-46.
17. M-L. Saboungi and Milton Blander: *J. Electrochem. Soc.*, 1977, Vol. 124 (1), pp. 6-13.
18. R. Reddy and V. Kumar: *Mater. Sci. Forum*, 2007, Materials Science Forum, Vols. 561-565, pp. 701-704.
19. S.G. Chatterjee: *Indian Chem Eng.*, 2009, Vol. 51 (3), pp. 177-193.
20. T. Madhavi, A.K. Golder, A.N. Samanta, and S. Ray: *J. Chem. Eng.*, 2007, Vol. 128, pp. 95-104.
21. K. Terasaka, J. Oka, and H. Tsuge: *Chem. Eng. Sci.*, 2002, Vol. 57, pp. 3757-3765.
22. C. Roizard and G. Wild: *Chem. Eng. Sci.*, 2002, Vol. 57, pp. 3479-3484.
23. R. Krishna and J.M. Van Baten: *Catal. Today*, 2003, Vol. 79-80, pp. 67-75.
24. F. Takemura and Y. Matsumoto: *Chem. Eng. Sci.*, 2000, Vol. 55, pp. 3907-3917.
25. R. S. Srinivasan, W. A. Gerth, and M.R. Powell: *J. Appl. Physiol.*, 1999, Vol. 86 (2), pp. 732-741.
26. S. Q. Yang, B. Du, and L.S. Fan: *Chem. Eng. Sci.*, 2007, Vol. 62 (1-2), pp. 2-27.
27. H. Tsuge, K. Terasaka, W. Koshida, and H. Matsue: *Chem. Eng. Sci.*, 1997, Vol. 52, pp. 3415-3420.
28. S. Taniguchi, A. Kikuchi, H. Matsuzaki, and N. Bessho: *Transactions ISIJ*, 1988, Vol. 28, pp. 262-270.
29. J.H. Meldon, O. O. Olawoyin, and D. Bonanno: *Ind. Eng. Chem. Res.*, 2009, Vol. 46 (19), pp. 6140 – 6146.
30. A.A.C.M Beenackers and W.P.M. Swaaij: *Chem. Eng. Sci.*, 1993, Vol. 48, pp. 3109-3139.
31. M.N.C Pinheiro: *Int. Comm. Heat Mass*, 2000, Vol. 27 (1), pp. 99-108.
32. W. Jang and M.M. Aral: *Environ. Fluid Mech.*, 2003, Vol. 3 (3), pp. 173-193.
33. E.P. Van Elk, M.C. Knaap, G.F. Versteeg: 'Application of the penetration theory for gas-liquid mass transfer without liquid bulk – differences with systems with a bulk', Symposium Series IChemE, 2006, 152, pp. 294-310.
34. P. Atkins and J. De Paula: 'Physical Chemistry', 2002, 7th edn., Macmillan, New York, NY.

35. Lecture of Surface Science and Technology Course (Fall 2012): 'Surfaces, Interfaces and their Applications: Adsorbates on Surfaces', Department of Materials, Swiss Federal Institute of Technology, Zurich, Switzerland.
36. A. T. Hubbard: 'Encyclopedia of Surface and Colloid Science', 2002, CRC Press, Boca Raton, FL.
37. M. A. K. Azad and S. R. Syeda: *J. Chem Eng.*, 2006, Vol. 24 (1), pp. 25-35.
38. Wen-Ching Yang: 'Handbook of Fluidization and Fluid-Particle Systems', 2003, CRC Press, Boca Raton, FL, pp. 772-776.
39. J. J. Carberry: 'Chemical and catalytic reaction engineering', 2001, Courier Dover Publications, Mineola, NY.
40. H. D. Baehr and Karl Stephan: 'Heat and Mass Transfer', 2011, Springer, New York, NY.
41. J. Szekely: 'Fluid Flow Phenomena in Metals Processing', 1979, Academic Press, New York, NY.
42. Q. Zheng and R. Reddy: *Metall. Mat. Trans.*, 2003, Vol. 34B, pp. 793-804.

Synthesis of Aluminum-Aluminum Nitride Nanocomposites by Gas-Liquid Reactions – Microstructural Evaluation and Mechanical Properties

Cecilia Borgonovo and Makhlouf M. Makhlouf

Department of Mechanical Engineering
Worcester Polytechnic Institute
Worcester, MA 01609

Keywords: nanocomposites, in-situ manufacturing, gas/liquid reaction, aluminum, lithium, aluminum nitride, nitridation, dispersion

Abstract

Nano-particle reinforced aluminum materials exhibit promising mechanical and thermal properties such as high specific strength, hardness, stiffness, and resistance to creep and thermal degradation. Unfortunately, processing these materials is challenging and numerous attempts have been made to overcome the typical issues associated with their synthesis. These methods include mechanical alloying, powder metallurgy, powder infiltration and spray deposition. However, most of these methods are expensive and time consuming. Manufacturing methods that are based on mechanical agitation are cost-effective, but particle agglomerates tend to form due to Van der Waals forces associated with the high surface energy of nano-particles. In-situ fabrication of the reinforcement in the metal matrix is an answer to many of these challenges. In this method, the nano-sized particles are formed directly within the melt by means of a chemical reaction between a specially designed aluminum alloy and a gas. In this publication, we report on the synthesis of aluminum-aluminum nitride nanocomposites by the reaction of a nitrogen-containing gas with molten aluminum-lithium alloy. The role of matrix chemistry, gas composition, and processing time on particle amount, size and distribution has been assessed. The effect of stirring velocity of the gas impeller on particle size and clustering tendency has been addressed. A dispersion index has been defined to quantify the homogeneity of the microstructure and mechanical properties evaluation at room and high temperatures has been pursued for different particle concentration levels.

1. Introduction

Composites reinforced with ceramic particles such as Al_2O_3 or SiC are gradually being used in many automotive and aircraft applications, and more recently in the microprocessor industry. In the automobile industry, aluminum alloy composites lower the overall weight of the vehicle and enhance component strength, stiffness, wear resistance and high temperature properties. In the microprocessor industry, composite materials improve heat

extraction and heat dissipation from critical components thus allowing higher processing speeds and superior performance. Particle size has an undeniably strong influence on the failure mode, strength, and ductility of composite materials. Decreasing the size of the ceramic particles to the sub-micrometer range, or even better to the nanometer range, can lead to significant improvements in room temperature mechanical properties as well as enhanced thermal and electrical properties. Moreover, refining the size of the reinforcing particles limits microstructure degradation at high temperature, which is a necessary material property for highly-rated Diesel engine applications. However, the synthesis of a material with increased mechanical properties requires a reinforcement phase which is thermodynamically stable, less susceptible to cracking and well bound to the matrix. Conventional fabrication methods that are based on the addition of particles to the matrix (e.g., mechanical stirring, powder metallurgy, and infiltration techniques) have serious limitations when dealing with nanometer size particles; these include particle clustering and particle/matrix interface de-bonding. More recent fabrication methods, such as spray deposition, plasma synthesis, and ultrasonic-assisted cavitation all suffer from the lack of scalability and cost-effectiveness. In-situ creation of the reinforcing particles within the aluminum matrix has the potential to provide good particle distribution, small particle size, and a clean and thermodynamically stable particle/matrix interface. This process involves synthesizing the ceramic reinforcing nano-particles within the metal alloy by means of a controlled chemical reaction between a gas with a specific composition injected in the molten metal alloy through an impeller. The chemical composition of the reinforcing particles that form is dictated by the composition of the reacting gas and molten metal alloy. When nitrogen-bearing gases are employed for the reaction AlN are formed. Due to its attractive properties including high strength and hardness, good thermal conductivity (80-260 W m⁻¹ K⁻¹) and low thermal expansion coefficient (4.5X10⁻⁶ K⁻¹), aluminum nitride is an excellent reinforcement candidate for aluminum alloys. An advantage of this phase is also the lack of reaction between it and aluminum, on the contrary to the Al-SiC system, where the detrimental Al₄C₃ phase may be created. Borgonovo and Makhoulouf have analyzed the thermodynamics and the kinetics of the process and have shown that it is feasible on an industrial scale. They investigated two alloy systems; namely Al-Mg and Al-Li, and two nitrogen bearing gases, namely nitrogen and ammonia (or a combination of the two). Magnesium and Lithium serve the purpose of acting as oxygen getters to catalyze the nitridation reaction and mitigate the aluminum oxidation reaction, which is thermodynamically favorable even when the oxygen content in the nitrogen-bearing gas is extremely low (10⁻⁹ Pa). Lithium has been shown to be more effective than magnesium as only around 1.15 weight pct. lithium is necessary to synthesize the same amount of AlN as with around 15 weight pct. Mg in comparable processing times. In this contribution, the authors describe the effect of Li content of the matrix alloy, gas composition, processing time, and impeller rotation speed on the amount of the AlN formed, as well as on the size and distribution of the aluminum nitride particles in the matrix. A distribution index (DI) is developed in order to quantitatively describe particle dispersion.

2. Materials, Procedures and Apparatus

About 250 g of material was charged in a graphite crucible and placed in the mullite retort shown schematically in Fig.1. The mullite retort was positioned inside an electric resistance furnace. Borgonovo and Makhlouf¹⁻⁵ have underlined the importance of minimizing the oxygen content in the reaction chamber. For this reason, subsequent evacuation and backfilling of the retort with GRADE 5 Argon gas prior to heating is necessary. The impeller was immersed in the metal once the processing temperature (1,000 °C) was reached and the gas injection was started. The impeller head (the rotor) is 3D-printed from a ceramic powder (80 pct. Al₂O₃-20 pct. SiO₂) and coupled to an Inconel 601 tube by means of a large-pitch thread that is sealed with high temperature cement (Fig.2). The design of the rotor has been optimized to ensure uniform dispersion of the gas bubbles in the crucible and has a customized head with 24 holes each of which is 3 mm in diameter. Nitrogen gas (GRADE 5) and anhydrous ammonia (or a combination of the two gases) was used as reactive gas. Moisture traps and oxygen traps are used to purify the nitrogen-bearing gases so that the impurities are kept at the parts-per-billion (ppb) level. An oxygen-getting furnace set to 500 °C and filled with Cu coil was placed in line for further gas purification. The reaction temperature was kept constant at 1,000 °C, and the reaction time was varied between 2 and 4 hours. The gas flow rate was maintained between 0.4 and 0.6 l/min. After the desired reaction time, the melt was left to cool to room temperature in the furnace under an inert Ar atmosphere. Around 4 lbs. of molten A356 aluminum alloy was prepared in an induction furnace and transferred to the electric resistance furnace in preparation to the addition of the Al-Li/AlN composite material. The master composite material was added to the molten A356 once the temperature reached 730 °C. Silicon metal was added to compensate for the dilution of the A356 alloy with Al from the composite alloy. Three different levels of reinforcement were produced. A flow of Argon gas (GRADE 5) was kept in the furnace to minimize oxidation. After a few minutes, the titanium ultrasonic probe shown in Fig.3 was dipped in the metal to degas it. The power unit of the ultrasonic degasser has a maximum limit of 1500 W. Degassing was performed at ultrasonic intensities varying from 50 pct. to 80 pct. The intensity was lowered when the ultrasonic probe showed signs of overheating. Ultrasonic processing was performed for around 25 minutes, after which the temperature of the metal is raised to 780 °C prior to pouring in a standard ASTM-E8 permanent mold that has been preheated to 400 °C. This mold is used to cast specimens for tensile property measurements. A356 base alloy without addition of the composite material was ultrasonically degassed for the same length of time and poured in the same mold to produce tensile test specimens for comparison.

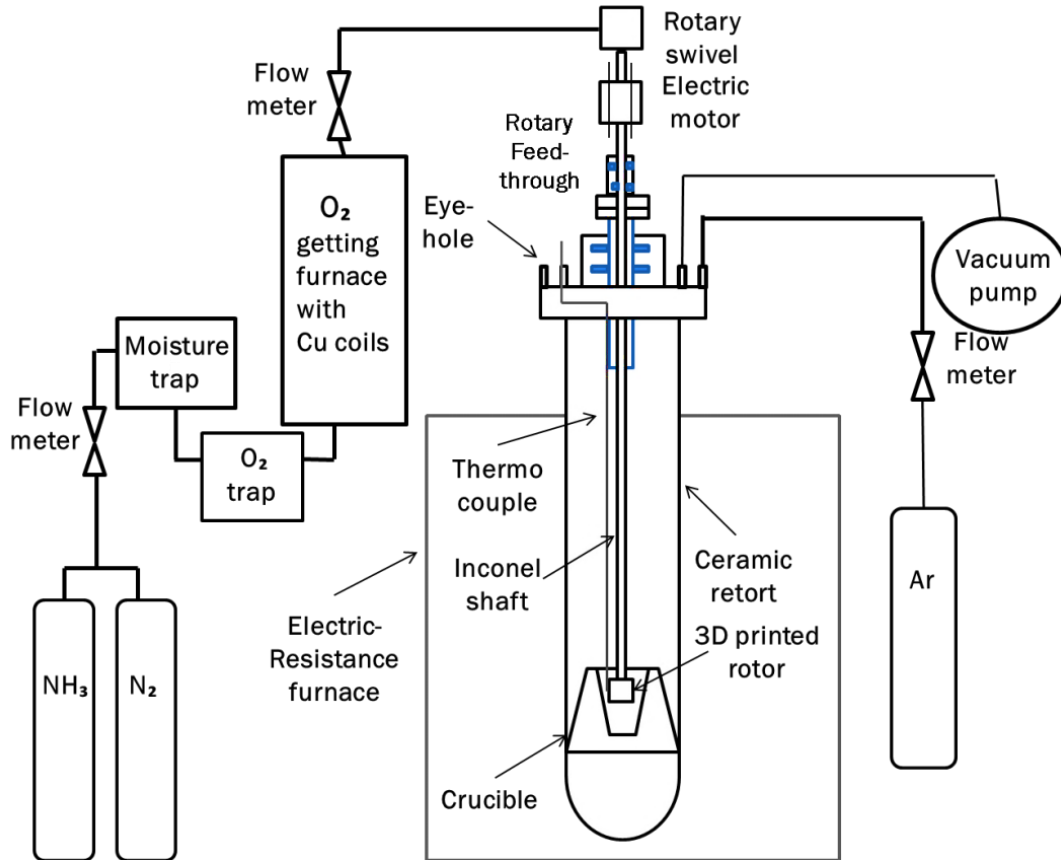


Figure 38. Schematic representation of the apparatus.

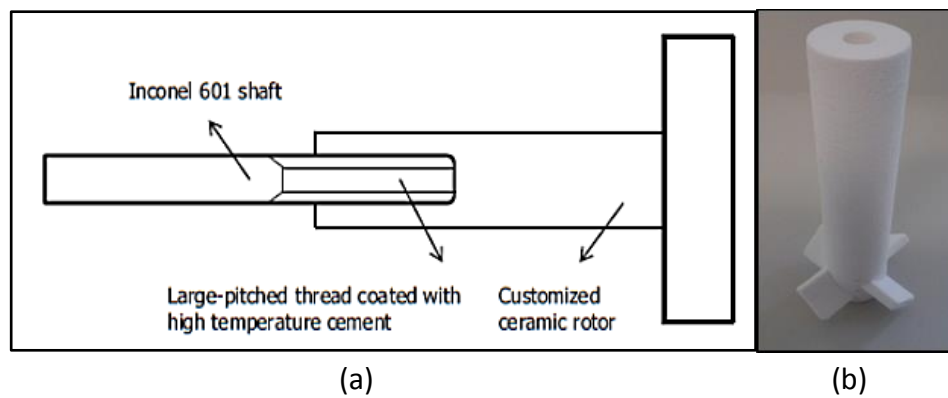


Figure 39. (a) Schematic representation of the shaft assembly, and (b) the printed ceramic rotor.

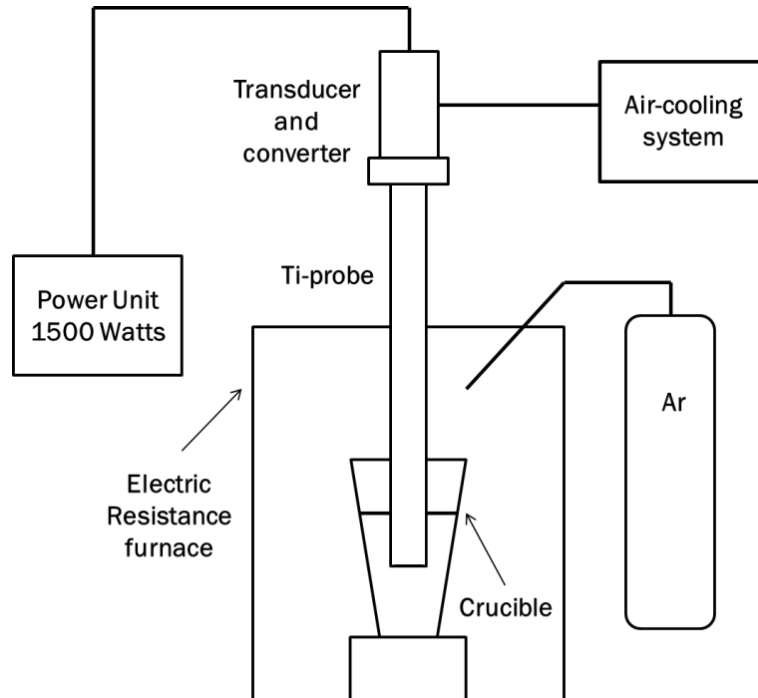


Figure 40. Schematic representation of the ultrasonic degassing system.

High purity Al (99.9999%) and Al-5%wt. Li master alloy were used as starting materials. Some of the Al-Li master alloy was diluted to 2.5 wt. pct. Li in a separate furnace prior to use. Table 1 summarizes the design of experiments. After each experiment, samples from the resulting composite material were prepared and etched with diluted 10 vol. pct. NaOH. Three concentrations of aluminum nitride particles in A356 aluminum matrix alloy were prepared by introducing appropriate amounts of Al-Li/AlN composite master alloy in the melt. These are: 0.5 vol. pct., 1 vol. pct., and 2 vol. pct. In each case, the microstructure was examined by a scanning electron microscope (SEM) coupled with an energy dispersive X-ray spectrometer. The samples were also examined by X-ray diffraction (XRD). A Matlab-based computer program (Appendix 1) together with image analysis was used to quantitatively characterize the microstructure of the resulting material. This includes calculating volume fraction of AlN particles, average AlN particle size, and average AlN cluster size.

Rockwell B hardness of the composite materials was measured utilizing a total load of 100Kg_f. On average 20 hardness measurements were made on each sample. A minimum of 6 specimens was used to determine the room temperature tensile properties of the material. The measurements were performed according to ASTM standard B557. All measurements were performed with a Universal Testing machine. Strain was measured with an axial extensometer with a gage length of 2 inches. The extensometer was used until the specimen fractured and the testing machine ramp rate was 0.05 in/min. A minimum of 3 specimens was used to determine the elevated temperature properties of the material. The

tensile tests were performed at 300°C according to ASTM standard E21 with a Universal Testing machine. Strain was measured with a high temperature extensometer. The extensometer was used until the specimen fractured and the testing machine ramp rate was 0.05 in/min. Specimens were heated to 300°C, held at temperature, and tested to fracture in an environment chamber. The chamber temperature did not vary by more than $\pm 3^\circ\text{C}$. The data from both room temperature and elevated temperature tensile property measurements was analyzed to obtain ultimate tensile strength (UTS), yield strength (YS), elongation (e), and modulus of elasticity (E).

Table 1. Design of Experiments.

Experiment #	Alloy	Gas	Processing time	Rotational speed
1	Al-5 wt% Li	N ₂	2	250
2	Al-5 wt% Li	N ₂	4	250
3	Al-5 wt% Li	N ₂ +NH ₃ (1:1)	2	250
4	Al-5 wt% Li	N ₂ +NH ₃ (1:1)	4	250
5	Al-5 wt% Li	NH ₃	2	250
6	Al-5 wt% Li	NH ₃	4	250
7	Al-2.5 wt% Li	N ₂	2	250
8	Al-2.5 wt% Li	N ₂	4	250
9	Al-2.5 wt% Li	N ₂ +NH ₃ (1:1)	2	250
10	Al-2.5 wt% Li	N ₂ +NH ₃ (1:1)	4	250
11	Al-2.5 wt% Li	NH ₃	2	250
12	Al-2.5 wt% Li	NH ₃	4	250
13	Al-2.5 wt% Li	N ₂ +NH ₃ (1:1)	4	300
14	Al-2.5 wt% Li	N ₂	2	450

3. Results and Discussion

1.1 Microstructure Characterization

Table 2 shows the quantitative results of the microstructure characterization. No AlN was detected in the samples when N₂ gas is injected in Al-5pct. Li alloy for 2 hours. When the processing time is increased to 4 hours, XRD analysis (Fig. 4) shows the presence of AlN.

The quantitative analysis reveals fairly small AlN particles that are about 600nm in size distributed in the alloy matrix. When the reacting gas is ammonia + nitrogen, the volume of AlN particles that forms increases compared to the case when only N₂ gas is used, and the average particle size is around 400 nm. Some clustering of the particles occurs when the gas mixture is injected for 2 hours, but the average cluster size was relatively small – around 1300 nm. Further increase in the volume fraction of AlN particles occurs when ammonia only is used as reactive gas. In this case, 48 volume pct. of AlN particles formed after processing for 4 hours. The microstructure appears to be very homogeneous for both 2 and 4 hours processing times (Figs. 5 and 7). Clustering seems to be significantly diminished, the average cluster size is reduced to around 1 μ m, and the average particle size is also reduced to 300nm. Fig. 6 shows semi-Gaussian particle size distribution around the average particle size.

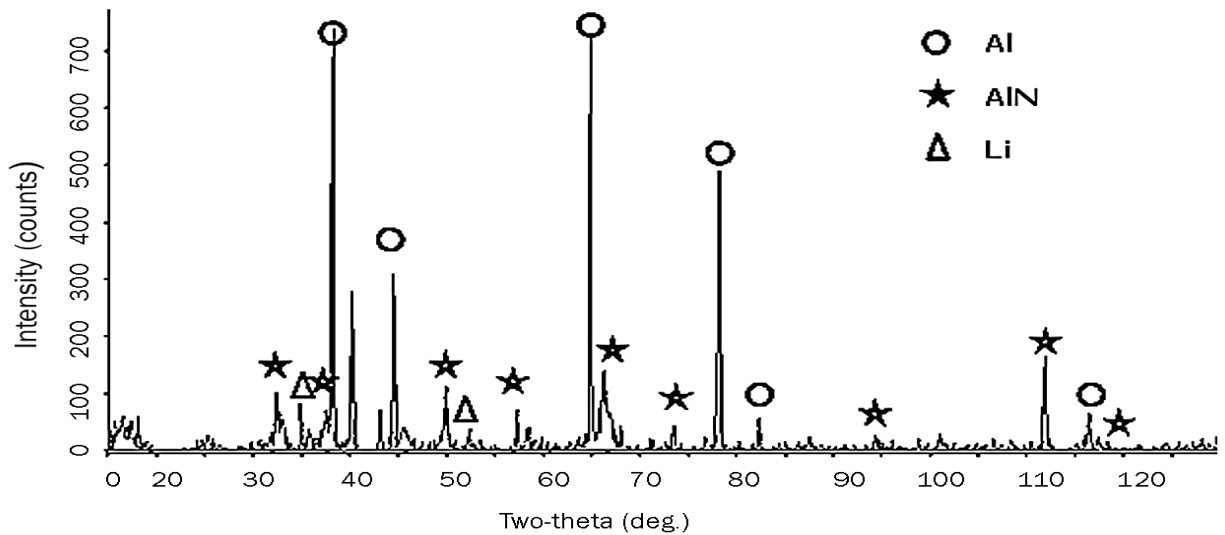


Figure 41. XRD pattern of the Al-AIN composite produced by Experiment #2.

Table 2. Summary of microstructure characteristics of materials produced according to the experiments shown in Table 1.

Experiment #	Vol. pct. AlN	Average particle size (nm)	Average cluster size (nm)
1	-	-	-
2	6.2	643 nm	1540 nm
3	9.5	489 nm	1327 nm
4	26	453 nm	1552 nm
5	21	274 nm	966 nm
6	48	312 nm	1114 nm
7	-	-	-
8	-	-	-
9	-	-	-
10	7.4	655 nm	924 nm
11	12.8	409 nm	1012 nm
12	31	293 nm	785 nm
13	11	208 nm	435 nm
14	4	58 nm	n/a

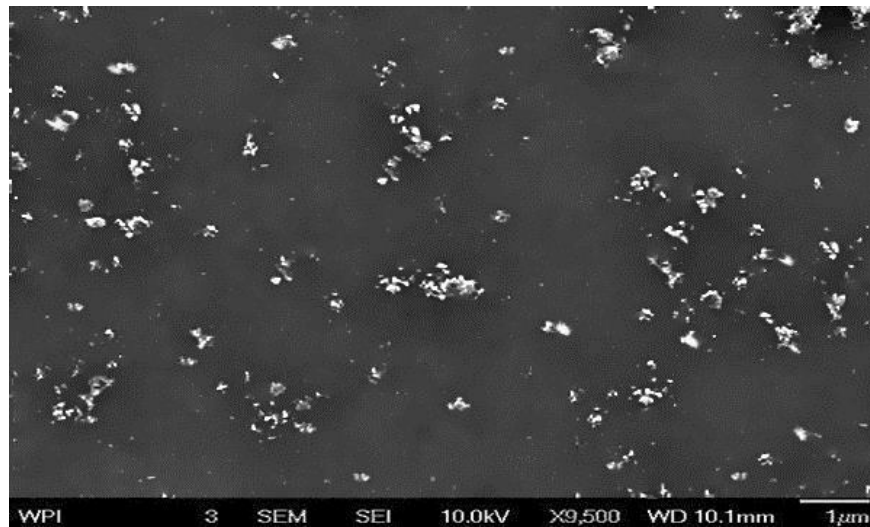


Figure 42. SEM photomicrograph showing AlN particles produced in Experiment #5.

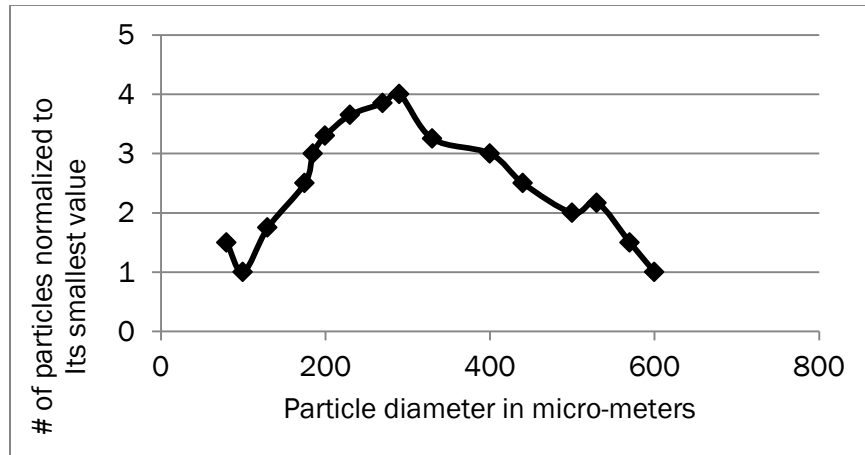


Figure 43. Particle size distribution in material produced according to Experiment #5.

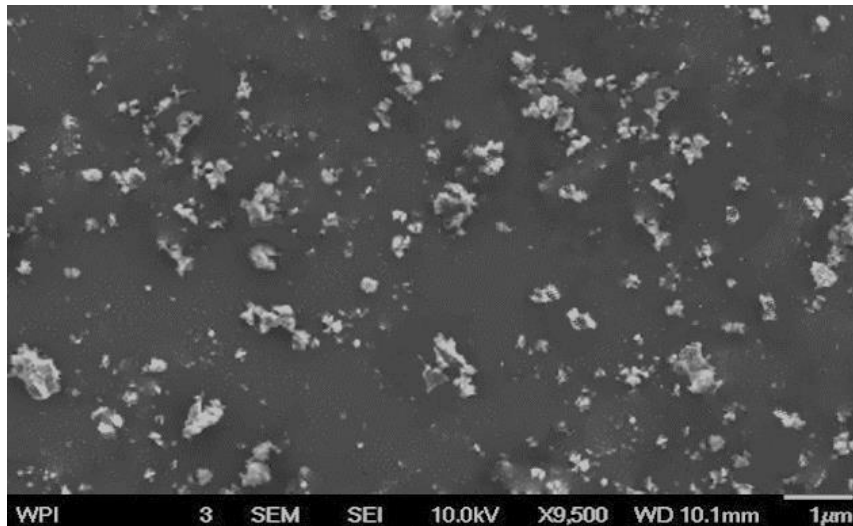


Figure 44. SEM photomicrograph showing AlN particles produced in Experiment #6.

When ammonia is used with the 2.5 wt. pct. Li alloy, the average AlN particle size is decreased to around 400 nm for the 2 hours processing time, and 300nm for the 4 hours processing time. The volume fraction of AlN is 31 pct. for the 4 hours processing time, which is almost 30 pct. lower than when the 5 weight pct. Li alloy is used. In the experiments performed with the 2.5 weight pct. Li alloy, no AlN particles were detected when nitrogen only was used as reactive gas for 2 or 4 hours. Also, no AlN particles were found when the mixture of nitrogen and ammonia gases was injected in the alloy for 2 hours; however, when the processing time is increased to 4 hours, around 7 volume pct. AlN was formed as shown in the XRD pattern of Fig. 8 and SEM micrograph of Fig. 9. The average cluster size is less than 500 nm and the average particle size is around 200 nm. The particle size distribution is also homogeneous, as shown in Fig. 10.

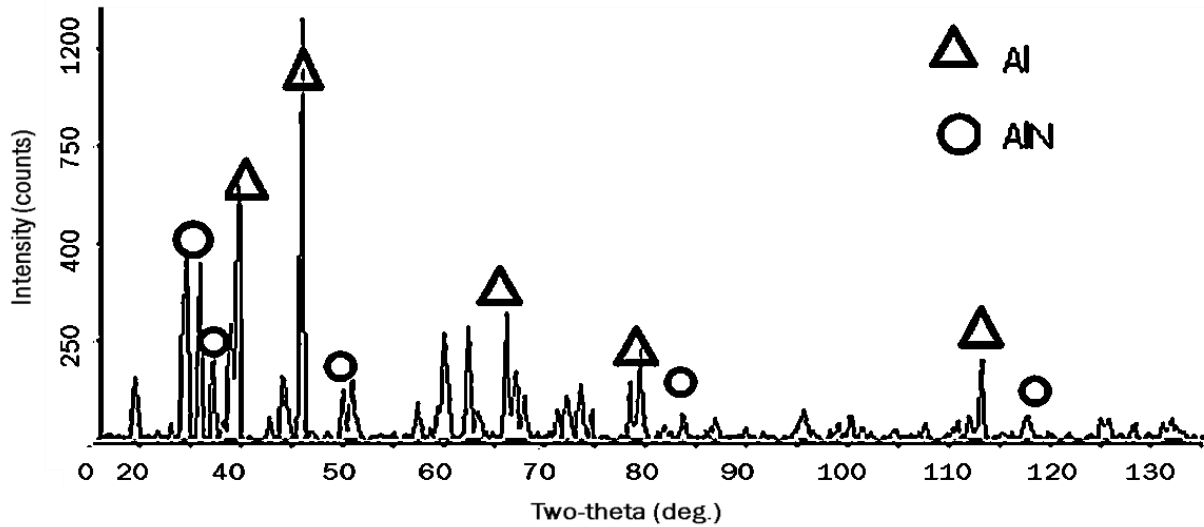


Figure 45. XRD pattern of the Al-AlN composite produced by Experiment #13.

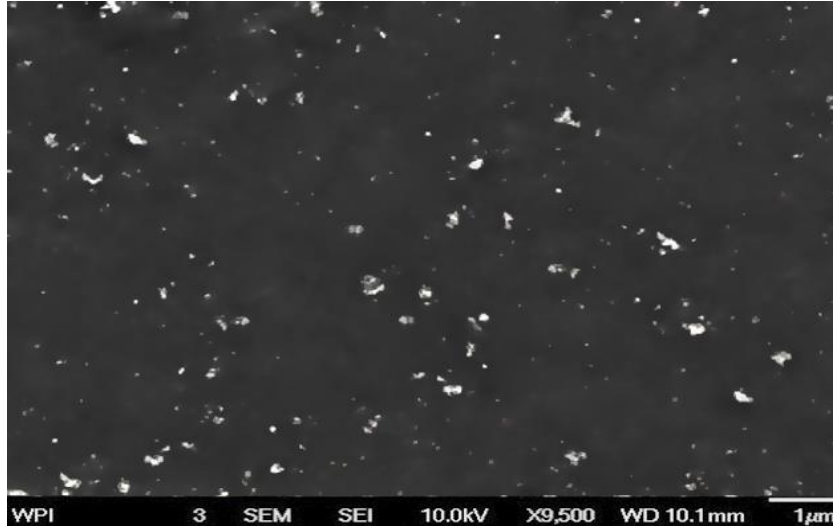


Figure 46. SEM photomicrograph showing AlN particles produced in Experiment #13.

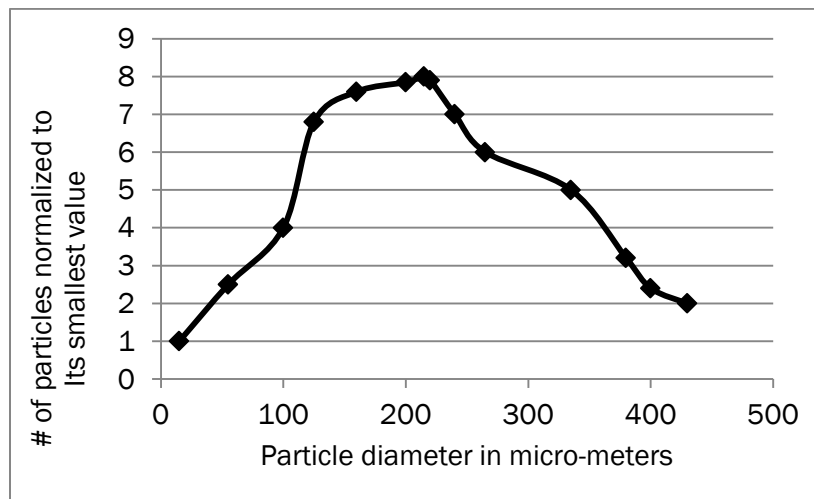


Figure 47. Particle size distribution in material produced according to Experiment #13.

It has been observed [1-5] that Li acts as a catalyst for the nitridation reaction. The role of Li in aluminum nitridation has been investigated by Scholz and Greil [7] and by Borgonovo and Makhlof []. Based on phase equilibrium calculations in the Al-Li-O-N system, Li combines with oxygen to form Li_2O at low oxygen levels and LiAlO_2 at higher oxygen levels according to reactions (1) and (2).



Aluminum nitridation may also occur because of the ability of Li to remove the gaseous reaction products from the reaction site so that equilibrium conditions are never achieved. The continuous flow of the nitrogen-bearing gas in the furnace chamber removes the evaporating species (Li and Li_2O) from the reaction chamber, thus maintaining non-equilibrium conditions that generate very high mass flow of volatilizing Li. Therefore, the high partial pressure of the Li-based vaporized species in the furnace environment causes nitridation of aluminum on the surface of the melt first. Channels in the aluminum-lithium melt formed by the rising nitrogen bubbles and the stirring action of the impeller are probably responsible for nitridation of the bulk of the metal. The role of ammonia has been extensively analyzed by Borgonovo and Makhoul [1]. During nitridation with ammonia, hydrogen dissociates from nitrogen at around 1000°C and functions as an oxygen getter to lower the oxygen content of the system thus increasing the permissible oxygen partial pressure for nitridation. Also, hydrogen may enhance the adsorption of nitrogen at the gas bubble-metal melt interface thereby improving the rate of AlN formation. In addition to this, the dissociation of ammonia releases atomic nitrogen, which is more easily chemisorbed on the bubble surface and diffused into the molten metal than molecular nitrogen.

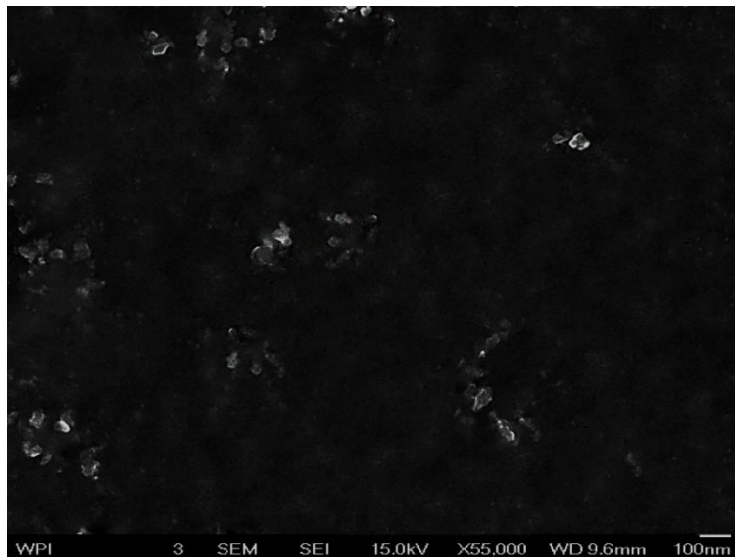


Figure 48. SEM photomicrograph showing AlN particles produced in Experiment#14.

In Experiment 14, the rotation speed is increased to 450 rpm in order to examine the effect of impeller rotation speed on AlN particle size and clustering. Microstructure of the resulting material is shown in Fig.11. Table 2 shows the microstructure parameters for the composite material as computed by the Matlab-based program [6]. The particle size is around 60 nm and clusters that are larger than the average particle size are not detected. Only 4 volume pct. volume pct. AlN formed in this material, which is probably due to the shorter gas injection time. The smaller particle size is a direct consequence of bubble break up that leads to smaller gas bubbles. It is common practice to correlate increase in rotational speed

to bubble break-up, although this is valid only for certain systems, such as liquid foams. In order to predict the bubble size resulting from mechanical stirring, it is useful to calculate Weber number, We . This dimensionless number is defined by Taylor, and it reflects the balance between the viscous forces that tend to deform the bubble and the interfacial forces that tend to maintain its spherical shape. The Weber number is given by Eq. (3)

$$We_{cr} = \frac{\mu \dot{\gamma} d_{bm}}{\alpha \sigma} \quad (3)$$

where μ is the dynamic viscosity, $\dot{\gamma}$ is the shear rate, d_{bm} is the mean bubble diameter, σ is the gas/liquid interfacial tension, and α is a coefficient which can range from 1 to 2. When We becomes larger than a critical value, We_{cr} , bubble break-up is expected to occur [8-11]. The critical Weber diameter can be determined experimentally. For the very low values of dynamic viscosity of aluminum at 1000°C, it has been shown that We only depends on shear rate, which is directly proportional to the rotation speed, N , for Newtonian fluids and on $N^{3/2}$ for Non-Newtonian fluids [9,11]. Therefore, the bubble diameter decreases with increasing rotation speed according to Eq. (4)

$$d_{bm} \propto \frac{1}{N^{(1+1.5)}} \quad (4)$$

Fig. 12 shows that for speeds higher than 450 rpm, the bubble size doesn't decrease significantly, and it eventually reaches a constant value.

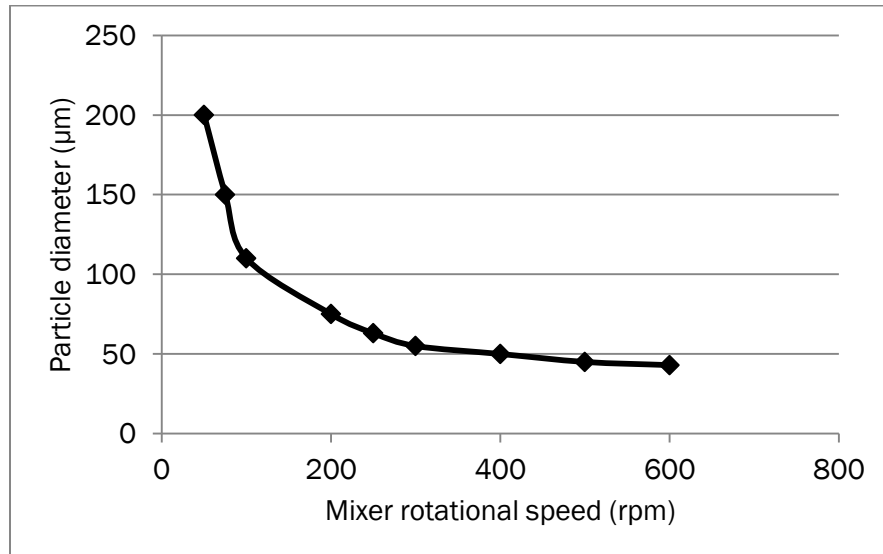


Figure 49. Mean bubble diameter versus rotational speed⁸.

The process parameters of Experiment #14 were used to make the material to be added to commercial A356 foundry alloy.

A distribution index (DI) based on the *box counting method* was defined in order to quantitatively determine particle distribution in the matrix. In this method, the matrix is divided into a number of small uniform boxes. Selection of an appropriate box size is important, and it is related to the number of tracked particles. This quantity was determined with the help of the Matlab-based program (Appendix 1) [6]. Jones [12] determined the box size such that on average there is one particle per box. If the box size is chosen such that for a perfectly random distribution of N particles, 98 pct. of the boxes contain at least one particle each, then the box size s for a unit square domain (1×1) is approximately given by

$$s \sim 2N^{-\frac{1}{2}} \quad (5)$$

Since N is a known parameter, the domain can be easily divided into boxes of size s , and then the dispersed particles in each box are counted. For example, tracking 1,600 particles requires 400 boxes in the entire domain. Since:

$$s \sim 2(1600)^{\frac{1}{2}} \sim 0.05$$

Then, the number of boxes per domain side is $\frac{1}{0.05} = 20$

Total number of boxes (assuming a square domain) = $20^2 = 400$. This results in a maximum of 4 particles (n_{max}) per box in a homogeneously mixed situation. We can define a Distribution Index for each box (D_i) as:

$$D_i = \frac{n_i}{n_{max}} \quad \text{if } n_i \leq n_{max} \quad (6)$$

$$D_i = 1 \quad \text{if } n_i \geq n_{max} \quad (7)$$

where n_i is the number of particles in box i . The Distribution Index DI is then defined as

$$DI = 1 - \frac{1}{N} \sum_{i=1}^N D_i \quad (8)$$

The distribution indices calculated for the materials produced according to Table 2 are shown in Table 3. The DI varies from 0 for a totally clustered dispersion to 1 for perfect dispersion. It can be noticed from Table 3 that higher rotation speeds provide improved particle distribution and that when ammonia is present in the gas mixture enhanced particle dispersion is achieved.

Table 3. Distribution Index (DI).

Experiment #	Distribution Index (DI)
1	-
2	0.58
3	0.37
4	0.51
5	0.82
6	0.74
7	-
8	-
9	-
10	0.31
11	0.73
12	0.65
13	0.78
14	0.67

Fig. 13 shows the increase in Hardness of the composite material. It can be noticed that the most improvement is attained when ammonia is used as the reaction gas, when Li is at the higher level (5 weight pct.), and when the rotation speed of the impeller is increased.

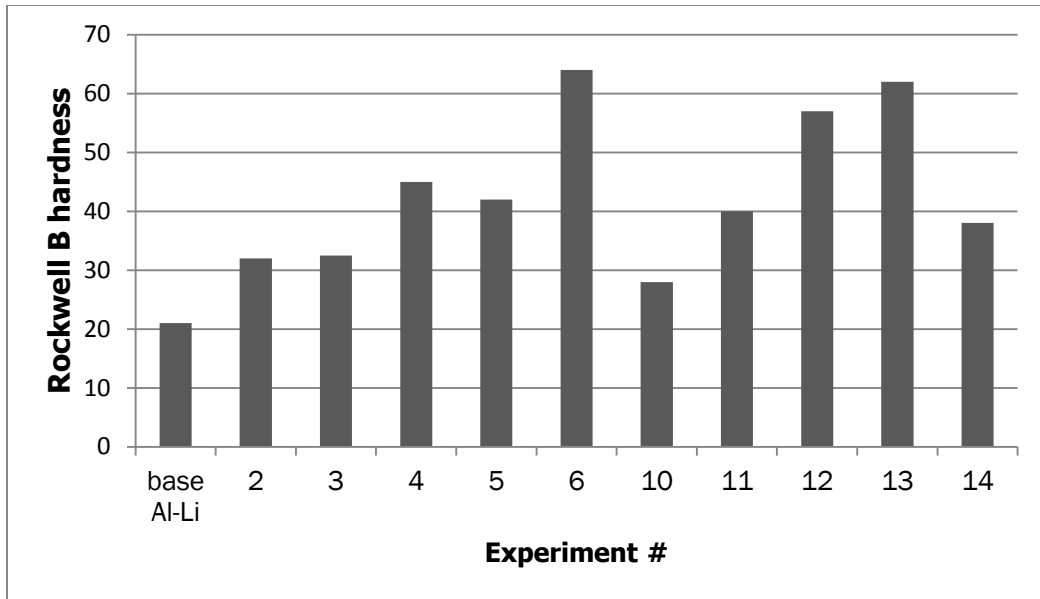


Figure 50. Measured Rockwell B Hardness.

a. Mechanical Properties

Figs. 14-17 show the room temperature tensile properties of A356/AlN composite materials. Fig.14 shows that the improvement in ultimate tensile strength is around 46 pct. for 2volume pct. AlN and the improvement in UTS is linearly proportional to the amount of AlN added to the matrix. Yield strength also increases by about 90 pct. Fig. 15 shows that an improvement in YS of about 50 pct. may be achieved by adding as little as 0.5 volume pct. AlN. Fig.16 shows that elongation experiences a small decrease (only 10 pct.) with up to 1 volume pct. AlN. At 2 volume pct. AlN, elongation decreases by 50 pct. Fig.17 shows that the Young's modulus increases by 100 pct. over that of the base alloy when 0.5 volume pct. AlN is added, and by 120 pct. when 2 volume pct. AlN is added.

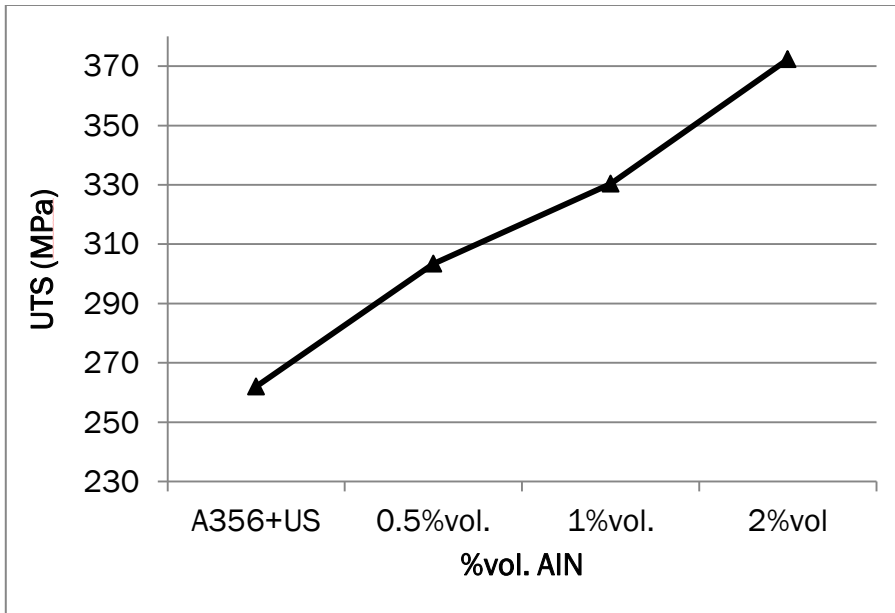


Figure 51. Room temperature UTS as function of volume pct. AlN.

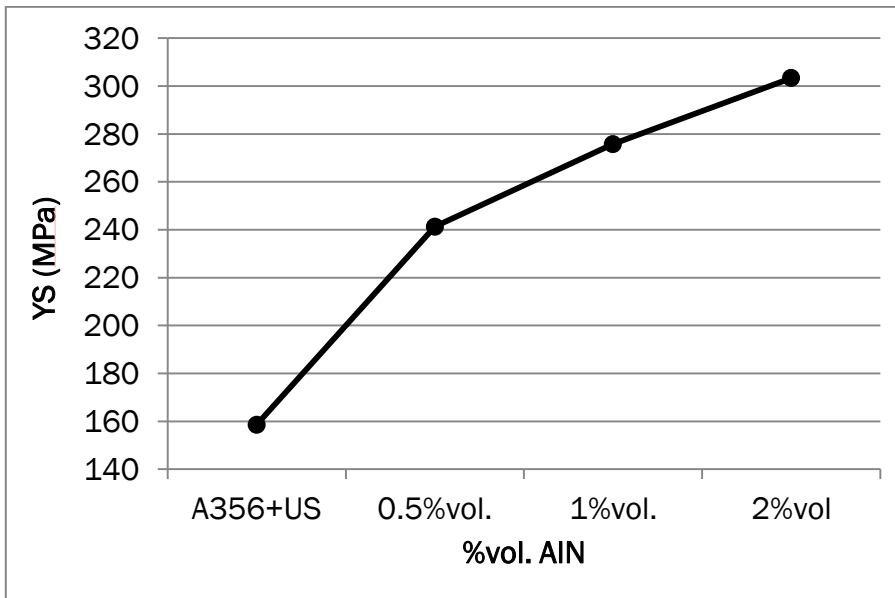


Figure 52. Room temperature YS as function of volume pct. AlN.

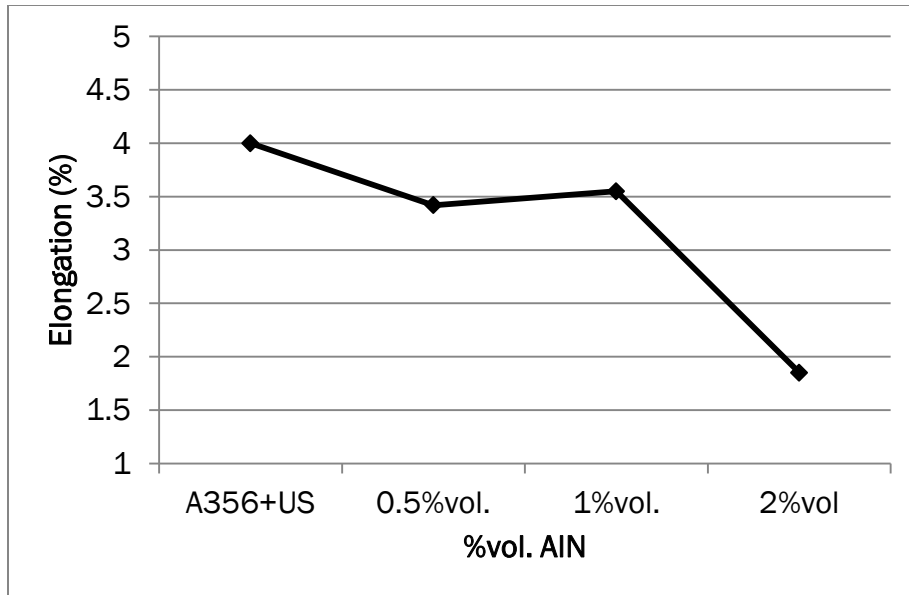


Figure 53. Room temperature UTS as function of volume pct. AlN.

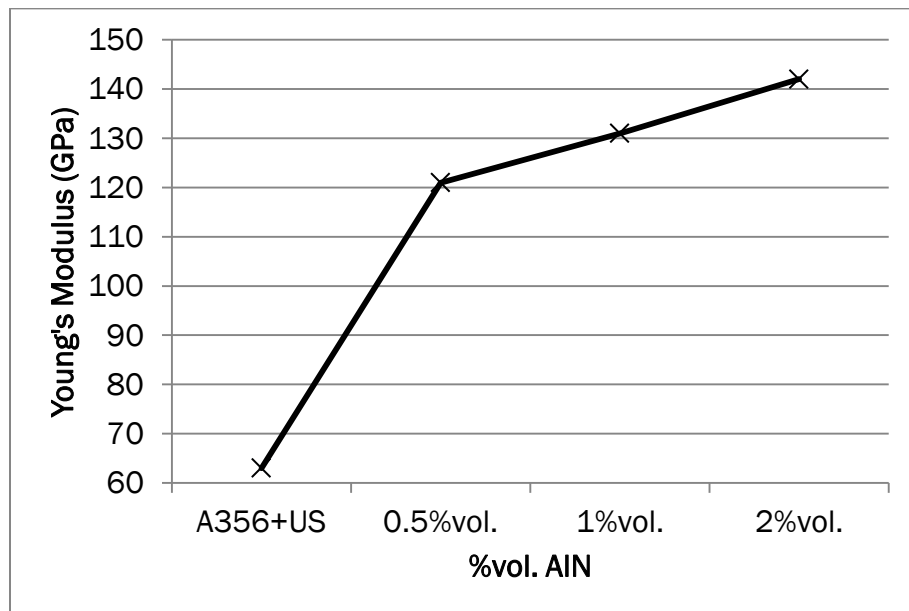


Figure 54. Room temperature Young's modulus as function of volume pct. AlN.

The presence of AlN in the matrix can be confirmed by SEM analysis (Figs.18-20) AlN particles are very homogeneously distributed both for the A356 reinforced with the lower amount of AlN and the highest. Moreover, particles have retained good dispersion even around the area of the Si needles, which is normally subjected to heavily clustering. The strengthening effect of AlN addition can be most likely attributed to Orowan effect or

dislocation bowing. This will be further confirmed by TEM analysis. It is unlikely that strengthening through particle shearing would contribute to strengthen the material since AlN are a very hard and brittle phase, and the size in our case (60-80 nm) is generally too big for particle shearing to take place. Fig.21 compares the surface fracture of the base metal A356 with A356/1%vol. AlN. It can be noticed that the morphology of the fracture of the composite has sharper dimples which indicated the decrease of ductility in the composite material.

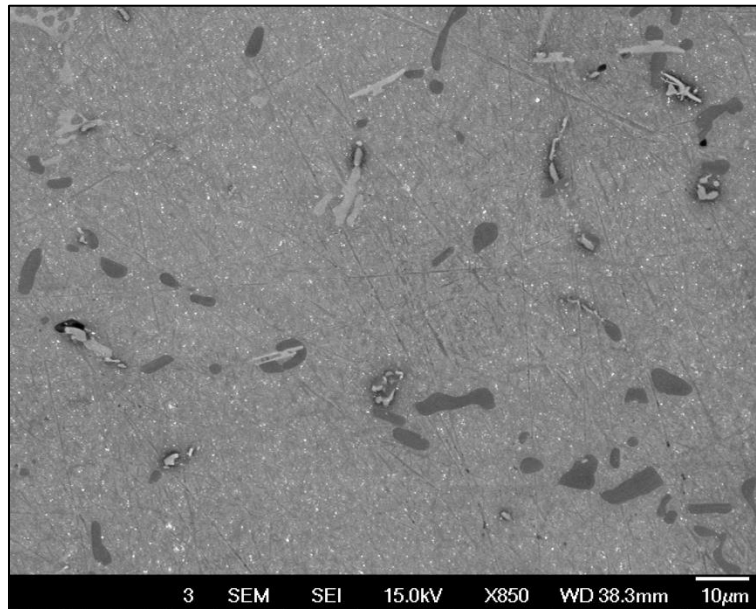


Figure 55. A356/AlN. Low magnification. 2%vol. AlN.

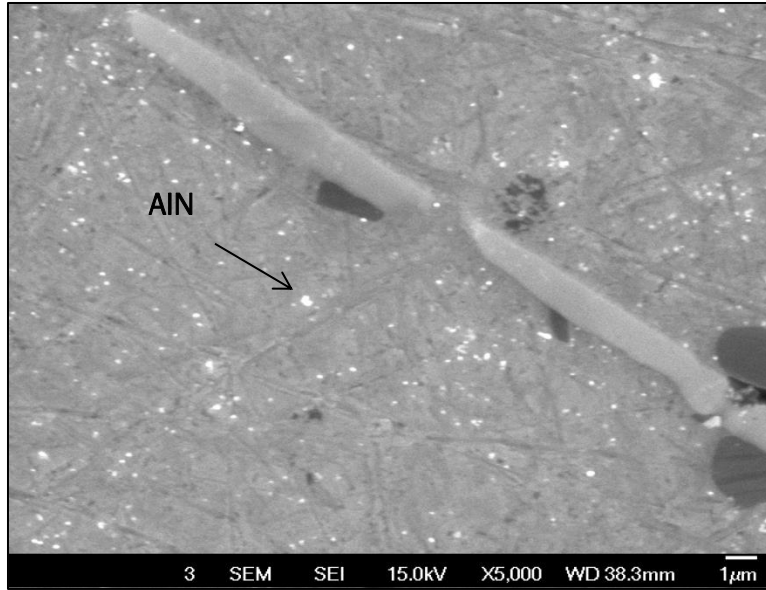


Figure 56. A356/AIN. High magnification. 2%vol. AIN.

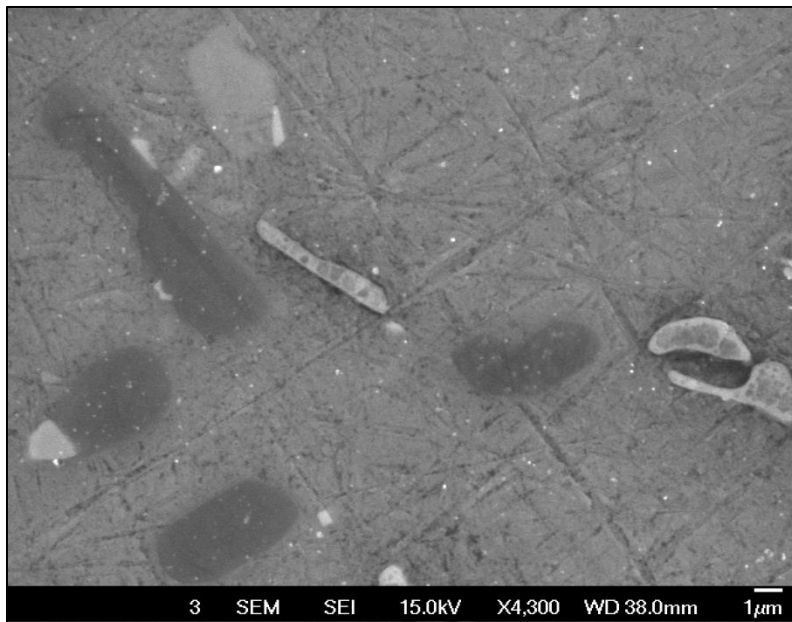


Figure 57. A356/AIN. High magnification. 1%vol. AIN.

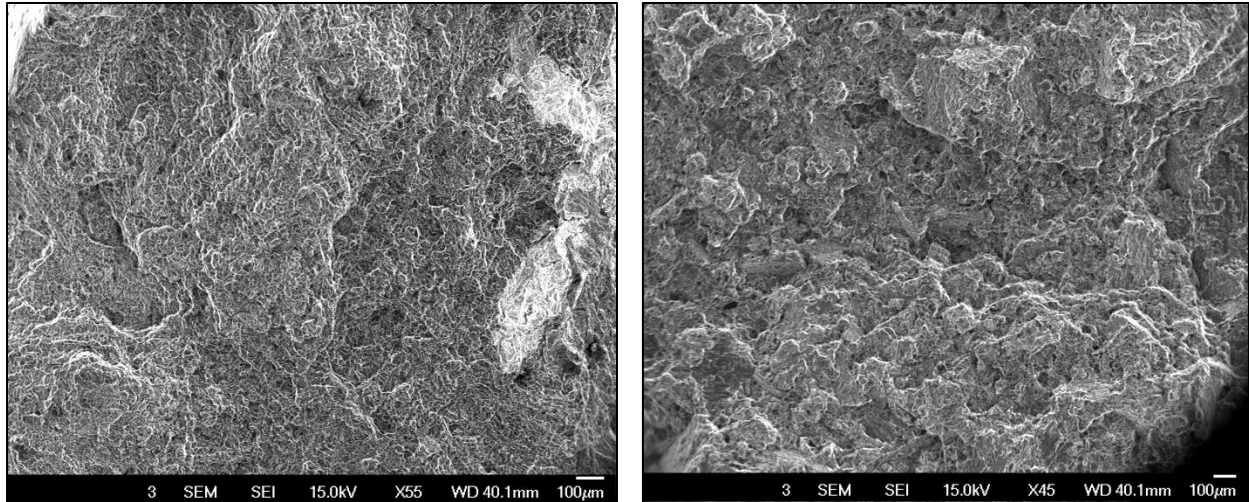


Figure 58. Left) Surface fracture of A356 base metal processed with ultrasonic energy; right) A356/1%vol.AIN processed with ultrasonic energy.

Ultrasonic processing has proved to be effective in degassing as previously reported by other works¹³⁻¹⁵, as it can be observed from the lack of porosity both in SEM images and on the surface fractures. UTS, YS and Young's modulus at 300 °C have also been determined for 0.5%vol. and 1%vol. of AIN (Figs.22-24). The increase in UTS is around 40% for the material reinforced with 1%vol. of AIN (Fig.22). YS is also enhanced and follows almost a linear improvement spanning from 25% for 0.5%vol. of AIN to almost 50% for 1%vol. of AIN (Fig.23). The most significant result is the dramatic increase in Young's modulus of about 200% for 0.5%vol. AIN and 240% for 1%vol. AIN (Fig.24).

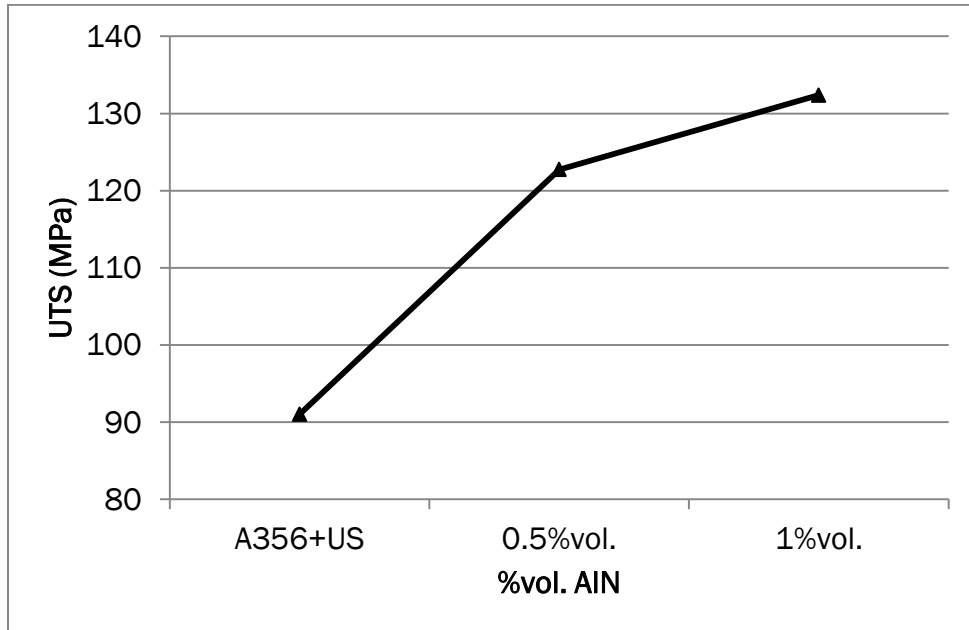


Figure 59. Elevated temperature (300 °C) UTS as function of volume pct. AlN.

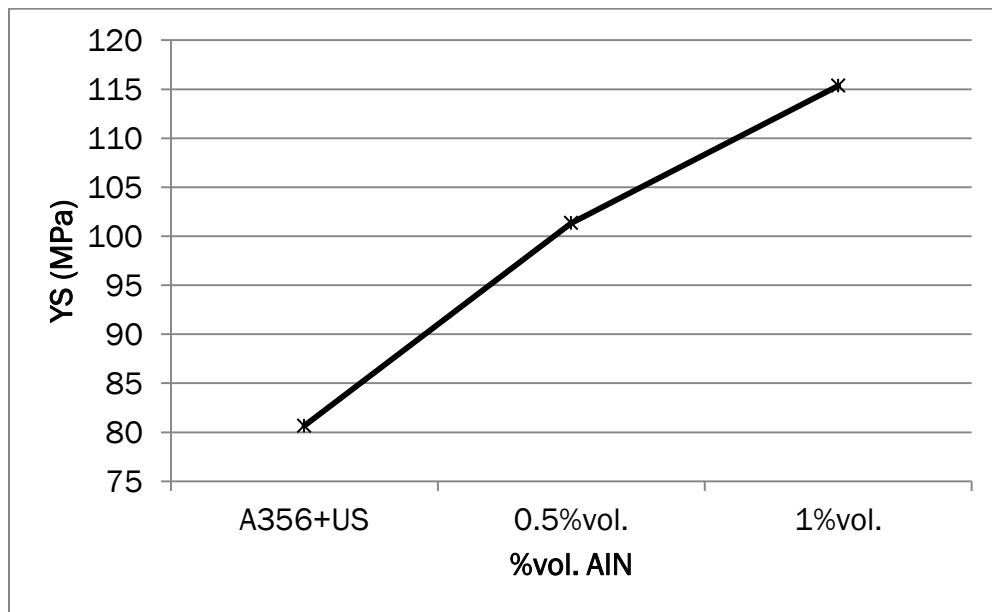


Figure 60. Elevated temperature (300 °C) YS as function of volume pct. AlN.

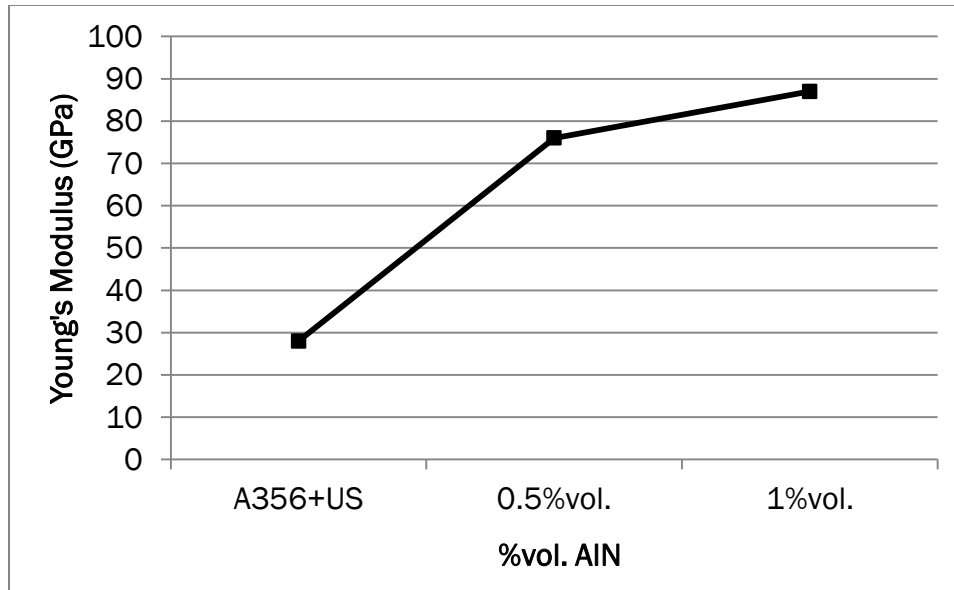


Figure 61. Elevated temperature (300 °C) Young's modulus as function of volume pct. AlN.

4. Conclusions

In this work, the experimental results of the in-situ gas liquid process have been presented. The effect of process variables of vol.% of AlN synthesized, size of AlN and cluster size has been devised. Particle size has been brought down to around 60 nm for high impeller rotational speed and particle clusters are almost absent. It has been noticed that ammonia enhances the nitridation reaction as well as high amounts of Li. This is most likely due to their oxygen-getter actions. Impeller speed mainly affect particle size by affecting the size of the gas bubbles. A distribution index (DI) between 0 and 1 has been defined and used to quantitatively evaluate particle dispersion. Ultrasonic energy has shown to be efficient in degassing the material. Mechanical properties both at room and high temperature (300 °C) show a dramatic increase. The increase in YS and Young's modulus is almost 100% at room temperature while the UTS is about 46% for 2%vol. of AlN. The strengthening effect of the particle is likely to Orowan bowing, but further TEM investigation will be carried out to confirm this. UTS and YS have been both improved by around 50% at high temperature. The Young's Modulus at 300 °C has also increased of around 200%.

5. References

1. Borgonovo and M.M. Makhlof: "A Novel Method for Manufacturing Aluminum-Aluminum Nitride Nanocomposites," Proceedings of MS&T, Columbus, Ohio, 2011.
2. C. Borgonovo and M.M. Makhlof: "The Synthesis of Die-Castable Nano-Particle Reinforced Aluminum Matrix Composite Materials by In-Situ Gas-Liquid Reaction," Proceedings of High Tech Die Casting, Vicenza, Italy, 2012.

3. C.Borgonovo and M.M. Makhlof: "In-Situ Manufacturing of Nano-Particle Reinforced Metal Matrix Composites," Proceedings of AFS, Columbus, Ohio, 2012.
4. C.Borgonovo and M.M. Makhlof: "In-Situ Manufacturing of Aluminum Based Metal Matrix Composites," Proceedings of the 15th European Conference on Composite Composite Materials, Venice, Italy, 2012.
5. C. Borgonovo, D. Apelian, and M.M. Makhlof, *JOM*, 2011, Vol. 63 (2), pp. 57-64.
6. H. S. Share and D. L. Burris, *Polymer*, 2010, Vol. 51, pp. 719-729.
7. H. Scholz and P. Greil, *J. Eur. Ceram. Soc*, 1990, Vol. 6 (4), pp. 237-242.
8. C. Balerin, P. Aymard, F. Ducept, S. Vaslin, and G. Cuvelier, *J. Food Eng.*, 2007, Vol. 78, pp. 802-809.
9. G.I. Taylor: "The Viscosity of a Fluid Containing Small Drops of Another Fluid," Proceedings of the Royal Society, 1932, A138, pp. 41-48.
10. J.R. Davis: 'ASM Specialty Handbooks: Aluminum and Aluminum Alloys', ASM International, 1993.
11. J.A. Sanchez Perez, E.M. Rodriguez Porcel, J.L. Casas Lopez, J.M. Fernandez Sevilla, and Y. Chisti, *J. Chem Eng.*, 2006, Vol. 124, pp. 1-5.
12. G. Karniadakis, A. Beskok, and N. Aluru (eds.): 'Microflows and Nanoflows: Fundamentals and Simulations', 2005, Springer, New York, NY.
13. G.I. Eskin, *Ultrason. Sonochem.*, 1995, Vol. 2 (2), pp.137-141.
14. H. Xu, X. Jian, T.T. Meek, and Q. Han: 'Ultrasonic Degassing of Molten Aluminum under Reduced Pressure', *Light Metals 2005*, Edited by Halvor Kvande, TMS (The Minerals, Metals & Materials Society), 2005, pp.915-919.
15. V. Rundquist and K. Manchiraju: 'Ultrasonic Degassing and Processing of Aluminum', *Light Metals 2013*, Edited by Barry Sadler, TMS (The Minerals, Metals & Materials Society), 2013, pp. 949-955.

APPENDIX 1: Matlab-Based Calculation Code for the Dispersion Factor (DI)

How does it work?

Uniform particle dispersion is desirable in order to achieve improved mechanical properties and therefore, a reliable final component. Mean free space length (also called inter-particle distance) is a scale-dependent measure of the homogeneity of particle distribution. Fig. 1a shows a perfectly uniform dispersion, while Fig. 1b is characterized by some clustered particles. It can be seen how the distance between particles increases in Fig. 1b, where the dispersion is non-homogeneous. For decreasing particle size and increasing particle loading, the inter-particle distance is reduced.

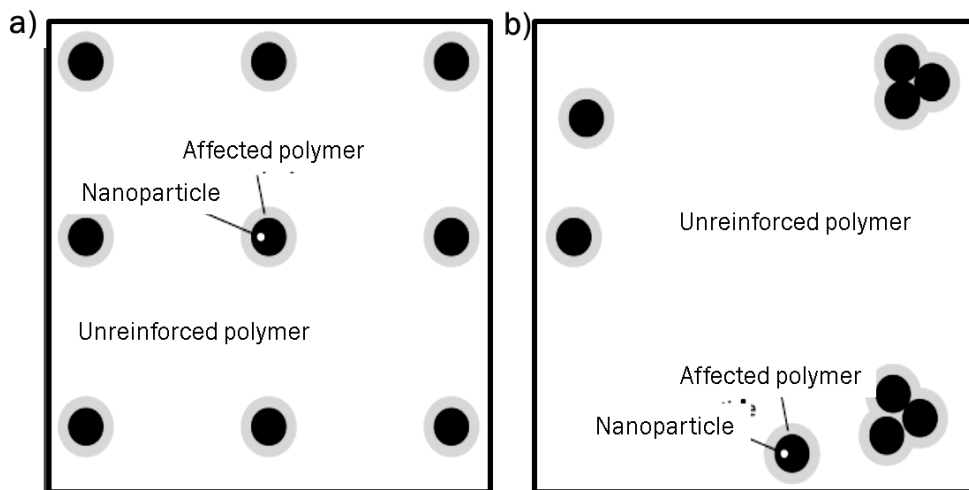


Figure 62. Illustrations of two possible dispersion states for nanoparticles within a polymer matrix: a) a uniform dispersion, b) a more realistic dispersion with two small clusters of particles¹.

Share et al.¹ have formulated a Matlab-based computer program able to characterize particle dispersion in the matrix. The first step is to convert the SEM or TEM micrograph into black and white bitmap image. The program computes the inter-particle free-space length first, being the free-space length defined as the width of the largest randomly placed square (on the bitmap image) for which the most probable number of intersecting particles is zero - equivalent to the use of the Poisson distribution for random systems-. Initially, a square of a given length is randomly placed on the image. The number of intersecting particles is counted and stored. This procedure is repeated a statistically significant number of times to compute the most probable number of intersecting particles -the “mode”- for the characteristic square length using the particle occurrence histogram is used (intersection occurrence vs. number of particles/square).The code iterates on square size to find the

largest square for which the most probable number of intersecting particles in a randomly placed square is zero. By inverting the black and white tones of the bitmap image, the program is able to compute average particle size and cluster size using the same procedure.

CODE¹

```
function [af,ll] = dispersion()
clear
clc
close all

syms log1l y n;

% Version check for SORT function
log1l = input('Is the version of MATLAB 7.0 or later? (Y/N) : ', 's');

if strcmpi(log1l, 'y') ==1;
    vzn = 1;
else
    vzn = 0;
end

%%%%%%%%%%%%%%%%%%%%%%%%%%%%%%%%%%%%%%%%%%%%%%%%%%%%%%%%%%%%%%%%%%%%%%%%%%
%%%%%%%%%%%%%%%%%%%%%%%%%%%%%%%%%%%%%%%%%%%%%%%%%%%%%%%%%%%%%%%%%%%%%%%%%% Read TEM b/w bitmap and generate pixel matrix 'A' %%%%%%%%%%%%%%%%%%%%%%%%%%%%%%%%%%%%%%%%%%%%%%%%%%%%%%%%%%%%%%%%%%%%%%%%%%%
%%%%%%%%%%%%%%%%%%%%%%%%%%%%%%%%%%%%%%%%%%%%%%%%%%%%%%%%%%%%%%%%%%%%%%%%%%

[filename,PathName] = uigetfile('*.bmp','Select the .BMP image');

A = imread([PathName,filename], 'bmp');

offx=ceil(size(A,1)/2); %Offset for periodic boundary
offy=ceil(size(A,2)/2); %Offset for periodic boundary

%%%%%%%%%%%%%%%%%%%%%%%%%%%%%%%%%%%%%%%%%%%%%%%%%%%%%%%%%%%%%%%%%%%%%%%%%%
%%%%%%%%%%%%%%%%%%%%%%%%%%%%%%%%%%%%%%%%%%%%%%%%%%%%%%%%%%%%%%%%%%%%%%%%%% Area fraction calculation %%%%%%%%%%%%%%%%%%%%%%%%%%%%%%%%%%%%%%%%%%%%%%%%%%%%%%%%%%%%%%%%%%%%%%%%%%%
%%%%%%%%%%%%%%%%%%%%%%%%%%%%%%%%%%%%%%%%%%%%%%%%%%%%%%%%%%%%%%%%%%%%%%%%%%

filledcells=0;
totalcells=0;

for i=1:size(A,1);
    for j=1:size(A,2);
        totalcells=totalcells+1;
        if A(i,j)<150;
            filledcells = filledcells+1;
        end
    end
end
af=filledcells/totalcells;

%%%%%%%%%%%%%%%%%%%%%%%%%%%%%%%%%%%%%%%%%%%%%%%%%%%%%%%%%%%%%%%%%%%%%%%%%%
%%%%%%%%%%%%%%%%%%%%%%%%%%%%%%%%%%%%%%%%%%%%%%%%%%%%%%%%%%%%%%%%%%%%%%%%%% Create data matrix which contains periodic boundary condition %%%%%%%%%%%%%%%%%%%%%%%%%%%%%%%%%%%%%%%%%%%%%%%%%%%%%%%%%%%%%%%%%%%%%%%%%%%
%%%%%%%%%%%%%%%%%%%%%%%%%%%%%%%%%%%%%%%%%%%%%%%%%%%%%%%%%%%%%%%%%%%%%%%%%%
```

```

%%%%%%%%% Top layer: Top quarter of the data matrix
for i = 1:offx;
    for j = 1:offy;
        Matrix(i,j)=A(offx+i,(offy+j));
    end
end

for i = 1:size(A,1);
    for j = 1:offy;
        Matrix(i+offx,j)=A(i,j+offy);
    end
end

for i = 1:offx;
    for j = 1:offy;
        Matrix(i+offx+size(A,1),j)=A(i,j+offy);
    end
end

%%%%%%%%% Middle layer: Middle two-rows of data matrix
for i = 1:offx;
    for j = 1:size(A,2);
        Matrix(i,j+offy)=A(i+offx,j);
    end
end

for i = 1:size(A,1);
    for j = 1:size(A,2);
        Matrix(i+offx,j+offy)=A(i,j);
    end
end

for i = 1:offx;
    for j = 1:size(A,2);
        Matrix(i+offx+size(A,1),j+offy)=A(i,j);
    end
end

%%%%%%%%% Bottom layer: Bottom quarter of data matrix
for i = 1:offx;
    for j = 1:offy;
        Matrix(i,j+offy+size(A,2))=A(i+offx,j);
    end
end

for i = 1:size(A,1);
    for j = 1:offy;
        Matrix(i+offx,j+offy+size(A,2))=A(i,j);
    end
end

for i = 1:offx;
    for j = 1:offy;
        Matrix(i+offx+size(A,1),j+offy+size(A,2))=A(i,j);
    end
end

```

```

syms logi y n;

%%%%%%%%%%%%%%%%%%%%%%%%%%%%%%%%%%%%%%%%%%%%%%%%%%%%%%%%%%%%%%%%%%%%%%%%
%%%%%%%%%%%%%%%%%%%%%%%%%%%%%%%%%%%%%%%%%%%%%%%%%%%%%%%%%%%%%%%%%%%%%%%% Define initial square parameters %%%%%%%%%
%%%%%%%%%%%%%%%%%%%%%%%%%%%%%%%%%%%%%%%%%%%%%%%%%%%%%%%%%%%%%%%%%%%%%%%%

scale1= input('Enter approximate width of TEM image in nanometers: ');
scale= scale1/size(A,2);
xf1 = input('Enter initial guess of characteristic square width in
nanometers: ');
xf = xf1/scale1;
Nsquares = input('Enter number of random squares to use for analysis: ');

fprintf('\n\n')
fprintf('Computation may take several seconds to a few minutes, depending on
input parameters\n Press Ctrl+C any time to terminate computation\n\n')

s2=size(A,1)*size(A,1);

%%%%%%%%%%%%%%%%%%%%%%%%%%%%%%%%%%%%%%%%%%%%%%%%%%%%%%%%%%%%%%%%%%%%%%%%
%%%%%%%%%%%%%%%%%%%%%%%%%%%%%%%%%%%%%%%%%%%%%%%%%%%%%%%%%%%%%%%%%%%%%%%% First count to Nsquares (corresponding to manual input of 'xf') %%%%%%%%%
%%%%%%%%%%%%%%%%%%%%%%%%%%%%%%%%%%%%%%%%%%%%%%%%%%%%%%%%%%%%%%%%%%%%%%%%

length = ceil(xf*size(A,2));
for i = 1:Nsquares;
    x=ceil(rand*size(A,1))+offx;
    y=ceil(rand*size(A,2))+offy;
    counter=0;
    for s = 1:length;
        for t = 1:length;
            mx=x-floor(length/2)+s;
            my=y-floor(length/2)+t;
            if Matrix(mx,my)<150;
                counter=counter+1;
            end
        end
    end
    P(i)=counter;
end
data=P';
bimreal=mode(data);

h1=hist(P,2500);
[m,n1]=max(h1);
l=xf;

boxar=length^2;

if boxar==bimreal
    isbimo=1;
    h1(1,2500)=0;
    [m,n1]=max(h1);
else
    isbimo=0;
end

```

```

if n1~=1

%%%%%%%%%%%%%%%%%%%%%%%%%%%%%%%%%%%%%%%%%%%%%%%%%%%%%%%%%%%%%%%%%%%%%%%%%%%%%%
%%%%%%%%%%%%%%%%%%%%%%%%%%%%%%%%%%%%%%%%%%%%%%%%%%%%%%%%%%%%%%%%%%%%%%%%%%%%%% Automatic iteration to obtain Free Space Length %%%%%%%%%%%%%%%%%%%%%%%%%%%%%%%%%%%%%%%%%%%%%%%%%%%%%%%%%%%%%%%%%%%%%%%%%%%%%%%
%%%%%%%%%%%%%%%%%%%%%%%%%%%%%%%%%%%%%%%%%%%%%%%%%%%%%%%%%%%%%%%%%%%%%%%%%%%%%%
margin=1;
while margin > .05

    while n1~=1
        xfnew=xf/2;
        l=xf-xfnew; %==xf/2
        length = ceil(l*size(A,1));
        for i = 1:Nsquares;
            x=ceil(rand*size(A,1))+offx;
            y=ceil(rand*size(A,2))+offy;
            counter=0;
            for s = 1:length;
                for t = 1:length;
                    mx=x-floor(length/2)+s;
                    my=y-floor(length/2)+t;
                    if Matrix(mx,my)<150;
                        counter=counter+1;
                    end
                end
            end
            P(i)=counter;
        end
        data=P';
        bimreal=mode(data);
        boxar=length^2;

        h2=hist(P,2500);

        if boxar==bimreal
            isbimo=1;
            h2(1,2500)=0;
            [m,n1]=max(h2);
        else
            isbimo=0;
            [m,n1]=max(h2);
        end

        xf=xfnew;

    end

    if n1==1
        if vzn == 1;
            SRT=sort(h2,'descend');
        else
            SRT=fliplr(sort((h2)));
        end

        margin=1-(SRT(2)/SRT(1));

        if margin > 0.05

```

```

xfjumpup=2.5*xf;
xf=xfjumpup;

xfnew=xf/2;
l=xf-xfnew; %==xf/2
length = ceil(l*size(A,1));
for i = 1:Nsquares;
    x=ceil(rand*size(A,1)+offx);
    y=ceil(rand*size(A,2)+offy);
    counter=0;
    for s = 1:length;
        for t = 1:length;
            mx=x-floor(length/2)+s;
            my=y-floor(length/2)+t;
            if Matrix(mx,my)<150;
                counter=counter+1;
            end
        end
    end
    P(i)=counter;
end
data=P';
bimreal=mode(data);
boxar=length^2;

h2=hist(P,2500);

if boxar==bimreal
    isbimo=1;
    h2(1,2500)=0;
    [m,n1]=max(h2);
else
    isbimo=0;
    [m,n1]=max(h2);
end

xf=xfnew;

else
end
else
    continue
end

end
end

%%%%%%%%%%%%%%%%%%%%%%%%%%%%%%%%%%%%%%%%%%%%%%%%%%%%%%%%%%%%%%%%%%%%%%%%
%%%%%%%%%%%%%%%%%%%%%%%%%%%%%%%%%%%%%%%%%%%%%%%%%%%%%%%%%%%%%%%%%%%%%%%% Display results %%%%%%%%%%%%%%%%%%%%%%%%%%%%%%%%%%%%%%%%%%%%%%%%%%%%%%%%%%%%%%%%%%%%%%%%%
%%%%%%%%%%%%%%%%%%%%%%%%%%%%%%%%%%%%%%%%%%%%%%%%%%%%%%%%%%%%%%%%%%%%%%%%

l1=l*size(A,2)*scale;
disp('Value of required box width is (in nanometers): ')
disp(ceil(l1))

```

```

disp('Particle area fraction (where particles are represented by black
pixels): ')
disp(af)

hist(P,2500), xlabel('# of particle pixels in a box'), ylabel('# of
occurrences')

%%%%%%%%%%%%%%%%%%%%%%%%%%%%%%%%%%%%%%%%%%%%%%%%%%%%%%%%%%%%%%%%%%%%%%%%
%%%%%%%%%%%%%%%%%%%%%%%%%%%%%%%%%%%%%%%%%%%%%%%%%%%%%%%%%%%%%%%%%%%%%%%% Manual Mode %%%%%%%%%%%%%%%%%%%%%%%%%%%%%%%%%%%%%%%%%%%%%%%%%%%%%%%%%%%%%%%%%%%%%%%%%
%%%%%%%%%%%%%%%%%%%%%%%%%%%%%%%%%%%%%%%%%%%%%%%%%%%%%%%%%%%%%%%%%%%%%%%%

logi = input('Automatic iteration completed. Continue to manual mode? (Y/N)
:', 's');

while strcmpi(logi, 'y') == 1;
    xf1 = input('Enter desired square width in nanometers: ');
    xf = xf1/scale1;
    Nsquares = input('Enter number of random squares to use for analysis:
');

    s2=size(A,1)*size(A,1);

    %%%%%%%%%%%%%%%%%%%%%%%%%%%%%%%%%%%%%%%%%%%%%%%%%%%%%%%%%%%%%%%%%%%%%%%%%
    %%%%%%%%%%%%%%%%%%%%%%%%%%%%%%%%%%%%%%%%%%%%%%%%%%%%%%%%%%%%%%%%%%%%%%%%% Calculate box size for manual input%%%%%%%%%%%%%%%%%%%%%%%%%%%%%%%%%%%%%%%%%%%%%%%%%%%%%%%%%%%%%%%%%%%%%%%%
    %%%%%%%%%%%%%%%%%%%%%%%%%%%%%%%%%%%%%%%%%%%%%%%%%%%%%%%%%%%%%%%%%%%%%%%%%

    length = ceil(xf*size(A,2));
    for i = 1:Nsquares;
        x=ceil(rand*size(A,1))+offx;
        y=ceil(rand*size(A,2))+offy;
        counter=0;
        for s = 1:length;
            for t = 1:length;
                mx=x-floor(length/2)+s;
                my=y-floor(length/2)+t;
                if Matrix(mx,my)<150;
                    counter=counter+1;
                end
            end
        end
        P(i)=counter;
    end
    data=P';
    bimreal=mode(data);
    boxar=length^2;

    h1=hist(P,2500);

    if boxar==bimreal
        isbimo=1;
        h1(1,2500)=0;
        [m,n1]=max(h1);
    else
        isbimo=0;
        [m,n1]=max(h1);
    end
end

```

```

zerocount=0;
for j=1:size(P,2);
    if P(j)==0;
        zerocount=zerocount+1;
    end
end

%%%%%%%%%%%%%%%%%%%%%%%%%%%%%%%%%%%%%%%%%%%%%%%%%%%%%%%%%%%%%%%%%%%%%%%%
%%%%%%%%%%%%%%%%%%%%%%%%%%%%%%%%%%%%%%%%%%%%%%%%%%%%%%%%%%%%%%%%%%%%%%%% Display results %%%%%%%%%%%%%%%%%%%%%%%%%%%%%%%%%%%%%%%%%%%%%%%%%%%%%%%%%%%%%%%%%%%%%%%%%
%%%%%%%%%%%%%%%%%%%%%%%%%%%%%%%%%%%%%%%%%%%%%%%%%%%%%%%%%%%%%%%%%%%%%%%%

hist(P,2500), xlabel('# of particle pixels in a box'), ylabel('# of
occurrences')
disp('Number of boxes with a zero black-pixel count: ')
disp(zerocount)
logi = input('Enter parameters again? (Y/N) :', 's');

end

end

function [result,percents]=mode(x)
%MODE
% Finds the mode of a 2d matrix.
% [result perecents]=mode(matrix)
% where result is the mode of the matrix
% and percents is the amount of difference within the mode
% ORIGINALLY TABULATE.m by B.A. Jones
% Changes by David Li, UCSB updated: 4-8-2004

[Mo,No]=size(x);
x=reshape(x,Mo*No,1);

y = x(find(~isnan(x)))+1;

maxlevels = max(y(:));
minlevels = min(y(:));
[counts values] = hist(y,(minlevels:maxlevels));
total = sum(counts);

result=-1;
index=1;
while(counts(index) ~= max(counts))
    index=index+1;
end
result=values(index)-1; %disp(result);

percents =counts(index)/total;

end

```

References

1. H. S. Share and D. L. Burris, *Polymer*, 2010, Vol. 51, pp. 719-729.

APPENDIX 2

Compilation of Articles by the Authors on
In-Situ Gas-Liquid Process

SYNTHESIS OF DIE-CASTABLE NANO-PARTICLE REINFORCED ALUMINUM MATRIX COMPOSITE MATERIALS BY IN-SITU GAS-LIQUID REACTIONS

Cecilia Borgonovo, Makhlouf M. Makhlouf
Advanced Casting Research Center
Worcester Polytechnic Institute, Worcester, USA

ABSTRACT

Nano-particle reinforced aluminum matrix composites are attractive engineering materials for many automotive and aerospace applications because they exhibit numerous desirable mechanical and thermal properties, such as high specific strength, hardness, stiffness, and resistance to creep and thermal degradation. Unfortunately, making these materials is not easy and most of the methods that have been developed so far for their synthesis are either not robust, inefficient, or not cost effective. In this publication, we report on the synthesis of die-castable aluminum-aluminum nitride nano-composite materials by the reaction of a nitrogen-containing gas with molten aluminum-lithium alloy. Specifically, we report on the effect of (1) the lithium content of the alloy, (2) the composition of the reactive gas, and (3) the reaction time on (a) the amount, (b) the average size, and (c) the average cluster size of the aluminum nitride reinforcing particles; as well as (d) the hardness and (e) the thermal stability of the composite material.

KEYWORDS

Aluminum, lithium, nano-composites, in-situ process, nitrogen-bearing gas, aluminum nitrides.

INTRODUCTION

Global efforts are continually being made in order to improve fuel economy in the automotive and aerospace industries. Fuel efficiency standards require manufacturers to increase fuel efficiency by 5% per year starting from 2012. Nano-particle reinforced metal matrix composites, particularly those based on an aluminum alloy matrix allow decreasing the weight of the vehicle while enhancing the strength and stiffness of components, which leads to significant improvements in the fuel efficiency of the vehicle. Traditionally, such materials are produced by powder metallurgy [1], mechanical alloying [2], spray deposition [3], and several casting methods that involve stirring particles of the reinforcing phase in the molten metal alloy [4] or infiltration methods [5]. Since these conventional fabrication techniques involve adding exogenous reinforcing particles to the metal alloy, they suffer from several drawbacks including contamination, interfacial reactions between the particles and the alloy matrix, and clustering of the particles due to their poor wettability by the matrix alloy [3,6]. A class of novel nano-composite material fabrication processes in which the particles are formed within the parent phase (in-situ) by means of a chemical reaction has been recently developed. Belonging to this class is the gas injection process, which is based on introducing a reactive gas into a molten metal to cause a chemical reaction that produces the reinforcing particles [6]. Uniform particle distribution, lack of contamination,

and clean interfaces between the reinforcing particles and the matrix can be achieved by this process, and the process is easily scalable and inexpensive. The present study focuses on the synthesis of Al-AlN nano-composites, which has received considerable attention in recent years [7-10]. Aluminum nitride has low density (3.026 g/cm^3), low coefficient of thermal expansion ($4.5 \times 10^{-6} \text{ K}^{-1}$ in the temperature range 293-673 K), and good thermal conductivity ($110\text{-}170 \text{ W.m}^{-1}\text{.K}^{-1}$), which makes it an attractive material for electronic substrates and optoelectronic parts. Moreover, AlN is much more wettable by aluminum than other compounds, such as Al_2O_3 , is chemically stable and does not decompose or in aluminum. However, and despite their many attractive characteristics, Al-AlN nanocomposites have not been widely used because of the high cost of AlN nano-powders. Zheng and Reddy [7-10], Hou et al. [11], Huashun et al. [12] and others [13,14,15] have demonstrated the feasibility of synthesizing Al-AlN nanocomposites by the gas injection process. The mechanism of AlN formation has also been discussed, as well as the detrimental effect of oxygen on the nitridation of aluminum [8]. In this paper, we report on the synthesis of die-castable aluminum-aluminum nitride nano-composite materials by the reaction of a nitrogen-containing gas with molten aluminum-lithium alloy. Specifically, we report on the effect of (1) the lithium content of the alloy, (2) the composition of the reactive gas, and (3) the reaction time on (a) the amount, (b) the average size, and (c) the average cluster size of the aluminum nitride reinforcing particles; as well as (d) the hardness and (e) the thermal stability of the composite material.

MATERIALS AND PROCEDURES

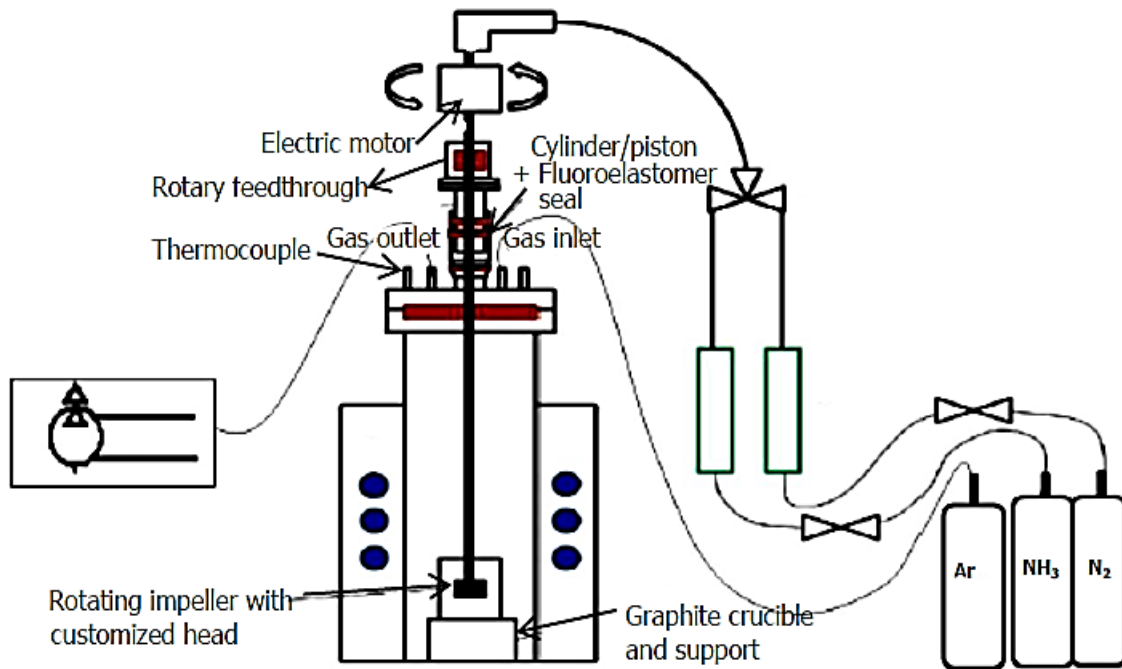


Fig. 63. Apparatus used to synthesize Al-AlN composite materials.

Fig. 1 shows a schematic representation of the apparatus used in the gas injection process. It consists of a mullite retort placed inside a resistance furnace. A graphite crucible was used to melt the alloy. The gas bubbling impeller has a customized head with 24 holes each 3 mm in diameter. The rotor head was printed from a ceramic powder (80% Al₂O₃- 20% SiO₂) and coupled to an Inconel 601 tube by means of a large-pitched thread that is sealed with a high temperature cement. Al-5 wt% Li master alloy was used as the starting material and high purity Al (99.9999%) was added when dilution of the master alloy was required. The total weight of the charge was about 250g. Nitrogen gas (GRADE 4) and anhydrous ammonia were used as reactive gases. Drierite traps, moisture traps, and oxygen traps were used to purify the nitrogen-bearing gases so that the impurities are at the parts-per-billion (ppb) level. The reaction temperature was kept constant at 1000 °C, and the reaction time was varied between 2 and 4 hours. The gas flow rate [0.4 and 0.6 liter per min (lpm)] was maintained by a flow meter. After the desired reaction time, the melt was left to cool down to room temperature in the furnace under an inert atmosphere.

Table 1 summarizes the design of experiments. After each run, samples from the resulting composite material were removed and etched with diluted 10 vol% NaOH. The microstructure of each sample was examined by a scanning electron microscope (SEM) coupled with an energy dispersive X-ray spectrometer. The samples were also examined by X-ray diffraction (XRD). A Matlab-based computer program [16] was optimized and used to quantitatively characterize the microstructure, including calculating the volume fraction of the AlN particles, the mean free space length, the average AlN particle size, and the average AlN cluster size. The free space length is a scale-dependent measure of particle distribution and can be related to the other microstructural variables. It decreases with increasing volume percentage of particles, decreasing particle size and cluster size. The hardness of the composite materials was measured with the Rockwell B scale utilizing a total load of 100Kgf. On average 15-20 hardness measurements were made on each sample. Thermal stability of the AlN particles was assessed by holding the samples at 450°C for 24 hours in an electrical box furnace and then measuring the increase in size of the AlN particles.

Table 4. Design of Experiments.

Experiment #	Alloy composition	Gas composition	Processing time
1	Al-5 wt% Li	N ₂	2
2	Al-5 wt% Li	N ₂	4
3	Al-5 wt% Li	N ₂ / NH ₃ =1/1	2
4	Al-5 wt% Li	N ₂ / NH ₃ =1/1	4
5	Al-5 wt% Li	NH ₃	2
6	Al-5 wt% Li	NH ₃	4
7	Al-2.5 wt% Li	N ₂	2
8	Al-2.5 wt% Li	N ₂	4

9	Al-2.5 wt% Li	N ₂ / NH ₃ =1/1	2
10	Al-2.5 wt% Li	N ₂ / NH ₃ =1/1	4
11	Al-2.5 wt% Li	NH ₃	2
12	Al-2.5 wt% Li	NH ₃	4

RESULTS AND DISCUSSION

Microstructure characterization – Table 2 shows the quantitative results of the microstructure characterization. No AlN was detected in the samples when N₂ gas is injected in Al-5 wt% Li alloy for 2 hours. When the processing time was increased to 4 hours, XRD analysis (Fig. 2) shows the presence of AlN. Both the quantitative analysis and the micrograph (Fig. 3) reveal a uniform distribution of fairly small AlN particles (~600nm) in the alloy matrix. When ammonia was mixed with nitrogen, the volume of AlN particles that formed increased after 2 and 4 hours processing time compared to the case when only N₂ gas was used and the average particle size was around 400 nm. However, some clustering of the AlN particles occurred when the gas mixture was injected for 2 hours, but the average cluster size was relatively small – around 1300 nm as seen in Fig. 4. For 4 hours processing time, the average particle size remains more or less the same, but the average cluster size slightly increases to 1500 nm as seen in Fig. 5. Further increase in the volume of AlN particles occurred when ammonia only is used as the reactive gas. In this case, 48 vol% of AlN particles formed after processing for 4 hours. The microstructure appears to be very homogeneous for both processing times (Figs. 6 and 7). Clustering seems to be significantly diminished, the average cluster size is reduced to around 1µm, and the average particle size is also reduced to 300nm.

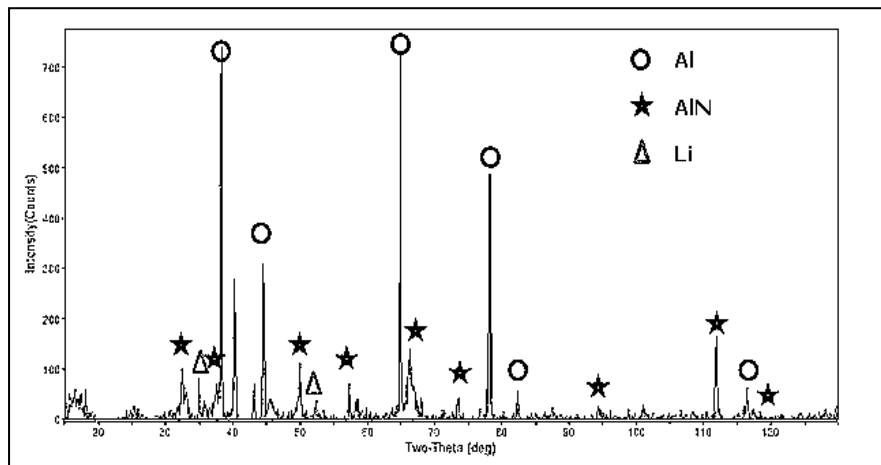


Fig. 64. XRD pattern of the Al-AlN composite produced by Experiment #2.

Table 5: Microstructure parameters of the composite materials processed according to Table 1.

Experiment #	Volume fraction (%)	Mean free space length (nm)	Average particle size (nm)	Average cluster size (nm)
1	-	-	-	-
2	6.2%	1890 nm	643 nm	1540 nm
3	9.5%	1723 nm	489 nm	1327 nm
4	26%	1262 nm	453 nm	1552 nm
5	21%	1649 nm	274 nm	966 nm
6	48%	861 nm	312 nm	1114 nm
7	-	-	-	-
8	-	-	-	-
9	-	-	-	-
10	7.4%	2670 nm	655 nm	924 nm
11	12.8%	2416 nm	409 nm	1012 nm
12	31%	1635 nm	293 nm	785 nm

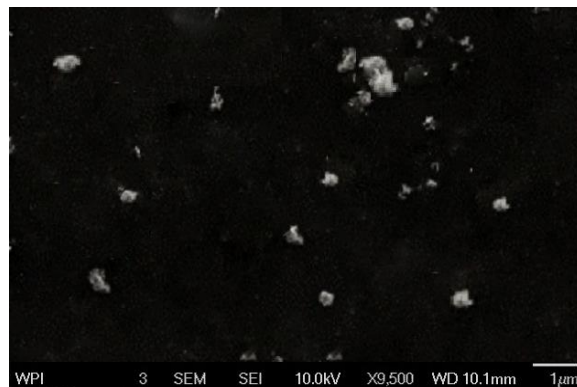


Fig. 65. SEM image of the Al-AIN composite produced by Experiment #2.

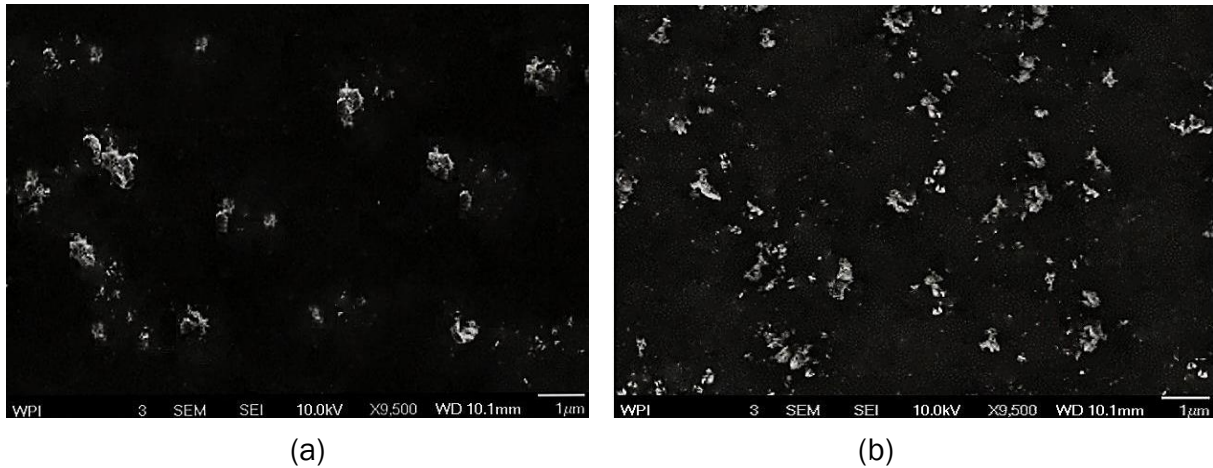


Fig. 66. SEM image of the Al-AlN composite produced by (a) Experiment #3, and (b) Experiment #4.

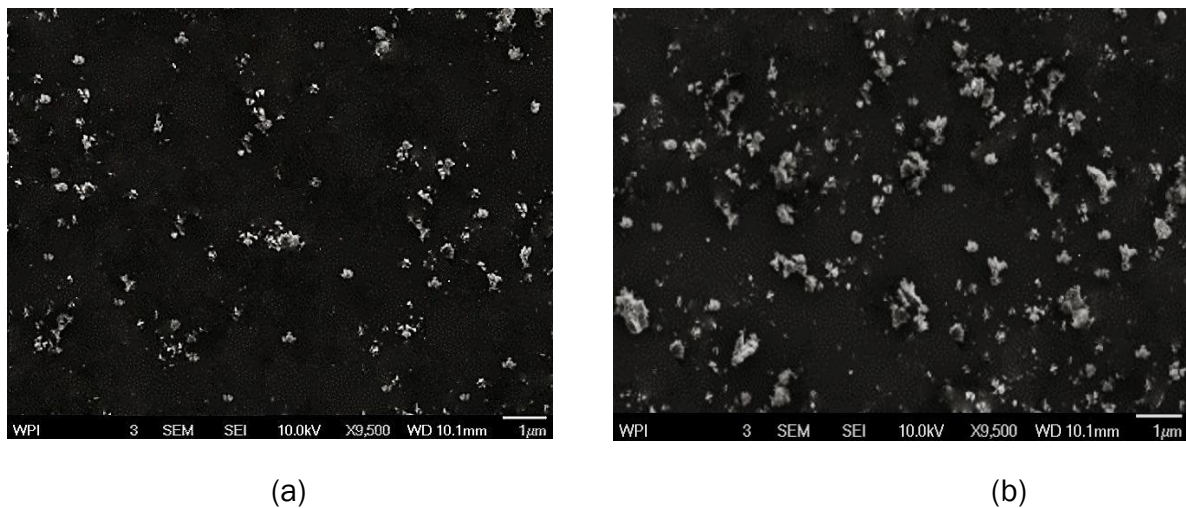


Fig. 67. SEM image of the Al-AlN composite produced by (a) Experiment #5, and (b) Experiment #6.

In the experiments performed with the 2.5 wt% Li alloy, no AlN particles were detected when nitrogen only was used as reactive gas for 2 or 4 hours. Also, no AlN particles were found when the mixture of nitrogen and ammonia gases was injected in the alloy for 2 hours; however, when the processing time was 4 hours, around 7 vol% AlN was formed as seen in Fig. 6. This amount is about four times less than the amount that formed when the Al-5 wt% Li alloy was used. Also, the large mean free space length of this composite material (2670 nm) reveals that clustering is more severe than in previous experiments, despite the fact that the average cluster size is less than 1 μm and the average particle size is around 650 nm. When ammonia is used with the 2.5 wt% Li alloy, the average AlN particle size is decreased to around 400 nm for 2 hours processing time, and 300nm for the 4 hours processing time. The volume fraction of AlN is 31% for the 4 hours processing time, which is almost 30% less than when the 5 wt% Li alloy is used. Localized clustering can still be observed (See Figs. 7 and 8), but the average cluster size is around 700 nm.

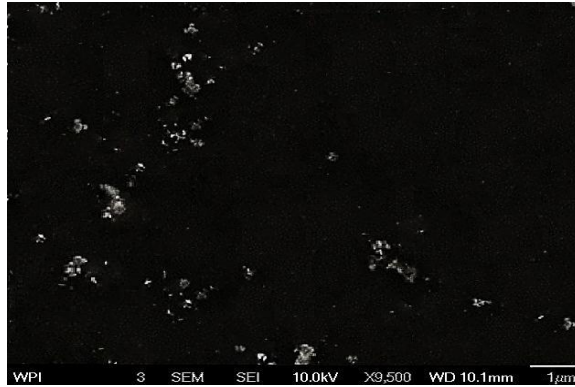
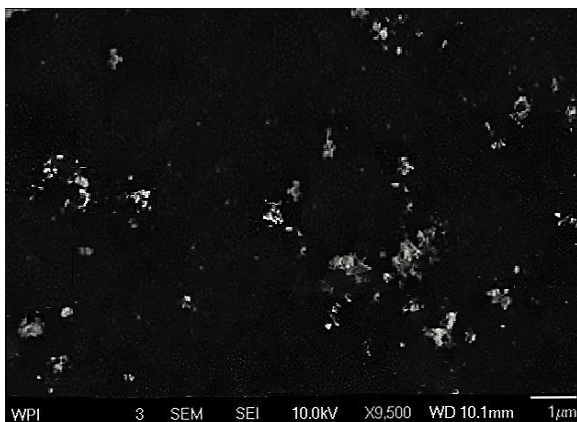
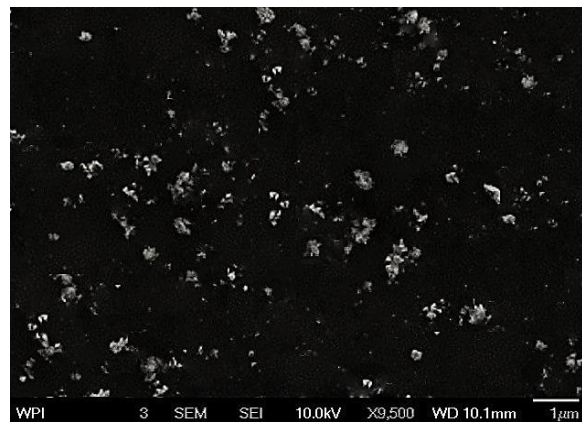


Fig. 68. SEM image of the Al-AIN composite produced by Experiment #10.



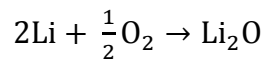
(a)



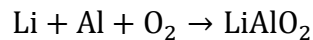
(b)

Fig. 69. SEM image of Al-AIN composite produced by (a) Experiment #11, and (b) Experiment #12.

The role of Li in aluminum nitridation has been investigated by Scholz and Greil [17]. They indicate that Li may act as an “oxygen-getter” to locally lower the oxygen content in aluminum and allow the nitridation reaction, which competes with aluminum oxidation, to take place. According to phase equilibrium calculations in the Al-Li-O-N system, Li combines with oxygen to form Li_2O at low oxygen levels and LiAlO_2 at higher oxygen levels according to reactions (1) and (2).



(1)



(2)

Aluminum nitridation may also occur because of the ability of Li to remove the gaseous reaction products from the reaction site so that equilibrium conditions are never achieved. The continuous flow of the nitrogen-bearing gas in the furnace chamber removes the evaporating species (Li and Li_2O) from the reaction chamber, thus maintaining non-equilibrium conditions that generate very high mass flow of volatilizing Li. Therefore, the high partial pressure of the Li-based vaporized species in the furnace’s environment causes nitridation of aluminum on the surface of the melt first. Channels in the aluminum-lithium

melt derived from the rising nitrogen bubbles and the stirring action of the impeller are probably responsible for nitridation of the bulk of the metal.

Hardness and thermal stability – Fig. 8 shows the measured hardness values of the composite materials shown in Table 2. The hardness measurements made on the samples produced with the 5 wt% Li alloy have an error range of 14%, while hardness measurements made on the samples produced with the 2.5 wt% Li alloy have an error range of 20%. This is most likely due to “macro” agglomeration, i.e. particles, and also clusters, located on interconnected paths so as to create a relatively large mean length of free space. Accordingly, it is possible that during measuring the hardness, the indenter has a higher tendency to hit areas of the metal matrix where there are almost no particles. Notice how the hardness values dramatically increase for the materials produced in Experiments #6 and #12. This is because of the high volume fraction of AlN particles in these materials.

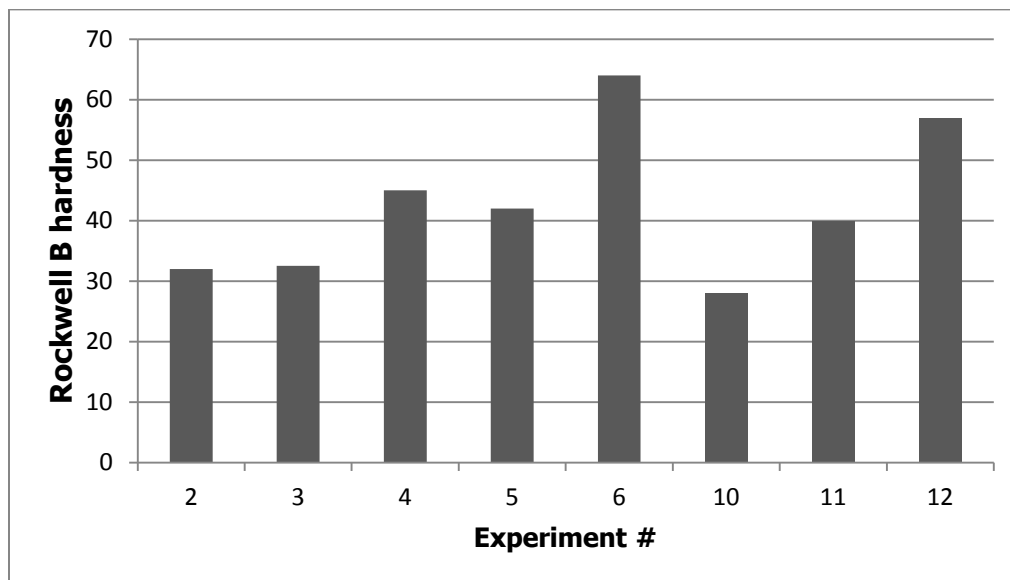


Fig. 70. Measured hardness of the Al-AlN composite materials shown in Table 2.

Thermal stability – The thermal stability of the Al-AlN composite materials was assessed by measuring the increase in size of the AlN particles after the samples were maintained at 450°C for 24 hours. In all samples, the average particle size did not change ($\pm 5\%$ accuracy) except for the sample produced in Experiment #2 in which the average AlN particles size increased by about 14%. This sample will be further analyzed in order to find the reason for this behavior.

SUMMARY AND CONCLUSIONS

- Al-AlN composite material was synthesized by the reaction of a nitrogen-containing gas with molten aluminum-lithium alloy.
- The effect of different lithium levels in the molten aluminum alloy, gas composition, and processing time on the structure of the composite material was investigated.

- The average size of the AlN particles was found to be in the sub-micron range and the average size of the AlN clusters was found to be around 1 μm .
- Lithium in the melt acts as a catalyst for the aluminum nitridation reaction and results in composites with a higher volume fraction of AlN.
- Ammonia as the reactive gas results in composites with a higher volume fraction of AlN particles. Also, as expected, longer processing times (4 hours compared to 2 hours) result in composites with a higher volume fraction of AlN.
- Particle clustering appears to be more severe for the 2.5wt% Li alloy than in the 5 wt% Li alloy although the average cluster size is smaller.
- Hardness measurements show a significant increase when ammonia is used as the reactive gas and for longer processing times.
- The Al-AlN composites produced with this in-situ method have excellent thermal stability.

ACKNOWLEDGMENTS

The authors gratefully acknowledge the member companies of the Advanced Casting Research Center (ACRC) for their support of this work, and for their continued support of research focused on the science and technology of metal casting at Worcester Polytechnic Institute.

REFERENCES

1. Z.Y. MA, Y. LIA, Y. LIANG, L.F. ZHENG and S.C. TJONG, Mater. Sci. Eng. A219, (1996), p.229.
2. D.L. ZHANG, J. LIANG and J. WU, Mater. Sci. Eng. A375–377, (2004), p.911.
3. P.M. AJAYAN, L.S. SCHADLER and P.V. BRAUN, Nanocomposite Science and Technology. Wiley-VCH, Weinheim (2003).
4. L. XIAODAN, Z. YUCHUN, Q. FENG and Z. HAIXI, Preparation of Metal Matrix Composites Reinforced with Nano-SiC Particles by Stir Casting Technique.Proc.139th Annual Meeting and Exhibition TMS, Seattle (2010).
5. S. GIERLOTKA, Solid State Phenom. 101-102, (2005), p.157.
6. C.C. KOCH, Nanostructured Materials: Processing, Properties, and Applications. William Andrew, Norwich (2006).
7. Q. ZHENG, B. WU and R.G. REDDY, Adv. Eng. Mater. 5, (2003), p.167.
8. Q. ZHENG and R.G. REDDY, Effects of Oxygen Impurities on In-situ Formation of AlN-Al Composites from Nitrogen Bubbling Gas, Affordable Metal Matrix Composites for High Performance Applications II. Edited by A.B. Pandey, K.L. Kendig, J.J Lewandowski and S.R. Shah, TMS, Warrendale (2003), p.125.
9. Q. ZHENG and R.G. REDDY, J. Mater. Sci. 39, (2004), p.141.
10. Q. ZHENG and R.G. REDDY, High Temp. Mater. Proc. 22, (2003), p.63.
11. Q. HOU, R. MUTHARASAN and M. KOCZAK, Mater.Sci.Eng. A195 (1995), p.121.
12. Y. HUASHUN, J.D. KIM and S.B. KANG, Mater.Sci.Eng. A386, (2004), p.318.

13. S. TYAGI, Q. ZHENG and R.G. REDDY, In Situ Synthesis of AlN Reinforced Magnesium Alloy Composites Using Gas Bubbling Method, Aluminum 2004, edited by S. K. Das, TMS, Warrendale (2004), p.63.
14. C. BORGONOVO and D. APELIAN, Mater.Sci.Forum 678, (2011), p.115.
15. C. BORGONOVO, D. APELIAN and M.M. MAKHLOUF, JOM-J. Min. Met. Mat. S. 63, (February 2011), p.57.
16. H.S. SHARE and D.L. BURRIS, Polymer 51, (2010), p.719.
17. H. SCHOLZ and P. GREIL, J.Mater.Sci. 26, (1991), p. 669

Aluminum Nanocomposites via Gas Assisted Processing

Cecilia Borgonovo^a and Diran Apelian^b

Metal Processing Institute, WPI, Worcester, MA 01609 USA

^acborgonovo@wpi.edu ^bdapelian@wpi.edu

Keywords: lightweight, nanocomposites, aluminum, magnesium, gas-assisted process, nitridation.

Abstract. Aluminum nitride (AlN) possesses superior thermal and electrical properties and is an ideal candidate for high-temperature, as well as for packaging and optoelectronic applications. Aluminum based composites reinforced with AlN have been manufactured via an in situ gas-assisted process, where nitrogen gas is injected in the molten aluminum at 1273-1323 K. The process is carried out in an inert atmosphere in order to avoid oxygen contamination. Addition of Mg lowered the oxygen content in the melt by forming MgO and thus favoring the nitridation reaction. The reinforcement phase has been detected throughout the casting in two morphologies: pockets of powders and embedded in the microstructure. Particle size formed in the matrix varied from 1- 3 μm to sub-micron scale.

Introduction

Particulate reinforced metal matrix composites have been widely used in modern engineering applications. With the development of nanotechnologies, the particulate size progressively scaled down to the nano-level. Aluminum matrix nanocomposites reinforced with ceramic particles (AlN, Al₂O₃, SiC) are gradually being implemented into production in automotive, electronic or aircraft industries due to their promising mechanical and thermal properties: higher strength, hardness, stiffness, dimensional stability at high temperatures, and creep resistance. However, obtaining a composite material non-susceptible to cracking and whose ductility is retained requires the successful dispersion of the reinforcement phase in the matrix [1]. Numerous attempts have been made to overcome particle agglomeration and to establish an industrially scalable and cost-effective route for the fabrication of nanocomposite materials.

Several near-commercial manufacturing methods have been pursued, such as mechanical alloying, powder metallurgy, infiltration techniques and spray deposition. All these techniques involve the addition of ceramic reinforcements to the matrix materials (*ex-situ processes*), which may be in molten or powder form. However, they are expensive and do have their own limitations, especially when the reinforcement size is in the nano-scale range. Agitation

techniques are cost-effective, but agglomeration due to Van der Waals forces cannot be avoided. Surface contamination also affects the reliability of ex-situ techniques through interfacial reactions and poor wettability between matrix and reinforcement. Particle dispersion via ultrasonic processing has been achieved but the process suffers from scalability issues.

A class of novel composites, in which the reinforcements are synthesized by chemical reactions (*in-situ processes*), addresses the challenges associated with manufacturing of nanocomposites. Compared to ex-situ methods, these in-situ processes exhibit cleaner and thermodynamically stable interfaces, resulting in less degradation at elevated-temperatures and strong interfacial bonding. Moreover, the in-situ formed particles are finer in size and their distribution in the matrix is uniform.

Among the wide range of in-situ techniques, the synthesis of nitride particles by means of a gas-assisted reaction, patented by Koczak and Kumar [2], has shown promise. Aluminum nitride is a refractory compound characterized by attractive properties such as high thermal conductivity, high electrical resistance, low dielectric constant, and a thermal expansion coefficient similar to silicon [3,4]. Hou et al. [3] have been able to manufacture aluminum matrix composites reinforced with AlN with a diameter smaller than 0.1 μm . Zheng et al. [5] have converted 14% weight of Mg-Al alloy into aluminum nitrides with a diameter of 400 nm. Tyagi et al. [6] also manufactured aluminum nitrides with a diameter smaller than 1 μm by bubbling ammonia gas in an Mg-Al melt. The composite material is formed in three stages: reactive gas dissociation, synthesis of reinforcing phases and kinetics of their growth [1,7]. Reinforcement particles are created as a result of the intensive exothermic reaction of gas cavities with metal alloying additions, such as Mg, Ti, and Si [1]. Significant advantages of this method are the possibility of applying casting techniques for forming the products [8], and of tailoring the matrix-reinforcement system by selecting reactive gas and alloying elements. However, the gas-assisted reaction process is affected by challenging control of process variables and repeatability issues. In addition, the temperatures necessary for the reaction to occur are high (1000-1300 C° depending on the gas and the matrix) [9,10].

The aim of the present investigation is to highlight the dynamics of aluminum nitridation and the mechanism of nitride formation *via* the injection of nitrogen gas in the melt.

Experimental Details

A stainless steel sealed resistance chamber was evacuated and purged several times with Argon gas (Grade 5, Aimtek). During the heating process, inert atmosphere was maintained by constantly injecting Argon at a flow rate of 0.2 l/min. The ceramic crucible was placed at the bottom of the chamber where the temperature profile is more uniform. Two K-type thermocouples inserted in the furnace walls and inside the crucible were used to monitor the temperature. Once the process temperature (1000 C°) was achieved, a 1.5 mm diameter alumina tube was submerged in the melt and High Purity Nitrogen gas (99.9999% purity, Aimtek) bubbled for 6 to 8 hours through the tube at a flow rate of 0.1 l/min and a pressure of 0.1 MPa. Two high capacity oxygen-and moisture- removal traps were used in series at the gas inlet. Each trap had the capability to lower the oxygen content to less than 1 ppb and the moisture level to less than 10 ppb. Alloy compositions selected for the experiments are 100wt% Al and Al-15wt% Mg. Each casting involved the melting of 150 g of metal previously ultrasonically cleaned for 20 minutes. X-Ray Diffraction (XRD) analysis was also performed in order to detect the presence of nitrides and secondary phases. Field Emission Gun SEM has been employed for microstructure observation, Energy Dispersive X-ray (EDS) microanalysis and X-ray mapping.

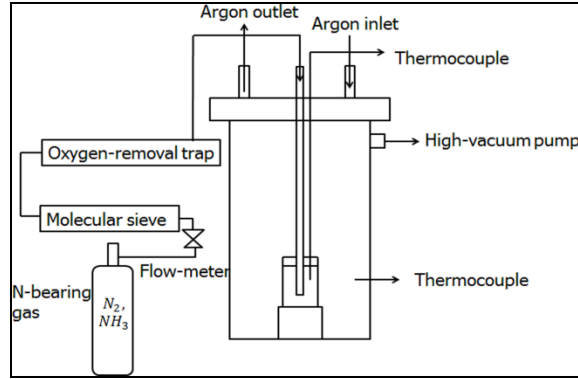
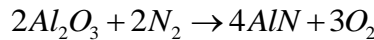


Fig.71: Experimental set-up.

Results and Discussion

No AlN were detected in the matrix when pure Al was used as the parent material. Such result can be attributed to the presence of oxygen in the Nitrogen gas, which has a detrimental effect on aluminum nitridation. Oxygen preferentially reacts with aluminum to form aluminum oxide, inhibiting the nitridation reaction [7,10,11]. This has been demonstrated empirically by measuring the time required to form aluminum nitride and the time required to form aluminum oxide, where it has been found that the rate of nitridation of aluminum is several orders of magnitude slower than the rate of its oxidation at any given temperature [11]. Thermodynamic analysis of the equilibrium reaction (Eq.1) confirms the preferential formation of Al₂O₃ versus AlN. The Gibbs free energy calculation (Eq.2) shows that the permissible oxygen partial pressure for the nitridation reaction P_{O_2} at 1000°C is around 10⁻¹⁹ Pa and directly proportional to the process temperature T .



(1)

$$\Delta G = 2,057,400 - 184.4T \cong -RT \ln \left(\frac{P_{O_2}}{P_{atm}} \right)^3 \rightarrow P_{O_2} = 18.9 - \frac{82,487.4}{T} \quad (2)$$

This very low oxygen content is not achievable with commercially available nitrogen gases. Moreover, the processing temperature for aluminum alloys should not exceed 1000°C. This is mainly dictated by the cost of energy and deterioration of the furnace furniture. Therefore, efforts have been made to minimize oxygen in the reaction chamber by passing the stream of nitrogen gas through traps filled with deoxidizing materials (such as Cu and Mn) and evacuating the furnace chamber prior to melting. Yet, oxygen in the system remains high enough to render the current technology inefficient for the synthesis of Al-AlN composite materials through direct nitridation of aluminum.

This suggests that nitridation of aluminum requires the presence of a catalyst such as Mg. Several publications refer to this mechanism as more likely to be responsible for nitride formation than direct nitridation [5,10,12]. The addition of 15% Mg to the aluminum matrix was investigated and resulted in the synthesis of a consistent amount of aluminum nitrides.

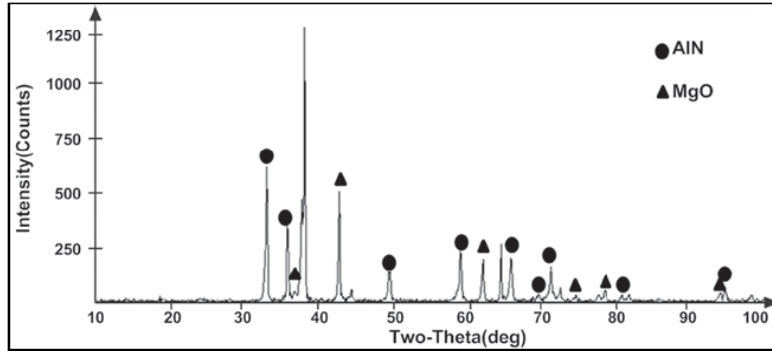


Fig.72: XRD pattern of the upper part of the crucible for Al-15% wt. Mg.

XRD analysis (Fig.2) of the upper part of the crucible confirms strong peaks for AlN along with peaks for MgO (periclase). SEM analysis shows the presence of AlN throughout the length of the resultant casting. AlN particles have been found in two different morphologies: (i) embedded in the microstructure in the lower section of the casting (Fig. 3), and (ii) as pockets of powder in the upper section of the casting (Fig. 4). In the powder phase, MgO is located on the AlN particles and tightly connected with them. The size of AlN is $\sim 1 \mu\text{m}$ for AlN embedded in the microstructure and in the submicron range (around $0.4 \mu\text{m}$) in the powder phase. Size control as well as optimized nitride distribution along the casting still remains an issue and it is currently being studied at WPI.

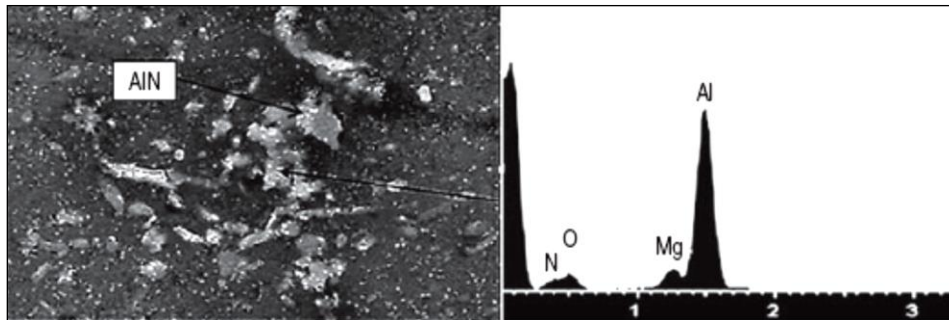


Fig.73: SEM image and EDS spectrum of AlN embedded in the matrix in the lower section of the casting. Al-15% wt. Mg matrix.

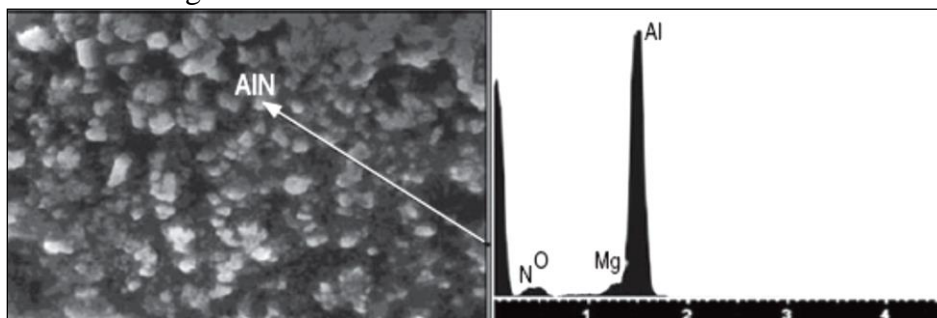


Fig.74: SEM image and EDS spectrum of pockets of AlN and MgO powder in the lower section of the casting. Al-15% wt. Mg matrix.

The catalytic action of Mg can be explained as follows. At high temperatures, Mg vaporizes (Eq.3) and acts as an “oxygen-getter”. It combines with oxygen to form MgO (Eq.4) and thus locally lowers the partial pressure of the residual oxygen in the nitriding gas.



$$P_{\text{O}_2} = \gamma_{\text{Mg}}^{-2} x_{\text{Mg}}^{-2} \exp\left(\frac{2\Delta G_3 + \Delta G_4}{2RT}\right)$$

(5)

Depending on the temperature and the concentration of Mg, the equilibrium partial pressure of O₂ is given by Eq. 5, where γ_{Mg} is the activity coefficient of Mg, x_{Mg} is the Mg concentration, ΔG_3 and ΔG_4 are the standard Gibbs energy changes for reactions 3 and 4, respectively. From thermodynamic data reported in the literature, the partial pressure of the residual oxygen for 15 wt.% Mg in aluminum matrix is in the range of 0.1 Pa (versus 10⁻¹⁹ of pure Al matrix), which can be achieved by commercial deoxidizing traps.

Concluding Remarks

Aluminum nitridation via gas-assisted nitridation of aluminum is feasible. The in-situ route to manufacture nanocomposites has the potential to be a commercial process where scalability, homogeneous distribution and cost-effectiveness are important criteria. AlN particles, whose thermal and electrical properties are exceptional, have been successfully synthesized. They have been observed throughout the bulk and they are present in two morphologies: (i) embedded in the matrix, and (ii) as pockets of powder with MgO. The size of AlN ranges from 0.4 μm to about than 1 μm. The catalytic action of Mg as “oxygen-getter” has also been confirmed by the absence of AlN in the pure aluminum matrix, and by MgO tightly connected to the nitride phase. Mg lowers the local oxygen partial pressure in the melt, allowing aluminum nitridation to occur.

The control of AlN particle size and the kinetics of the nitridation process need further study. This work is continuing to establish the mechanisms to address the kinetics of the reaction in order to enable us to attain particles that are in the nano-range.

Acknowledgments

The authors gratefully acknowledge the member companies of the Advanced Casting Research Center for their support of this work, and for their continued support of research focused on the science and technology of metal casting at Worcester Polytechnic Institute.

References

- [1] S.C. Tjong, Z.Y. Ma, *Mat. Sci. Eng.* Vol. 29 (2000), pp. 49-113.
- [2] M.J. Koczak and K.S. Kumar, U.S. Patent 4,808,372.370. (1989)
- [3] Q. Hou, R. Mutharasan and M. Koczak, *Mat. Sci. Eng.* Vol. A195 (1995), pp. 121-129.
- [4] J. Haibo, K. Chen, Z. Heping, S. Agathopoulos, O. Fabrichnaya, and J.M.F. Ferreira, *J. Crystal Growth*, Vol. 281 (2005), pp. 639–645.
- [5] Q. Zheng and R. Reddy, *Metall. Mater. Trans.* Vol. 34B (2003), pp. 793-805.
- [6] S.Tyagi, Q.Zheng and R. Reddy, *Aluminum 2004*, edited by S. K. Das, TMS, Warrandale,

(2004), pp. 63-72.

[7] Q. Zheng and R. Reddy, *Adv. Eng. Mater.* Vol. 5 No. 3 (2003), pp. 167-173.

[8] M.K.Prenkumar and M.G.Chu, *Mat. Sci. Eng.* Vol. A202 (1995), 172-178.

[9] Q. Zheng and R.G. Reddy, *Affordable Metal Matrix Composites for High Performance*

Applications II, ed. A.B. Pandey, K.L. Kendig, J.J. Lewandowski, and S.R. Shah (Warrendale,

PA: TMS, 2003), pp. 125–134.

[10] Q. Zheng and R.G. Reddy, *J. Mater. Sci.* Vol. 39 (2004), pp. 141–149.

[11] H. Scholz and P. Greil, *J. Mater. Sci.* Vol. 26 No. 3 (1991), pp. 669–677.

[12] M. I. Pech-Canul, R.N. Katz and M. M. Makhlof, *Metall. Mater. Trans.* Vol. 31A (2000), pp. 565-573.

In-situ Manufacturing of Nano-Particle Reinforced Metal Matrix Composites

C. Borgonovo

Advanced Casting Research Center, Worcester Polytechnic Institute, Worcester, Massachusetts

M.M. Makhlof

Advanced Casting Research Center, Worcester Polytechnic Institute, Worcester, Massachusetts

ABSTRACT

Aluminum matrix nano-particle composite materials exhibit promising mechanical and thermal properties such as high specific strength, hardness, stiffness, and resistance to creep and thermal degradation. Unfortunately, processing these materials is not easy and numerous attempts have been made to overcome the typical issues associated with their synthesis. These methods include mechanical alloying, powder metallurgy, powder infiltration and spray deposition [1,2]. However, most of these methods are expensive and each one of them has its own limitations. Manufacturing methods that are based on mechanical agitation are cost-effective, but the particles tend to agglomerate because of the excessive Van der Waals forces associated with nano-sized particles [3]. The agglomerated particles can be dispersed by ultrasonic vibrations, but the use of ultrasonic devices on the foundry floor is not practical and the method is not easily scalable [4]. In-situ fabrication of the particles in the metal matrix is an answer to many of these challenges. In this method, the nano-sized particles are formed directly within the melt by means of a chemical reaction between a specially designed aluminum alloy and a gas. In this publication, we report on the synthesis of aluminum-aluminum nitride nano-composites by the reaction of a nitrogen-containing gas with molten aluminum-lithium alloy.

Keywords: lightweight, nanocomposites, aluminum, magnesium, lithium, aluminum nitride, in-situ processing.

INTRODUCTION

Particle-reinforced metal matrix composites, particularly aluminum alloy matrix composites, have been used as structural materials in the aerospace, the automotive, the domestic, and more recently the microprocessor industries. In the automobile industry, aluminum alloy and magnesium alloy composites lower the overall weight of the vehicle and enhance component strength and stiffness. In the microprocessor industry, composite materials improve heat extraction and heat dissipation from critical components thus allowing higher processing speeds and superior performance. Despite these benefits, the large size (typically from a few to several hundred micrometers) of the ceramic reinforcing particles in traditional composite materials increase the tendency of

the material to cracking during mechanical loading, which can lead to premature failure of components. Particle size has an undeniably strong influence on the failure mode, strength, and ductility of composite materials. Therefore, decreasing the size of the ceramic particles to the sub-micrometer range, or even better to the nanometer range, can lead to significant improvements in room temperature mechanical properties as well as enhanced thermal and electrical properties. Moreover, refining the size of the reinforcing particles limits microstructure degradation at high temperature, which is a necessary material property for highly-rated Diesel applications [6]. However, conventional fabrication methods that are based on the addition of particles to the matrix (e.g., mechanical stirring [3], and infiltration techniques [5], powder metallurgy [7,8]) have serious limitations when dealing with nanometer size particles, e.g., particle clustering and particle/matrix interface de-bonding. More recent fabrication methods, such as spray deposition [1], ultrasonic-assisted cavitation [4], and plasma synthesis [9] all suffer from the lack of scalability and cost-effectiveness. On the other hand, in-situ creation of the reinforcing particles within the aluminum matrix has the potential to provide good particle distribution, small particle size, and a clean and thermodynamically stable particle/matrix interface [10]. This process involves synthesizing the ceramic reinforcing nano-particles within the metal alloy by means of a controlled chemical reaction between a suitable gas and a suitable molten metal alloy. The chemical composition of the reinforcing particles that form is dictated by the composition of the reacting gas and molten metal alloy [11-14]. Two alloy systems are used in the current investigation: Al-Mg and Al-Li and a nitrogen-bearing gas – namely nitrogen + anhydrous ammonia – is injected in the molten alloy to form aluminum nitride (AlN) particles. The feasibility of the process is investigated, and the role of (1) the alloy composition, (2) the oxygen content of the reaction atmosphere, and (3) the processing time on the characteristics of the resulting Al-AlN composite material is characterized.

MATERIALS AND PROCEDURES

Two hundred grams of either (1) Al-20 wt.% Mg or (2) Al-Li C460 alloy are ultrasonically cleaned and then placed in a refractory crucible. The crucible is positioned in the stainless steel sealed resistance furnace shown in Fig. 1 and the furnace chamber is evacuated and flushed with Nitrogen gas (Grade 5). This process is repeated three times in order to remove oxygen and any other contaminating agents from the furnace atmosphere. The alloy is heated at a rate of 10°C/min from room temperature to just below its liquidus temperature

of about 600 °C (1,112 °F), and 5 °C/min from such temperature to the process temperature of 1000 °C (1832 °C). K-type thermocouples are placed in the furnace wall and inside the crucible. The reaction gas – either nitrogen or anhydrous ammonia (C-Grade) is then injected into the metal alloy for different processing times through an 80 cm-long × 4 mm diameter alumina tube. The gas flow rate is kept constant at 1 l/min. The crucible is at a 10° angle to the horizontal so that the reaction gas is efficiently dispersed within the molten alloy. High capacity moisture and oxygen traps are used to dry the reaction gas and to minimize the oxygen content before it enters the furnace. Once formed, the composite material ingot is left to cool in the furnace under an inert atmosphere (the cooling rate is about 3°C/min).

Characterization of the microstructure of the composite ingot is performed by X-Ray Diffraction (XRD), Scanning Electron Microscopy (SEM), and Energy Dispersive Spectroscopy (EDS). Samples are extracted from locations near the upper and the lower parts of the ingot in order to provide a representative structure and particle distribution along the length of the ingot. Image analysis software (ImageJ) is used to quantify the volume percentage of AlN particles formed in the ingot. Hardness measurements are performed via indentation.

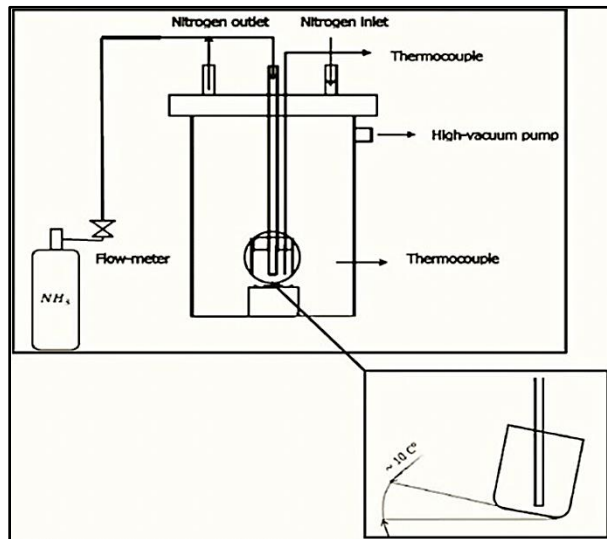


Fig. 1. Schematic representation of the apparatus.

Table 1. Chemical composition (in wt %) of Alloy C460.

Si	Li	Fe	Cu	Mn	Mg	Zn	Ti	Al
0.02	1.16	0.03	2.65	0.26	0.27	0.82	0.02	Bal.

Table 2. Design of Experiments.

Experiment #	Alloy	Gas	Time (hr.)
--------------	-------	-----	------------

1	Al-20wt.%Mg	N ₂	6
2	Al-20wt.%Mg	NH ₃	2 ^d
3	C460	NH ₃	6
4	C460	NH ₃	4

RESULTS

EXPERIMENT # 1

XRD (Fig. 2) and image analyses of the resulting ingot show the formation of AlN particles in the alloy. On average there is about 6 vol.% AlN particles that are equally distributed in the upper and lower sections of the ingot. Small discontinuities that resemble cracks are observed in the ingot. These may be attributed to ineffective mixing of the Al and Mg constituents of the alloy which give rise to composition gradients within the ingot.

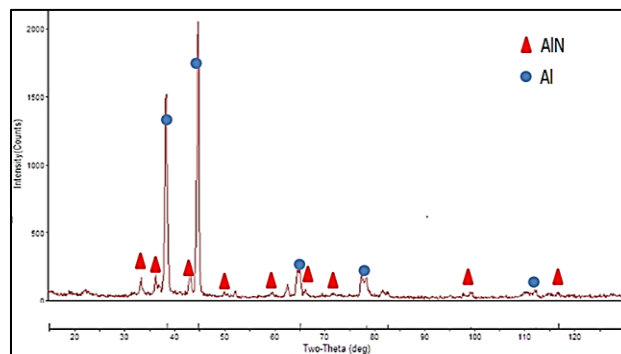


Fig. 2. XRD spectrum of AlN in Al-20 wt.% Mg composite synthesized by means of nitrogen gas.

The AlN particles are detected mainly along these discontinuities (Fig. 3) and their orientation shows that they nucleated on the Mg-rich side of the crack and proceeds towards the Al-rich areas. This confirms the fact that Mg acts as a catalyst for the aluminum nitridation reaction [15,16,17]. The AlN phase appears as a net of interconnected particles with a rod-like and polygonal morphology developing along the discontinuities. The cross section is fairly large, ranging from 1 to 3 μm . The different crystallographic orientation of the particles reveals a powder-like morphology.

^d Processing time has been chosen to be 2 because of the high reactivity of 20 wt% Mg and ammonia has

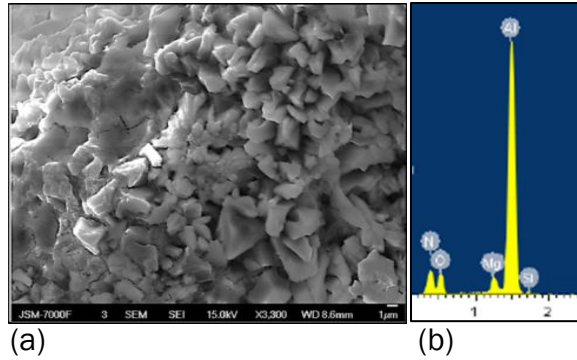


Fig. 3. (a) SEM image of AlN particles along matrix discontinuities, and (b) EDS spectrum of the Al-20wt%Mg-AlN composite synthesized by nitrogen gas.

EXPERIMENT # 2

Fig. 4 shows the XRD pattern obtained from this ingot. In this case, the average conversion to AlN is 17 vol.%.

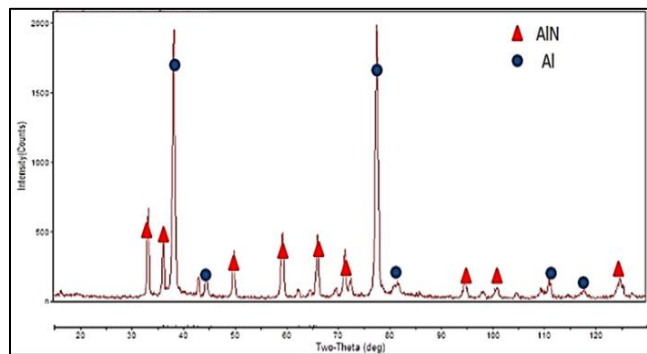


Fig. 4. XRD spectrum of AlN in Al-20 wt.% Mg matrix synthesized by ammonia gas.

Similar to Experiment #1, the unsatisfactory mixing between Mg and Al causes non-homogeneous distribution of the aluminum nitride particles. However, in this case the AlN particles are not located along cracks in the matrix; but rather, they are embedded in the matrix.

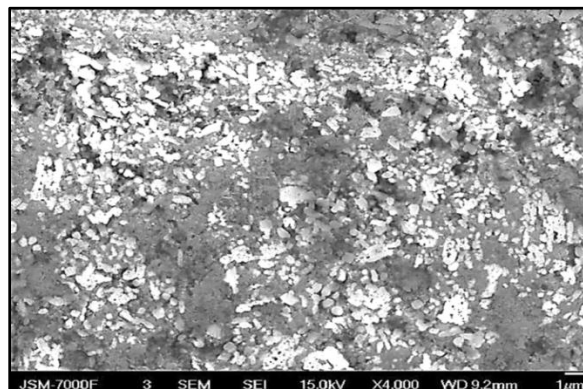


Fig. 5. SEM image of AlN particles detected in the Mg-rich areas of the Al-20wt.%Mg matrix. The ingot is synthesized with ammonia gas.

The conversion to AlN in the Mg-rich areas of the matrix is substantial, while only a few particles are detected in the Mg-depleted regions (Fig. 5). Particle size is very homogeneous throughout the microstructure and averages around 0.6 μm , and the particles are more or less spherical in shape.

EXPERIMENTS # 3 AND # 4

As shown in Table 4, the amount of AlN formed in experiments #3 and #4 are comparable to one another.

Table 4. Vol.% AlN formed in C460 alloy.

Processing time	Vol.% AlN
C460. 4 hrs.	11
C460. 6 hrs.	13

AlN are detected both in the upper and lower parts of the ingot. The top section of the ingot (shown in Figure 6) contains about 20% more AlN particles than the bottom section (shown in Figure 7).

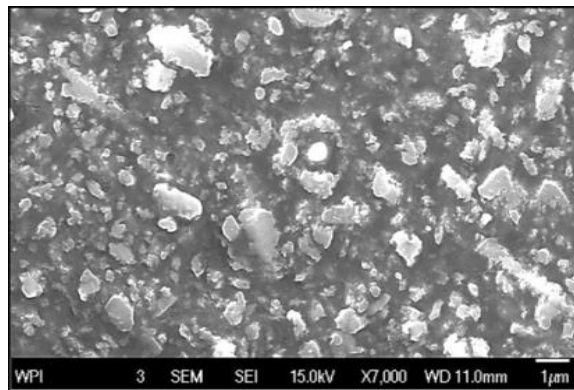


Fig. 6. SEM image of AlN particles in the top section of C460-AIN ingot synthesized by ammonia gas.

It can be seen that in this case, the interface between the AlN particle and the alloy matrix is improved and that the distribution of AlN particles in the alloy matrix is considerably enhanced. The size of the AlN particles ranges from 200 nm to 500 nm (Figure 8). However, a narrow particle size distribution and complete elimination of particle clustering are still not achieved as some larger size particles and aggregates of small particles can be detected in the matrix (Figure 6). Vigorous stirring of the molten metal may break these particle clusters and may provide a finer gas bubble size which will help formation of smaller AlN particles.

Grain size is a useful indicator of the distribution of the reinforcing particles since the addition of particles constraints grain growth and strengthens the matrix [18]. The grain size

of the C460 matrix alloy that is cast under similar conditions to those used to make the composite material is shown in Figure 9(a). The average grain size is about 6 mm. The average grain size of the composite material is shown in Figure 9(b) and is only about 2.5 mm.

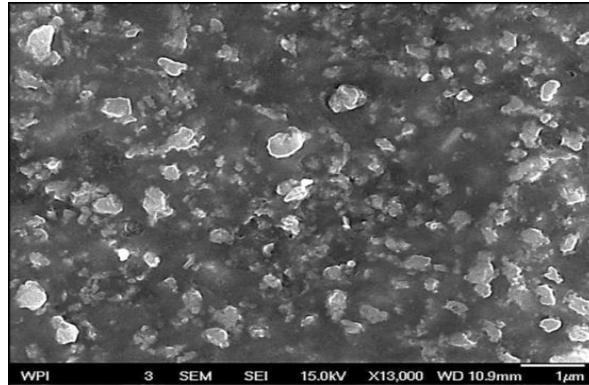


Fig. 7. SEM image of AlN particles in the bottom of C460-AlN ingot synthesized with ammonia gas.

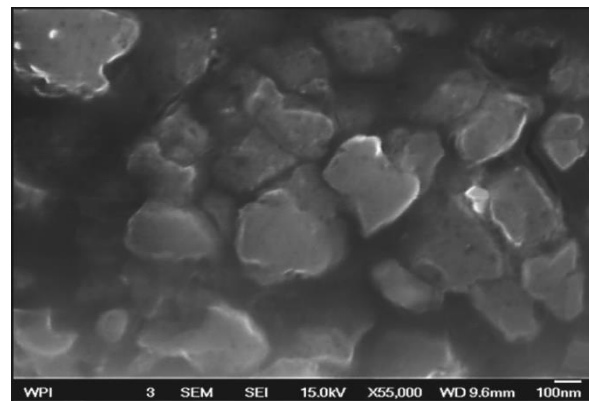
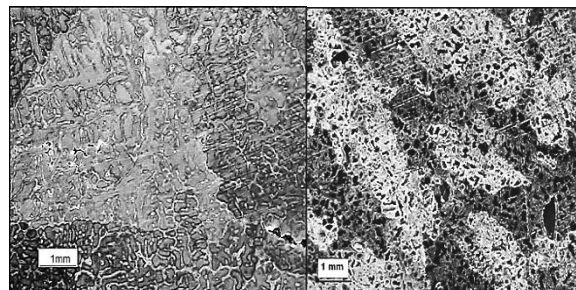


Fig. 8. SEM image of nano-size AlN particles formed in C460 alloy synthesized by ammonia gas.

The results of hardness measurements performed using scale “R” for soft materials (1/2 inch ball, 10 kg_f preload, and 50 kg_f load) are shown in Table 5. The small decrease in hardness observed for 6 hours processing time may be attributed to pores that formed in the matrix created by the entrapment of ammonia gas in the ingot during the later stages of the process.



(a) (b)

Fig. 9. optical micrographs showing grain size of (a) C460 alloy, and (b) C460-AlN composite. Graff-Sargent's etchant.

Table 5. Hardness values for C460 alloy and for C460-AlN composite.

Alloy	Hardness
Unprocessed C460	76
C460/AlN. 4 hrs.	118
C460/AlN. 6 hrs.	113

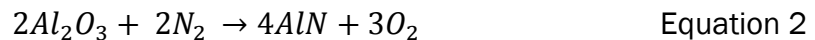
DISCUSSION

EFFECT OF CHEMICAL COMPOSITION OF THE MATRIX ALLOY ON ALUMINUM NITRIDATION

Previous investigations by the authors [19,20] show that nitridation of pure aluminum does not lead to the formation of AlN particles and direct nitridation of aluminum according to the reaction shown in Eq. (1) will not occur:



This can be attributed to the detrimental effect of oxygen which hinders the nitridation reaction even when present in very small amounts in the nitriding gas or in the furnace environment [13]. Studies demonstrate that the rate of aluminum nitridation is several orders of magnitude slower than the rate of aluminum oxidation at any given temperature [21]. The partial pressure of oxygen that is necessary for the formation of nitrides – and not oxides – can be quantified by means of a thermodynamic balance of the competing reactions as follow:



$$\Delta G = 2,057,400 - 184.4T \quad \text{Equation 3}$$

$$\Delta G = -RT \ln \left(\frac{P_{O_2}}{P_{atm}} \right)^3 \quad \text{Equation 4}$$

$$\rightarrow P_{O_2} = 18.9 - \frac{82,487.4}{T} \quad \text{Equation 5}$$

At 1000 °C (1832 °F), the partial pressure of oxygen (P_{O_2}) that allows formation of AlN is around 10^{-13} MPa. Such a low oxygen pressure is difficult to attain even after passing the nitrogen gas through de-oxidating traps. Alloying elements such as Mg and Li act as catalysts for what is known as *indirect nitridation* of aluminum [12,22,23]. Studies by Zheng et al. [17], Hou et al. [24] and Haibo et al. [25] propose that the mechanism follows the reactions depicted by Eqs. (6) and (7)



The authors provide a different view [20] based on the fact that magnesium nitrides are not detected in the material or in the reaction vessel, while MgO has been found to nucleate in the same locations where AlN forms. The catalytic action of Mg (via formation of MgO) may be explained as follow: at high temperatures, Mg vaporizes and acts as an “oxygen-getter”. Mg combines with oxygen and thus it locally lowers the partial pressure of the residual oxygen in the nitriding gas. The reactions are given by Eqs. (8), (9), and (10)



$$P_{O_2} = \gamma_{Mg}^{-2} x_{Mg}^{-2} \exp\left(\frac{2G_8 + G_9}{2RT}\right) \quad \text{Equation 10}$$

In Eq. (10), γ is the activity coefficient of Mg, x is the Mg concentration, G_8 and G_9 are the standard Gibbs energy changes for Eqs. (8) and (9), respectively. From thermodynamic data reported in the literature, the partial pressure of the residual oxygen can be derived to be in the range of 10^{-6} MPa.

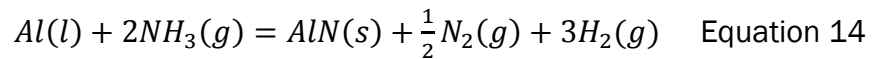
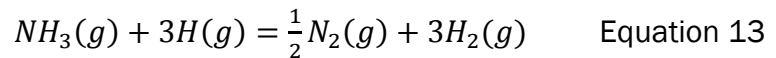
Despite its beneficial “oxygen-getting” action, 20wt.% Mg is a very large amount to be added to aluminum. Casting conditions become more challenging to control and the tendency of Mg to burn can compromise the integrity of the casting. Previous studies on aluminum nitridation [26] show that the addition of small quantities of lithium (1.5-2 wt.%) significantly enhances the rate of AlN formation. Lithium in small amounts also provides a cleaner casting and considerably enhances the matrix strength. The experimental results reported in the current work confirm the enhanced nitriding action of Li. Only 1.16 wt.% Li provides about 11 vol.% AlN when ammonia is injected in the matrix for 4 hours, whereas in order to synthesize 17 vol.% AlN, 20 wt.% Mg is necessary for an injection time of 2 hours. This is mainly due to the extreme reactivity of Li which comes into play in Eq. (10). Scholz and Greil in [26] analyze the nitridation behavior of an Al-2.3 wt.% Li melt and calculate considerably high conversion rates (up to 1 wt.% per minute) even when using an un-purified nitrogen gas. They confirmed the “oxygen-getting” action of Li and hypothesize that Li evaporation helps in breaking the oxide layer on the top of the melt which hinders the nitridation of bulk aluminum. On the other hand, the high tendency of Li to float towards the surface of the molten metal (see Table 5 and compare the measured Li concentration in the top and bottom sections of the ingot) hinders uniform distribution of the AlN particles within the ingot as is the case in Experiments #3 and #4.

Table 5. Measured chemical composition of the C460-AlN composite material of Experiment # 4.

	Li	Fe	Cu	Mn	Mg	Zn	Ti
Top	0.83	0.04	1.8	0.14	0.01	0.69	0.02

EFFECT OF REACTIVE GAS COMPOSITION ON ALUMINUM NITRIDATION

The rate of nitridation of Al-20 wt.% Mg alloy is eight times higher when ammonia gas is used compared to when nitrogen gas is used. The effectiveness of ammonia in the nitridation process has been previously reported [11,27,28]. During nitridation with ammonia, hydrogen dissociates from nitrogen at around 1000 °C (~1832 °F) and functions as an oxygen getter to lower the oxygen content in the reaction sites, thus increasing the permissible oxygen partial pressure for nitridation. Also, hydrogen may enhance the adsorption of nitrogen at the gas bubble-metal melt interface thereby improving the rate of AlN formation. In addition to this, the dissociation of ammonia releases atomic nitrogen, which can be more easily chemisorbed on the bubble surface and diffused into the molten metal than molecular nitrogen [11]. The reactions that describe nitridation with ammonia are shown as Eqs. (11) through (14):



SUMMARY AND CONCLUSIONS

In-situ nitridation of aluminum alloy melts to form aluminum nitride reinforced composite materials is feasible. It is found that:

- Ammonia has an eight times higher nitridation rate than nitrogen when used to nitride an Al- 20 wt.% Mg alloy. Particle size and particle distribution in the metal matrix are also influenced by the type of reactive gas: Nitridation with ammonia gas produces a more uniform particle distribution and smaller particles than nitridation with nitrogen gas (0.6 μm versus 1-3 μm).
- Lithium is more efficient than magnesium in catalyzing the nitridation reaction. Only 1.15 wt.% Li produces around 11vol.% AlN particles whereas 20 wt% Mg is needed to form 17 vol.% AlN particles. The tendency of lithium to evaporate causes the top section of the ingot to be 20-25% enriched with AlN particles compared to the bottom section. Segregation of Li towards the top of the melt and its undesirable effects may be mitigated by vigorously stirring the melt during nitridation. This can be efficiently done with a rotating impeller. An apparatus that incorporates melt stirring is being constructed and will be used in future experiments.

- Particle distribution in the Li containing alloy is improved when ammonia gas is used instead of nitrogen gas. In this case, the particle size is more uniform and the particle shape is almost spherical. The grain size is considerably decreased and the hardness enhanced by around 50%.
- The mechanism of nitride formation is illustrated and the role of alloying elements acting as “oxygen-getters” is explained. The higher reactivity of ammonia gas compared to nitrogen gas has also been discussed.

ACKNOWLEDGMENTS

The authors gratefully acknowledge the member companies of the Advanced Casting Research Center (ACRC) for their support of this work, and for their continued support of research focused on the science and technology of metal casting at Worcester Polytechnic Institute.

REFERENCES

1. Ajayan, P.M., Schadler, L.S., Braun, P.V., “Nanocomposite Science and Technology,” Wiley-VCH, Weinheim, DE (2003).
2. Koch, C.C., “Nanostructured Materials: Processing, Properties, and Applications,” William Andrew, Norwich, NY (2006).
3. Xiaodan, L., Yuchun, Z., Feng, Q., Haixin, Z., “Preparation of Metal Matrix Composites Reinforced with Nano-SiC Particles by Stir Casting Technique,” TMS 139th Annual Meeting and Exhibition, Supplemental Proceedings, Vol. 2, Seattle (2010).
4. Yang, Y., Lan, J., Li, X., *Material Science and Engineering*, Vol. A380, pp. 378-383 (Elsevier 2004).
5. Gierlotka, S., *Solid State Phenomena*, Vols. 101-102, pp.157-164 (Trans Tech 2005).
6. Zebarjad, S.M., Sajjadi, S.A.,Vahid Karimi, E.Z., *Research Letters in Materials Science*, pp. 1-4 (Hindawi Publishing Corporation 2008).
7. Ma, Z.Y., Lia, Y., Liang, Y., Zheng, L.F., Tjong, S.C., *Materials Science and Engineering*, Vol. A219, pp. 229-231 (Elsevier 1996).
8. Zhang, D.L., Liang, J., Wu, J., *Materials Science and Engineering*, Vols. A375–377, pp. 911–916 (Elsevier 2004).
9. Gell, M., *Material Science and Engineering*, Vol. A204, pp. 246–251 (Elsevier 1995).
10. Lee, K.B., Sim, H.S., Heo, S.W., Cho, S.W., Kwon, H., *Metals and Materials International*, Vol. 6, Issue 1, pp. 25-32 (Springer 2000).
11. Zheng, Q., Wu, B., Reddy, R.G., *Advanced Engineering Materials*, Vol. 5, Issue 3, pp. 167-173 (Wiley-VCH 2003).
12. Tyagi, S., Zheng, Q., Reddy, R.G., “In Situ Synthesis of AlN Reinforced Magnesium Alloy Composites Using Gas Bubbling Method,” Aluminum 2004, edited by S. K. Das, TMS, pp. 63-72 (Warrendale 2004).
13. Zheng, Q., Reddy, R.G., “Effects of Oxygen Impurities on In-situ Formation of AlN-Al Composites from Nitrogen Bubbling Gas,” Affordable Metal Matrix Composites for High Performance Applications II, edited by Pandey, A.B., Kendig, K.L, Lewandowski, J.J. and Shah, S.R., TMS, pp. 125-134 (Warrendale 2003).

14. Zheng, Q., Reddy, R.G., *Journal of Material Science*, Vol. 39, pp. 141-149 (Springer 2004).
15. Koczak, M.J., Kumar, K.S., U.S. Patent No. 4,808,372 (1989).
16. Ye, H.Y., Liu, X.Y., Luan, B., *Journal of Materials Processing Technology*, Vol. 166, pp. 79–85 (Elsevier 2005).
17. Zheng, Q., Reddy, R.G., *High Temperature Materials and Processes*, Vol. 22, Issue 2, pp. 63-71 (De Gruyter 2003).
18. Askeland, D. R., Fulay, P.P., Wright, W.J., “The Science and Engineering of Materials”, Sixth Edition, Cengage Learning, Florence, KY (2010).
19. Borgonovo, C., Apelian, D., *Materials Science Forum*, Vol. 678, pp. 115-123 (Trans Tech Publications 2011).
20. Borgonovo, C., Apelian, D., Makhlof, M. M., *Journal of Materials*, Vol. 63, Issue 2, pp. 57-64 (TMS February 2011).
21. Daniel, B.S.S., Murthy, V.S.R., *Materials & Design*, Vol. 76, Issue 3, pp.155-161 (Elsevier 1995).
22. Pech-Canul, M.I., Katz, R.N., Makhlof, M.M., *Metallurgical and Materials Transactions*, Vol. 31A, pp. 565-573 (Springer 2000).
23. Jinxiang, L., Xiuying, G., Jianfeng, C., Qun, W., Yuhui, S., Qin, G., *Thermochimica Acta*, Vol. 253, pp. 265-273 (Elsevier 1995).
24. Hou, Q., Mutharasan, R., Koczak, M., *Materials Science and Engineering*, Vol. A195, pp. 121-129 (Elsevier 1995).
25. Haibo, J., Chen, K., Zeping, Z., Agathopoulos, S., Fabrichnaya, O., Ferreira, J.M.F., *Journal of Crystal Growth*, Vol. 281, pp. 639–645 (Elsevier 2005).
26. Scholz, H., Greil, P., *Journal of Material Science*, Vol. 26, Issue 3, pp. 669-677 (Springer 1991).
27. Huashun, Y., Kim, J.D., Kang, S.B., *Materials Science and Engineering*, Vol. A386, pp. 318–325 (Elsevier 2004).
28. Reddy, R.G., Kumar, V., *Materials Science Forum*, Vols. 561-565, pp. 701-704 (2007).

Manufacture of Aluminum Nanocomposites: A Critical Review

Cecilia Borgonovo^a and Diran Apelian^b

Metal Processing Institute, Worcester Polytechnic Institute
Worcester, MA 01609 USA

^acborgonovo@wpi.edu, ^bdapelian@wpi.edu

Keywords: lightweight, nanocomposites, agglomeration, manufacturing routes, ex-situ processing, in-situ processing, gas-liquid reactions.

Abstract. In the last two decades, metal matrix nanocomposites have witnessed tremendous growth. Particulate-reinforced nanocomposites have been extensively employed in the automotive industry for their capability to withstand high temperature and pressure conditions. Several manufacturing approaches have been used to fabricate them. Non-homogeneous particle dispersion and poor interface bonding are the main drawbacks of conventional manufacturing techniques. A critical review of nanocomposite manufacturing processes is presented; the distinction between ex-situ and in-situ processes is discussed in some detail. Moreover, in-situ gas/liquid processes are elaborated and their advantages are discussed. The thermodynamics and kinetics of the reaction between the precursor gas and the liquid metal have been analyzed and their role on particle formation studied. This critical review will provide the reader with an overview of nanocomposite manufacturing methods along with a clear understanding of advantages and disadvantages.

Metal-matrix Composites in Context

Metal-matrix composites are a hybrid material in which rigid ceramic reinforcements are embedded in a ductile metal alloy matrix. They tailor the best properties of two different materials, such as ductility and toughness of the metallic matrix and the high modulus and strength of ceramic reinforcements. Their first application can be traced back to the late 1960s, with the development of a steel-wire reinforced copper alloy [1]. The aerospace industry led the application and use of composite materials in spacecrafts components. High-performance and high-integrity materials are required for extreme environments and critical applications such as for space missions. It is interesting to note that during its lifetime, the International Space Station will undergo 175,000 thermal cycles from +125 C° to -125 C° as it moves in and out of the Earth's shadow. During the last 4 decades, aluminum matrix composites were specifically developed to meet both aerospace and defense needs. Continuous boron fiber reinforced aluminum was used in the Space Shuttle Orbiter as the frame and rib truss members in the mid-fuselage section; there are other applications such as landing gear drag link yielding 45% weight savings. A Gr/Al composite is the constituent of a high-gain antenna boom for the Hubble Space Telescope. This boom (3.6 m long) offers the stiffness required to maintain the position of the antenna during space maneuvers. In the 1980's and early 1990's, metal matrix composite development programs were in vogue and there was much activity at all major aluminum producers. Alcan, through its Duralcan subsidiary, established a 25 million pound per year production capability for particulate-reinforced aluminum composites. The Aluminum Association convened the Aluminum Metal Matrix Composites Working Group, a product of which was the ANSI H35.5 standard that established a nomenclature system for aluminum composites [2]. As expected, metal matrix composites found applications in a variety of other markets such as automotive, electronic packaging, industrial product and recreational products [3]; though not a conclusive list, the components given below illustrate applications that utilize Al based composites:

- *Chevrolet Corvette and GM S/T pick-up truck drive shafts*
- *Plymouth Prowler brake rotors and GM EV-1 brake drums*
- *Toyota diesel engine pistons*
- *Pratt & Whitney 4000 series engine fan exit guide vanes*
- *Motorola's Iridium Satellites and GM EV-1 electronic packaging applications*
- *F-16 fighter aircraft ventral fins and fuel access covers*
- *Bicycle components and golf clubs*

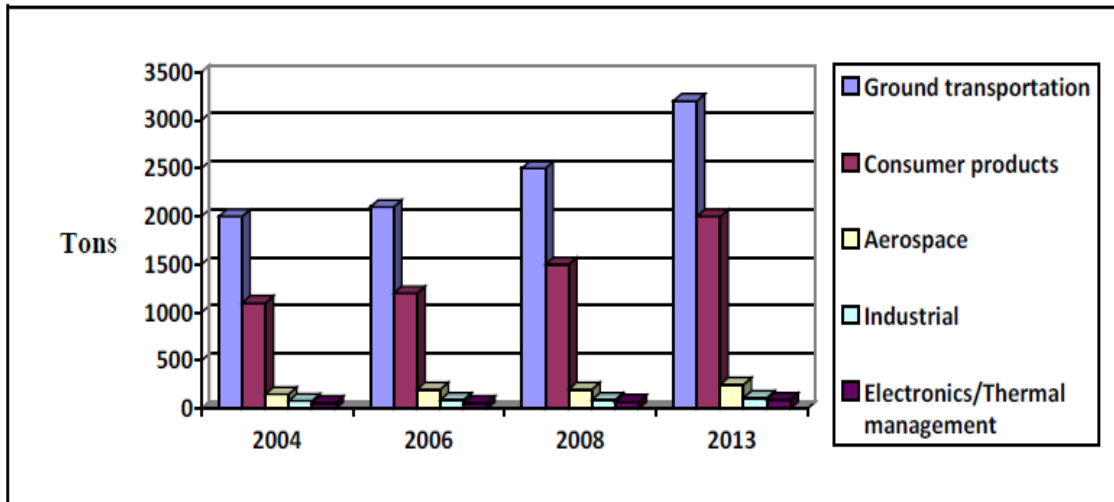


Fig.1. Global outlook of metal-matrix composites by application segment (2004-2013). Source: BCC Research.

An almost 70% increase in metal matrix composites is estimated to occur in the use of Al in vehicles from 2004 to 2013, see Fig.1. The choice of aluminum alloys as matrix is dictated by the compelling need to have vehicles with low fuel consumption and reduced emissions for a sustainable future. Because of their high strength-to-weight ratio, aluminum alloys are considered to be an alternative to conventional steels and to the more expensive superalloys. The amount of aluminum per automobile produced in USA has increased from 251 lb. of 1999 to 280 lb. forecast for 2014 [4,5]. In Europe it went from 220 lb. of 1999 to 462 lb. forecast for 2014 [6], see Fig.2. Aluminum-based composites have contributed to such growth by improving strength and hardness of the aluminum matrix, broadening the application field to more highly-rated regimes.

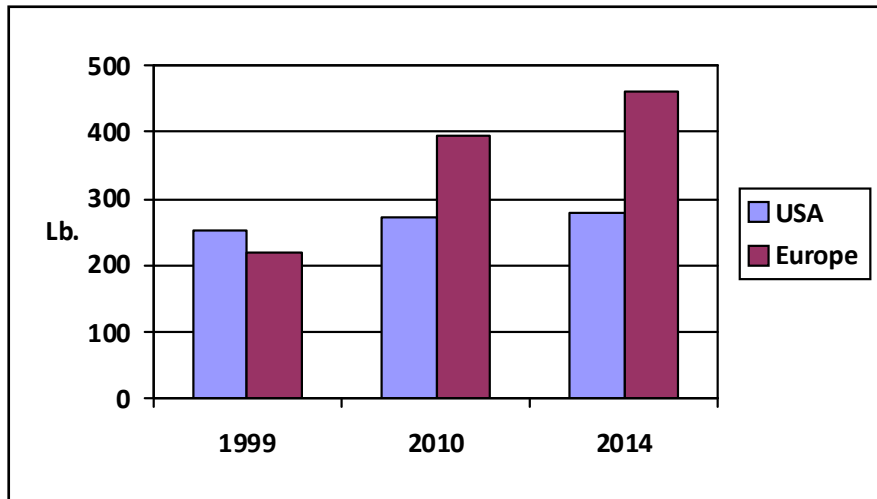


Fig.2. Amount of aluminum per automobile in USA and Europe (1999-2014) [4-6].

When compared to ferrous sand casting, high-production of metal matrix composite components through die casting, squeeze casting and semi-solid molding can compete effectively in terms of cost. In the commercial aircraft industry, weight savings has been estimated to be around \$450/kg; and in spacecraft, it can reach \$40,000/kg. For what concerns the automotive industry, Ford Motor Co. has placed the value of weight reduction at between \$0.35-3.50/kg depending on vehicle platform. In freight transport, the weight savings of a component translates to additional freight that can be hauled. For heavy-duty trucks, such savings has been valued from \$2-16/kg depending on the equipment's operational cycle [7]. Aluminum metal matrix composite also win out on iron components in terms of marketability and maintainability. Though metal matrix composites offer many advantages, they do have shortcomings such as low fracture toughness, low strength and hardness at high temperatures and poor machinability. The main concern of machining particulate metal matrix composites is the extremely high tool wear due to the abrasive action of the ceramic reinforcing particles. Tool selection is limited to a small group of extremely hard and expensive materials. The cutting tool must be able to withstand intermittent cutting of hard (reinforcement) and soft (matrix) materials. Polycrystalline diamond tools are often recommended for machining this particular class of materials and the high cost of such tools together with the need of frequent tooling changes increases the cost of the machining process [8]. Conventional machining methods have applied on composites with poor results. Non-traditional processes like waterjet, abrasive waterjet cutting, electrical discharge machining, ultrasonic machining and laser cutting provide precision finish but are characterized by very high costs and slow machining rates [9]. Therefore, machining still remains an issue to address since it will continue to be a necessary step to produce the required close dimensional tolerances and surface finish.

There is a compelling need for an aluminum-based material whose strength at high temperatures is retained and whose manufacturing process can be adapted to existing industrial infrastructures. Nanocomposite aluminum matrix materials have emerged as a viable alternative to overcome the limitations of aluminum (micro-) composites. Tensile strength, hardness and fracture toughness are enhanced as well as dimensional stability at high temperatures, see Fig.3 [12]. They currently represent a market segment of \$ 250 million, 80% of which is covered by automotive applications. Nanoparticles in castings are considered to be the most promising segment in casting material development [10]. However nanocomposites are challenging to produce as structural components due to difficulties in attaining a homogeneous distribution of the nano-phased particles. Clusters of secondary phases are detrimental for the final component performances and also affect post-processing techniques and the ability to machine the part. Representative metal nanocomposite systems and associated attributes are given in Table 1 [11].

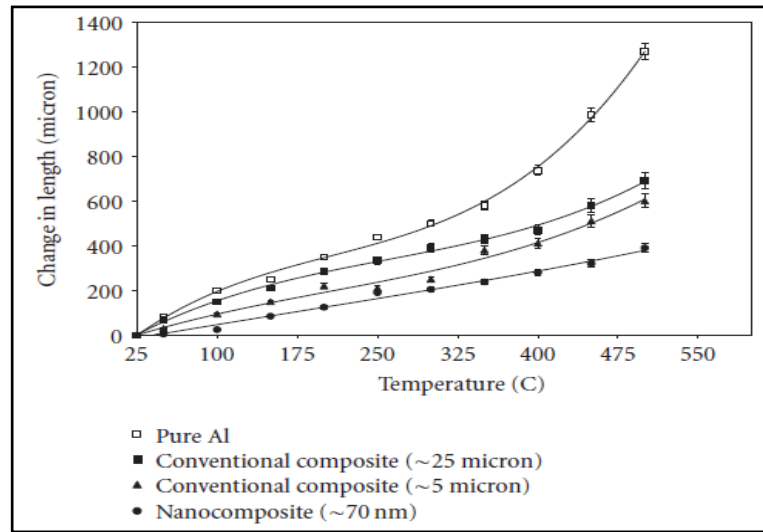


Fig.3. The variation of change in length versus temperature for aluminum and its composites at constant SiC content (7.5 Vol% SiC) [12].

Matrix/Nano-sized Reinforcement	Properties
Al/SiC Mg/SiC Al/Al ₂ O ₃ Mg/Al ₂ O ₃	<i>Improved ultimate strength, hardness and elastic modulus</i>
Al/AlN	<i>Higher compression resistance and low strain rate</i>
Ni/PSZ (partially-stabilized zirconia) and Ni/YSZ (yttria-fully stabilized zirconia)	<i>Improved hardness and strength</i>
Cu/Al ₂ O ₃	<i>Improved microhardness</i>

Table 1. Metal Nanocomposite Systems of Interest and Associated Attributes [11].

Nano-particle reinforced composites. Nano-particles have progressively replaced other discontinuous reinforcement structures such as nano-fibers, nano-wires or nano-platelets. SiC, TiC, WC, TaC, TiB₂, AlN, and Al₂O₃ are some of the most common types of nano-particles that have been utilized. The characteristics of nano-particle reinforced composites can be summarized as follows:

- drastic change of fracture mode from inter-granular fracture in monolithic metal to trans-granular fracture in nano-composites;
- moderate to significant improvement in strength;
- moderate improvement of fracture toughness;
- significant improvement of creep resistance, thermal shock resistance, and wear resistance;
- enhancement of dimensional stability at high temperatures.

Zebarjad et al. [13] compared the effect of 25 μm , 5 μm , and 70 nm SiC particles on dimensional stability in an aluminum alloy. The temperature sensitivity of aluminum decreases in the presence of both micro and nano-sized silicon carbide, though the effect of nano-sized silicon carbide on dimensional stability is much higher than that of micro-sized ones. Ren and Chan [13] added SiC nano-particles (50 nm) to 7075 aluminum alloy. They pointed out that this resulted in increased wear resistance and high temperature creep resistance compared to the same alloy reinforced with larger sized 13 μm SiC particles. Furthermore, the volume percentage of nano-particles needed to achieve this result was considerably smaller than in the case of the 13 μm SiC particles. Similarly, the tensile strength of an aluminum alloy reinforced with 1 % volume of Si_3N_4 (10 nm) has been found to be comparable to that of the same alloy reinforced with 15 % volume of SiC particle in the micro-sized range (3.5 μm); the yield strength of the nano-metric composite being significantly higher than that of the micro-metric one [14]. The existence of a threshold size (“critical size”) below which the addition of particles improves properties has been reported – see Table 2) [11]. It must be noted that the mechanism responsible for property improvements remains a matter of debate among researchers.

Properties	<i>Critical Reinforcement size (nm)</i>
Catalytic activity	<5
Softening of hard magnetic materials	<20
Change of refractive index	<50
Producing electromagnetic phenomena such as super paramagnetism	<100
Strengthening and toughening	<100
Modifying hardness and plasticity	<100

Table 2. Critical Size for Properties Improvement in Nanocomposites [11].

Strengthening theory based on a continuum approach is not useful; since it ignores the influence of particles on micromechanics of deformation - i.e., location of particles, grain size, and dislocation density. Several discontinuous approaches have been formulated to include particle effects. The modified shear lag theory [16] of Nardone and Prewo, the Eshelby- based particle-compounded model and the EMA (effective medium approximation) model by Stroud are the most popular ones [16]. They take into account one or more of the following strengthening mechanisms:

- *Orowan mechanism*: the stress that must be applied to force dislocations to by-pass an obstacle (such as a particle) is the principle of the Orowan strengthening mechanism. The stress arises due to the resistance of closely spaced hard particles as dislocations pass through. If the particles are coarse (in the micro-size range) and the inter-particle spacing is large, the Orowan effect is not significant [16]. When highly dispersed nano-sized particles are present, Orowan strengthening becomes more favorable. Creep resistance and thermal stability are consistently enhanced. TEM (transmission electron microscopy) observations

reveal strong dislocation bowing and tangling around the particles, confirming the operating mechanism [15, 16].

- *Thermal mismatch*: matrix and reinforcement have different coefficients of thermal expansion. During cooling of the component, plastic deformation is produced in the matrix at the various interfaces. These deformations increase the density of dislocation [16].
- *Load-bearing*: the strong bond due to the cohesion between particles and the matrix contributes to load-bearing capacity [16].

When all these factors are taken into account, the increase in mechanical properties with the decrease in size can be estimated.

Critical Issues in Processing of Nanocomposites

The main challenge for nanocomposites is how to make them – the processing routes to manufacture them. Dispersing the second phase particles in the matrix and achieving a strong interfacial bond are the two main processing challenges. Most fabrication processes fall short of fulfilling these tasks. Clusters of particles and weak matrix-reinforcement interfaces compromise the ability of the composite material to function under extreme conditions, such as high temperature and pressure typical of automotive applications (especially Diesel engines).

Uneven dispersion and agglomeration. Agglomeration is a common phenomenon that occurs when a solid particle comes into contact with a non-wetting medium [17, 18]. The clustered particles significantly reduce the failure strain of the composite; degradation is attributed to preferential nucleation of cracks in clustered regions. Final fracture is produced by the crack propagating to other clusters. Clustering occurs due to combined effects of agglomeration, sedimentation (particle settling rate) and particles pushing by the advancing solidus-liquidus interface. Particle clustering occurs since the system tends to minimize its free energy. A solid inclusion is never perfectly smooth: its surface is covered with cavities filled with gas, which contribute to increasing the system's Gibbs energy. This can be seen by analyzing the equation describing the Gibbs energy of a gas-liquid-solid system [17]:

$$\Delta G = (\mu_g(T, P) - \mu_l(T, P)) + \gamma_{lg} \Delta S_{lg} + \gamma_{sg} \Delta S_{sg} + \gamma_{sl} \Delta S_{sl} \quad (1)$$

where T is the temperature, P the pressure in the liquid, μ_g and μ_l the chemical potentials of gas and the liquid, ΔS is the change in interfacial areas and γ surface energies. When the particle size is brought down to the nano-scale range, surface energy is enhanced by three orders of magnitude (Table 3), introducing strong instability in the system and hindering particle wetting by the molten metal.

Particle size [cm]	Total surface area [cm ²]	Surface energy [J/g]
0.1	28	5.6×10^{-4}
0.01	280	5.6×10^{-3}
0.001	2.8×10^3	5.6×10^{-2}
10^{-4}	2.8×10^4	0.56
10^{-7}	2.8×10^7	560

Table 3. Variation of Surface Energy with Particle Size (1 g of sodium chloride) [20].

The natural tendency towards equilibrium is the “spring” that allows the system to assume a physical configuration for which the Gibbs energy is lowered to a minimum value. With this perspective, agglomeration acts like a “stability configuration”: several nano-particles cluster in one micro-agglomerate (Fig.4), providing a less extended total interfacial area. The dynamics of the relative motion of two nano-sized particles has been extensively studied [18, 20]. Due to the complexity of the problem, the analysis is usually limited to two main mechanisms: Brownian diffusion/motion (or perikinetic aggregation), and inter-particle forces (electrostatic and Van der Waals). External forces are not considered and particle inertia is neglected.

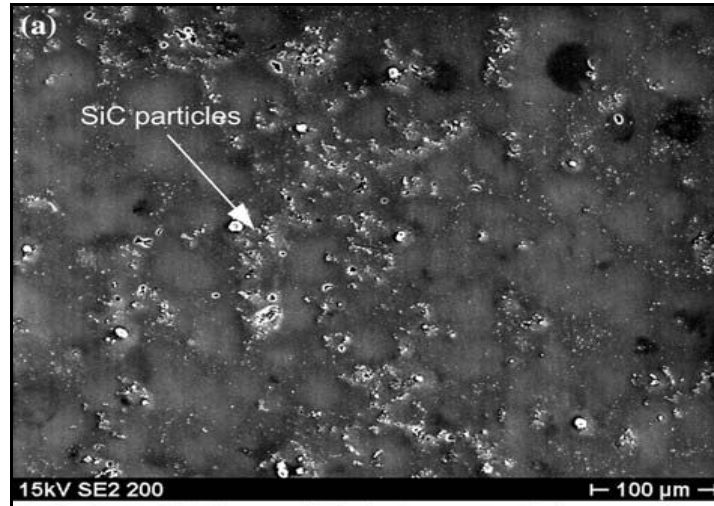


Fig. 4. Clusters of SiC nano-particles [19].

Brownian motion. It has been demonstrated [18] that a suspended particle is randomly bombarded from all sides by thermally-excited molecules coming from the liquid. Brownian diffusion ensures continuous collision between particles [19]. It can be defined as the incessant random motion exhibited by microscopic particles immersed in a fluid. Einstein noticed that if one solid inclusion is small enough to behave like a gas molecule, it is continuously collided by liquid molecules and displaced as a consequence. The magnitude of the displacement follows a Gaussian statistic distribution according to the relation:

$$d = \sqrt{\frac{2kTt}{6\eta\pi r}} \quad (2)$$

where η is the viscosity of the medium, t the time, r the particle radius, T the temperature and k the Boltzmann's constant. The displacement increases with decreasing particle radius, thus enhancing the probability of a collision to occur. It has been confirmed [18] that for particles smaller than $3.5 \mu\text{m}$, Brownian motion totally dominates the agglomeration dynamics. The aggregation rate for 20 nm particles has been evaluated to be four orders of magnitude higher when compared to particles in the range of $1 \mu\text{m}$ [20]. This behavior can be explained by the fact that as the particle size increases the potential energy of repulsion increases, thus making aggregation less likely.

Inter-particle forces: Van der Waals attraction and electrostatic repulsion. According to Van der Waals, the non-ideality of gases can be attributed to the existence of molecular or atomic interactions [21]. Such dynamic interactions are established between the instantaneous dipoles formed in an atom's orbiting electrons. Thus, the resulting force is weak and becomes significant only at a short particle distance. Hamaker [21] found such interactions to exist between particles and modified Van der Waals' formulation through the so called “additivity concept” (single atoms or molecules make up the particle). When the cavities located on a solid inclusion are filled with

gas, negative Van der Waals forces come into play, causing particle agglomeration. Attraction is favorable because it reduces the value of the Gibbs free energy by θ :

$$\theta = \frac{-Ar}{12H^2} \quad (3)$$

where A is the Hamaker constant, which depends on the polarization properties of the molecules on the particle surface, r is the reduced particle radius and H the inter-particle distance [18]. When the dimension of the particle is smaller than $1 \mu\text{m}$, Van der Waals forces dominate. Coulomb force of repulsion competes with Van der Waals attraction. It can be noted from Fig.5 that the electrostatic repulsion is overcome by the Van der Waals attraction force for a inter-particle distance down to 1 nm . For smaller values, the Born repulsion of adjacent electron clouds dominates.

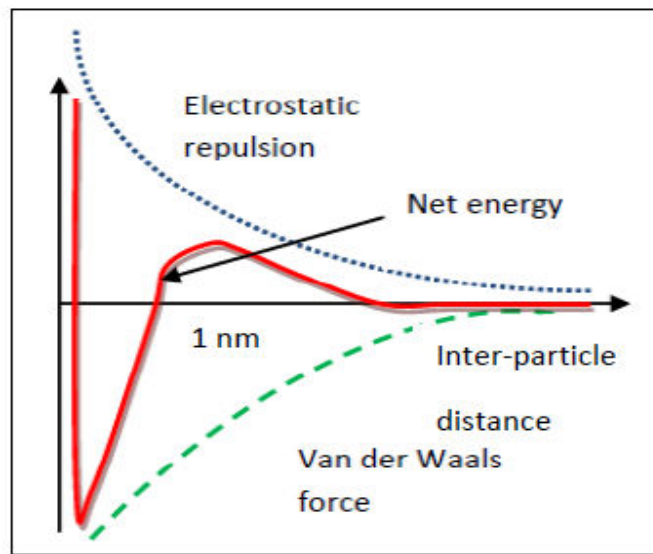


Fig. 5. Forces acting between two particles [20].

Interface debonding. Interface bonding between particles and the matrix is critical as it affects load transfer from the matrix to the particle and for delaying the onset of particle–matrix decohesion. Voids nucleation and growth have also been observed to be correlated with the loss of coherency at particle/matrix interface. All these aspects have a profound effect on the strength and stiffness of the composite. Interface debonding caused by large thermal mismatch between metal and ceramic has been noticed to be the main mechanism responsible for fracture of the material [22]. Matsunaga et al. [23] measured the effect on strength and fracture toughness of surface oxidation of SiC particles, according to the reaction:



They detected enhanced strength only for thick oxide layers ($1.4 \mu\text{m}$), while fracture toughness consistently decreased after the oxidation process for all temperatures and exposure times. Therefore, crack initiation on particle surface is more likely to occur, affecting life duration of the component. It's difficult to determine whether cracking of the oxide layer is responsible for the failure mechanism of the composite materials. Exposure of clusters of bare particles on the fractured surface (Fig.6) could be an indication of such phenomenon. EDS analysis confirms the presence of silicon dioxides on particles surface (Fig.7). Other studies [24,25,26] found that the wettability of the reinforcement by liquid aluminum is improved when an oxide coating is applied. However, the very thin film character of silicon dioxide makes it brittle, fragile and easy to break-down during particle incorporation and vigorous stirring. In addition to this, when a high percentage

of coating material is used in the oxidation process the interfacial bonding between particle and matrix is degraded and a typical bondless morphology underlines the non-wetting characteristic between both surfaces. Therefore, wettability is enhanced only for specific coating thickness and for layers that are continuous, which is a feature connected to the nature of the heat treatment. Oxidation in air has shown not to improve the contact angle between particle and matrix [27], whereas it is improved in oxygen supported atmosphere. Large thermal mismatches between particle and matrix can also cause interface debonding and fracture upon cooling to room temperature [28].

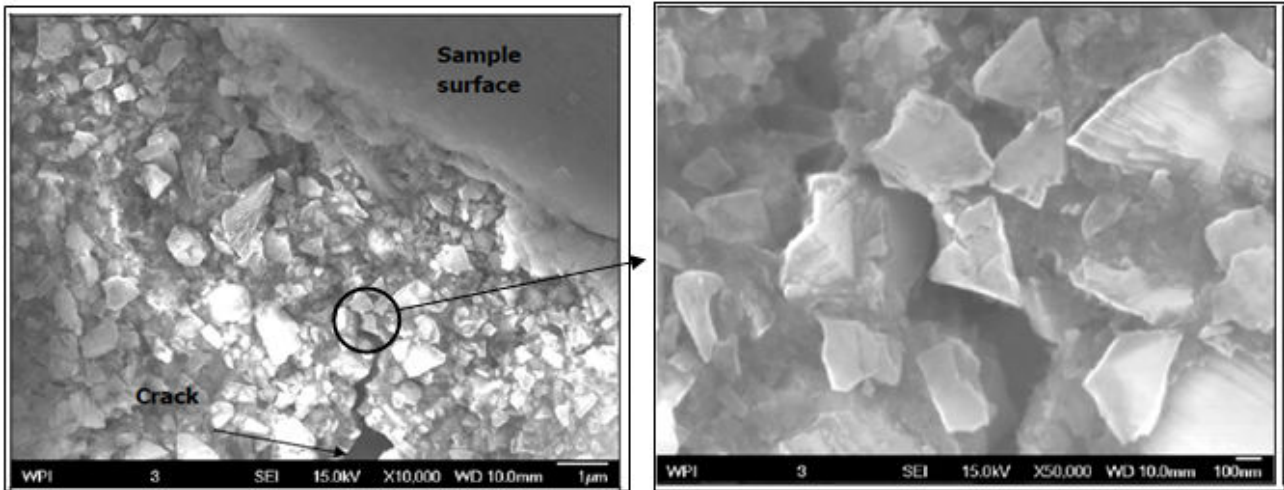


Fig.6. SiC nano-particles on an A356 aluminum alloy fractured surface.

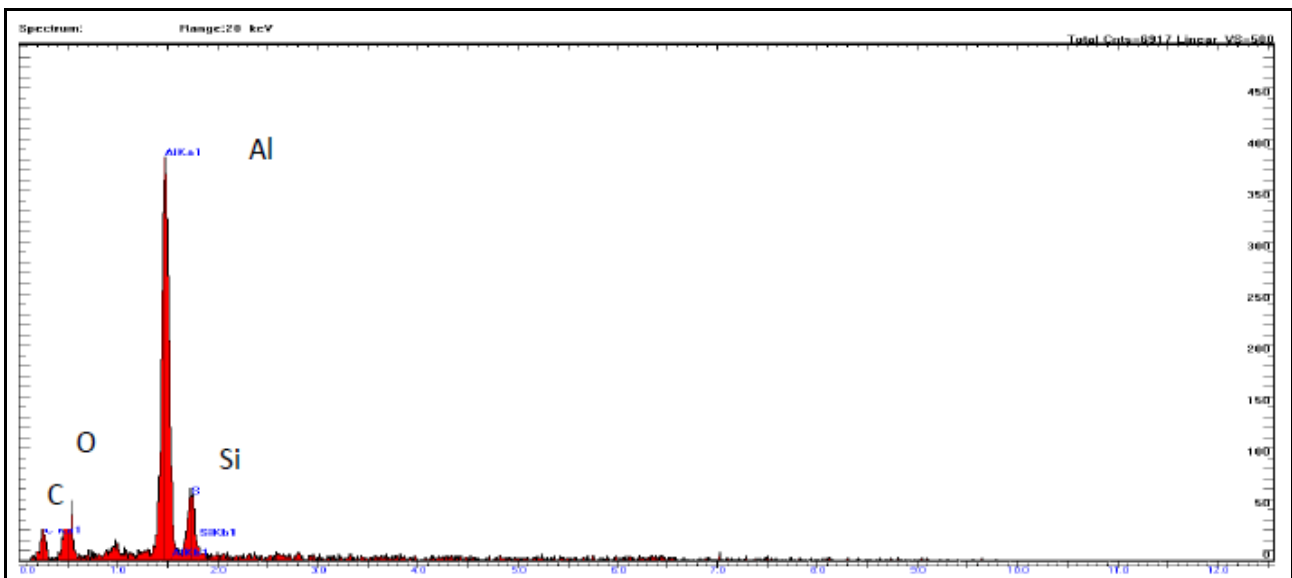


Fig.7. EDS spectrum of a SiC nano-particle on the fractured surface.

Manufacturing Routes

Classification of processing routes. Metal matrix composite manufacturing processing can be divided into two general categories: ex-situ and in-situ. Ex-situ is when the reinforcement is externally added to the matrix. In-situ synthesis involves the production of reinforcements within the matrix during the processing stage [33, 34]. The same classification applies for nanocomposite manufacturing as well. Ex-situ manufacturing techniques can be further classified into two main processing schemes [33,36]: solid-state and liquid-state. In some instances when the processing is in the semi-solid range (such as in droplet consolidation or similar techniques) then the classification could be further expanded to solid-state, liquid-state and semi-solid state. For the purposes of this review we will limit ourselves to the first two processing routes. Among solid-state techniques, powder metallurgy and mechanical attrition are the most popular ones. The nano-scale can be easily reached, although the cost of the powder is significantly high. Interfacial and surface wetting issues are considerably diminished. This is because both phases remain in the solid state, where diffusivity is much lower [29, 30]. The final products are generally affected by a high amount of porosity, which strongly decreases the fatigue resistance and requires further metalworking. When the process involves attrition at high temperatures chemical modification of the initial constituents is likely to occur [31, 32]. Liquid-state routes can be sorted into four major categories: infiltration, agitation, spraying and ultrasonic cavitation based solidification. Semi-solid casting of nanocomposite materials is still an open field; a novel method of melting, compacting and solidifying semi-solid billets has been tested in [35]. Liquid metal is generally less expensive and easier to handle than powders, and the shape flexibility constitutes a significant advantage. Liquid-state processes are generally fast and easy to scale-up. Despite this, they are affected by the lack of wettability of the reinforcement and by interfacial reactivity. Moreover, they are often limited to low melting point metals [29, 30]. In-situ metal matrix composites are not affected by the shortcomings typical of ex-situ composites, although control of process variables still remains an issue. In-situ fabrication methods can be divided into two major categories according to the physics of the process itself: “*reactive*” routes, where the reinforcement is synthesized within the metal matrix through a gas-liquid, liquid-liquid, or solid-liquid reaction, or “*morphological*” routes, where a favorable composite architecture evolves as a consequence of processing.

Other methods, which cannot be used for mass production of near net shape parts can be traced in the literature [31,36]. The most important are laser deposition, spray deposition, sol gel synthesis, nano-sintering and electroplating. They are costly, time and energy consuming processes. Therefore, their application is unlikely to be extended to the industrial scale. Such techniques are generally used for coating and thin films deposition. In this review, only mass production methods see table, which could be adapted to existing industrial infrastructure and can meet the need to large production volumes will be taken into account.

Process	System (matrix/reinforcement)	Reinforcement size	Main features
<i>Ex-situ: solid-state</i> (Section 3.2.1)			
- Powder metallurgy	Al/ Al ₂ O ₃ , Al/Si ₃ N ₂	15-100 nm	+ Near net shape; + Industrially scalable; - Non homogeneous particle size distribution; - Costly.
- Mechanical attrition and alloying	Al-Fe/ Al ₅ Fe ₂ , Al/ Al ₄ C ₃ , Al/SiC	9-27 nm	
<i>Ex-situ: liquid state</i> (Section 3.2.2)			
- Stir casting	Al/SiC	40 nm	+ Industrially compatible + Industrially scalable; + Inexpensive; - Particle clustering and debonding.
- Ultrasonic cavitation based solidification	Al-Si/SiC, Al/ Al ₂ O ₃	< 100 nm, 10 nm	+ Good particle dispersion; + Inexpensive; - Industrially non-scalable.
- Infiltration	Al-Cu-Mg/ Al ₂ O ₃	50 nm	+ Good mechanical properties; - Expensive equipment (preform); - Un-easy to scale up.
<i>In situ: reactive routes</i> (Sections 3.3.1,3.3.2,3.3.3)			
- Combustion synthesis	Al/ TiB ₂	30-100 nm	+ Good particle dispersion and particle/matrix bonding; + Inexpensive; + Industrially scalable; - Difficult process control.
- Exothermic dispersion	Al/ TiB ₂	< 0.7 μm	
- Substitutional chemical reaction	Al/ Al ₃ Zr + Al ₂ O ₃ Cu-Ti/ TiB ₂	80 nm 50 nm	
- MixAlloy by Sutek	Cu/ TiB ₂	50 nm	
- Gas-liquid process	Al alloys/AlN, SiC, TiC	100-500 nm	
<i>In-situ: morphological</i> (Section 3.3.4)			
- Rapid solidification	Al-Fe/ Al _{100-x} Fe _x , Al/TiC	20-150 nm, 40-80 nm	

Table 4. Manufacturing Methods for Metal Matrix Nanocomposites (Mass Production).

Ex-situ methods**Solid state**

Powder metallurgy. Prior work in synthesizing nanocomposites involves the use of powder metallurgy techniques, which are usually not cost-effective. Blending of matrix and reinforcement

powders followed by hot or cold pressing and sintering is a standard fabrication sequence; a schematic of a typical powder metallurgy (P/M) processing scheme is shown in Fig.8. In P/M processing, agglomeration can be minimized only if the size of the matrix powder is in the size range of the reinforcement phase. In addition, further working of the product via P/M may cause the reinforcement phase to break up and deform the surrounding matrix, leading to stress concentration and cracking [34]. The advantages of the process are flexibility and the ability to produce near-net shaped components. The size range of metal powders available on the market is quite wide which it is an advantage. P/M has been used [14] to add 50 nm alumina particles to aluminum powder. The process consists in wet mixing (aluminum powder mixed with varying volume fraction of Al_2O_3 powder in a pure ethanol slurry), followed by drying at 150°C and cold isostatic pressing to compact the powder. The compacted powder is then vacuum sintered at 620°C (approximately 60°C below the melting temperature of aluminum). Massive clustering has been observed, and its occurrence increases with decreasing particle size. Ma et al. [37] fabricated via P/M processing nanometric silicon-nitride reinforced aluminum composites. They reported the presence of several agglomerates in the aluminum matrix. Peng et al. [38] created a novel and simplified process for producing aluminum matrix nanocomposites reinforced with oxide particles. The novelty lays in the use of Al_2O_3 surface layers existing on matrix aluminum particles as the ceramic reinforcement. A good distribution has been achieved, although the process does not allow satisfactory control of the process. Moreover, the effectiveness and the scalability of the method remain to be proven.

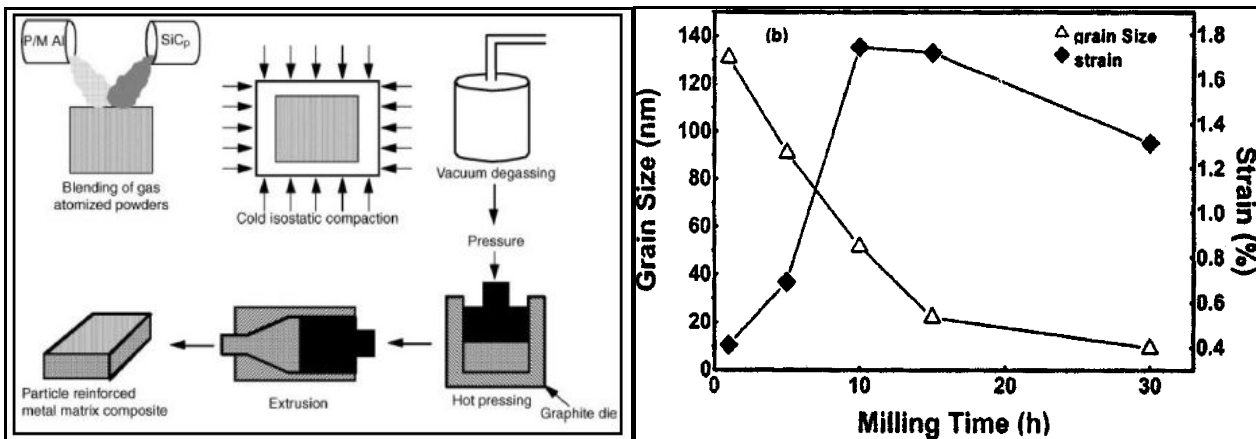


Fig.8. Processing routes for particulate reinforced composites [34].

Fig. 9. Grain size and strain vs. milling for WC particles [39].

Mechanical attrition and alloying. Mechanical alloying was invented in 1980 to manufacture particle strengthened metal alloys. In the last ten years, the method of high-energy milling gained much attention as a non-equilibrium process able to produce nano-scale microstructures. A variety of ball mills have been developed for different purposes including tumbler mills, attrition mills, shaker mills, vibratory mills, and planetary mills [32]. In the high-energy ball milling process, alloying occurs as a result of repeated breaking up and welding of matrix and reinforcement particles. Both powders are subjected to severe plastic deformation due to collision with the milling tool. Deformation occurs at high strain rates; thus, after extended milling (Fig.9), the average powder grain size can be reduced to few nanometers [32,39]. It should be noted that aluminum nanocomposites with the trade-name DISPAL, reinforced with Al_4C_3 particles, are manufactured via mechanical alloying [14]. Flexibility and scalability are key advantages of the process; contamination by the milling tool and the atmosphere are the main disadvantages of the process. Milling of refractory metals (tungsten) in a high-frequency shaker for extended times can result in iron contamination of more than 10 at% [38]. To prevent contamination, the process should be carried out in an inert atmosphere and the mills ought to be coated. Another major issue is the

occurrence of chemical reactions as a consequence of converting mechanical energy into thermal energy [32]. Zhang et al. [40] proved that there exists a particle size below which further size reduction cannot be performed, since the stress necessary to break the particles is above the process capabilities. The stress required for processing can be expressed as:

$$\sigma_f = \frac{K_c}{\sqrt{\pi a_c}} \quad (5)$$

Where σ_f is the fracture stress, K_c the fracture toughness and a_c size of material defects. When the particles are reduced to the nano-range, the likelihood of having internal defects and surface notches are considerably reduced. In this case, σ_f will approach the theoretical strength of the ceramic material. The impact stress of silicon-carbides is over 15 GPa, which is the value needed to fracture a “perfect” (with no defects) ceramic. Such stress is not achievable with conventional high-energy mechanical mills. Furthermore, nano-particles produced by attrition do not possess uniform size distribution and the process is limited to materials with very poor thermal conductivity [41].

Liquid state

Stir casting. Stir mixing techniques, widely utilized to mix micron size particles in metallic melts [34, 41] have recently been modified for dispersing small volume percentages of nanosize reinforcement particles in metallic matrices [41]. The restraints correlated with mixing nanosize particles in metallic melts are:

- Particle introduction into the melt;
- Particle clustering;
- Weak bond between matrix and reinforcement because of surface contamination of the externally added reinforcement.

Because of increased surface area together with the reduction in particle size, inserting the particles in the melt and homogeneously dispersing them is a challenge. The increase of interfacial energy raises the free energy of the system, causing agglomerates to form. Xiaodan et al. [42] managed to avoid agglomeration of 40 nm SiC particles in aluminum by designing an experimental setup consisting in fusion, vacuum, and stir parts. In fact, simple stirring by means of a lance or rod does not overcome particle clustering. Alternative stirring tools have also been developed to improve the dispersion. Ultrasonic based solidification has been the most successful one.

Ultrasonic cavitation based solidification. High-intensity ultrasonic waves (above 25 W/cm²) can generate strong non-linear effects in the liquid such as transient cavitation and acoustic streaming [43]. These waves produce a dispersive effect and tend to homogenize the microstructure of the melt [44]. An ultrasonic probe is immersed into the melt to create the acoustic field (Fig.10) and nano-sized particles are added during the process. The acoustic bubbles burst, creating hot micro-spots that locally raise the temperature of the melt. This enhances particle wettability and favors good dispersion. It has been measured [43] that with a 3.5 kW ultrasonic power, the ultimate strength and yield strength were improved more than 60% and 100% (Fig.11). In addition, 2.0 vol% SiC nano-particles improved hardness by 20% [45].

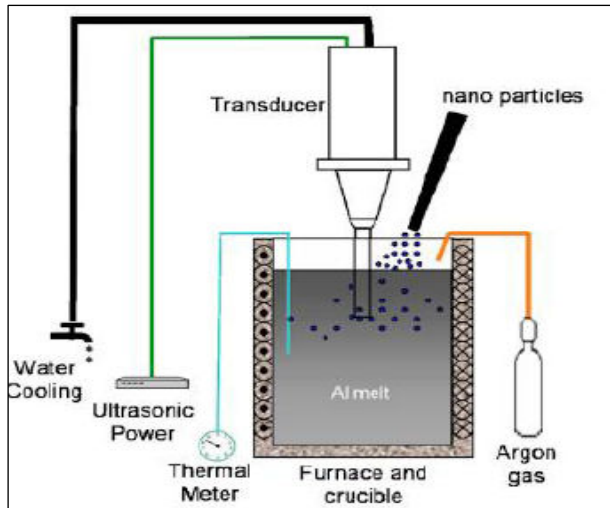


Fig.10. Schematic of ultrasonic solidification processing [43,44].

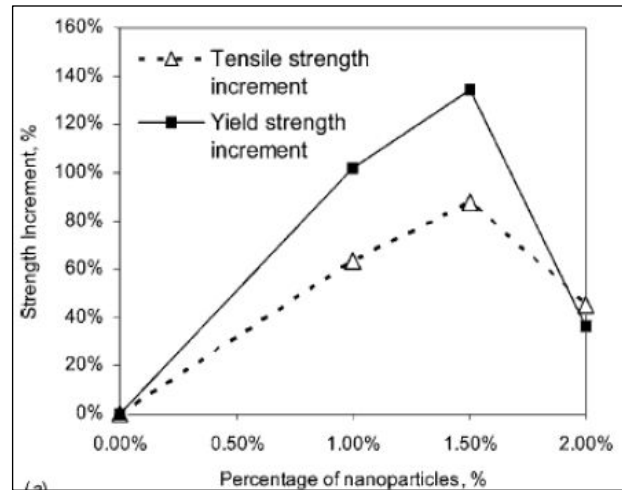


Fig. 11. Strength vs. percentage nano-particles added percentage [45].

One drawback of this technique is the dissolution of the oscillating probe in contact with the molten metal. To overcome such difficulty a non-contact method, where the ultrasonic probe is not in direct contact with the liquid metal, was attempted to disperse 10 nm Al_2O_3 particulates in aluminum matrix [46]. In this method the mold was subjected to ultrasonic vibration. The reinforcement was found to be uniformly distributed. The amount of material processed with ultrasonic cavitation based solidification generally does not exceed 200 g. The ultrasonic power necessary to achieve good particle dispersion is proportional to the amount of material processed. Therefore, industrial scale quantities would require enormous and costly power supplies.

Infiltration. The process consists of infiltrating a porous preform. Capillary forces and viscous drag through preform interstices hinder wetting of the preform by the melt. Evans et al. [30] observed from an “energetic” standpoint that metals generally do not bond to non-metals, and that the chemistry of the system must be modified, or external pressure must be applied. Chemical modification includes coating, adding special elements to the melt, or using special atmospheres [47,30]. Mechanical force reduces porosity and improves interfacial bond. Pressures of around ten atmospheres are needed to infiltrate the melt into 1 μm wide pores [30]. As a result, preform fragmentation, deformation and unevenly reinforced castings [47] may result. Kaptay [48] noted that that when the partially infiltrated liquid metal reaches the “equilibrium depth” (the depth at which interfacial forces are zero), further infiltration will occur by additional pressure. The threshold pressure is given by:

$$P_{\text{threshold}} = \frac{\pi}{R\sqrt{3}}(1.63\sigma_{lv} - W) \quad (6)$$

Where R is the particle radius, W the adhesion energy and σ_{lv} the interfacial energy between the liquid and vapor phases. The lower the particle radius, the higher is the threshold pressure. When pressures of some GPa are applied, nano-materials can be manufactured. Gierlotka et al. [49] used a toroid cell at pressures up to 7.7 GPa and temperatures up to 2000 °C for the infiltration of an alumina preform with a grain size of 10 nm. Schultz et al. [50] succeeded in the infiltration of an alumina preform with particle size of 50 with Al alloy A206. The composite showed an increase in hardness by 19% compared to the base alloy. The downside of the infiltration technique is the high cost of nano-sized ceramic preform. The latter is a significant disadvantage.

In brief, Ex-situ processes as described above have their distinct advantages and disadvantages. In general however, Ex-situ processes suffer from:

- Thermodynamic incompatibility: interfacial reactions between the reinforcements and the matrix may occur. Detrimental phases such as Al_4C_3 and Ti_5Si_3 have been detected in composite materials manufactured through mechanical stir casting;
- Contamination: oxide layers around the particles increase the surface energy, decreasing wettability of the system [51];
- Inhomogeneous microstructures: particle agglomeration and clustering occur.

In-situ methods

When nano-composite materials are synthesized via In-situ processes, fabrication issues associated with ex-situ methods are mitigated or completely alleviated. The benefits that in-situ manufacturing methods provide are [52]:

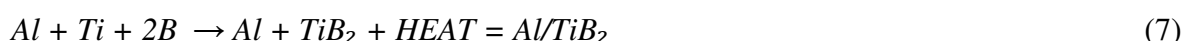
- Thermodynamic stability at high temperatures;
- Clean interface between particle and matrix, resulting in strong interfacial bonding. Detrimental phases are eliminated and the creation of the nascent interface can be guided by process control. Wear resistance is enhanced as a result;
- Range of particle size in the nanocomposite are lower than via Ex-situ processes;
- Improved distribution yields to superior mechanical properties;
- Composites with a broad variety of matrix materials (aluminum, titanium, copper, nickel and iron) and reinforcing particles (borides, carbides, nitrides, oxides and their mixtures) can be produced;
- Process is scalable and cost effective.

Commercial applications are still limited by the complexity of the reactions and the lack of knowledge concerning these techniques. The two classes of processes –reactive and morphological are described and discussed below.

Reactive processes: *solid-liquid state*

Elements or compounds react in the presence of a third liquid metallic phase that acts as a solvent medium. The reinforcement is generated via diffusion of components in the metal matrix [52]. Combustion synthesis, XD process, mixed salt reaction, direct metal oxidation and reactive synthesis are examples of solid-liquid processes. There are detailed below.

Combustion synthesis. Combustion synthesis (see Fig.12) -or self-propagating high-temperature synthesis (SHS)- was invented by Merzhanov et al. [53]. A mixture of powdered elements is initially prepared and pressed into cylindrical pellets. Electrically heated coils or a laser act as the heat source that initiates a chemical reaction between the various elements. The solvent can be molten Al, Mg, or Ti where other non metallic elements, such as C and B, are present. The ceramic compounds are burnt via ignition waves at a temperature higher than the melting point of the metal matrix. A typical reaction is:



The highly exothermic nature of the process allows it to be self-sustaining and is energy efficient. The heat released during the reaction keeps the propagation front stable by heating up the unreacted portion of the sample. The equipment is simple, processing times are short due to very high combustion rates (0.15 m/s) and metastable phases can be synthesized. In addition, volatile impurities are evaporated due to high temperature of the process. Although a variety of shapes and

geometries can be attained, porosity (up to 10%) in the final component still remains an issue. Further processing such as high-pressure consolidation is a necessary step. At present, a major program is underway between WPI and Colorado School of Mines to explore using combustion synthesis to die cast Al and Mg engine components that contain 20-40% second phases.



Fig.12. Combustion synthesis process [54].

Exothermic dispersion (XD process). The XD process was developed by Martin Marietta Corporation and has been extensively applied to the manufacturing of light-weight materials [52]. Jet engine turbine blades with weight savings of 30% to 50% have been fabricated with this process. It is a sustained high-temperature synthesis whose driving force is the difference of melting temperatures of the components. Ceramic phases and a third metallic phase are emplaced together and heated above the melting point of the metallic phase. The ceramic phases release heat and interact, forming very fine (nano-sized) particulates [52, 55], Fig.13. Particle size and distribution are system-dependent. It depends on the thermal conductivity of the environment and the amount of heat developed during the reaction. Tailoring the composition of the initial species can regulate the volume percentage of reinforcement. The exothermic reaction eliminates oxides and provides clean interfaces [52]. Hot isostatic pressing of the final component is necessary in order to reduce porosity.

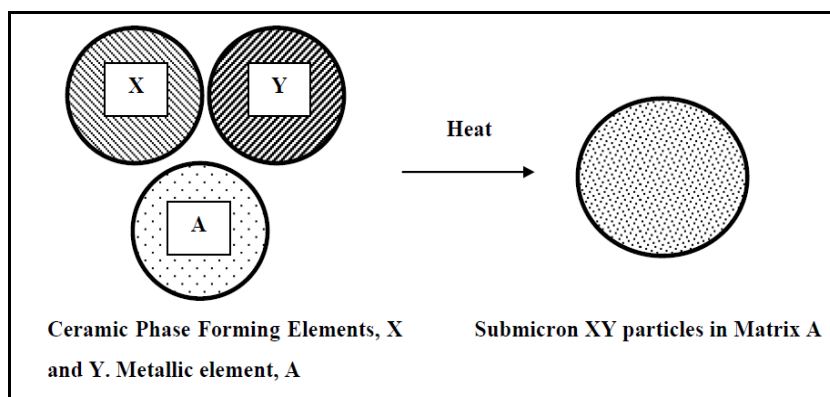
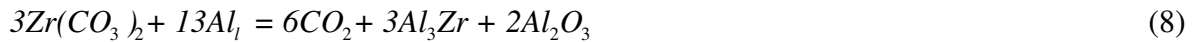


Fig.13. Schematic diagram of XD process [52].

Substitutional chemical reaction. An in situ copper matrix composite with 3.5 wt.% TiB_2 was prepared by thermic reactions of B_2O_3 , carbon as reduction agent and titanium in copper-titanium

melt [56]. The in situ-formed TiB_2 particles with a size of about 50 nm exhibited a homogenous dispersion in the copper matrix. Due to their reinforcement, the tensile strength and hardness of the in situ Cu– TiB_2 composite significantly improved. The in-situ composite also had a high electrical conductivity. Zhao et al. [57] synthesized nano-sized Al_2O_3 and Al_3Zr particles in aluminum in the system Al– $\text{Zr}(\text{CO}_3)_2$ according to the reaction:



A magnetic field is also applied in order to enhance the chemical reaction. The mean particle size is about 80 nm, and the nano-sized particles are well distributed in the Al matrix. The ultimate tensile strength and yield strength of the nanocomposites are enhanced with increasing of particulate volume fraction, and are higher than that of the Al nanocomposites synthesized under zero magnetic field.

Reactive processes: *liquid-liquid state*

The MixAlloy Process patented by Sutek Corporation [58] has been applied to manufacture nanocomposite materials. Two streams of metal melts containing ceramic inclusions interact with each other in a reaction chamber to form refractory particles. The mixture is then rapidly cast or atomized. Titanium boride particles in a copper matrix have been manufactured with this method. It has been reported [52] that particle sizes around 50 nm have been achieved. In the first process disclosure by Nam.P.Suh [58], the impingement between the metal streams is direct, while in a subsequent patent [59] the impingement is indirect. In this manner, instability in the metal streams are mitigated. The impingement may not provide adequate energy to mix the metal streams; in addition, un-reacted elements have been detected, even though the stoichiometry is locally maintained [59].

Reactive Processes: *gas-liquid state*

The gas-liquid process belongs to the category of in-situ techniques. A gas is injected into the aluminum melt composed by one or more elements. Such gas reacts chemically with the melt and form the reinforcement phase (Fig.14). Refractory elements can also be added to the melt to tailor the precipitates. Table 5 shows gases, matrices and secondary phases that can be synthesized, together with the chemical reactions involved [60-66] (Fig. 15). Tyagi et al. [67] manufactured aluminum nitrides with a diameter smaller than 1 μm , by bubbling ammonia gas in an Mg-Al melt. The temperature was kept at 900 $^\circ\text{C}$ and the gas was purged for 70 minutes with a constant flow rate. Shyu et al. [65] bubbled methane gas in Al-Ti melt to form TiC particles. The yield strength increased up to 18 % and the hardness by 20%. The size of the particles was smaller than 0.1 μm .

Precursor gas	Matrix composition	Reinforcement phase	Chemical reaction
N-bearing gas: N_2, NH_3	Pure Al, Al-Ti, Al-Si, Al-Mg, Al-Mg-Ti, Al-Mg-Si	AlN, TiN, TaN	$2NH_3 \rightarrow N_2 + 3H_2$ (1) $Al(l) + \frac{1}{2}N_2 = AlN$ (2) $Al-Ti + \frac{1}{2}N_2 \rightarrow Al + TiN$ (3) $Al-Ta + \frac{1}{2}N_2 \rightarrow Al + TaN$ (4)
C-bearing gas: CH_4	Al-Ti, Al-Si	TiC, SiC, Al_4C_3	$CH_4 + Ar \rightarrow C + 2H_2 + Ar$ (5) $Al-Si + C \rightarrow Al + SiC$ (6) $Al-Ti + C \rightarrow Al + TiC$ (7) $Al-Si + C \rightarrow Al-Si + Al_4C_3$ (8)

Table 5. Gas-Liquid Process Gases, Matrices, Products and Reactions.

The process is characterized by:

- Negligible costs. Gas is relatively inexpensive [60]. The particles are found in-situ alleviating the cost of expensive second phase nano-particles;
- Surface contamination is eliminated thus enhancing interfacial bonding;
- The thermodynamics of the process can be controlled to suppress the formation of unfavorable phases [60,61].
- Homogeneous microstructures are obtained. The particles are naturally dispersed in the metal matrix, Fig. 15 [60].

Some limitations of the process are [65]:

- The temperatures necessary for the reaction to occur are high (1300-1600 K depending on the gas and the matrix);
- High apparent viscosity hinders the production of high percentages of reinforcement;
- Process times may be lengthy as the kinetics are challenging;
- The method is not applicable to materials with high melting temperatures.

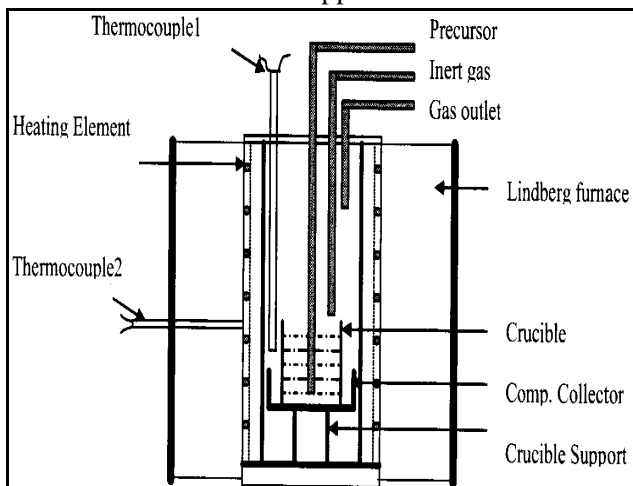


Fig.14. Schematic of gas-liquid process [61].

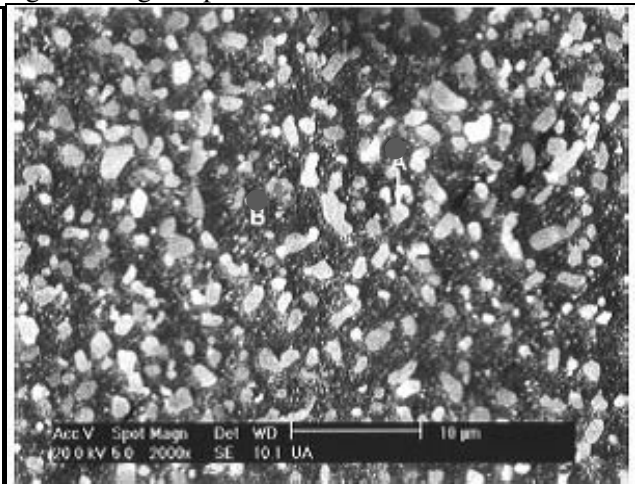


Fig. 15. AlN particles in Al matrix via gas-liquid process [60].

Morphological processes: rapid solidification

Nayak et al. [68] have melted under argon atmosphere Al-Fe alloys. Rapid solidification processing of the molten alloys was carried out by a single roller melt spinner with a copper wheel at different linear wheel speeds with cooling rates estimated to be in the range of 104–105 K/s.

Ultra-fine $\text{Al}_{100-x}\text{Fe}_x$ precipitates embedded in the α -Al matrix were found in the melt spun Al–2.5 % Fe alloy as shown in Fig.16. Most of the precipitates here are less than 20 nm in size that structurally resemble some nanoquasicrystalline (NQ) phase. Increasing iron content up to 5% gives a cellular microstructure of around 150 nm in size. TiC have also been fabricated by melting a mixture of Al, Ti, and graphite powder under argon atmosphere [36]. Chill block melt spinning was used to prepare rapidly solidified samples in ribbon form. The TiC particles were found to be 40-80 nm in size and some clusters detected at the grain boundaries.

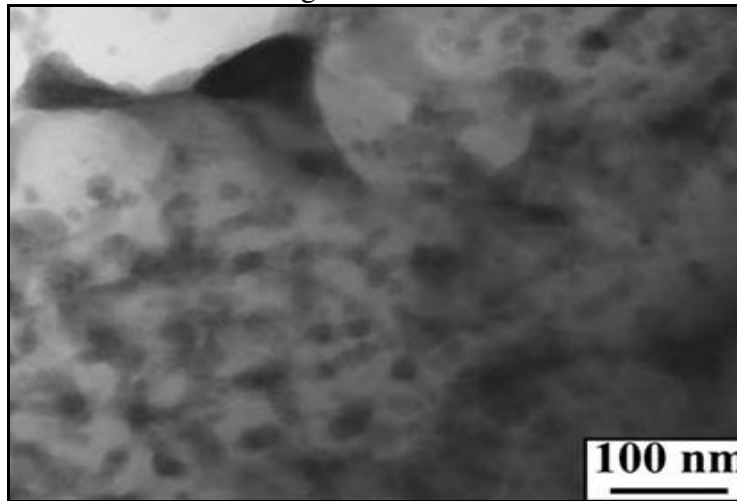


Fig.16. $\text{Al}_{100-x}\text{Fe}_x$ precipitates embedded in the α -Al matrix [68].

Concluding Remarks

The various pathways to manufacture metal matrix nanocomposites have been presented and discussed in this critical review. It is quite clear that the challenges we face in manufacturing nanocomposites for structural applications are daunting. *Scalability* is a critical issue; there are many reported methods for producing small quantities in a laboratory setting. However, commercial production on a large scale is another matter. To be able to manufacture nanocomposites with a *homogeneous distribution* of the second phase nano-sized particles is also another critical issue.

As presented and discussed in this review, this requirement remains to be the most difficult one especially for ex-situ processing methods. Homogeneous distribution of the nano-sized particles is more readily attainable via in-situ processing methods. Ex-situ methods are characterized by the difficulty to introduce the reinforcement in the melt and effectively disperse it (liquid state), as well as porosity and distortion in the final component (solid state). Lastly, cost is a major factor, as the processing method selected needs to be *cost-effective*. Composite materials (both micro- and nano-scale) are difficult to machine because of the wear action of reinforcement particles on the cutting tool. Therefore, there is the impellent need to select manufacturing methods which can provide near-net shape, so that the machining step could be eliminated. The knowledge of properties of the composite material, such as *tribological properties*, is fundamental for the design stage. Such data greatly differ from the matrix properties and have a consistent impact on the behavior of the final component. For instance, friction coefficients influence coupling and therefore lubrication between parts of an automotive assembly, as well as coefficients of thermal expansion have to be taken account when the cooling system of a component subjected to high temperatures is designed. The optimal method to determine such properties for nanocomposite materials needs to be established.

References

- [1] S.Rawal: J.Mater. Vol. 53 (2001), pp.14-17.
- [2] Information on
http://www.secat.net/answers_view_article.php?article=Aluminum_Matrix_Composites.html
- [3] Information on <http://www.almmc.com/>
- [4] Information on [http://www.thefreelibrary.com/Increased aluminum in automobiles saving weight and fuel consumption-a0159786251](http://www.thefreelibrary.com/Increased+aluminum+in+automobiles+saving+weight+and+fuel+consumption-a0159786251)
- [5] A.Wielgat: Automot. Ind. (2002).
- [6] Information on <http://news.alibaba.com/article/detail/metalworking/100187048-1-metals-knowledge%253A-automotive-trends-aluminum%252C.html>
- [7] Information on [http://www.thefreelibrary.com/Justifying Aluminum Metal Matrix Composites in an Era of Cost Redution-a060015013](http://www.thefreelibrary.com/Justifying+Aluminum+Metal+Matrix+Composites+in+an+Era+of+Cost+Redution-a060015013)
- [8] M. El-Gallaba and M. Skladb: J. Mater. Process. Tech. Vol. 83 (1998), pp. 277–285.
- [9] S. Jahanmir, M. Ramulu and P. Koshy in: *Machining of Ceramics and Composites*, edited by CRC Press, (1999).
- [10] Mod. Cast. (September 2010), p.3.
- [11] P.E.C. Camargo, K. G. Satyanarayama and F. Wypych: Mater. Res. Vol. 12 (2009), pp. 1-39.
- [12] S. M. Zebarjad, S. A. Sajjadi and E. Z. Vahid Karimi: Res. Lett. Mater. Sci. (2008), pp. 1-4.
- [13] Information on <http://www.materials.unsw.edu.au/NanoWeb>
- [14] Information on scales.colorado.edu/classes/MCEN5208_F2004/.../lit_Fischer.doc
- [15] Information on http://etd.lib.nsysu.edu.tw/ETD-db/ETD-search-c/view_etd?URN=etd-0717106-184541
- [16] Q. Zhang and D. L. Chen: Scripta Mater. Vol. 54 (2006), pp. 1321–1326.
- [17] M. Cournil, F.Gruy, P. Cugniet, P. Gardina and H. Saint-Raymond in *Model of Aggregation of Solid Particles in Nonwetting Liquid Medium*, Centre SPIN, URA CNRS 2021, Ecole Nationale Supérieure des Mines de Saint-Etienne.
- [18] Information on <http://www2.ocean.washington.edu/oc540/lec02-26/>
- [19] G Cao, J. Kobliska, H. Konishi, and X. li: Metall. Mater. Trans. Vol. 39A (2008), pp. 880-886.
- [20] S. Melis and A. Sorti: AIChE Journal Vol. 45 No. 7 (2009).
- [21] Rhonda Lee-Desautels: Educ. Reso. for Part. Techn. 051Q-Lee.
- [22] D. Bozic, M. Vilotijevic, V. Rajkovic and Z. Gnjidic: Mater. Sci. Forum Vol. 492 (2005), pp.487-492.
- [23] N. Matsunagaa, K. Nakahamaa, Y. Hiratab and S. Sameshimab: J. Ceram. Process. Res. Vol. 10 No. 3 (2009), pp. 319-324.
- [24] S. Shamsudin, M. M. Wahid and S. Jamaludin: 1st International Conference on Sustainable Materials (ICoSM2007) (2007).

- [25] W. Zhou and Z. M. Xu: *J. Mater. Process. Tech.* Vol. 63 (1999), pp. 358-363.
- [26] N.J. Fei, L. Katgerman and W. Kool: *J. Mater. Sci.* Vol. 29 No. 24 (1994), pp.6439-6444.
- [27] C. Tekmen, F. Saday, U. Cocen and L.Y. Ljungberg: *J. Compos. Mater.* Vol. 42 No. 16 (2008), pp. 1671-1771.
- [28] R. Kolhe, C.Y. Hui, E. Ustundag and S.L. Sass: *Acta Mater.* Vol. 44 No. 1 (1999), pp. 279-287.
- [29] S.Suresh, A. Mortensen and A. Needleman in *Fundamentals of Metal Matrix Composites*, edited by Butterworth-Heinemann, (1993).
- [30] A. Evans, C. San Marchi and A. Mortensen in *Metal Matrix Composites in Industry: An Introduction and a Survey*, edited by Springer, (2003).
- [31] P. M. Ajayan, L. S. Schadler and P. V. Braun in *Nanocomposite Science and Technology*, edited by Wiley-VCH, (2003).
- [32] C. C. Koch in *Nanostructured Materials: Processing, Properties, and Applications*, edited by William Andrew, (2006).
- [33] A. Evans, C. San Marchi, A. Mortensen, "Metal Matrix Composites in Industry: an Introduction and a Survey, Volume 1", Springer, 2003.
- [34] N. Chawla and K. Chawla in *Metal Matrix Composites*, edited by Birkhäuser, (2006).
- [35] N.K.Tolochko, A.A.Andrushevic and Yu A. Shienok: *Adv. Mater. Res.* Vols. 79-82 (2009), pp.425-428.
- [36] G.Cao in *Nanostructures & Nanomaterials: Synthesis, Properties & Applications*, edited by Imperial College Press, (2004).
- [37] Z.Y. Ma, Y.L. Lia, Y. Liang, L F. Zheng , J. BP and S.C. Tjong: *Mat. Sci. Eng.* Vol. A219 (1996), pp. 229-231.
- [38] J. Peng, U.S. Patent 7,297,310 (2007).
- [39] C. L. De Castro and B. S. Mitchell in *Synthesis, Functionalization and Surface Treatment of Nanoparticles*, edited by American Scientific Publishers (2002).
- [40] D.L. Zhang, J. Liang and J. Wu: *Mat. Sci. Eng.* Vols. A375-377 (2004), pp. 911-916.
- [41] Information on
http://www.sigmaaldrich.com/etc/medialib/docs/Aldrich/Brochure/al_chemfile_v5_n3.Par.0001.File.tmp/al_chemfile_v5_n3.pdf
- [42] L. Xiaodan: TMS 2010 139th Annual Meeting and Exhibition, Supplemental Proceedings, Vol. 2, Materials Characterization, Computation, Modelling and Energy.
- [43] Y.Yang and X.Li: *J. Manuf. Sci. Eng.* Vol.129 (2004), pp.497-501.
- [44] Y.Yang, J.Lan and X.Li: *Mat. Sci. Eng.* Vol. A380 (2004), pp. 378-383.
- [45] Y.Yang, X.Li and X.Cheng: *J. Mater. Sci.* Vol. 39 (2004), pp.3211-3212.
- [46] P.Padhi, S.C.Panigrahi and S.Ghosh: *AIF Conf. Proc.* 1063 (2008), pp.371-375.

- [47] R. Ashtana in: *Solidification Processing of Reinforced Metals*, Trans. Tech Publications,(1997).
- [48] G.Kaptay in Proc. of the 2nd Int. Conf. High Temperature Capillarity, edited by N.Eustathopoulos and N.Sobczak, published by Foundry Research Institute, Cracow, Poland (1998), pp. 388-393 .
- [49] S. Gierlotka: *Solid State Phenom.* Vols. 101-102 (2005), pp. 157-164.
- [50] B. F. Schultz: Ph.D, The University of Wisconsin – Milwaukee (2009), 208 pages, 3363450.
- [51] Q.Zheng, B.Wu and R.G. Reddy: *Adv. Eng. Mater.* Vol. 5 No. 3 (2003), pp. 167-173.
- [52] S.C. Tjong and Z.Y. Ma: *Mater. Sci. Eng.* Vol. 29 (2000), pp. 49-113.
- [53] A.G.Merzhanov, A.S.Rogachev and A.E.Sychev: *Dokl. Phys. Chem.* Vol.362 No. 1-3 (1998), pp.217-221.
- [54] Information on www.spaceflight.esa.int/.../combustion.jpg
- [55] C.M.Ward-Close, R. Minor and P.J. Doorbar: *Intermetallics* Vol. 4 (1996), pp.217-229.
- [56] J.Tu, N.Wang, Y.Yang and W.Qu: *Mater. Lett.* Vol. 52 No. 6 (2002), pp. 448-452.
- [57] Y.Zhao, S.Zhang, G.Chen, X.Cheng and Q.Wang: *Compos. Sci. and Techn.* Vol. 68 (2008), pp. 1453-1470.
- [58] Nam P. Suh Sutek Corporation, U.S. Patent 4278622 and 4279843 (1981).
- [59] Nam P. Suh Sutek Corporation, U.S. Patent 4,706,730 and 4,890,662 (1987).
- [60] Q.Zheng and R.G.Reddy: *Metall. Mater. Trans.* Vol. 34B (2003), pp. 793-805.
- [61] Q. Zheng, B.Wu and R.G. Reddy: *Adv. Eng. Mater.* Vol. 5 No. 3 (2003), pp. 167-173.
- [62] Q. Zheng and R.G. Reddy: *J. Mater. Sci.* Vol. 39 (2004), pp. 141-149.
- [63] R. G. Reddy, US Patent 6,343,640 (2002).
- [64] R.F. Shyu, F.T. Weng and C.T. Ho: *J. Mater. Process. Technol.* Vol. 122 (2002), pp. 301–304.
- [65] R.F. Shyu and C.T. Ho: *J. Mater. Process. Technol.* Vol. 171 (2006), pp. 411–416.
- [66] M.Dyzia and J.Sleziona: *Arch. Mater. Sci. Eng.* Vol. 31 (2008), pp.17-20.
- [67] S.Tyagi, Q.Zheng and R. Reddy: *Aluminum* 2004, edited by S. K. Das, TMS, Warrandale, (2004), pp. 63-72.
- [68] S. S. Nayak, B.S.Murty and S.K.Pabi: *Bull. Mater. Sci.* Vol. 31 No. 8 (2008), pp. 249-254.

Advances in Metal Matrix Composites

10.4028/www.scientific.net/MSF.678

Manufacture of Aluminum Nanocomposites: A Critical Review

10.4028/www.scientific.net/MSF.678.1

DOI References

- [11] P.E.C. Camargo, K. G. Satyanarayama and F. Wypych: Mater. Res. Vol. 12 (2009), pp. 1-39.
doi:10.1590/S1516-14392009000100002
- [12] S. M. Zebarjad, S. A. Sajjadi and E. Z. Vahid Karimi: Res. Lett. Mater. Sci. (2008), pp. 1-4.
doi:10.1155/2008/835746
- [19] G Cao, J. Kobliska, H. Konishi, and X. li: Metall. Mater. Trans. Vol. 39A (2008), pp. 880-886.
doi:10.1007/s11661-007-9453-6
- [26] N.J. Fei, L. Katgerman and W. Kool: J. Mater. Sci. Vol. 29 No. 24 (1994), pp.6439-6444.
doi:10.1007/BF00354001
- [27] C. Tekmen, F. Saday, U. Cocen and L.Y. Ljungberg: J. Compos. Mater. Vol. 42 No. 16 (2008), pp. 1671-1771.
doi:10.1177/0021998308092217
- [29] S.Suresh, A. Mortensen and A. Needleman in Fundamentals of Metal Matrix Composites, edited by Butterworth-Heinemann, (1993).
doi:10.1115/1.2900781
- [30] A. Evans, C. San Marchi and A. Mortensen in Metal Matrix Composites in Industry: An Introduction and a Survey, edted by Springer, (2003).
doi:10.1016/S1359-6462(03)00441-X
- [31] P. M. Ajayan, L. S. Schadler and P. V. Braun in Nanocomposite Science and Technology, edited by Wiley-VCH, (2003).
doi:10.1002/3527602127.index
- [34] N. Chawla and K. Chawla in Metal Matrix Composites, edited by Birkhäuser, (2006).
doi:10.1007/s11837-006-0231-5
- [49] S. Gierlotka: Solid State Phenom. Vols. 101-102 (2005), pp. 157-164.
doi:10.4028/www.scientific.net/SSP.101-102.157
- [61] Q. Zheng, B.Wu and R.G. Reddy: Adv. Eng. Mater. Vol. 5 No. 3 (2003), pp. 167-173.
doi:10.1002/adem.200390027
- [62] Q. Zheng and R.G. Reddy: J. Mater. Sci. Vol. 39 (2004), pp. 141-149.
doi:10.1023/B:JMSC.0000007738.14116.fd
- [11] P.E.C. Camargo, K. G. Satyanarayama and F. Wypych: Mater. Res. Vol. 12 (2009), pp. 1-39.
doi:10.1590/S1516-14392009000100002
- [12] S. M. Zebarjad, S. A. Sajjadi and E. Z. Vahid Karimi: Res. Lett. Mater. Sci. (2008), pp. 1-4.
doi:10.1155/2008/835746
- [19] G Cao, J. Kobliska, H. Konishi, and X. li: Metall. Mater. Trans. Vol. 39A (2008), pp. 880-886.
doi:10.1007/s11661-007-9453-6
- [26] N.J. Fei, L. Katgerman and W. Kool: J. Mater. Sci. Vol. 29 No. 24 (1994), pp.6439-6444.
doi:10.1007/BF00354001

- [27] C. Tekmen, F. Saday, U. Cocen and L.Y. Ljungberg: *J. Compos. Mater.* Vol. 42 No. 16 (2008), pp. 1671-1771.
doi:10.1177/0021998308092217
- [29] S.Suresh, A. Mortensen and A. Needleman in *Fundamentals of Metal Matrix Composites*, edited by Butterworth-Heinemann, (1993).
doi:10.1115/1.2900781
- [30] A. Evans, C. San Marchi and A. Mortensen in *Metal Matrix Composites in Industry: An Introduction and a Survey*, edited by Springer, (2003).
doi:10.1016/S1359-6462(03)00441-X
- [31] P. M. Ajayan, L. S. Schadler and P. V. Braun in *Nanocomposite Science and Technology*, edited by Wiley-VCH, (2003).
doi:10.1002/3527602127.fmatter
- [34] N. Chawla and K. Chawla in *Metal Matrix Composites*, edited by Birkhäuser, (2006).
doi:10.1007/s11837-006-0231-5
- [49] S. Gierlotka: *Solid State Phenom.* Vols. 101-102 (2005), pp. 157-164.
doi:10.4028/www.scientific.net/SSP.101-102.157
- [61] Q. Zheng, B.Wu and R.G. Reddy: *Adv. Eng. Mater.* Vol. 5 No. 3 (2003), pp. 167-173.
doi:10.1002/adem.200390027
- [62] Q. Zheng and R.G. Reddy: *J. Mater. Sci.* Vol. 39 (2004), pp. 141-149.
doi:10.1023/B:JMSC.0000007738.14116.fd

Aluminum Nanocomposites via Gas Assisted Processing

Cecilia Borgonovo^a and Diran Apelian^b

Metal Processing Institute, WPI, Worcester, MA 01609 USA

^acborgonovo@wpi.edu ^bdapelian@wpi.edu

Keywords: lightweight, nanocomposites, aluminum, magnesium, gas-assisted process, nitridation.

Abstract. Aluminum nitride (AlN) possesses superior thermal and electrical properties and is an ideal candidate for high-temperature, as well as for packaging and optoelectronic applications. Aluminum based composites reinforced with AlN have been manufactured via an in situ gas-assisted process, where nitrogen gas is injected in the molten aluminum at 1273-1323 K. The process is carried out in an inert atmosphere in order to avoid oxygen contamination. Addition of Mg lowered the oxygen content in the melt by forming MgO and thus favoring the nitridation reaction. The reinforcement phase has been detected throughout the casting in two morphologies: pockets of powders and embedded in the microstructure. Particle size formed in the matrix varied from 1- 3 μm to sub-micron scale.

Introduction

Particulate reinforced metal matrix composites have been widely used in modern engineering applications. With the development of nanotechnologies, the particulate size progressively scaled down to the nano-level. Aluminum matrix nanocomposites reinforced with ceramic particles (AlN, Al₂O₃, SiC) are gradually being implemented into production in automotive, electronic or aircraft industries due to their promising mechanical and thermal properties: higher strength, hardness, stiffness, dimensional stability at high temperatures, and creep resistance. However, obtaining a composite material non-susceptible to cracking and whose ductility is retained requires the successful dispersion of the reinforcement phase in the matrix [1]. Numerous attempts have been made to overcome particle agglomeration and to establish an industrially scalable and cost-effective route for the fabrication of nanocomposite materials.

Several near-commercial manufacturing methods have been pursued, such as mechanical alloying, powder metallurgy, infiltration techniques and spray deposition. All these techniques involve the addition of ceramic reinforcements to the matrix materials (*ex-situ processes*), which may be in molten or powder form. However, they are expensive and do have their own limitations, especially when the reinforcement size is in the nano-scale range. Agitation techniques are cost-effective, but agglomeration due to Van der Waals forces cannot be avoided. Surface contamination also affects the reliability of *ex-situ* techniques through interfacial reactions and poor wettability between matrix and reinforcement. Particle dispersion via ultrasonic processing has been achieved but the process suffers from scalability issues.

A class of novel composites, in which the reinforcements are synthesized by chemical reactions (*in-situ processes*), addresses the challenges associated with manufacturing of nanocomposites. Compared to *ex-situ* methods, these *in-situ* processes exhibit cleaner and thermodynamically stable interfaces, resulting in less degradation at elevated-temperatures and strong interfacial bonding. Moreover, the *in-situ* formed particles are finer in size and their distribution in the matrix is uniform.

Among the wide range of in-situ techniques, the synthesis of nitride particles by means of a gas-assisted reaction, patented by Koczak and Kumar [2], has shown promise. Aluminum nitride is a refractory compound characterized by attractive properties such as high thermal conductivity, high electrical resistance, low dielectric constant, and a thermal expansion coefficient similar to silicon [3,4]. Hou et al. [3] have been able to manufacture aluminum matrix composites reinforced with AlN with a diameter smaller than $0.1\ \mu\text{m}$. Zheng et al. [5] have converted 14% weight of Mg-Al alloy into aluminum nitrides with a diameter of 400 nm. Tyagi et al. [6] also manufactured aluminum nitrides with a diameter smaller than $1\ \mu\text{m}$ by bubbling ammonia gas in an Mg-Al melt. The composite material is formed in three stages: reactive gas dissociation, synthesis of reinforcing phases and kinetics of their growth [1,7]. Reinforcement particles are created as a result of the intensive exothermic reaction of gas cavities with metal alloying additions, such as Mg, Ti, and Si [1]. Significant advantages of this method are the possibility of applying casting techniques for forming the products [8], and of tailoring the matrix-reinforcement system by selecting reactive gas and alloying elements. However, the gas-assisted reaction process is affected by challenging control of process variables and repeatability issues. In addition, the temperatures necessary for the reaction to occur are high ($1000\text{-}1300\ \text{C}^\circ$ depending on the gas and the matrix) [9,10].

The aim of the present investigation is to highlight the dynamics of aluminum nitridation and the mechanism of nitride formation *via* the injection of nitrogen gas in the melt.

Experimental Details

A stainless steel sealed resistance chamber was evacuated and purged several times with Argon gas (Grade 5, Aimtek). During the heating process, inert atmosphere was maintained by constantly injecting Argon at a flow rate of 0.2 l/min. The ceramic crucible was placed at the bottom of the chamber where the temperature profile is more uniform. Two K-type thermocouples inserted in the furnace walls and inside the crucible were used to monitor the temperature. Once the process temperature ($1000\ \text{C}^\circ$) was achieved, a 1.5 mm diameter alumina tube was submerged in the melt and High Purity Nitrogen gas (99.9999% purity, Aimtek) bubbled for 6 to 8 hours through the tube at a flow rate of 0.1 l/min and a pressure of 0.1 MPa. Two high capacity oxygen-and moisture-removal traps were used in series at the gas inlet. Each trap had the capability to lower the oxygen content to less than 1 ppb and the moisture level to less than 10 ppb. Alloy compositions selected for the experiments are 100wt% Al and Al-15wt% Mg. Each casting involved the melting of 150 g of metal previously ultrasonically cleaned for 20 minutes. X-Ray Diffraction (XRD) analysis was also performed in order to detect the presence of nitrides and secondary phases. Field Emission Gun SEM has been employed for microstructure observation, Energy Dispersive X-ray (EDS) microanalysis and X-ray mapping.

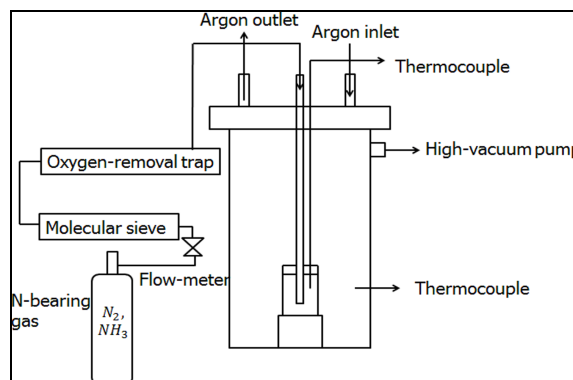


Fig. 1: Experimental set-up.

Results and Discussion

No AlN were detected in the matrix when pure Al was used as the parent material. Such result can be attributed to the presence of oxygen in the Nitrogen gas, which has a detrimental effect on aluminum nitridation. Oxygen preferentially reacts with aluminum to form aluminum oxide, inhibiting the nitridation reaction [7,10,11]. This has been demonstrated empirically by measuring the time required to form aluminum nitride and the time required to form aluminum oxide, where it has been found that the rate of nitridation of aluminum is several orders of magnitude slower than the rate of its oxidation at any given temperature [11]. Thermodynamic analysis of the equilibrium reaction (Eq.1) confirms the preferential formation of Al_2O_3 versus AlN. The Gibbs free energy calculation (Eq.2) shows that the permissible oxygen partial pressure for the nitridation reaction P_{O_2} at $1000^\circ C$ is around 10^{-19} Pa and directly proportional to the process temperature T .



$$\Delta G = 2,057,400 - 184.4T \cong -RT \ln \left(\frac{P_{O_2}}{P_{atm}} \right)^3 \rightarrow P_{O_2} = 18.9 - \frac{82,487.4}{T} \quad (2)$$

This very low oxygen content is not achievable with commercially available nitrogen gases. Moreover, the processing temperature for aluminum alloys should not exceed $1000^\circ C$. This is mainly dictated by the cost of energy and deterioration of the furnace furniture. Therefore, efforts have been made to minimize oxygen in the reaction chamber by passing the stream of nitrogen gas through traps filled with deoxidizing materials (such as Cu and Mn) and evacuating the furnace chamber prior to melting. Yet, oxygen in the system remains high enough to render the current technology inefficient for the synthesis of Al-AlN composite materials through direct nitridation of aluminum.

This suggests that nitridation of aluminum requires the presence of a catalyst such as Mg. Several publications refer to this mechanism as more likely to be responsible for nitride formation than direct nitridation [5,10,12]. The addition of 15% Mg to the aluminum matrix was investigated and resulted in the synthesis of a consistent amount of aluminum nitrides.

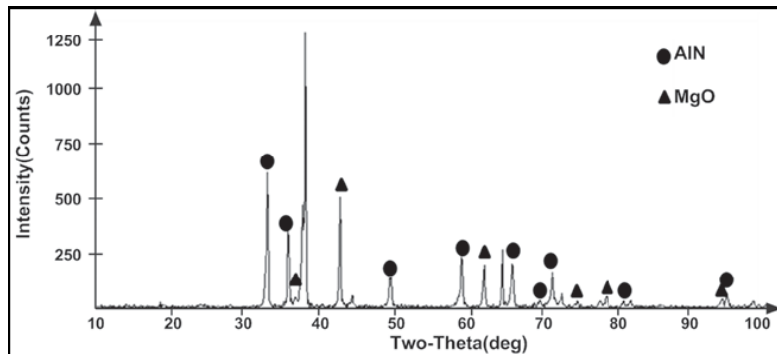


Fig.2: XRD pattern of the upper part of the crucible for Al-15%wt. Mg.

XRD analysis (Fig.2) of the upper part of the crucible confirms strong peaks for AlN along with peaks for MgO (periclase). SEM analysis shows the presence of AlN throughout the length of the resultant casting. AlN particles have been found in two different morphologies: (i) embedded in the microstructure in the lower section of the casting (Fig. 3), and (ii) as pockets of powder in the upper section of the casting (Fig. 4). In the powder phase, MgO is located on the AlN particles and tightly connected with them. The size of AlN is $\sim 1 \mu m$ for AlN embedded in the microstructure and in the submicron range (around $0.4 \mu m$) in the powder phase. Size control as well as optimized nitride distribution along the casting still remains an issue and it is currently being studied at WPI.

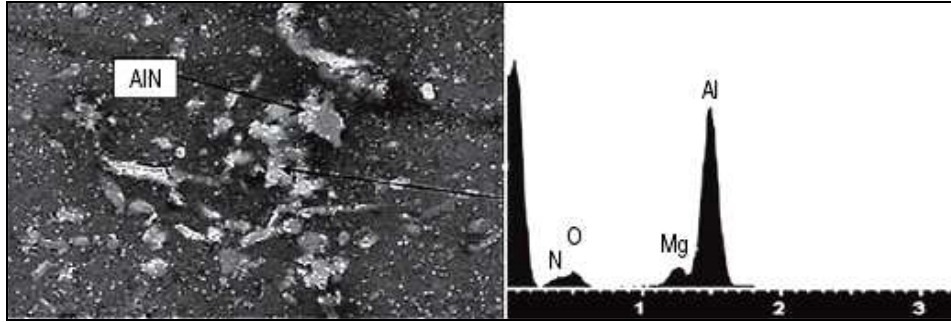


Fig.3: SEM image and EDS spectrum of AlN embedded in the matrix in the lower section of the casting. Al-15%wt. Mg matrix.

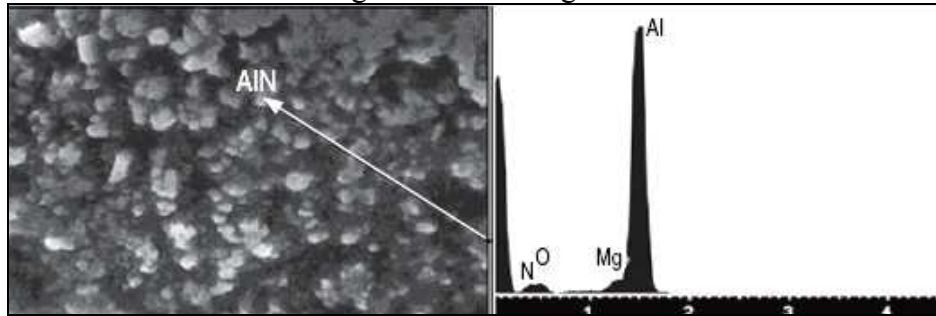


Fig.4: SEM image and EDS spectrum of pockets of AlN and MgO powder in the lower section of the casting. Al-15%wt. Mg matrix.

The catalytic action of Mg can be explained as follows. At high temperatures, Mg vaporizes (Eq.3) and acts as an “oxygen-getter”. It combines with oxygen to form MgO (Eq.4) and thus locally lowers the partial pressure of the residual oxygen in the nitriding gas.



$$P_{O_2} = \gamma_{Mg}^{-2} x_{Mg}^{-2} \exp\left(\frac{2\Delta G_3 + \Delta G_4}{2RT}\right) \quad (5)$$

Depending on the temperature and the concentration of Mg, the equilibrium partial pressure of O_2 is given by Eq. 5, where γ_{Mg} is the activity coefficient of Mg, x_{Mg} is the Mg concentration, ΔG_3 and ΔG_4 are the standard Gibbs energy changes for reactions 3 and 4, respectively. From thermodynamic data reported in the literature, the partial pressure of the residual oxygen for 15 wt.% Mg in aluminum matrix is in the range of 0.1 Pa (versus 10^{-19} of pure Al matrix), which can be achieved by commercial deoxidizing traps.

Concluding Remarks

Aluminum nitridation via gas-assisted nitridation of aluminum is feasible. The in-situ route to manufacture nanocomposites has the potential to be a commercial process where scalability, homogeneous distribution and cost-effectiveness are important criteria. AlN particles, whose thermal and electrical properties are exceptional, have been successfully synthesized. They have been observed throughout the bulk and they are present in two morphologies: (i) embedded in the matrix, and (ii) as pockets of powder with MgO. The size of AlN ranges from 0.4 μm to about than 1 μm . The catalytic action of Mg as “oxygen-getter” has also been confirmed by the absence of AlN in the pure aluminum matrix, and by MgO tightly connected to the nitride phase. Mg lowers the local oxygen partial pressure in the melt, allowing aluminum nitridation to occur.

The control of AlN particle size and the kinetics of the nitridation process need further study. This work is continuing to establish the mechanisms to address the kinetics of the reaction in order to enable us to attain particles that are in the nano-range.

Acknowledgments

The authors gratefully acknowledge the member companies of the Advanced Casting Research Center for their support of this work, and for their continued support of research focused on the science and technology of metal casting at Worcester Polytechnic Institute.

References

- [1] S.C. Tjong, Z.Y. Ma, *Mat. Sci. Eng. Vol. 29* (2000), pp. 49-113.
- [2] M.J. Koczak and K.S. Kumar, U.S. Patent 4,808,372.370. (1989)
- [3] Q. Hou, R. Mutharasan and M. Koczak, *Mat. Sci. Eng. Vol. A195* (1995), pp. 121-129.
- [4] J. Haibo, K. Chen, Z. Heping, S. Agathopoulos, O. Fabrichnaya, and J.M.F. Ferreira, *J. Crystal Growth*, Vol. 281 (2005), pp. 639–645.
- [5] Q. Zheng and R. Reddy, *Metall. Mater. Trans. Vol. 34B* (2003), pp. 793-805.
- [6] S.Tyagi, Q.Zheng and R. Reddy, *Aluminum 2004*, edited by S. K. Das, TMS, Warrendale, (2004), pp. 63-72.
- [7] Q. Zheng and R. Reddy, *Adv. Eng. Mater. Vol. 5 No. 3* (2003), pp. 167-173.
- [8] M.K.Prenkumar and M.G.Chu, *Mat. Sci. Eng. Vol. A202* (1995), 172-178.
- [9] Q. Zheng and R.G. Reddy, *Affordable Metal Matrix Composites for High Performance Applications II*, ed. A.B. Pandey, K.L. Kendig, J.J. Lewandowski, and S.R. Shah (Warrendale, PA: TMS, 2003), pp. 125–134.
- [10] Q. Zheng and R.G. Reddy, *J. Mater. Sci. Vol. 39* (2004), pp. 141–149.
- [11] H. Scholz and P. Greil, *J. Mater. Sci. Vol. 26 No. 3* (1991), pp. 669–677.
- [12] M. I. Pech-Canul, R.N. Katz and M. M. Makhlof, *Metall. Mater. Trans. Vol. 31A* (2000), pp. 565-573.

Light Metals Technology V

10.4028/www.scientific.net/MSF.690

Aluminum Nanocomposites via Gas Assisted Processing

10.4028/www.scientific.net/MSF.690.187

DOI References

[3] Q. Hou, R. Mutharasan and M. Koczak, *Mat. Sci. Eng. Vol. A195* (1995), pp.121-129.

doi:10.1016/0921-5093(94)06511-X

[4] J. Haibo, K. Chen, Z. Heping, S. Agathopoulos, O. Fabrichnaya, and J.M.F. Ferreira, *J. Crystal Growth*, Vol. 281 (2005), p.639–645.

doi:10.1016/j.jcrysgr.2005.04.024

[11] H. Scholz and P. Greil, *J. Mater. Sci. Vol. 26 No. 3* (1991), p.669–677.

doi:10.1007/BF00588302

[12] M. I. Pech-Canul, R.N. Katz and M. M. Makhlof, *Metall. Mater. Trans. Vol. 31A* (2000), pp.565-573.

doi:10.1023/A:1004758305801

[3] Q. Hou, R. Mutharasan and M. Koczak, *Mat. Sci. Eng. Vol. A195* (1995), pp.121-129.

doi:10.1016/0921-5093(94)06511-X

[4] J. Haibo, K. Chen, Z. Heping, S. Agathopoulos, O. Fabrichnaya, and J.M.F. Ferreira, *J. Crystal Growth*, Vol. 281 (2005), p.639–645.

doi:10.1016/j.jcrysgr.2005.04.024

[11] H. Scholz and P. Greil, *J. Mater. Sci. Vol. 26 No. 3* (1991), p.669–677.

doi:10.1007/BF00588302

[12] M. I. Pech-Canul, R.N. Katz and M. M. Makhlof, *Metall. Mater. Trans. Vol. 31A* (2000), pp.565-573.

doi:10.1023/A:1004758305801

Processing of Lightweight Metal Matrix Composites *via* In-Situ Gas/Liquid Reaction

Cecilia Borgonovo^a and Diran Apelian^b

Metal Processing Institute, Worcester Polytechnic Institute
Worcester, MA 01609 USA

^acborgonovo@wpi.edu, ^bdapelian@wpi.edu

Keywords: lightweight, composites, aluminum, magnesium, gas/liquid reaction, nitridation.

Abstract. Aluminum nitride (AlN) possesses superior thermal and electrical properties and is an ideal candidate for high-temperature, as well as for packaging and optoelectronic applications. Aluminum based composites reinforced with AlN have been manufactured via an in situ gas-assisted process, where a nitrogen-bearing gas is injected in the molten aluminum at 1273-1323 K. The process is carried out in an inert atmosphere in order to avoid oxygen contamination. Addition of Mg lowered the oxygen content in the melt by forming MgO and thus favoring the nitridation reaction. Particle size formed in the matrix varied from 1- 3 μm to sub-micron scale depending on the gas injection time. Longer bubbling times give rise to improved reinforcement dispersion. Addition of Si is detrimental for the synthesis of AlN; Mg₂Si phase precipitates, replacing the formation of MgO and hindering the nitridation reaction. The challenges of controlling the kinetics are discussed.

Introduction

Aluminum based nanocomposites have increasingly gained attention as weight-saving functional materials with improved mechanical properties. Carbide or nitride particles are added to the aluminum matrix to attain superior hardness, wear resistance and dimensional stability at high temperatures. Several manufacturing methods such as mechanical stirring, infiltration and powder metallurgy have been employed to date and the subject has been covered in some detail in a critical review by the authors [1]. None of the ex-situ conventional processes meet the three key challenges: *scalability, homogeneous distribution, and cost-effectiveness*. In contrast, in-situ synthesis routes offer pathways that address key challenges in the manufacture of nanocomposites for structural applications [2,4,5]. The secondary phase is created in-situ through a chemical reaction; the in-situ creation of the reinforcement phase ensures clean and thermodynamic stable interfaces and good particle dispersion. Moreover, it is possible to produce composites with a broad variety of matrix materials (aluminum, titanium, copper, nickel and iron) and reinforcing particles (borides, carbides, nitrides, oxides and their mixtures).

Among the wide range of in-situ techniques, the synthesis of nitride particles by means of a gas-assisted reaction has shown promise. Hou et al. [3] have been able to manufacture aluminum matrix composites reinforced with AlN with a diameter smaller than 0.1 μm . Zheng et al. [4] have converted 14% weight of Mg-Al alloy into aluminum nitrides. The process involves the introduction of a nitrogen-bearing gas in the melt so that nitridation of aluminum takes place. Control of process variables (processing temperature and time amongst others) can tailor the amount and size of the reinforcement in the matrix [4,5]. Aluminum nitride is a refractory compound characterized by attractive properties such as high thermal conductivity, high electrical resistance, low dielectric constant, and a thermal expansion coefficient similar to silicon [6]. It is suitable for producing substrates and packaging materials in high-power integrated circuits, as well as coatings, insulators and optoelectronic devices. Although liquid nitridation has been widely

investigated over the years, the mechanism (and kinetics of formation) of AlN is not well understood. Two different formation mechanisms have been identified: direct nitridation according to the reaction $2Al + N_2 \rightarrow 2AlN$ and indirect nitridation assisted by a catalyst such as magnesium. The latter involves the formation of an intermediate phase (Mg_3N_2) through the reaction $3Mg + N_2 \rightarrow Mg_3N_2$ followed by the substitution reaction $Mg_3N_2 + 2Al \rightarrow 2AlN + 3Mg$. Several publications refer to this mechanism as more likely to be responsible for nitride formation than direct nitridation [8,9,11]. Shtapitanonda and Margrave [10] observed the tendency of magnesium nitrides to form in the gaseous phase after the volatilization of magnesium when melted in a controlled atmosphere. The substitution reaction takes place once the Mg_3N_2 phase is in contact with the melt. Pech-Canul et al. [11] pointed out how the formation of magnesium nitrides is kinetically more favored than the formation of AlN. Moreover, they confirmed the occurrence of the substitution reaction to form AlN, which is a more thermally stable compound at around the process temperature range (1273-1373 K). Despite this, there is no agreement about the formation mechanism (direct or indirect). Dopants (Mg, Si) and oxygen content in the reactive gas have been found to be important parameters. Scholz and Greil [12] stated that for higher Mg/Si ratio and for decreasing oxygen content in the gas, the conversion from Al to AlN is more favorable. Jinxiang et al. [13] investigated the influence of Mg and Si on the rate of nitride formation, underlining the predominant role of magnesium over silicon. Zheng and Reddy [7] found that amount of nitrides formed are increased when ammonia is used as a reactive gas. Ammonia's oxygen-getter action, due to the dissociation of nitrogen and hydrogen at around 1273 K, results in lower oxygen content and thus a lower oxygen partial pressure in the melt. The detrimental effect of oxygen is clear when the thermodynamics of the system are analyzed. The Ellingham diagram of the reaction through which aluminum oxides are formed $4Al + 3O_2 \rightarrow 2Al_2O_3$ shows a lower Gibbs free energy compared to the Gibbs energy of the nitridation reaction (Fig.1).

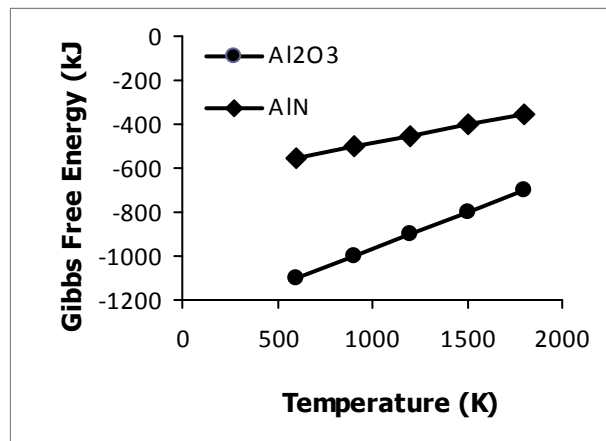


Fig.1. Ellingham diagram for the nitridation and oxidation of aluminum.

Studies of the initial nitridation period of aluminum at 673 K and higher show that the rate of nitridation is much slower than the rate of oxidation at a given temperature [13]. The aim of this work is to establish the feasibility of aluminum nitridation *via* in-situ gas/liquid reaction. The effect of the addition of catalysts such as Mg and Si has been investigated and a mechanism of nitride formation proposed.

Experimental Procedure

Experiments were carried out in a sealed stainless steel resistance furnace with a temperature range of 1223-1273 K; the setup is shown in Fig.2. The temperature is measured by two K-type

thermocouples placed in the furnace walls and inside the crucible. Alloy compositions selected for the experiments are 100wt% Al, Al-15wt% Mg, Al-15wt%Mg-8wt%Si (see Table 1). Both commercial NH_3 -99.998% pure- and High-Purity N_2 -99.9999% pure- (purchased from AIMTEK) were employed as reactive gases. Pure Al ingots (purchased from ALCOA) were sectioned and ultrasonically cleaned in acetone for 20 minutes. For each experiment, 150 g of metal was melted; alloying elements were added to the pure Al in the reaction crucible and placed in the furnace. A uniform temperature distribution in the crucible was ensured by properly placing it in the furnace. A fiberscope camera was inserted laterally in the furnace walls to ensure alignment between the crucible and the nitrogen-bearing injection tube. Prior to every run, the chamber was cleaned in order to avoid contamination of the melt by impurities such as dust and coating material. Once the gas-delivery tubes and the thermocouples were fixed in place, the furnace was sealed. The chamber was subsequently evacuated and purged with High Purity Argon Grade 5 gas four times in order to minimize oxygen presence inside the furnace. During the heating process, inert atmosphere is maintained by constantly injecting Argon at a flow rate of 0.2 l/min. The reaction temperature is 1273 K and it is held constant by an adjustable power controller. When the reaction temperature was reached, an alumina tube of 1.5 mm diameter is submerged in the melt and nitrogen-bearing gas is bubbled through the tube at a flow rate of 0.1 l/min and a gas pressure of 0.1 MPa. Two high capacity oxygen-and moisture-removal traps were used in series at the gas inlet. Each trap can lower the oxygen content to less than 1 ppb and moisture levels to less than 10 ppb.

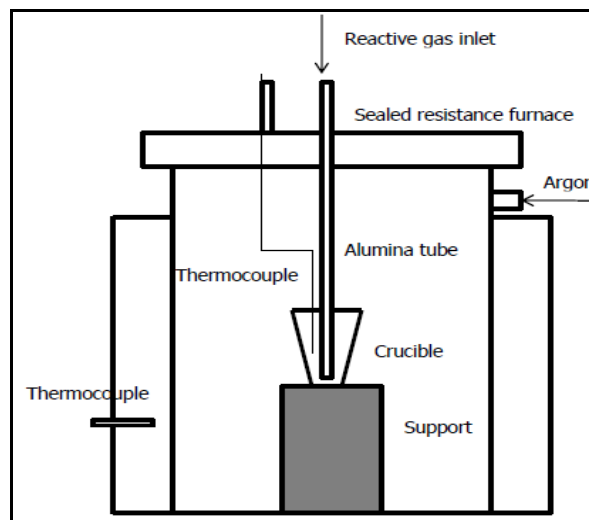


Fig.2. Schematic of in-situ gas/liquid process.

The gas was bubbled through the melt for a designated time and the furnace power was turned off. The metal is left to cool down in the inert atmosphere in order to avoid oxygen contamination. Samples were taken from bottom, middle and top part of the crucible to characterize reinforcement distribution at different lengths. The samples were mounted in green phenolic powder and polished according to standard procedures; the sample was then cleaned ultrasonically for 20 minutes to remove residuals of alumina and colloidal silica. The samples were sputter-coated with carbon so that the AlN particles are conductive for Scanning Electron Microscopy (SEM). X-Ray Diffraction (XRD) analysis was performed in order to detect the presence of nitrides and secondary phases. Field Emission Gun SEM has been employed for microstructure observation, Energy Dispersive X-ray (EDS) microanalysis and X-ray mapping.

<i>Experiment</i>	<i>Gases</i>	<i>Al alloying elements</i>		<i>Process time (hr.)</i>
		<i>Mg (wt%)</i>	<i>Si (wt%)</i>	
1	Al + N ₂	0	0	2, 6, 8
	Al + NH ₃	0	0	
2	Al + N ₂	15	0	2, 6, 8
	Al + NH ₃	15	0	
3	Al + N ₂	15	8	2, 6, 8
	Al + NH ₃	15	8	

Table 1. Details of Nitridation Experiments.

Results and Discussion

Pure Al was bubbled with both nitrogen and ammonia gas for 30 minutes, 1 hour and 2 hours, respectively, under evacuated and inert atmosphere (Experiment 1- Table 1). XRD analysis of the top, middle and bottom part of the crucible revealed that no nitrides were formed. This result suggests that a catalyst (such as Mg) needs to be added to the metal in order for the nitridation reaction to occur - as suggested by previous work [7, 8, 11]. In order to investigate the role of magnesium on the nitridation reaction, 15wt% was added to pure Al (Experiment 2). The results differ depending on the bubbling time. When the de-oxidized nitrogen is injected in the melt for 30 minutes no aluminum nitrides are detected. Whereas, when Nitrogen gas was injected in the Al-Mg melt for 1 h, a consistent amount of nitrides was observed. XRD analysis confirms strong peaks of AlN in the upper part of the crucible along with MgO (Fig.3). SEM analysis shows the presence of AlN with two different morphologies: embedded in the microstructure (Fig.4a) or as AlN powder (Fig.4b). In the powder phase, MgO is observed on the AlN particles and tightly connected with them. The size of the aluminum nitrides ranges from 1 to 3 μm while submicron MgO is also detected. The bubbling time was further increased to 2 hours and AlN was observed throughout the whole casting. AlN is present with two different morphologies - embedded in the microstructure (Fig.5a), and pockets of powder (Fig.5b). XRD analysis reveals AlN and MgO peaks also in the middle/bottom part of the crucible. The peaks in middle/bottom part of the crucible are less intense than at the top of the casting and have XRD patterns similar to that in Fig.3. In sum, the amount of AlN in the middle of the casting is less than the top of the casting. The average size of AlN is smaller for shorter injection times compared to when gas injection for longer times – i.e., 2 hrs. The size of the AlN formed is around 1 μm for the particles embedded in the microstructure and ~ 0.5 μm in the powder phase. Size control still remains an issue and kinetics and control of particle size work is continuing at the Metal Processing Institute (WPI). No difference was noticed in AlN formation between the use of ammonia and nitrogen gas. Ammonia quickly dissociates into nitrogen and hydrogen when in the injection tube. In addition, the use of ammonia is undesirable because of the high amount of porosity that is observed at the center/bottom of the casting (Experiment 3, when injected for 2 hours). This is explained by the fact that the fraction of AlN formed is initially limited to the upper portion of the melt, which increases the viscosity of the melt in this region. As a result, the melt traps more hydrogen causing porosity.

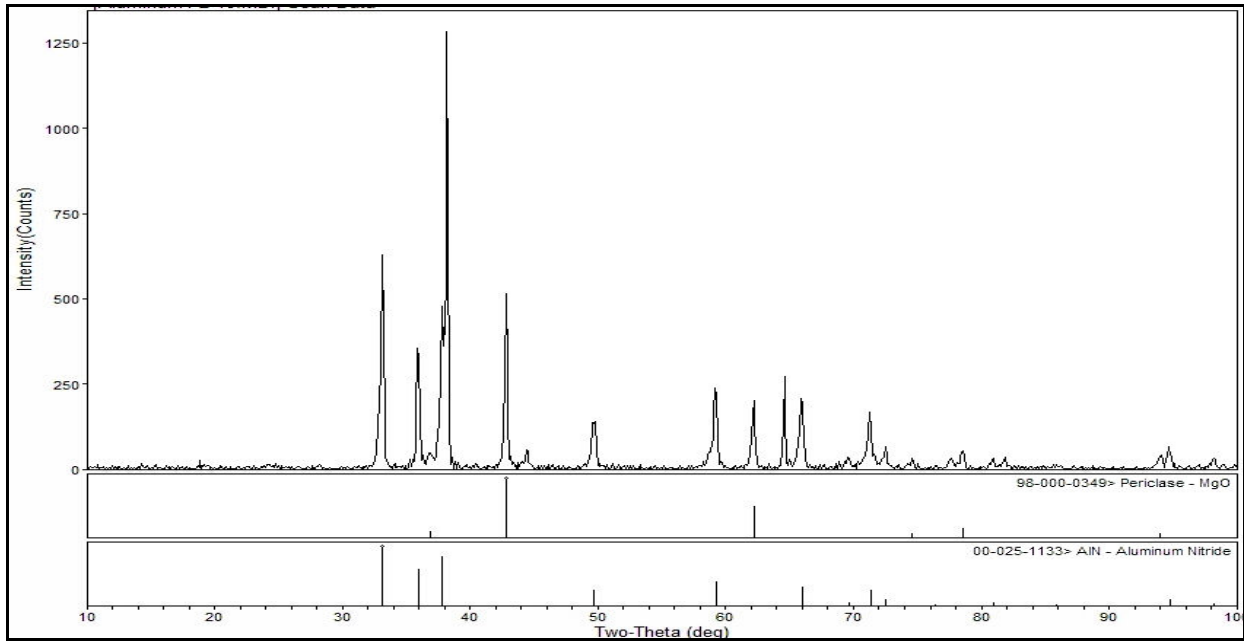


Fig.3. XRD pattern of the upper part of the crucible for 1 h injection time (Experiment 2).

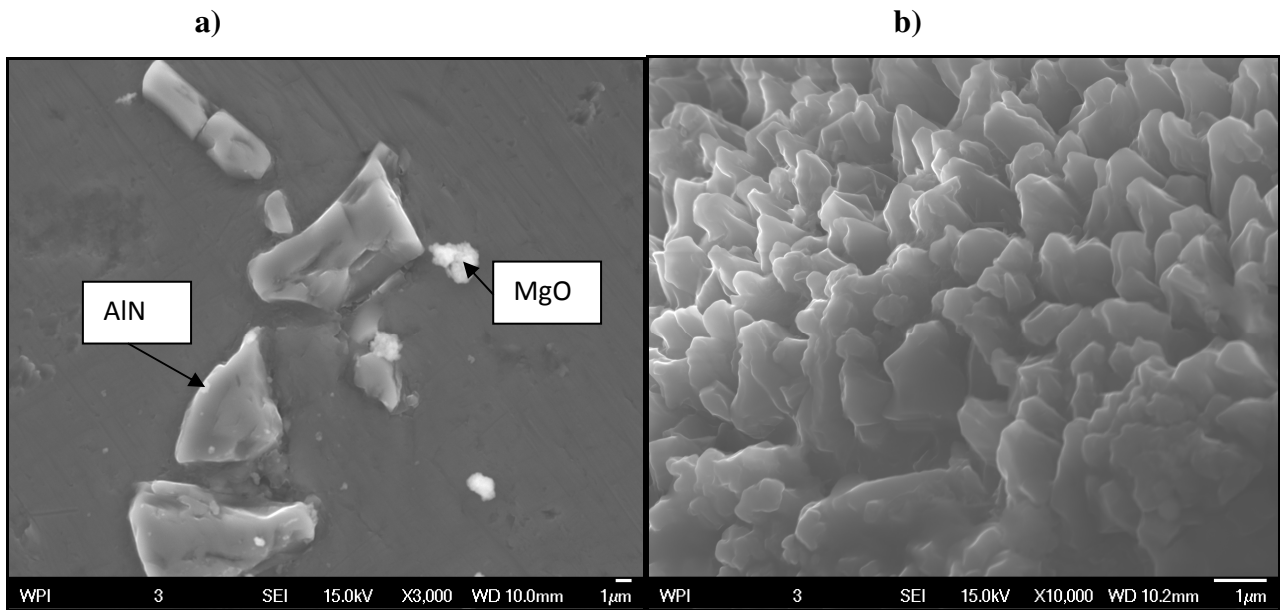


Fig.4. a) SEM image of AlN imbedded in the matrix in the upper part of the crucible; b) Pockets of AlN and MgO powder in the upper part of the crucible Experiment 2) - 1 hour injection time.

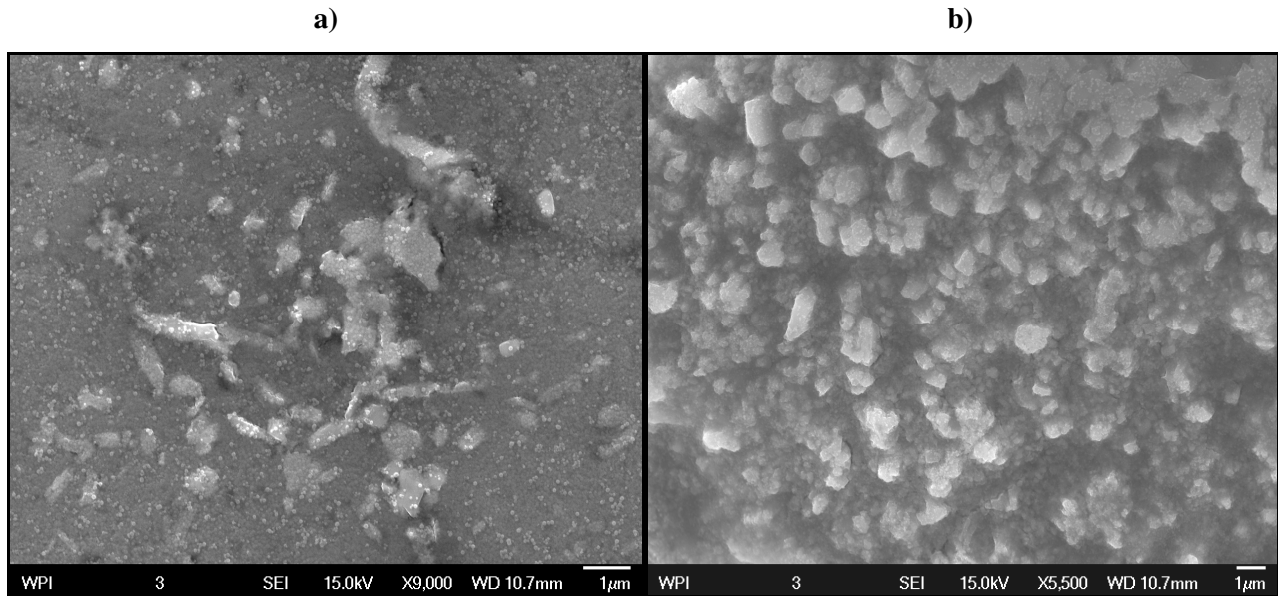


Fig.5. a) SEM image of AlN imbedded in the matrix in the middle part of the crucible; b) Pockets of AlN and MgO powder in the middle part of the crucible (Experiment 2, 2 hours gas injection time).

Silicon is an important element for fluidity and its influence on the nitridation of aluminum was investigated (Experiment 3). The literature contains contradictory information about Si's effect when it is added to the melt together with Mg [10,11,12]. In these experiments, when 8wt% Si was added to the Al-Mg melt, AlN was not formed whether nitrogen or ammonia gas was used. XRD pattern reveals strong peaks of silicide phase - Mg_2Si (Fig.6). EDS (Fig.7b) and X-ray mapping further confirm the presence of the silicide phase. Oxygen is undesirable since it favors the formation of aluminum oxides versus aluminum nitrides. It can be noticed (Fig.8) that the permissible oxygen partial pressure for nitridation is $e-16$ MPa at 1273 K, value that can be hardly achieved with commercial oxygen traps. The presence of MgO together with AlN suggests that the former could act as an oxygen-getter to reduce the oxygen partial pressure in the melt. At this point, aluminum nitrides form by direct nitridation according to the reaction $2Al + N_2 \rightarrow 2AlN$. Therefore, nitridation does not occur *indirectly* by substitution with Mg but through a *Mg assisted direct* reaction. The Ellingham diagram of MgO, AlN and the Al-Mg substitution reaction is given in Figure 9. It can be noted that MgO is thermodynamically stable over a wide range of temperatures and that indirect nitridation $Mg_3N_2 + 2Al \rightarrow 2AlN + 3Mg$ is less favorable than the sequence $2Mg + O_2 \rightarrow 2MgO$ and $2Al + N_2 \rightarrow 2AlN$. When silicon is added to the melt, AlN and MgO are not formed, while Mg_2Si phase formed as evidenced by the microstructural analysis. It is hypothesized that the synthesis of the silicide phase is favorable compared to synthesis of MgO, and that Mg in the melt was depleted by the precipitation of Mg_2Si . An important note concerning the temperature of formation of MgO, and therefore of AlN is worth making. The formation of Mg_2Si starts at 923 K and is completed at 823 K (Fig.10). Therefore, MgO formation must occur at temperatures equal or smaller than 953 K. This leads us to note that direct nitridation of aluminum takes place during the cooling process and not at temperatures ~ 1273 K.

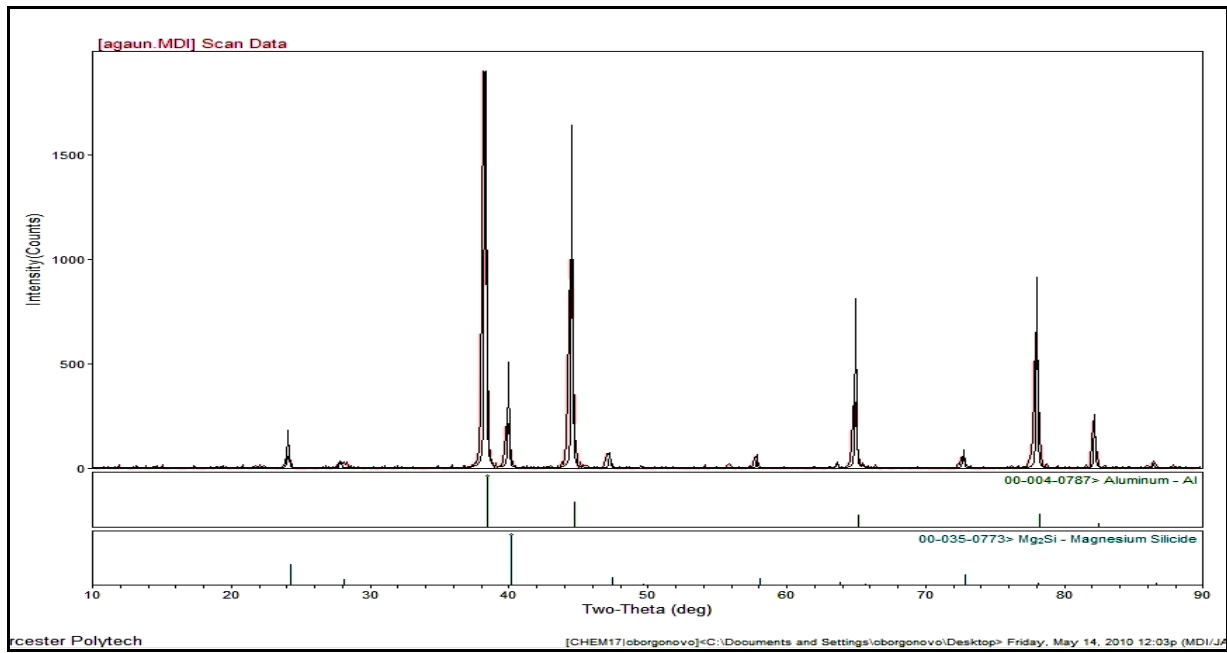


Fig.6. XRD pattern of Al-Mg-Si microstructure (Experiment 3).

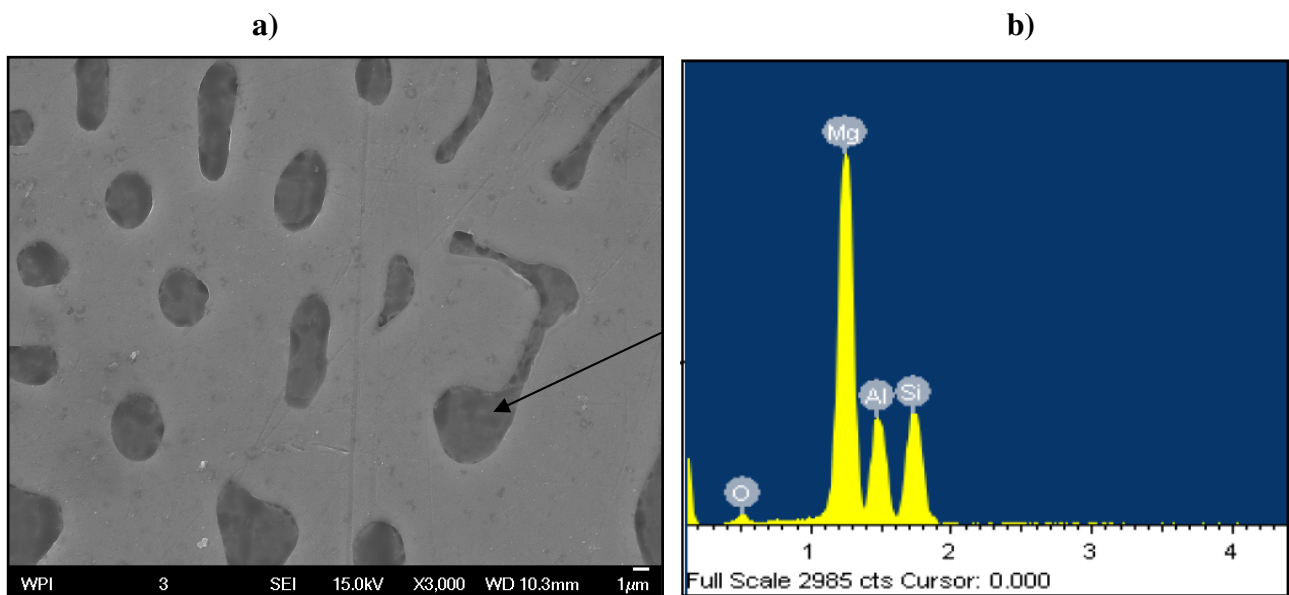


Fig.7. a) SEM magnification of the magnesium silicide phase; b) EDS analysis.

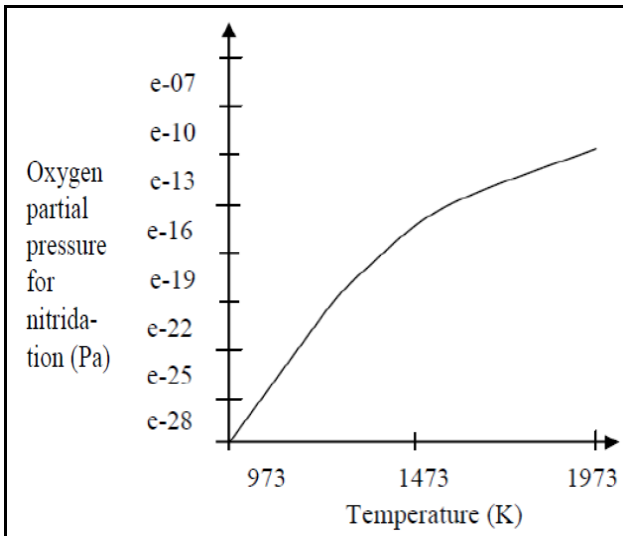


Fig.8. Maximum oxygen partial pressure for nitridation vs. temperature.

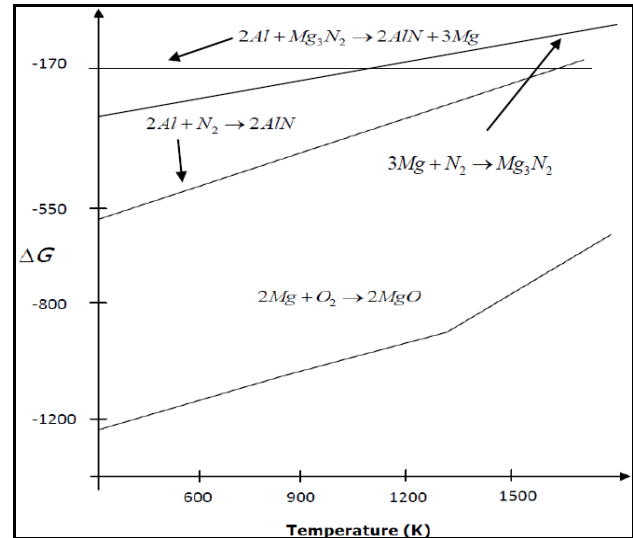


Fig.9 Ellingham diagram for indirect nitridation and Mg assisted direct nitridation.

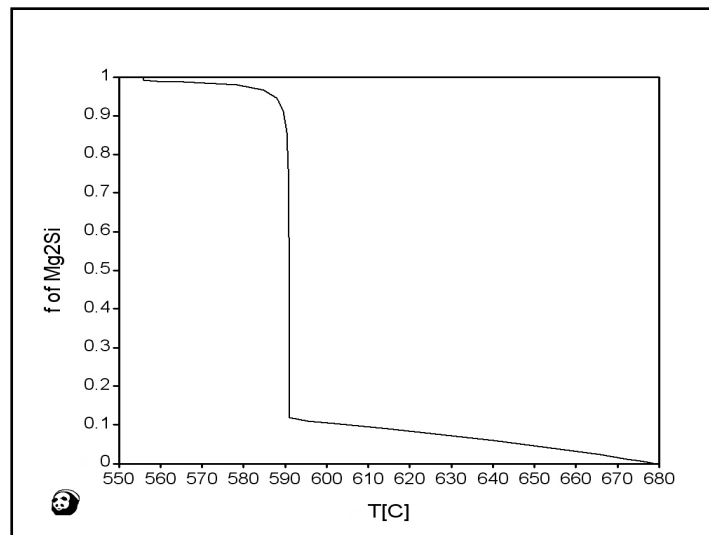


Fig.10. Fraction solid of magnesium silicide formed vs. temperature (Pandat Software).

Conclusions

Gas-assisted nitridation of aluminum is feasible. The in-situ route to manufacture nanocomposites has the potential to be a commercial process where scalability, homogeneous distribution and cost-effectiveness are important criteria.

AlN particles, whose thermal and electrical properties are exceptional, have been successfully synthesized. Specifically:

- Particle sizes in the sub-micron range were achieved when the gas was injected in the melt for 2 hours.
- Distribution is improved for longer injection times. For shorter bubbling times (1 hour) AlN were observed only on the upper section of the casting, while for longer times (2 hours) AlN was found throughout and particularly the middle and bottom sections of the casting.

- Ammonia does not improve the rate of nitride formation and causes an increase in porosity especially for long injection times. This can be attributed to the entrapment of hydrogen in the upper part of the crucible where viscosity is higher due to AlN and MgO that synthesize at an early stage.
- Addition of Mg in the casting is fundamental for the mechanism of formation of AlN. When pure aluminum was used as matrix, no reinforcement was formed. XRD analysis and SEM observation showed the presence of MgO along with AlN. This suggests an alternative hypothesis about the mechanism of formation of nitrides. Oxygen content is lowered and AlN forms through direct nitridation or through *direct Mg-assisted nitridation*.
- Silicon totally hinders the nitridation reaction. No MgO has been detected but magnesium silicide is present in the microstructure. This suggests that Mg₂Si suppresses the formation of MgO. Since the latter precipitates during cooling, aluminum nitridation may take place at lower temperatures during cooling.

The control of AlN particle size and the kinetics of the nitridation process need further study. This work has shown that the process is feasible and that this in-situ approach has merit and has commercial potential. The aim of producing nano sized (30-40 nm particles) was not achieved in these experiments; however, the pathway to do so was clearly laid out. This work is continuing to establish the mechanisms to address the kinetics of the reaction in order to enable us to attain particles that are not submicron but rather in the nano range.

Acknowledgements

The authors gratefully acknowledge the member companies of the Advanced Casting Research Center (ACRC) of the Metal Processing Institute for their support of this work, and for their continued support of research focused on the science and technology of metal casting at Worcester Polytechnic Institute.

References

- [1] C.Borgonovo and D.Apelian: submitted to Mat. Sci. Forum (2010).
- [2] S.C. Tjong, Z.Y. Ma: Mat. Sci. Eng. Vol. 29 (2000), pp. 49-113.
- [3] Q. Hou, R. Mutharasan and M. Koczak: Mat. Sci. Eng. Vol. A195 (1995), pp. 121-129.
- [4] S.Tyagi, Q.Zheng and R. Reddy: *Aluminum 2004*, edited by S. K. Das, TMS, Warrendale, (2004), pp. 63-72.
- [5] H.Z. Ye, X.Y. Liu and B. Luan: J. Mater. Process. Tech. Vol. 166 (2005), pp. 79–85.
- [6] J. Haibo, K. Chen, Z. Heping, S. Agathopoulos, O. Fabrichnaya and J.M.F. Ferreira: J. Cryst. Growth Vol. 281 (2005), pp. 639–645.
- [7] Q. Zheng and R. Reddy: Metall. Mater. Trans. Vol. 34B (2003), pp. 793-805.
- [8] Q. Zheng and R. Reddy: Adv. Eng. Mater. Vol. 5 No. 3 (2003), pp. 167-173.
- [9] Q. Zheng and R. Reddy: J. Mater. Sc. Vol. 39 (2004), pp. 141-149.
- [10] P. Shtapitanonda and J. Magrave: Symposium at University of Wisconsin-Madison (1956).
- [11] M. I. Pech-Canul, R.N. Katz and M. M. Makhlof: Metall. Mater. Trans. Vol. 31A (2000), pp. 565-573.
- [12] H. Scholz and P. Greil: J. Mater. Sc. Vol. 26 (1991), pp. 669-677.
- [13] L. Jinxiang , G. Xiuying , C. Jianfeng , W. Qun, S. Yuhui and G. Qin: Thermochem. Acta Vol. 253 (1995), pp. 265-273.

Advances in Metal Matrix Composites

10.4028/www.scientific.net/MSF.678

Processing of Lightweight Metal Matrix Composites via *In Situ* Gas/Liquid Reaction

10.4028/www.scientific.net/MSF.678.115

Aluminum Nanocomposites for Elevated Temperature Applications

C. Borgonovo, D. Apelian, and M.M. Makhlof

Aluminum casting alloys conventionally used in the automotive and aerospace industries (i.e., Al-Zn-Mg, and Al-Cu-Mg systems) are able to achieve excellent tensile strength at room temperature. At high temperatures, such alloys lose dimensional stability and their mechanical properties rapidly degrade. Aluminum-based nanocomposites show the potential for enhanced performance at high temperatures. The manufacturing process, however, is difficult; a viable and effective method for large-scale applications has not been developed. In the current study, an innovative and cost-effective approach has been adopted to manufacture Al/AlN composites. A nitrogen-bearing gas is injected into the melt and AlN particles synthesize in-situ via chemical reaction. In a preliminary stage, a model able to predict the amount of reinforcement formed has been developed. AlN dispersoids have been successfully synthesized in the matrix and the model has been experimentally validated.

INTRODUCTION

Aluminum nanocomposites are a novel class of lightweight materials that possess excellent mechanical properties and improved dimensional stability at high temperatures; applications of interest are for aerospace, automotive, defense, etc. However, the conventional processing methods for the production of metal matrix nanocomposites are sub-optimal.^{1,2} For example, semi-solid processing methods may not evenly distribute the reinforcing particles in the matrix alloy.³ Infiltration techniques are difficult to scale up and may not be cost-effective.⁴ Ultrasonic cavitation techniques provide a homogeneous microstructure but the

flux densities needed for scale up are difficult to attain.⁵ Powder metallurgy and mechanical attrition methods result in residual microporosity, deterioration of the interface between the matrix and the reinforcement, and high processing costs.^{6,7} In order to overcome the disadvantages associated with these ex-situ conventional processing routes, a novel approach has been followed where the reinforcement is not externally added but is formed within the parent phase (in-situ) via chemical reaction(s) between elements or between elements

and compounds.¹

A variety of in-situ techniques, such as directional solidification, heavy deformation processing, self-propagating high-temperature synthesis, exothermic dispersion, reactive hot pressing, direct reaction synthesis, and vapor-liquid-solid reaction process, etc., have been developed. These processes are broadly classified based on the reacting phases, i.e. liquid-gas, liquid-solid, and solid-solid reactions.⁸ Liquid-gas reaction processing involves the injection of a reactive gas into the melt and has shown promise to be a viable method;^{8,9} gas and alloy composition determine which phases form. Uniform dispersion of the reinforcement, clean and coherent particle-matrix interfaces, thermodynamical stability of the composite material and cost effectiveness are key process characteristics. The liquid-gas reaction process allows one to manufacture a wide range of matrix materials (aluminum, titanium, copper, nickel, and iron), and secondary phases (nitrides, borides, carbides, oxides, and their mixtures).^{9,10}

Liquid-gas processing approaches where the gas is in direct contact with the melt surface have been reported;⁸⁻¹² direct melt oxidation (DIMOX) and direct melt nitridation (PRIMEX) follow the liquid-gas reaction approach; however the melt is in a static/flowing gas environment.^{10,11} Gas injection, which is the process we have developed and refined, differs from direct melt reaction techniques in that the synthesis of the reinforcement is not limited to the surface of the melt, but occurs throughout the depth of the melt. Direct melt reaction techniques such as DIMOX and PRIMOX are suitable for singular phase reinforced composites, whereas a large number of reinforcing constitu-

How would you...

...describe the overall significance of this paper?

This paper describes a methodology and a conceptual framework to manufacture Al-based nanocomposites in a cost-effective way. It gives a pathway to make nanocomposites directly from melt.

...describe this work to a materials science and engineering professional with no experience in your technical specialty?

Al-based alloys cannot be used above 285°C as the precipitation hardening mechanism falls apart. Nano-composite Al alloys can be utilized at temperatures above 300°C which gives the opportunity to use them for a variety of elevated temperature applications.

...describe this work to a layperson?

Diesel engines are quite effective in that energy usage is less. Diesel is quite effective and gets excellent mileage (miles/gallon). However, diesel engines operate at higher temperatures than internal combustion engines. Al alloys fall short for many diesel applications as the Al does not maintain its strength at elevated temperatures. Nanocomposites open up a way for us to use Al for diesel applications.

ents can be formed with the gas injection method. The price one pays is that with the gas injection process control is more difficult.¹⁰ Gas injection was first developed by Koczak and Kumar;¹² they investigated both nitrogen-bearing gases (forming AlN, TiN, and their mixtures) and carbon-bearing gases (forming SiC, TiC, and their mixtures) in aluminum alloys matrix.

Among various reinforcements for aluminum alloys, AlN offers high thermodynamic stability and good wettability. Moreover, its high thermal conductivity, high electrical resistance, low dielectric constant, and a thermal expansion coefficient similar to that of silicon make it a good candidate for thermal management applications, as well as for coatings, insulators and optoelectronic devices.^{9,13} It must be pointed out that AlN powder is relatively expensive, and thus a deterrent when considering AlN/Al for cost-effective applications. Thus, in-situ fabrication of AlN/Al composites by the reaction of a nitrogen-bearing gas with molten Al is an attractive manufacturing route. Although liquid nitridation has been widely investigated, the mechanism for AlN formation is not well understood; as expected, process control without a sound understanding of the underpinning mechanism has not been developed. In addition, the effect of alloying elements such as Mg and Si still remains unclear. Two different formation mechanisms have been identified: direct nitridation according to the reaction $2Al + N_2 \rightarrow 2AlN$ and indirect nitridation assisted by a catalyst such as magnesium. The latter involves the

formation of an intermediate phase (Mg_3N_2) through the reaction $3Mg + N_2 \rightarrow Mg_3N_2$ followed by the substitution reaction $Mg_3N_2 + 2Al \rightarrow 2AlN + 3Mg$. This mechanism is more likely to be responsible for nitride formation than direct nitridation.¹⁴⁻¹⁹ Hou et al.⁹ have manufactured AlN sub-micron composites in an Al-Mg matrix via nitrogen injection and have verified the theory of indirect nitridation. Pech-Canul et al.¹⁵ have shown that the formation of magnesium nitrides is kinetically more favorable than the formation of AlN. However there is no good agreement and understanding of indirect nitridation in Al melts.

Nitridation studies have confirmed the detrimental effect of oxygen on nitride formation.²⁰⁻²² Oxidation of aluminum is a more exothermic reaction, and is more favorable than nitridation. Daniel et al.¹⁰ found that nitridation is more sensitive than oxidation to reaction temperature and partial pressure of the reactant gas. They also have shown that moisture in the reactive gas hinders the synthesis of AlN. Zheng et al.^{17,23} confirmed that when nitrogen gas is replaced by ammonia gas, hydrogen dissociates and acts as an oxygen getter, reducing the oxygen partial pressure in the melt and enhancing the rate of aluminum nitridation. The effect of Si on AlN formation is also unclear. Scholz and Greil²⁴ stated that low Si contents favor nitridation. Jinxiang et al.²² investigated the influence of Mg and Si on the rate of nitride formation, underlining the predominant role of magnesium over silicon. Zheng et al.²³ have reported successful formation of AlN

Table I. Nitridation Gas Injection Processing Conditions

Experiment	Gases	Al Alloying Elements		Process
		Mg (wt.%)	Si (wt.%)	Time (h)
1	Al + N ₂	0	0	2, 6, 8
2	Al + N ₂	15	0	2, 6, 8
3	Al + N ₂	15	8	2, 6, 8

in an Al-Si melt when processed with ammonia gas.

In this paper we show the feasibility of AlN formation in Al melts via injection of a nitrogen-bearing gas; we have done this both through a comprehensive mathematical model as well as experimental verification.

METHODOLOGY

Procedure and Apparatus

The synthesis of AlN in Al melts was carried out in a sealed electric resistance furnace (Figure 1). Al (99.9%), Al-15wt.%Mg and Al-15wt.%Mg-8wt.%Si charges of approximately 150 g were heated in a BN-coated conical alumina crucible placed in a stainless steel chamber. The crucible was located in the lower part of the furnace and temperature control throughout the melt was ensured. Mg and Si were added in the form of Al-50%Mg master alloy and pure Si. The furnace was first evacuated to 10^{-2} – 10^{-3} Torr and subsequently purged with argon (Grade 5) gas. This operation was repeated three times before backfilling the furnace with argon. The furnace was heated to 1,000°C, measured by K-type thermocouples inserted in the furnace wall and in the crucible. During the heating cycle, argon gas was introduced into the system at a rate of 0.2 l/min. was maintained. Once temperature was stabilized at 1,000°C, a BN-coated alumina tube was inserted in the melt and nitrogen gas (Grade 5) was injected through the melt for different processing times (Table I); a gas flow rate of 0.5 l/min. was maintained. Two high capacity oxygen-and moisture-removal traps were used. The active material in each trap can lower the oxygen content to less than 1 ppb and moisture levels to less than 10 ppb. Once gas injection was completed, the tube was extracted

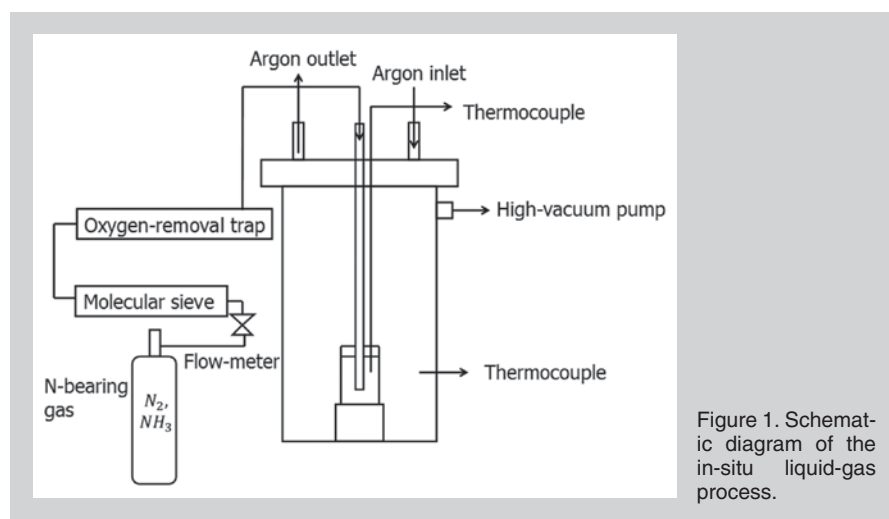


Figure 1. Schematic diagram of the in-situ liquid-gas process.

and the melt was left to cool down in the furnace in an argon atmosphere.

Microstructure and reaction products were investigated via scanning electron microscopy (SEM, JEOL JMS-5610 equipped with EDS) and x-ray diffraction (XRD, D/MAX2200, Rigaku) using Cu K radiation operated at 36 kv and 26 mA. The amount of aluminum nitrides formed was determined by weighing the sample before and after the gas injection process and calculating by considering the ratio of molecular weight of AlN and atomic weight of nitrogen. Samples were sectioned from the bottom, the middle, and the top parts of the casting to characterize

the distribution of AlN particles in the matrix.

Model Formulation

The feasibility of nitridation can be mathematically expressed by Equation 1, where W_{AlN} is the total amount of AlN formed during the process. t is the injection time, A_t is the total gas-liquid interface and θ_{AlN} is the rate of formation of AlN particles. (All equations are shown in the table.) Calculation of A_t and θ_{AlN} is necessary in order to determine W_{AlN} . The bubble diameter d_b affects A_t according to Equation 2, where N_b is the number of gas bubbles in the melt and A_t is the bubble area.

The bubble diameter also affects θ_{AlN} according to Equation 3, where E is an enhancement factor, K_L is the mass transfer coefficient, C^* is the nitrogen concentration at the gas-liquid interface and C_i is the initial nitrogen concentration in the melt. Both E and K_L can be derived from the bubble diameter, d_b .

Calculation Domains and Assumptions

The process is modeled on two calculation domains:

- Two dimensional (2-D) domain considering the overall evolution of the gaseous flow in the crucible

Equations	
$W_{AlN} = \int_0^t A_t \theta_{AlN} dt > 0$	(1)
$A_t = N_b A_b = N_b \pi \left(\frac{d_b}{2}\right)^2$	(2)
$\theta_{AlN} = EK_L (C^* - C_i)$	(3)
$N_b = \tau f_b$	(4)
$f_b = \frac{V_s}{V_{bo}}$	(5)
$V_{bo} = \frac{4\pi}{3} \left(\frac{d_{bo}}{2}\right)^3$	(6)
$d_{bo} = \left(\frac{6d_{no}\sigma}{g(\rho_l - \rho_g)}\right)^{1/3}$	(7)
$V_g = \frac{P_m T}{P_{GO} T_m} V_m$	(8)
$f_b = \frac{79.5TQ}{0.001P_{atm} + 4\sigma}$	(9)
$\frac{dr_b}{dt} = \frac{(P_g - P_l)}{4\eta} - \frac{\sigma}{2\eta}$	(10)
$C^* = \frac{P_G}{He}$	(11)
$\frac{d}{dt} \left(\frac{4\pi P_G r_b^3}{3RT} \right) = 4\pi r_b^2 D \frac{\partial c}{\partial r} \Big _{r=r_b}$	(12)
$D = 3.75 \times 10^{-7} \exp\left(\frac{-3184}{T}\right)$	(13)
$\frac{\partial c}{\partial t} = D \frac{\partial^2 c}{\partial r^2}$	(14)
$P_{GOd_{no}} = P_{atm} + \rho_l g h + \frac{4\sigma}{d_{no}}$	(15)
$K_L = \sqrt{\frac{D}{\rho t_c}}$	(16)
$E = \frac{\sqrt{M' \left(E_i - \frac{E}{E_i} - 1 \right)}}{\tanh \sqrt{M' \left(E_i - \frac{E}{E_i} - 1 \right)}}$	(17)
$M' = \frac{\pi}{4} k_c C_{Al} t_d$	(18)
$E_i = \sqrt{\frac{D}{D_{Al}}} + \frac{C'_{Al}}{C^*} \sqrt{\frac{D_{Al}}{D}}$	(19)
$2Al_2O_3 + 2N_2 \rightarrow 4AlN + 3O_2$	(20)
$\Delta G = 2,057,400 - 184.4T \cong -RT \ln \left(\frac{P_{O_2}}{P_{atm}} \right)^3 \rightarrow P_{O_2} = 18.9 - \frac{82,487.4}{T}$	(21)
$Mg(l) = Mg(g)$	(22)
$2Mg(g) + O_2(g) = 2MgO$	(23)
$P_{O_2} = \gamma_{Mg}^{-2} \gamma_{Mg}^{-2} \exp\left(\frac{2G_{22} + G_{23}}{2RT}\right)$	(24)

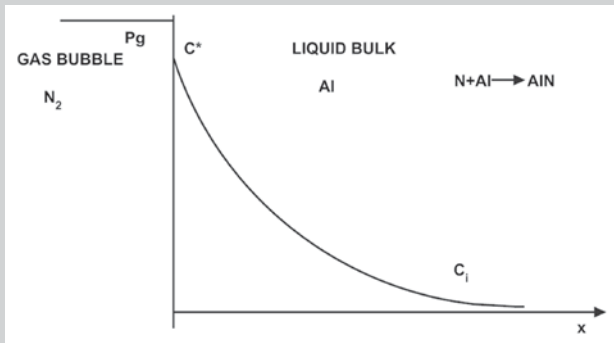


Figure 2. Schematic diagram of the diffusion domain in the melt (Higbie's Penetration Theory^{28,32})

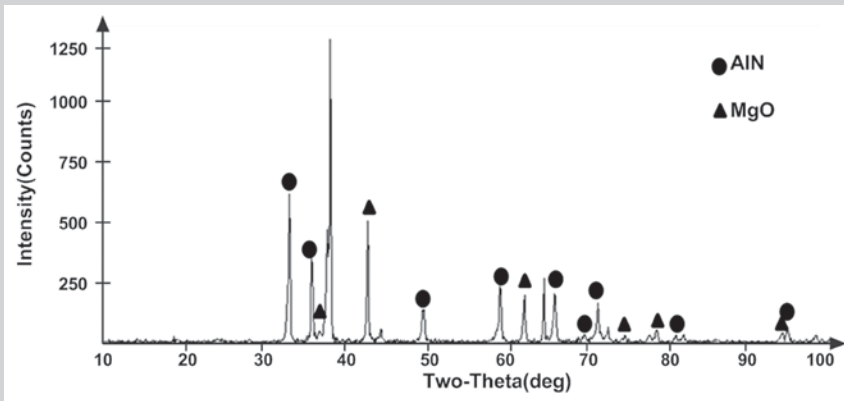


Figure 3. XRD pattern of the upper part of the crucible. Processing time = 6 h.

- One-dimensional domain considering the kinetics of particle formation at the gas-liquid interface ahead of the gas bubble

The following assumptions were made:

- The bubble is spherical
- Finite liquid domain
- Gas in the bubble is pure and obeys the ideal gas law
- Bubble surface is contaminant-free
- Bubbles do not interact with one another
- Liquid phase resistance controls mass transfer in the melt
- Mass transfer in the liquid phase is ruled by Higbie's penetration theory^{27,28,32}
- Effects of the confining crucible walls on the bubbles are negligible
- Influence of melt composition (addition of alloying elements) on the nitridation reaction is negligible

The bubbly flow module and PDE mode of COMSOL Multi-physics were used to solve the coupled partial differential equations and determine the bubble radius and gas flow veloci-

ty in the liquid. Two mesh modes were used for the 2-D domain: a boundary layer at the boundaries and a free mesh on the sub-domain. A boundary layer

mesh is a mesh with dense element distribution in the normal direction along specific boundaries. It is typically used for fluid flow problems to resolve the thin boundary layers along the no-slip boundaries where a layered quadrilateral mesh is employed.

Total Gas-Liquid Interface Area (A_l)

The number of gas bubbles in the melt, N_b is calculated by Equation 4, where τ is the bubble residence time in the melt and f_b is the frequency of gas bubble formation at the nozzle and is defined by Equation 5. Here V_g is the volume flux of the gas at the nozzle and V_{bo} is the volume of the detaching bubble given by Equations 6 and 7,²⁵ where d_{bo} is the diameter of the detaching bubble. V_g is derived from the ideal gas law approximation, given in Equation 8, where P_{in} , T_{in} , V_{in} is the state of the gas at the inlet of the injection tube. Substituting Equations 6, 7, and 8 into Equation 5 allows f_b to be calculated as Equation 9.

It can be noted that the frequency of bubble formation increases with increasing temperature and gas flow rate, whereas it decreases with increasing interface energy and pressure in the furnace.

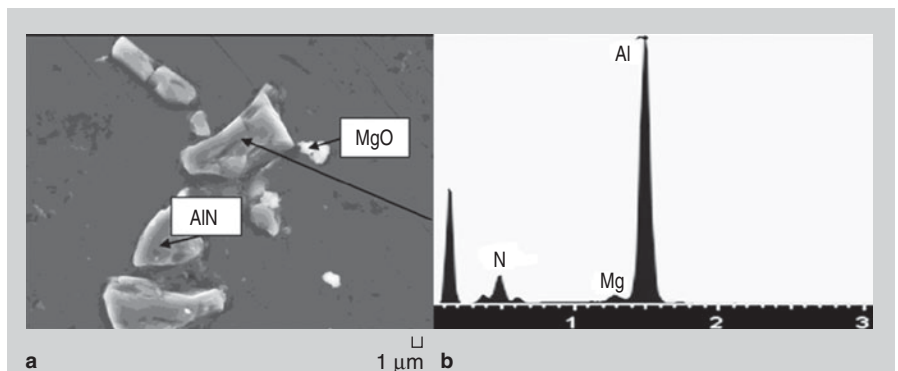


Figure 4. (a) SEM image and (b) EDS spectrum of AIN imbedded in the matrix in the upper part of the crucible. Processing time = 6 h.

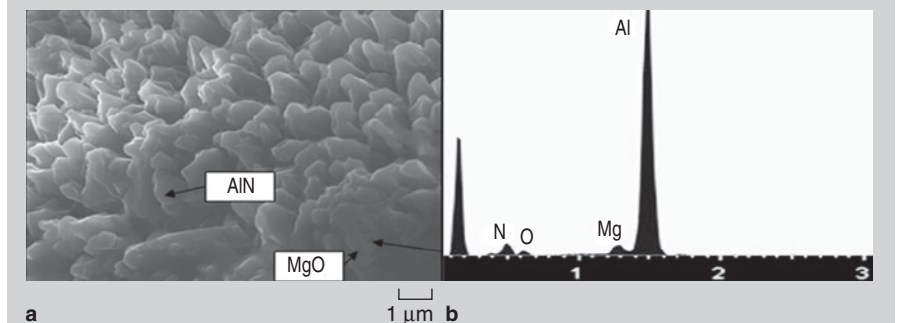


Figure 5. (a) SEM image and (b) EDS spectrum of pockets of AIN and MgO powder in the upper part of the crucible. Processing time = 6 h.

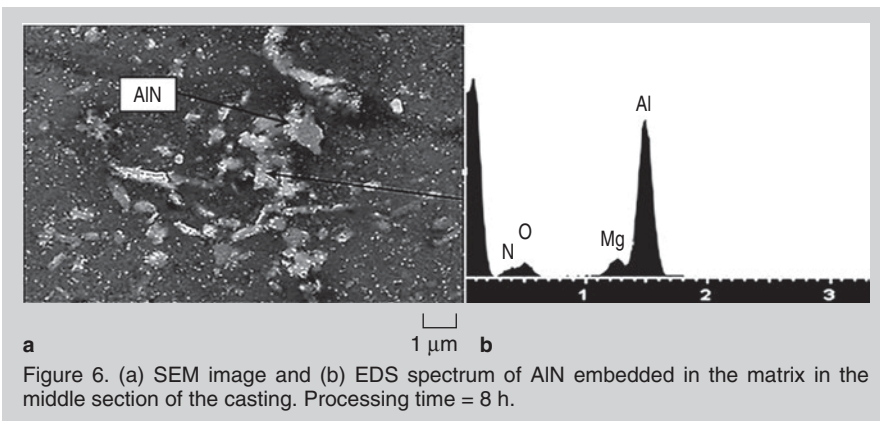


Figure 6. (a) SEM image and (b) EDS spectrum of AlN embedded in the matrix in the middle section of the casting. Processing time = 8 h.

atoms in the melt after diffusion, and thus it increases the nitrogen concentration gradient between the bubble surface and the melt. The enhancement factor (E) is a non-dimensional index that accounts for such phenomenon. The enhancement factor for a first order chemical reaction such as the one between aluminum and nitrogen has been reported by Madhavi et al.²⁹ as Equations 17–19, where k_c is a kinetics constant for the direct nitridation reaction, D_{Al} is the diffusion coefficient of aluminum and C_{Al}^* is the aluminum concentration at the gas-liquid interface.

RESULTS AND DISCUSSION

Experimental

Pure aluminum was injected with nitrogen for 2, 6, and 8 hours at 1,000°C. XRD analysis of the top, middle and bottom sections of the cast product revealed that no nitrides were formed. This suggests that the nitridation reaction needs a catalyst such as Mg. The addition of 15% Mg to the aluminum was investigated and resulted in a consistent amount of nitrides for 6 and 8 hours processing times. In the case of nitridation for 6

Bubble Radius

A simplified expression of the Navier–Stokes equation for an isolated bubble rising in an incompressible liquid is used to calculate r_b , Equation 10,²⁶ where P_g is the pressure in the bubble, P_l the liquid pressure, σ the surface tension of aluminum and ν is the dynamic viscosity of the liquid. Pressure and concentration at the bubble surface are coupled through Henry's law (Equation 11) and mass balance (Equation 12). He is Henry's constant, where R is the ideal gas constant, T is the temperature, and D is the diffusion coefficient of nitrogen in aluminum whose dependence on temperature is expressed by Equation 13.

The concentration gradient at the bubble surface $\left. \frac{\partial c}{\partial r} \right|_{r=r_b}$ is determined by Fick's second law of diffusion in a steady liquid domain (the convection term is neglected), as given in Equation 14. The initial condition for the pressure in the gas bubble, P_{GO} is given by the hydrostatic pressure at the nozzle of the injection tube and is given by Equation 15, where P_{atm} is the atmospheric pressure, r_l is the liquid density, h is the crucible height, and d_{no} is the nozzle diameter of the injection tube. The initial condition for concentration at the bubble surface is derived from Henry's law with $P_g = P_{GO}$, while the initial condition for concentration in the liquid domain is zero.

Rate of Formation of AlN Particles

Diffusion of nitrogen atoms in the liquid is modeled by Higbie's penetration theory (Figure 2), which considers that the gas-liquid interface is composed of various elements con-

tinuously brought up to the interface from the melt.

The rate of formation of AlN is considered to be equal to the rate of nitrogen atoms diffusing in the melt, and can be calculated by Equation 3. Henry's Law ($C^* = P_g/pt_c$) applies at the gas-liquid interface. The mass transfer coefficient according to Higbie's Law is given by Equation 16,^{28,32} where t_c is the local diffusion time or contact time, i.e. the time that a single element spends in contact with the gas bubble. t_c is the time needed for diffusion to occur in the boundary layer. Bubble diameter and bubble velocity are considered when calculating t_c . Synthesis of AlN lowers the number of nitrogen

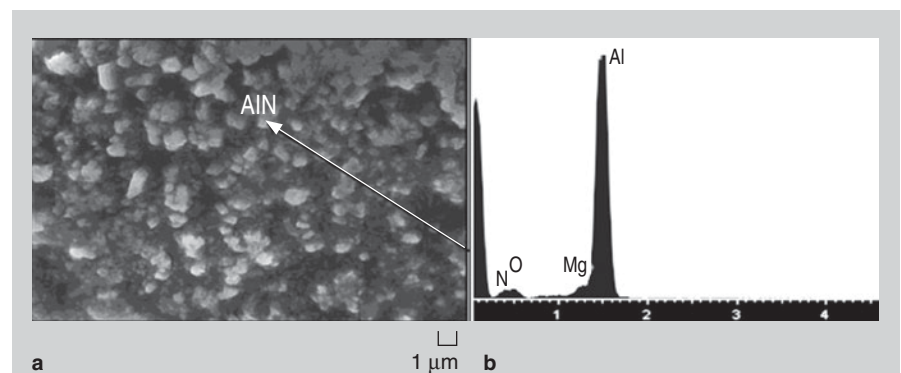


Figure 7. (a) SEM image and (b) EDS spectrum of pockets of AlN and MgO powder in the middle section of the casting. Processing time = 8 h.

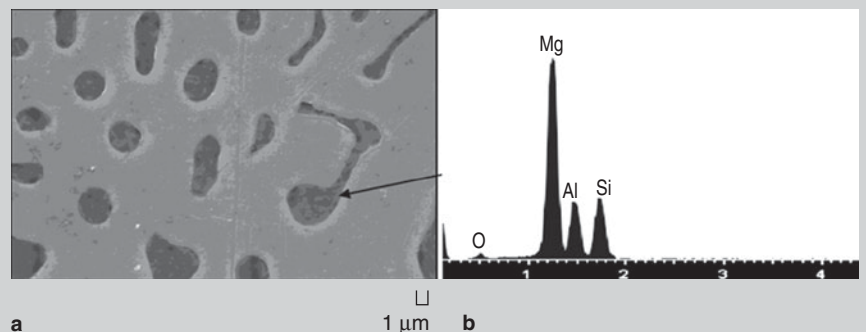


Figure 8. (a) SEM image and (b) EDS spectrum of magnesium silicide.

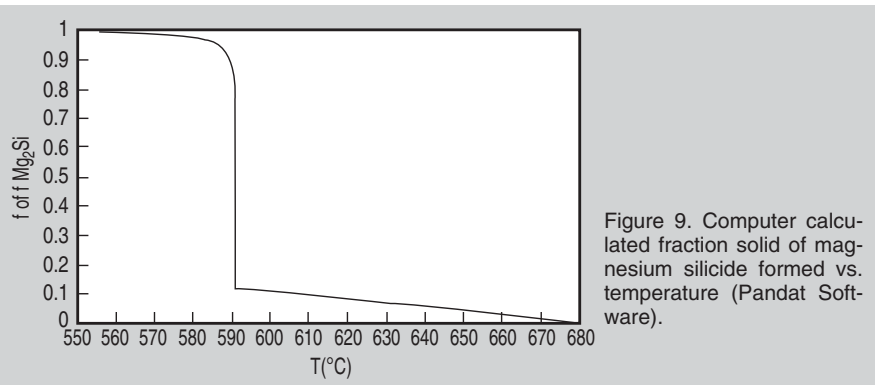


Figure 9. Computer calculated fraction solid of magnesium silicide formed vs. temperature (Pandat Software).

hours, XRD analysis confirms strong peaks of AlN in the upper part of the crucible along with peaks for MgO (periclase) (Figure 3). SEM and EDS analyses confirm the presence of two different morphologies of AlN: (i) embedded in the microstructure (Figure 4) or (ii) AlN + MgO powder (Figure 5). The size of aluminum nitrides formed ranges from 1 to 3 μm whereas the MgO particles were of submicron size.

When the bubbling time is increased to 8 hours, AlN was observed throughout the length of the resultant casting. The AlN particles were present in two different morphologies: (i) embedded in the microstructure (Figure 6), and (ii) as pockets of powder (Figure 7). XRD analysis reveals AlN and MgO peaks in the middle and bottom sections of the casting.

The peaks from the middle and bottom sections of the casting are less intense than those from the top section. It can be noted that the average size of AlN particles is smaller compared to the case when shorter bubbling times were used. Specifically, the AlN is $\sim 1 \mu\text{m}$ for AlN embedded in the microstructure and in the submicron range (around $0.4 \mu\text{m}$) in the powder phase. Size control still remains an issue and it is currently being studied at WPI. It is expected that rotating the injection tube will significantly improve the distribution of AlN particles in the matrix.

The principal role of Mg during the synthesis of AlN can be explained when the detrimental effect of oxygen on nitridation is considered. Studies have demonstrated that the rate of aluminum nitridation is several orders of magnitude slower than the rate of aluminum oxidation at any given temper-

ature.²⁴ According to the equilibrium reaction (Equation 20), at $1,000^\circ\text{C}$ the partial pressure of oxygen (P_{O_2}) that is necessary for formation of AlN is around 10^{-19} Pa (Equation 21). Such a low oxygen pressure is difficult to attain even after passing the nitrogen gas through deoxidating traps.

At high temperatures, Mg vaporizes and acts as an “oxygen-getter.” It combines with oxygen and thus it locally lowers the partial pressure of the residual oxygen in the nitriding gas. The reactions are given as Equations 22 and 23.

Depending on the temperature and the concentration of Mg, the equilibrium partial pressure of O_2 is given by Equation 24, γ is the activity coefficient of Mg, x is the Mg concentration, G_{22} and G_{23} are the standard Gibbs energy changes for reactions 22 and 23, respectively. From thermodynamic data reported in the literature, the par-

tial pressure of the residual oxygen for 15 wt.% Mg is in the range of 0.1 Pa. It can be stated that the mechanism of AlN formation is direct and assisted by Mg.

When silicon is added to the melt, XRD analyses reveal that AlN and MgO do not form, whereas Mg_2Si (magnesium silicide) precipitates as shown in Figure 8. It is hypothesized that the synthesis of the Mg_2Si phase is favored compared to the synthesis of MgO, and that the Mg content in the melt becomes depleted by the precipitation of the Mg_2Si phase. As a result, AlN cannot form due to the high oxygen content in the reactive gas. An important note concerning the temperature of formation of MgO, and thus AlN, is that the Mg_2Si phase begins to form at 680°C and its formation is complete at 550°C (Figure 9). Therefore, MgO formation must occur at temperatures equal or smaller than 680°C . This leads us to conclude that direct nitridation of aluminum occurs during cooling and not at temperatures $\sim 1,000^\circ\text{C}$.

Model Outcomes

Bubble Radius

The bubble may shrink due to the diffusion of nitrogen ahead of the gas-liquid interface (conservation of mass), and may also expand due to a decrease in the hydrostatic pressure as it rises in the melt. Expansion is slight-

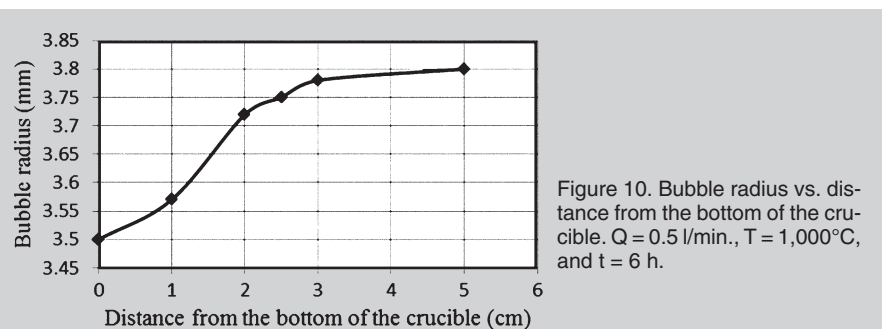


Figure 10. Bubble radius vs. distance from the bottom of the crucible. $Q = 0.5 \text{ l/min.}$, $T = 1,000^\circ\text{C}$, and $t = 6 \text{ h}$.

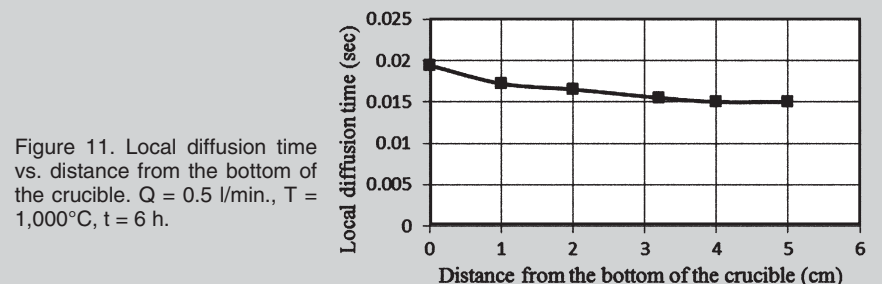


Figure 11. Local diffusion time vs. distance from the bottom of the crucible. $Q = 0.5 \text{ l/min.}$, $T = 1,000^\circ\text{C}$, $t = 6 \text{ h}$.

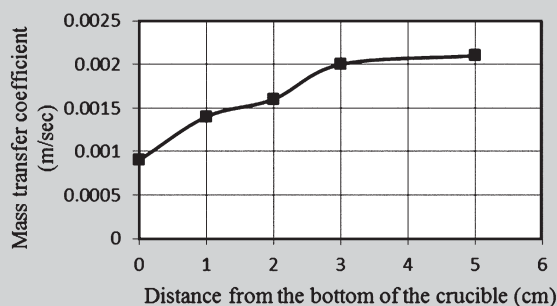


Figure 12. Mass transfer coefficient vs. distance from the bottom of the crucible. $Q = 0.5$ l/min., $T = 1,000^\circ\text{C}$, $t = 6$ h.

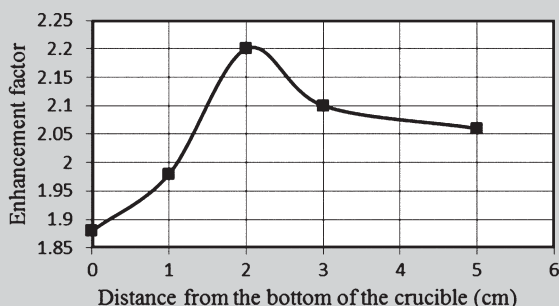


Figure 13. Enhancement factor vs. distance from the bottom of the crucible. $Q = 0.5$ l/min., $T = 1,000^\circ\text{C}$, $t = 6$ h.

ly predominant (Figure 10) but overall, the bubble radius remains nearly constant. This can be attributed to the small depth of the crucible used in our experiments (~5 cm) which limits the effect of both the hydrostatic pressure and the mass diffusion. The model has no restrictions and can be applied to domains of any size range. For industrial bubble columns (meters tall), the variation in bubble radius is expected to be larger. The detachment radius of 3.5 mm (large bubble regime) also induces dimensional stability of the bubble during its rise. Clift et al.³⁰ demonstrated that large bubbles ($r_b > 2$ mm) rising in a liquid tend to retain their size and their velocity.

Rate of Formation of AlN Particles

The bubble radius and velocity, the local diffusion time t_d , the mass transfer coefficient K_L , were used to calculate the Enhancement Factor E , which is used to determine the rate of aluminum nitride formation. Figures 11 and 12 show a slight decrease in the local diffusion time and an increase in the mass transfer coefficient as the bubble approaches the surface of the melt and expands. An explanation of this phenomenon is given by Pinheiro,³¹ who claims that when a gas bubble expands, the diffusion boundary layer ahead of the gas-liquid interface is stretched, and its thickness (δ) decreases. Hence, according to the relation $K_L = D/\delta$, the

mass-transfer coefficient increases. The lower diffusion time is also due to the decrease in the thickness of the diffusion boundary layer.

The enhancement factor remains nearly constant at 2 (Figure 13). It has been shown that for bubble column reactors the scatter in E as the bubble rises in the liquid is more consistent. Therefore, E is strictly correlated to the residence time of the bubble in the liquid, which in our case—small liquid pool—is limited. Figure 14 shows that the rate of formation of AlN particles in the melt increases in the upper part

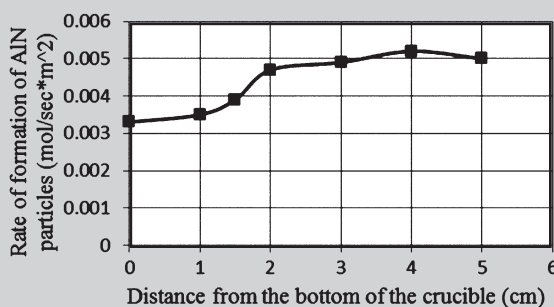


Figure 14. Rate of formation of AlN particles vs. distance from the bottom of the crucible. $Q = 0.5$ l/min., $T = 1,000^\circ\text{C}$, $t = 6$ h.

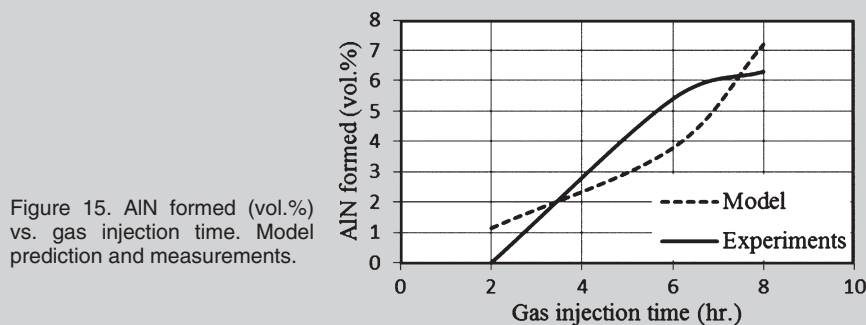


Figure 15. AlN formed (vol.%) vs. gas injection time. Model prediction and measurements.

of the crucible. This phenomenon has been experimentally confirmed, since AlN has been detected mainly in the upper section of the casting for all processing times.

Validation of the Model

In order to confirm the results of the model, the sample was weighed and compared with the base alloy. The weight loss due to evaporation has been taken into account by performing experiments under the same conditions but without injecting gas in the matrix alloy. The difference in molecular weight was also taken into account. Figure 15 shows that the model predictions and the experimental results are in good agreement. For two hours injection time, the model predicts the synthesis of some AlN, whereas no AlN was experimentally detected. It appears that the accuracy of the model increases with gas injection time. A comment concerning the effect of Mg addition on the validity of the model is worth making. The increase in the measured weight is due to the formation of AlN and MgO. The model does not take into account such phenomenon. The chemistry of the matrix, as well as the composition of the reactive gas, plays a fundamental role in the dynamics of the process. The model will be optimized by considering the effect of trace amounts of oxygen in the reactive gas and the addition of alloying elements.

CONCLUSIONS

Liquid-gas nitridation of aluminum is feasible. The in-situ route to manufacturing nanocomposites has the potential to be a commercial process where scalability and cost-effectiveness are important criteria. AlN particles, whose thermal and electrical properties are exceptional, have been successfully synthesized. It is found that:

- For higher injection times, the size of the AlN particles is in the sub-micron range and particles distribution is improved.
- The presence of Mg in the casting is necessary for the formation of AlN. When pure aluminum is used as a matrix, AlN did not form. XRD analysis and SEM observations showed the presence of MgO along with AlN. This suggests an alternative hypothesis about the mechanism of formation of nitrides. Oxygen content is lowered by the formation of MgO, and AlN forms through direct Mg-assisted nitridation.
- Silicon totally hinders the nitridation reaction. No MgO was detected, but magnesium silicide was present in the microstructure. This suggests that Mg₂Si suppresses the formation of MgO. Since the latter precipitates during cooling, aluminum nitridation may take place at lower temperatures during cooling.
- A reliable model for the prediction of the amount of AlN that forms has been developed and validated. The variation of local diffusion time, mass transfer coefficient, en-

hancement factor (E), and rate of AlN formation along the depth of the crucible was investigated. The rate of formation of AlN increases near the surface of the melt as the gas bubble expands during its rise. The model can be applied to domains of any size. The effect of alloying elements will be studied with the intent to further optimize the model.

ACKNOWLEDGEMENTS

The authors gratefully acknowledge the member companies of the Advanced Casting Research Center for their support of this work, and for their continued support of research focused on the science and technology of metal casting at Worcester Polytechnic Institute.

References

1. P.M. Ajayan, L.S. Schadler, and P.V. Braun, *Nanocomposite Science and Technology* (Weinheim, Germany: Wiley-VCH, 2003).
2. C.C. Koch, *Nanostructured Materials: Processing, Properties, and Applications* (Norwich, NY: William Andrew, 2006).
3. L. Xiaodan, Z. Yuchun, Q. Feng, and Z. Haixin, *Supplemental Proceedings, Volume 2, Materials Characterization, Computation, Modeling and Energy* (Warrendale, PA: TMS, 2010), pp. 295–300.
4. S. Gierlotka, *Solid State Phenomena*, 101-102 (2005), pp. 157–164.
5. Y. Yang, J. Lan, and X. Li, *Material Science and Engineering*, A380 (2004), pp. 378–383.
6. Z.Y. Ma, Y.L. Lia, Y. Liang, L.F. Zheng, J. Bi, and S.C. Tjong, *Materials Science and Engineering*, A219 (1996), pp. 229–231.
7. D.L. Zhang, J. Liang, and J. Wu, *Materials Science and Engineering*, A375–377 (2004), pp. 911–916.
8. Y. Huashun, J.D. Kim, and S.B. Kang, *Materials Science and Engineering*, A386 (2004), pp. 318–325.
9. Q. Hou, R. Mutharasan, and M. Koczak, *Materials Science and Engineering*, A195 (1995), pp. 121–129.
10. B.S.S. Daniel and V.S.R. Murthy, *Materials & Design*, 76 (3) (1995), pp. 155–161.
11. K.B. Lee, H.S. Sim, S.W. Heo, S.W. Cho, and H. Kwon, *Metals and Materials*, 6 (1) (2000), pp. 25–32.
12. M.J. Koczak and K.S. Kumar, "In Situ Process

for Producing a Composite Containing Refractory Material," U.S. patent 4,808,372.370 (1989).

13. J. Haibo, K. Chen, Z. Heping, S. Agathopoulos, O. Fabrichnaya, and J.M.F. Ferreira, *J. Crystal Growth*, 281 (2005), pp. 639–645.

14. P. Shtapitanonda and J. Magrave, "Kinetics of Nitridation of Mg and Al" (Paper presented at a symposium at the University of Wisconsin-Madison, 1956).

15. M.I. Pech-Canul, R.N. Katz, and M.M. Makhlof, *Metall. and Mats. Trans.*, 31A (2000), pp. 565–573.

16. H.Z. Ye, X.Y. Liu, and B. Luan, *J. Mats. Proc. Technol.*, 166 (2005), pp. 79–85.

17. Q. Zheng, B. Wu, and R.G. Reddy, *Adv. Engrg. Mats.*, 5 (3) (2003), pp. 167–173.

18. Q. Zheng and R.G. Reddy, *High Temperature Materials and Processes*, 22 (2) (2003), pp. 63–71.

19. S. Tyagi, Q. Zheng, and R.G. Reddy, *Aluminum 2004*, ed. S.K. Das (Warrendale, PA: TMS, 2004), pp. 63–72.

20. Q. Zheng and R.G. Reddy, *Affordable Metal Matrix Composites for High Performance Applications II*, ed. A.B. Pandey, K.L. Kendig, J.J. Lewandowski, and S.R. Shah (Warrendale, PA: TMS, 2003), pp. 125–134.

21. Q. Zheng and R.G. Reddy, *J. Mater. Sci.*, 39 (2004), pp. 141–149.

22. L. Jinxiang, Gao Xiuying, C. Jianfeng, W. Qun, S. Yuhui, and G. Qin, *Thermochimica Acta*, 253 (1995), pp. 265–273.

23. R.G. Reddy and V. Kumar, *Materials Science Forum*, 561-565 (2007), pp. 701–704.

24. H. Scholz and P. Greil, *J. Mater. Sci.*, 26 (3) (1991), pp. 669–677.

25. J. Szekely, *Fluid Flow Phenomena in Metals Processing* (New York: Academic Press, 1979).

26. C.E. Brennen, *Cavitation and Bubble Dynamics* (New York: Oxford University Press, 1995).

27. E.L. Cussler, *Diffusion: Mass Transfer in Fluid Systems* (New York: Cambridge University Press, 1997).

28. H.D. Baehr and K. Stephan, *Heat and Mass Transfer*, 2nd edition (New York: Springer, 2006).

29. T. Madhavi, A.K. Goldera, A.N. Samantaa, and S. Ray, *Chemical Engineering Journal*, 128 (2-3) (2007), pp. 95–104.

30. R. Clift, J.R. Grace, and M.E. Weber, *Bubbles, Drops and Particles* (New York: Academic Press, 1978).

31. M.N.C. Pinheiro, *Int. Communications in Heat and Mass Transfer*, 27 (1) (2000), pp. 99–108.

32. J.J. Carberry, *Chemical and Catalytic Reaction Engineering* (New Chemsford, MA: Courier Dover Publications, 2001).

C. Borgonovo, cborgonovo@wpi.edu, **D. Apelian**, dapelian@wpi.edu, and **M.M. Makhlof**, mmm@wpi.edu, are with the Metal Processing Institute, Worcester Polytechnic Institute, Worcester, MA.

D. Apelian is a TMS Member!

To read more about him, turn to page 14. To join TMS, visit www.tms.org/Society/Membership.aspx.

TMS